國立中山大學材料科學研究所

博士論文

Ti_3Al 基合金之低溫超塑性與應變誘發相變化研究

Low Temperature Superplasticity and Strain Induced Phase Transformation in Ti_3Al Based Alloy

研究生：楊凱琳 撰

指導教授：黃志青 博士

中華民國 九十二 年 十二 月

國立中山大學研究生學位論文審定書

本校材料科學研究所博士班
研究生 楊凱琳（學號：8836811 ）所提論文

Ti3Al基合金之低溫超塑性與應變誘發相變化研究

經本委員會審查並舉行口試，符合博士學位論文標準。

學位考試委員簽章：

何扭今教授
國立中山大學材料科學研究所

沈博彥
沈博彥教授
國立中山大學材料科學研究所

黃永茂教授
國立中山大學機械與機電工程學系

曹紀元教授
國立成功大學材料科學與工程學系

鄭憲清
鄭憲清教授
私立義守大學材料科學與工程學系

指導教授 黃志青
黃志青教授
國立中山大學材料科學研究所

所長 曾百亨
曾百亨教授
國立中山大學材料科學研究所

博碩士論文授權書

(國科會科學技術資料中心版本 92.2.17)

本授權書所授權之論文為本人在＿國立中山＿大學＿材料科學研究所＿九十二＿學年度第＿一＿學期取得＿博＿士學位之論文。

論文名稱：＿Ti_3Al 基合金之低溫超塑性與應變誘發相變化研究＿

■同意　□不同意　(政府機關重製上網)

本人具有著作財產權之論文全文資料，授予行政院國家科學委員會科學技術資料中心、國家圖書館及本人畢業學校圖書館，得不限地域、時間與次數以微縮、光碟或數位化等各種方式重製後散布發行或上載網路。

本論文為本人向經濟部智慧財產局申請專利(未申請者本條款請不予理會)的附件之一，申請文號為：＿＿＿＿＿＿，註明文號者請將全文資料延後半年再公開。

■同意　□不同意　(圖書館影印)

本人具有著作財產權之論文全文資料，授予教育部指定送繳之圖書館及本人畢業學校圖書館，為學術研究之目的以各種方法重製，或為上述目的再授權他人以各種方法重製，不限地域與時間，惟每人以一份為限。

上述授權內容均無須訂立讓與及授權契約書。依本授權之發行權為非專屬性發行權利。依本授權所為之收錄、重製、發行及學術研發利用均為無償。上述同意與不同意之欄位若未鉤選，本人同意視同授權。

指導教授姓名:黃志青

研究生簽名:　　　　　　　　　　學號:8836811

(親筆正楷)　　　　　　　　　　(務必填寫)

日期:民國　92 年 12 月 18 日

---

1. 本授權書（得自 http://sticnet.stic.gov.tw/sticweb/html/theses/authorize.html 下載或至 http://www.stic.gov.tw 首頁右下方下載）請以黑筆撰寫並影印裝訂於書名頁之次頁。
2. 授權第一項者，請確認學校是否代收，若無者，請個別再寄論文一本至台北市(106-36)和平東路二段 106 號 1702 室 國科會科學技術資料中心 王淑貞。(本授權書諮詢電話:02-27377746)
3. 本授權書於民國 85 年 4 月 10 日送請內政部著作權委員會(現為經濟部智慧財產局)修正定稿，89.11.21 部份修正。
4. 本案依據教育部國家圖書館 85.4.19 台(85)圖編字第 712 號函辦理。

學年度：92

學期：1

院校：國立中山大學

系所：材料科學研究所

論文名稱（中）：Ti_3Al **基合金之低溫超塑性與應變誘發相變化之研究**

論文名稱（英）：Low Temperature Superplasticity and Strain Induced Phase Transformation in Ti_3Al Based Alloy

學位類別：博士

語文別：英文

學號：8836811

提要開放使用：是

頁數：182

研究生(中)姓：楊

研究生(中)名：凱琳

研究生(英)姓：Yang

研究生(英)名：Kai-Lin

指導教授(中)：黃志青

指導教授(英)： J. Chih-Ching Huang

關鍵字(中)：鈦合金	**關鍵字(英)：**Titanium alloys
關鍵字(中)：超塑性	**關鍵字(英)：**Superplasticity
關鍵字(中)：變形機構	**關鍵字(英)：**Deformation mechanism
關鍵字(中)：相變化	**關鍵字(英)：**Phase transformation
關鍵字(中)：非等向性	**關鍵字(英)：**Anisotropy
關鍵字(中)：織構	**關鍵字(英)：**Texture
關鍵字(中)：背向散射電子繞射儀	**關鍵字(英)：**EBSD

TABLE OF CONTENTS

TABLE OF CONTENTS …… i

LIST OF TABLES …… iv

LIST OF FIGURES …… vi

ABSTRACT …… xiii

中文提要 …… xv

致謝 …… xvi

CHAPTER 1 Background and Research Motive …… 1

- 1.1 Introduction to Ti_3Al intermetallic compounds …… 1
  - 1.1.1 The characteristics of Ti_3Al …… 1
  - 1.1.2 The structures and properties of Ti_3Al …… 1
- 1.2 Processing for producing fine-grained Ti_3Al alloys …… 3
- 1.3 Introduction to superplasticity and deformation mechanisms …… 6
  - 1.3.1 Introduction to superplasticity …… 6
  - 1.3.2 Deformation mechanisms …… 11
- 1.4 Superplastic behavior in Ti_3Al alloys …… 13
  - 1.4.1 HTSP in Ti_3Al alloys …… 13
  - 1.4.2 LTSP in Ti_3Al alloys …… 17
  - 1.4.3 LTSP and HSRSP in other Ti based alloys …… 19
- 1.5 Phase transformation phenomena …… 21
- 1.6 Anisotropy during superplastic deformation …… 23
- 1.7 The texture analyses on Ti_3Al alloys …… 24
- 1.8 Introduction to electron back scatterred diffraction (EBSD) …… 28
  - 1.8.1 Advantages of EBSD …… 28
  - 1.8.2 The basic principles and set-up of a typical EBSD system …… 29

1.9 Motive of the research……31

CHAPTER 2 Experimental Methods……33

2.1 Materials……33

2.2 Mechanical tests……33

2.3 Anisotropic tests……34

2.4 Retention of microstructure for tensile specimens……35

2.5 Microstructure characteristics……35

2.5.1 OM and SEM observations……35

2.5.2 TEM observations……36

2.6 Volume fraction determinations……36

2.7 Texture analyses……37

CHAPTER 3 Experimental Results……39

3.1 Microstructure characterization of the as-received materials……39

3.2 Mechanical tests……40

3.2.1 Room temperature properties……40

3.2.2 Elevated temperature properties……40

3.3 Anisotropic tests……41

3.4 Microstructure evolutions……42

3.4.1 Static annealing……42

3.4.2 The crystal relationship between β and α_2'……45

3.4.3 Microstructural evolution during superplastic loading……46

3.5 Texture analyses……48

3.5.1 The as-received materials……48

3.5.2 Texture evolution during anisotropic tensile straining……53

3.5.2.1 Lower temperature at 750^{o}C……54

3.5.2.2 Higher temperature at 920^{o}C……55

3.5.2.3 Grain misorientation distributions at 750°C and 920°C....……56

3.5.2.4 Texture evolution as a function of superplastic strain……..…58

CHAPTER 4 Discussions……....……………………………………………….…60

4.1 Deformation mechanisms……………………….…………………….………...60

4.1.1 Apparent strain rate sensitivity (m_a) ………………………….……….60

4.1.2 Apparent activation energy (Q_a) …………….……………….…….…60

4.1.3 Threshold stress (σ_{th}), true strain rate sensitivity (m_t), and true activation energy (Q_t) ………………………………………………….………61

4.1.4 Deformation mechanisms during LTSP……...……………….……….63

4.2 Phase transformation characteristics………………………………….……64

4.2.1 β to α_2 transformation behaviors………………………………….……64

4.2.2 Deformation enhanced transformation…………………………….……67

4.2.3 Relationship between microstructure transformation and superplastic performance……………………………………………………………..……69

4.3 The relationship among texture, mechanical anisotropy and superplasticity…...…70

4.3.1 Texture evolution during thermomechanical treatment………………..…70

4.3.2 Texture evolution during superplasticity…………………………….……72

4.3.3 Influence from textures on the mechanical anisotropy……………..……73

4.3.3.1 Microstructure effects on the mechanical anisotropy………...73

4.3.3.2 Texture effects on the mechanical anisotropy……………..…73

CHAPTER 5 Conclusions……....…………………………………………………….76

REFERENCES…………………………………………………………………….…79

TABLES……………………………………………………………………………….86

FIGURES…………………………………………………………………………...106

LIST OF TABLES

Table 1 Summary of typical intermetallic compounds…..…….……………………….……86

Table 2 The main accommodation processes accommodated for GBS………..…………87

Table 3 Models of CGBS……………………………………………………………89

Table 4 Summary of HTSP in Ti_3Al base alloys………………….……………………91

Table 5 Summary of LTSP in Ti_3Al base alloys……………….…………………......92

Table 6 Summary of LTSP or HRSP in other Ti based alloys…………….……………93

Table 7 The crystal parameters of the Ti_3Al-Nb alloy…………….……………………...94

Table 8 Summary of tensile properties at different strain rates and temperatures. The elongations listed here are subjected to ±10% uncertainty…………………..95

Table 9 Anisotropic tensile test results performed at room temperature and an initial strain rate of $3x10^{-3}$ s^{-1}………………………………………………………..96

Table 10 Anisotropic tensile test results performed at elevated temperatures and an initial strain rate of $5x10^{-4}$ s^{-1}……………………………..……………………96

Table 11 The grain sizes and volume fractions in specimens statically annealed for 1.5 h and then water quenched………………...…………………..…………………...97

Table 12 Measurement of the α_2' thickness, h, and the relative volume fractions in specimens statically annealed at 800 and 850°C for different periods of time and then water quenched……………………………….……………………98

Table 13 The relative volume fractions in specimens statically annealed at 850°C for 1.5 h and then cooled under different conditions……………..……………………..98

Table 14 The α_2 grain size and relative volume fractions in the tensile loaded specimens deformed to failure……………………..……………….……………………..99

Table 15 Measurement of the α_2' thickness, h, and the relative volume fractions in specimens tensile loaded at 850°C and $5x10^{-4}$ s^{-1} to different engineering elongations or true strains ε........................……………….……………………100

Table 16 The misorientation angle distribution in the theoretically random case, the as-received alloy, and the 0^o post-SP specimens at 750 and 920°C……………101

Table 17 The misorientation angle distribution in the theor etical randomly case, and the post-SP 0^o specimen performed at 850°C and $5x10^{-4}$ s^{-1} to different true strains ε………………………………………………………………………………101

Table 18 The textures sharpness measured from the AR alloy and the post-SP specimens………………………………………………………………………..…102

Table 19 The apparent m_a-values and the true m_t-values at 700-850°C…………………103

Table 20 The apparent Q_a-values and the true Q_t-values at 700-850°C…………………..104

Table 21 Schmid factors calculated for the β phase………………………………………104

Table 22 Schmid factors calculated for the α_2 phase……………………………………..105

LIST OF FIGURES

Fig. 1 Ti-Al binary equilibrium phase diagram…..………………………………………106

Fig. 2 (a) Phase diagram of the Ti_3Al-Nb system, and (b) relative volume fractions of the α_2 and β phases in accordance with the equilibrium phase diagram……………107

Fig. 3 The crystal structures of the (a) α_2, (b) O, and (c) β phases……………………..108

Fig. 4 A vertical section along the Ti-27.5Al-Nb for the Ti-Al-Nb system. For Ti_3Al with the Nb content ~10 at%, the stable phases at the TMT processing temperature of ~1000-1200°C are only α_2 and B2……………..…………………………………109

Fig. 5 Illustration of the principle of an EBSD system…………………………………..110

Fig. 6 Illustration of the set-up of an EBSD system……………………………………..110

Fig. 7 Schematic Euler angles (φ_1, ϕ, φ_2), which would specify an orientation…………111

Fig. 8 Schematic illustration of the misorientation angle between two grains…………..111

Fig. 9 Schematic drawing of the specimen dimension for tensile tests at (a) elevated temperatures (with a gauge length of 5.5 mm), and (b) room temperature (with a gauge length of 10 mm)…………………………………………………………112

Fig. 10 Illustration of the design for quenching by liquid nitrogen……………………….113

Fig. 11 SEM micrograph showing the three-dimensional microstructure of the as-received material (the darker phase is the α_2 phase and the ligher one is the β phase)……114

Fig. 12 OM micrographs of the as-received material taken from the (a) rolling plane, (b) longitudinal plane, and (c) transverse plane………………………………………115

Fig. 13 (a) TEM micrograph of the as-received material, with the diffraction patterns taken from the (b) α_2 $[2\bar{1}\bar{1}0]$ and (c) β [001] zones………………………………….117

Fig. 14 Representative planer slip in the β phase…………………………………………118

Fig. 15 The (a) engineering and (b) true stress-strain curves recorded from tensile tests performed at room temperature (25^{o}C) and an initial strain rate of $3x10^{-3}$ s^{-1}........119

Fig. 16 The dependence of superplastic elongations as a function of loading temperature at four different initial strain rates……………………………………………………120

Fig. 17 The dependence of superplastic elongations as a function of strain rate at representative temperatures……………………………………………………………120

Fig. 18 The appearance of specimens before and after superplastic loading at 850^{o}C and $5x10^{-4}$ s^{-1}…………………………………………………………………………..121

Fig. 19 Typical true stress-strain curves recorded from tensile tests at different initial strain rates for the loading temperatures of (a) 700^{o}C, (b) 750^{o}C, (c) 800^{o}C, and (d) 850^{o}C...122

Fig. 20 The variation of engineering UTS as a function of loading temperature at 700-1000^{o}C……………………………………………………………………………124

Fig. 21 The stress-strain curves recorded from the anisotropic tests under an initial strain rate of $3x10^{-3}$ s^{-1} performed at (a) room temperature, and under an initial strain rate of $5x10^{-4}$ s^{-1} performed at (b) 750^{o}C, (c) 850^{o}C, and (d) 920^{o}C……………………125

Fig. 22 Representative anisotropic tensile specimens loaded at 920^{o}C and $5x10^{-4}$ s^{-1}……127

Fig. 23 Representative SEM micrographs showing the microstructures in the statically annealed specimens for 1.5 h for (a) 700^{o}C, (b) 750^{o}C, (c) 800^{o}C, (d) 850^{o}C, (e) 900^{o}C, and (f) 960^{o}C……………………………………………………………128

Fig. 24 TEM micrograph of the specimen statically annealed at 850^{o}C for 1.5 h, with the diffraction pattern taken from the $[11\bar{2}0]$ zone of the transformed α_2’ phase.…129

Fig. 25 TEM micrographs showing dislocation structures in the α_2 and β phases in the sample annealed at 850^{o}C for 1.5 h and then water quenched……………………130

Fig. 26 Typical SEM micrographs showing the microstructures evolution during static annealing at (a) 800^{o}C for 30 min, (b) 800^{o}C for 2.5 h, (c) 850^{o}C for 3 min, and (d)

850^{o}C for 1.5 h……………………………………………………………………131

Fig. 27 EBSD patterns taken from the (a) α_2’ grain and (b) β grain. The overlapped stereographic projections in (c) shows the orientation relationship between the α_2’ and β phases……………………………………………………………………132

Fig. 28 SEM micrographs showing the microstructures in the superplastically loaded specimens: (a) grip, 700^{o}C, (b) gauge, 700^{o}C, (c) grip, 800^{o}C, (d) gauge, 800^{o}C..133

Fig. 29 Variation of the α_2’ volume fraction as a function of the annealing or loading temperature……………………………………………………………………134

Fig. 30 SEM micrographs showing the microstructures in the gauge sections of the specimens loaded at 850^{o}C and 5x10^{-4} s^{-1} to a true strain of (b) ε=0.3, (c) ε=1.0, (d) ε=1.2, (e) ε=1.4, (f) ε=1.5 (failure), and then stopped and rapidly quenched by blowing liquid nitrogen. The true stress and strain curve is shown in (a), which is plotted from the measurements of these stopped specimens……………………135

Fig. 31 X-ray pole figures of the as-received material: (a) the β phase (200) plane with the maximum intensity contour level of 40, and (b) the α_2 phase $(11\bar{2}0)$ plane with maximum contour of 10……………………………………………………………137

Fig. 32 (a) Pole figures, (b) inverse pole figures, and (c) ODF of the β phase in the as-received specimen……………………………………………………………138

Fig. 33 The sequence for texture determination: (a) a {100} pole figure; (b) choose a standard projection to make all the {100} poles in (a) occupy the {100} pole family in (b); (c) {ND}<RD> could be identified……………………………………139

Fig. 34 Schematic illustration of the hexagonal system represented by {$OX_1X_2X_3$} and the cubic system represented by {OXYZ}…………………………………………140

Fig. 35 (a) Pole figures, (b) inverse pole figures, and (c) ODF of the α_2 phase in the as-received specimen……………………………………………………………141

Fig. 36 (a) The SEI image and phase map in the as-received specimen. The OIMs displace the orientation distribution of (b)-(d) in the β phase and (f)-(h) in the α_2 phase. By using the orientation color key (e) and (i), orientation in the β and α_2 phases are visualized, respectively……………………………………………………...142

Fig. 37 Five regions sampled from the β phase in the as-received specimen: strong {100}<011> rotated cube and weak $\{111\}<1\bar{2}1>$ textures are present in (a), (b), and (c); occasional strong {110}<001> Goss in (d); and strong $\{111\}<2\bar{1}\bar{1}>$ in (e)..144

Fig. 38 Five regions sampled from the α_2 phase in the as-received specimen: strong $\{11\bar{2}0\}$<0001> and weak $\{0001\}<\bar{1}100>$ and $\{11\bar{2}0\}<\bar{1}100>$ are present in (a), (b), and (c); strong $\{11\bar{2}0\}$<0001> and weak $\{0001\}<11\bar{2}0>$ and {0001} fiber in (d); strong $\{0001\}<11\bar{2}0>$ and weak $\{0001\}<\bar{1}100>$ and {0001} fiber in (e).…146

Fig. 39 (a) Pole figures, (b) inverse pole figures, and (c) ODF of the β phase in the 0^o specimen loaded at 750^oC and $5x10^{-4}$ s^{-1}………………………………………148

Fig. 40 (a) Pole figures, (b) inverse pole figures, and (c) ODF of the α_2 phase in the 0^o specimen loaded at 750^oC and $5x10^{-4}$ s^{-1}………………………………………149

Fig. 41 (a) Pole figures, (b) inverse pole figures, and (c) ODF of the β phase in the 45^o specimen loaded at 750^oC and $5x10^{-4}$ s^{-1}………………………………………150

Fig. 42 (a) Pole figures, (b) inverse pole figures, and (c) ODF of the α_2 phase in the 45^o specimen loaded at 750^oC and $5x10^{-4}$ s^{-1}………………………………………151

Fig. 43 (a) Pole figures, (b) inverse pole figures, and (c) ODF of the β phase in the 90^o specimen loaded at 750^oC and $5x10^{-4}$ s^{-1}…………………………………………152

Fig. 44 (a) Pole figures, (b) inverse pole figures, and (c) ODF of the α_2 phase in the 90^o specimen loaded at 750^oC and $5x10^{-4}$ s^{-1}…………………………………………153

Fig. 45 (a) {111} and (b) $\{11\bar{2}0\}$ standard stereographic projections……………………154

Fig. 46 (a) Pole figures, (b) inverse pole figures, and (c) ODF of the β phase in the 0^o specimen loaded at 920^oC and $5x10^{-4}$ s^{-1}…………………………………………155

Fig. 47 (a) Pole figures, (b) inverse pole figures, and (c) ODF of the α_2 phase in the 0^o

specimen loaded at 920^{o}C and 5x10^{-4} s^{-1}……………………………………………156

Fig. 48 Standard {0001} stereographic projection. After superplastic loading, the {0001}<$\bar{4}$310> texture is present in the α_2 phase in the 0^o specimens loaded at 750 and 920^{o}C……………………………………………………………………157

Fig. 49 (a) Pole figures, (b) inverse pole figures, and (c) ODF of the β phase in the 45^o specimen loaded at 920^{o}C and 5x10^{-4} s^{-1}……………………………………………158

Fig. 50 (a) Pole figures, (b) inverse pole figures, and (c) ODF of the α_2 phase in the 45^o specimen loaded at 920^{o}C and 5x10^{-4} s^{-1}……………………………………………159

Fig. 51 (a) Pole figures, (b) inverse pole figures, and (c) ODF of the β phase in the 90^o specimen loaded at 920^{o}C and 5x10^{-4} s^{-1}……………………………………………160

Fig. 52 (a) Pole figures, (b) inverse pole figures, and (c) ODF of the α_2 phase in the 90^o specimen loaded at 920^{o}C and 5x10^{-4} s^{-1}……………………………………………161

Fig. 53 Pole figures obtained from the 0^o specimens loaded at (a) 750^{o}C and (b) 920^{o}C. Orientation distributions become much more random at higher temperatures…162

Fig. 54 The random grain misorientation distribution in the cubic and hexagonal systems. Redrawn from ref. [105,106]……………………………………………………163

Fig. 55 Misorientation angle distributions of the (a) α_2 and (b) β phases in the AR alloy, (c) α_2 and (d) β phases in the post-SP 0^o specimens at 750^{o}C, (e) α_2 and (f) β phases in the post-SP 0^o specimens at 920^{o}C…………………………………………164

Fig. 56 SEM micrograph showing the microstructure at the fracture tip of the post-SP specimen loaded at 920^{o}C and 5x10^{-4} s^{-1}. The volume fraction of the light β phase and the darker α_2 phase are nearly 50% to 50%…………………………………165

Fig. 57 Texture evolution while superplastic loading at 850^{o}C and 5x10^{-4} s^{-1} to a true strain of (a) ε=0.3, (b) ε=1.0, (c) ε=1.2, (d) ε=1.5 (failure) in the β phase…………166

Fig. 58 Texture evolution while superplastic loading at 850^{o}C and 5x10^{-4} s^{-1} to a true strain of (a) ε=0.3, (b) ε=1.0, (c) ε=1.2, (d) ε=1.5 (failure) in the α_2 phase……………168

Fig. 59 Misorientation angle distribution of the α_2 and β phases at various true strain locations with ε~0.3, 1.0, 1.2 and 1.5 in the post-SP 0^o specimen performed at 850^oC and $5x10^{-4}$ s^{-1}: (a) ε=0.3, α_2 phase, (b) ε=0.3, β phase, (c) ε=1.0, α_2 phase, (d) ε=1.0, β phase, (e) ε=1.2, α_2 phase, and (f) ε=1.2, β phase, (g) ε=1.5, α_2 phase, and (h) ε=1.5, β phase.……………………………………………………………170

Fig. 60 The dependence of the flow stress versus the strain rate for (a) 700, (b) 750, (c) 800, and (d) 850^oC, from the slope the m_a-value can be extracted.……………………171

Fig. 61 Dependence on (1/T) for (a) ln ($\dot{e}$) under a fixed stress condition, and (b) ln (σ) under a fixed strain condition for 700-750^oC. From the slope, the apparent activation energy can be extracted……………………………………………..173

Fig. 62 Dependence on (1/T) for (a) ln ($\dot{e}$) under a fixed stress condition, and (b) ln (σ) under a fixed strain condition for 800-850^oC. From the slope, the apparent activation energy can be extracted………………………………………………174

Fig. 63 The plot for extracting the threshold stress σ_{th} at 700-750^oC by substituting n_t=4, 5, and 6……………………………………………………………………175

Fig. 64 The plot for extracting the threshold stress σ_{th} at 800-850^oC by substituting n_t=2.5, 3, and 3.5……………………………………………………………………176

Fig. 65 Dependence on (1/T) for (a) ln ($\dot{e}$) under a fixed stress condition, and (b) ln ($\sigma-\sigma_0$) under a fixed strain condition for 700-750^oC. From the slope, the apparent activation energy can be extracted……………………………………………..177

Fig. 66 Dependence on (1/T) for (a) ln ($\dot{e}$) under a fixed stress condition, and (b) ln ($\sigma-\sigma_0$) under a fixed strain condition for 800-850^oC. From the slope, the apparent activation energy can be extracted.……………………………………………178

Fig. 67 (a) Variation of the α_2' thickness as a function of the square root of annealing time, $t^{1/2}$, at 800 and 850^oC, and (b) the extraction of activation energy Q……………179

Fig. 68 (a) Variation of the double logarithm of the transformation percentage of the α_2'

phase as a function of lnt, and (b) the extraction of transformation exponent n….180

Fig. 69 Illustrations of the volume change from the β to α_2' phase……………………….181

Fig. 70 (0002) pole figures for the specimens under the following conditions: (a) hot rolling and then isochronally annealed for 1 h at (b) 850, (c) 900, (d) 960, (e) 1020°C…182

ABSTRACT

Ti_3Al based intermetallic alloys are attractive for aerospace and aircraft applications due to their superior high temperature properties. Excellent high temperature superplasticity in the Ti_3Al-Nb based alloy has been widely published. However, the alloys become brittle and hard to deform at temperatures below 600°C so that low temperature superplasticity is difficult to develop. In the current super α_2 Ti_3Al based alloy, the ordered BCC β phase is the continuous matrix, with the DO_{19} hexagonal α_2 grains ~2.2 μm in grain size distributed uniformly in the β matrix. The initial β and α_2 volume fractions are around 60% and 40%, respectively, and strong textures are present in both phases. Although the alloy exhibits superior superplastic elongations over 1000% at 920-1000°C, the elongation drops appreciably to 600% at 900°C, 330% at 850°C and 140% at 750°C.

Upon subsequent static annealing and superplastic loading at 700-960°C, the alloy tends to undergo β to α_2' phase evolution, approaching to the equilibrium phase partition at the respective temperature. The transformation seems to be enhanced during dynamic straining at temperatures lower than 900°C, suggesting the strain enhanced phase transformation. With the fine α_2' laths inside the β grains, the accommodation process across the BCC β grains is impeded, leading to premature failure and lower tensile elongations at lower temperatures.

Mechanical anisotropy is observed in this alloy and relatively higher tensile elongations are obtained in the 45° specimen as loaded at room temperature to 960°C. The texture characteristics appear to impose significant influence on the mechanical anisotropy at temperatures below 750°C (under the dislocation creep condition), as well as during the initial stage at a higher temperature of 920°C (under the superplastic flow condition). Systematic tracing of the texture evolution from the as-received to superplastically loaded specimens has been accomplished using electron backscattered diffraction. With the extensive dislocation motion plus a certain degree of grain boundary sliding and grain rotation during loading at 750°C, the α_2 grains gradually rotate to form the {0001} basal texture and some of the β grains concentrate into the $\{111\}<2\bar{1}\bar{1}>$ orientation. At higher temperatures such as 920°C, extensive grain boundary sliding proceeds and results in grain orientation distributions for the α_2 and β phases basically random in nature. Rationalizations for the mechanical anisotropy in terms of the Schimid factor calculations for the major and minor texture components in the α_2 and β phases provide consistent explanations for the deformation behavior at lower temperatures as well as the initial straining stage at higher temperatures.

中文提要

Ti_3Al 基介金屬合金因其具有優異的高溫性質，因此是目前航太工業上倍受矚目的材料。本 Ti-25Al-10Nb-3V-1Mo 合金在高溫 950-1000^{o}C 及低應變速率 10^{-4}-10^{-5} s^{-1} 下具有相當卓越之高溫超塑性, 伸長率高達 1000%以上, 低溫則在 850^{o}C (0.57 T_m) 及 $5x10^{-4}$ s^{-1} 的應變速率下可獲得 330%的低溫超塑性。本研究係探討 Ti_3Al 合金之低溫超塑性質, 並針對本研究中之重要發現, 超塑性應變所誘發的相變化行為, 做一整合性之分析及探討，進而建立低溫超塑性之變形機制，此發現將有助於 Ti_3Al 合金低溫超塑性之開發。

本合金乃經由熱機處理所製成具有雙相(α_2+β)組織之軋延薄板，細晶粒(2.2 μm)的 α_2 相均匀分佈在β母相中，兩相體積分率約 40%比 60%。在 700-960^{o}C 靜態退火及超塑性拉伸過程中發現，α_2'相會經由原子擴散的方式，由β相轉變而來。這些經由相變化所產生的板條狀α_2'相, 因其會在β相中形成, 且與原先的α_2 相具有相同之 DO_{19} 結晶構造, 係屬不易變形的六方晶系, 因此會阻礙超塑性變形時的差排調適過程, 使得延展性大為降低, 此乃是造成低溫超塑性無法達成的主要因素, 此外, 再加上應變誘發相變化結果, 使得α_2'相大量產生，造成 900^{o}C 以下低溫超塑性之開發之困難性，本研究將對此一行為做深入性之探討。

另外，在機械非等向性行為研究方面，由室溫至高溫的非等向性機性測試中發現，當拉伸軸與軋延軸夾 45^{o} 方向進行超塑性拉伸時，可獲得最佳之超塑性質。主要是因為軋延織構的存在，影響到差排的移動能力，所造成的非等向性機械行為。除此之外，本研究也利用背向散射電子繞射(EBSD)的方法，研究織構行為、觀察變形織構之演變及晶界滑移的程度，進而對變形機制做關聯性之整合。

致謝

首先，我要獻上最高的敬意來感謝影響我一生的恩師 黃志青教授，因為有您的鼓勵，才使我有勇氣去挑戰博士學位，儘管漫長的求學過程中，經歷許許多多的低潮，老師您的關心和勉勵，讓我能夠一直堅持下去，並順利取得博士學位，我要再次說聲，老師，謝謝您，您辛苦了。感謝成功大學曹紀元教授、義守大學鄭憲清教授，以及本校何扭今教授、沈博彥教授與黃永茂教授參與論文審查工作，儘管審查過程相當辛苦，但您們所提供的意見，讓學生受益匪淺，本論文也在您們的指導下更加完美。

另外，由衷感謝本所高伯威與白世榮老師，經常適時的勉勵我、鼓勵我，讓我倍感溫馨，還有各實驗室技術員王良珠學姊、陳貴香小姐、江宏達先生、王國強先生、李秀月小姐、古錦松先生、許鑾先生，以及對我特別照顧的華應麒大哥，感謝你們的協助與關心。還有不可少的是，感謝我的小老闆，王軼農博士，常給予我指導與鼓勵，謝謝你。當然，研究室所有成員的幫忙，自是無法細數的，剛進黃幫即受到王宗鼎及蕭一清學長的照顧，陪我一起經歷研究酸甜苦辣的最佳戰友佩汝，以及低潮時一直幫我加油打氣的珮芸，謝謝你們。更要感謝的是，成大楊建民學長的寶貴意見，陳志鵬學長、吳玉娟學妹、小毛學姊與痰忠義同學在實驗上的幫忙，以及伏和中學長先前為 Ti_3Al 合金研究所奠定的基礎，對我實有莫大的幫助。

最後，感謝愛我的家人，在天國最支持我的爸爸、媽媽，不斷為我祈禱的爺爺、奶奶，以及關心我的哥哥和最貼心的弟弟，所有關愛我的親戚朋友，因為有你們，才有今天的我。當然，俊傑，謝謝你支持我到關鍵的最後一刻，你也要加油！

謝謝所有關心 Karen 的大家。

CHAPTER 1 Background and Research Motive

1.1 Introduction to Ti_3Al intermetallic compounds

1.1.1 The characteristics of Ti_3Al

Intermetallic alloys with an ordered structure usually have superior high-temperature properties than metals (i.e. high-temperature strength, good oxidation resistance, and advanced creep characteristics). Ti_3Al based intermetallic alloys have the advantages of both superior high-temperature properties and low density, which are highly attractive for aerospace and aircraft applications [1]. Currently, Ti_3Al based intermetallic alloys have already replaced some superalloys. Table 1 [2] lists some typical intermetallic compounds currently interested. However, Ti_3Al based alloys are known to be brittle and have low toughness at low temperatures because of their ordered structures. As a result, titanium based intermetallic alloys usually require a complicated fabrication process due to the limits of their poor fabricability and machinability. In comparing the three titanium based intermetallic alloys, namely Ti_3Al, TiAl, and $TiAl_3$, Ti_3Al based alloys have been significantly improved their room-temperature ductility which led to a better workability than TiAl and $TiAl_3$ by adding the β-stabilizing elements such as Nb, V, Mo, etc., or with thermomechanical treatments to reduce the grain sizes.

1.1.2 The structures and properties of Ti_3Al

Figure 1 shows the Ti-Al binary equilibrium phase diagram [1]. The structure of pure Ti_3Al is DO_{19}, P63/mmc, an ordered hexagonal phase, which is termed as the α_2 phase at temperatures below about 1100°C. Various elements such as Nb, V, W, and Mo are often added to the pure Ti_3Al alloys to stabilize the β phase and hence increase ductility. As a result, Ti_3Al based alloys usually have a duplex α_2 and β phase at temperatures below the β-transus temperature, T_β. It can be referred from the Ti-Al-Nb ternary equilibrium phase diagram (see Fig. 2(a)) [3], since the β -stabilizing element Nb is often added into Ti_3Al alloys. The structure of the β phase may be a disordered BCC structure or an ordered BCC (called the B2) structure. For the Ti_3Al alloy containing Nb, the disordered β phase present above the order-disorder transition temperature, $T_{O\text{-}D}$, could be transformed into the ordered β phase region during cooling. Since the volume fractions of the α_2 and β phases play an important role to superplasticity, as described in Sec. 1.4.1, the relative volume fractions in accordance with the equilibrium phase diagram are shown in Fig. 2(b).

For commercial Ti_3Al alloys, there are several important systems, such as the regular α_2 (Ti-24at%Al-11%Nb), super α_2 (Ti-25at%Al-10%Nb-3%V-1%Mo) and orthorhombic (Ti-22at%Al-26%Nb) materials. Although the $T_{O\text{-}D}$ will vary with the Al or Nb content, in regular α_2 and super α_2 alloys the $T_{O\text{-}D}$ is in the temperature range of 1100-1200°C [4-7]. The crystal structures of the α_2 and β phases are present in Fig. 3 [8,9]. For the α_2 phase, with the Nb element added, Nb will occupy the same sites as the Ti atoms [10,11]. In contrast, for the β phase, Ti atoms occupy one of the two possible sublattices, and Al and Nb atoms share the other [9].

Ti_3Al appeared to be brittle and hard to machine and form at temperatures below 600°C, which is related to the ordered DO_{19} structure. With the presence of the anti-phase boundary which acts as obstacles for dislocation activities, deformation could also be retarded. The important slip systems of this hexagonal structure are described as follow [12].

(1) The main slip system of the <a> type dislocation in the prism, pyramidal, and basal planes: These include slip systems such as $\{10\bar{1}0\} < 11\bar{2}0 >$, $\{10\bar{1}\bar{1}\} < 11\bar{2}0 >$, and $\{0001\} < 11\bar{2}0 >$.

(2) The <c+a> type dislocation in the pyramidal plane: These include slip systems such as $\{10\bar{1}\bar{1}\} < 11\bar{2}3 >$ and $\{11\bar{2}2\} < 11\bar{2}3 >$.

The movement of dislocations are mainly the <a> type dislocation acting on the prism, pyramidal, and basal planes. The primary slip system might be the <a> type dislocation in the prism plane, i.e. $\{10\bar{1}0\} < 11\bar{2}0 >$, for the α_2 phase with DO_{19} hexagonal structure since the c/a ratio is less than the ideal value. Therefore, the <a> type dislocations in the basal plane and the pyramidal plane are the secondary slip systems but still the main slip systems. Although the <a> type dislocation in the prism plane is still the main slip system at 800°C, the <a> type dislocation could proceed cross slip and combine with the <c> type dislocation forming the <c+a> type dislocation, which could improve the ductility at temperatures above 800°C [13].

1.2 Processing for producing fine-grained Ti_3Al alloys

Superplasticity in Ti_3Al based alloys has been widely investigated in the past decade years [14-19]. These investigations have confirmed that grain boundary sliding is usually the rate-controlling mechanism, thus grain size and grain boundary structure play an important role for achieving grain boundary sliding. Ti_3Al based alloys usually exhibit excellent superplasticity as the grain sizes are reduced to a micro- or submicro-scale [14-19]. The related processes and grain-refinement methods for producing superplastic Ti_3Al based alloys are described below.

Miyazaki et al. [14] in 1990 reported that a Ti_3Al alloy with an ultrafine grain structure of ~1.5 μm exhibited superplastic properties. In this study, the mechanically alloyed powders which were made from elemental Ti (70 at%) and Al (30 at%) powders were hot pressed at 900°C under 100 MPa and then a 100% relative density could be achieved.

Dutta and Banerjee [15] in 1990 successfully fabricated a fine grain structure of Ti-24Al-11Nb alloy, which was made by consumable arc melted furnace under vacuum and then followed by hot forging and hot rolling. From the results of tensile tests, the highest elongation of 520% was achieved at 980°C and $3.3x10^{-4}$ s^{-1}.

Wu et al. [13,16] (1997) published that the Ti_3Al-Nb alloy showed superplastic elongation of 1083% at 1000°C and $2x10^{-4}$ s^{-1}. The alloy was prepared by arc melting with more than ten cycles re-melting to insure the homogeneity. To reduce the segregation, the re-melted alloys were then homogenized at 1100°C for 12 h. The homogenized alloys were subsequent following by a two-stage rolling process with a total reduction of 6:1. The alloys were processed with an initial hot rolling at 900°C with thickness reduction from 18 mm to 12 mm and were subsequently annealed at 1100°C for 1.5 h. Then the finished hot rolling were performed at 900°C with reduction from 12 mm to 3 mm. Finally, the as-rolled sheets were annealed at 1050°C for 1 h so as to fully recrystallize to achieve a final two-phase (α_2+β) microstructure. The resulting grain size of equiaxed α_2 phase was 4.5 μm dispersed in the β matrix.

Imayev et al. [17] (1999) found that submicrocrystalline structures could be formed in intermetallic alloys such as Ti_3Al-DO_{19}, TiAl-$L1_0$, Ni_3Al-$L1_2$, and Ni_3(Si,Ti)-$L1_2$ after isothermal forging. It was reported that these materials with grain refining to a submicrocrystalline level showed superplasticity at the temperature range of 600-900^{o}C, i.e. 200-400^{o}C below the temperature range for superplasticity in the materials with micron-sized grains. To refine the microstructure, the cast Ti-25Al (Ti_3Al) alloy was prepared by 6-8 steps of multi-directional isothermal forging at temperatures of 650-1050^{o}C and a strain rate range of 5x10^{-3}-5x10^{-4} s^{-1}. After forging, all billets were annealed for 2 h at a temperature 50^{o}C below the temperature of the final forging step. During hot deformation, dynamic recrystallization occurred and a Ti_3Al alloy with grain size of 0.3 μm was formed. Another Ti_3Al alloy with grain size of 8.5 μm was also prepared with similar procedures. In comparison, submicrocrystalline Ti_3Al alloy exhibited relatively higher superplastic properties. The decrease of grain size into submicrocrystalline state resulted in an abrupt enhancement of the superplastic properties.

Microcrystalline grain structures of the Ti_3Al-Nb alloy has also been produced by cross-rolling, as reported by Kim et al. [18] in 1999. The arc-melted materials were homogenized at 1200^{o}C for 12 h and then cross-rolled from 22 to 3 mm at 1020^{o}C. Subsequently, the rolled sheets were recrystallizated at 970^{o}C for 1, 6, and 74 h to result in different grain sizes of 3.6 μm, 5.3 μm, and 7.7 μm, respectively. They found that the elongation appeared to significantly depend on the grain size; and it increased drastically from 440 to 1280% as the grain size was reduced from 7.7 μm to 3.6 μm.

Zhang et al. [19] (2000) found that a Ti-24Al-14Nb-3V alloy containing the α_2, β, and O phases with a microcrystalline equiaxed grain structure could exhibit an excellent room temperature ductility of 29% and an elongation of 1129% at 960^{o}C and a strain rate of 7x10^{-3} s^{-1}. An ingot of this alloy was melted by vacuum consumable electrode arc melting with three cycles of melting steps to insure homogeneity. The ingot encasulated in mild steel cans were broken down in the β phase field of the temperature above 1080°C in air with a reduction of 80% in height. Subsequently, the ingot was forged in the α_2+B2 phase field of 1030-1080°C to yield billets. The billets were then cold rolled in the α_2+B2 phase field (1050°C). After one-pass cold rolling, vacuum annealing in the α_2+B2+O phase field and then quenching in high pure argon gas of the rolled sheets were performed. As a result, the foil with a thickness of 0.006-0.1 mm was obtained. The microstructure contained of fine equiaxed α_2 and O grains (~2-3 μm) distributed in the B2 matrix. The α_2+B2+O alloy with such structures led to an excellent ductility at both room and elevated temperatures.

As mentioned above, an ultra-fine grain size was indispensable to superplasticity of Ti_3Al based alloys. Thermomechanical treatments involving forging, rolling, and annealing were common processes to produce a fine grain structure favorable for grain boundary sliding and satisfactory superplasticity. As a consequence, it is worth noticing how grain size and other factors can affect the superplastic behavior. In what follows, the deformation behavior and superplastic properties are briefly introduced.

1.3 Introduction to superplasticity and deformation mechanisms

1.3.1 Introduction to superplasticity

Superplasticity is a phenomenon observed in polycrystalline materials which have uniform deformation and a very high elongation without pronounced necking prior to failure under uniaxial tension [20]. In general, it is termed superplasticity as elongation exceeds more than 200%. Superplasticity has been widely observed in metals, composites, intermetallc compounds, ceramics, and amorphous alloys [21-24]. Conventionally, there are three basic requirements for superplasticuty deformation [25,26]. Firstly, very small and stable grain sizes (typically less than ~10 μm for metals and ~2 μm for ceramics) are required and the fine-grained as well as equiaxed structures are maintained after elevated temperature deformation. Secondly, the high deformation temperature (typically around or greater than 0.8 T_m) is preferred. Thirdly, a proper strain rate is needed (approximately 10^{-3}-10^{-4} s^{-1}) since superplasticity is a diffusion-controlled process.

According to the Considere theory [27], necking occurs at the maximum load and the equation $ds/de = s$ is hold (s and e are the stress and strain). The criterion for resulting superplasticity rather than continuous necking is $ds/de > s$. Usually, the true stress is a function of strain, strain rate ($\dot{e}$), temperature (T), surface energy (g), etc., i.e.,

$$s = s(e,\ \dot{e},\ T,\ g, \ldots). \tag{1-1}$$

By partial differential Eq. (1-1) can be written as,

$$ds/de = (\partial s/\partial e) + (\partial s/\partial \dot{e})(d\dot{e}/de) + (\partial s/\partial T)(dT/de) + (\partial s/\partial g)(dg/de) + \ldots \tag{1-2}$$

The total ds/de is mostly contributed by the first term from work hardening for conventional tensile tests. In contrast, the second term from strain rate sensitivity becomes more important for superplastic flow. The third and fourth terms, either too small or too difficult to measure, are often ignored.

In terms of mechanical properties, the strain rate sensitivity, m, is an important parameter for determining the ability for a material to resist necking. The m-value can be characterized by the constitutive equation:

$$\sigma = K \cdot \dot{\varepsilon}^{m} \cdot \varepsilon^{n}, \tag{1-3}$$

with

$$m = (\partial \ln \sigma / \partial \ln \dot{\varepsilon}) = (\dot{\varepsilon} / \sigma)(\partial \sigma / \partial \dot{\varepsilon}), \tag{1-4}$$

$$n = (\partial \ln \sigma / \partial \ln \varepsilon) = (\varepsilon / \sigma)(\partial \sigma / \partial \varepsilon), \tag{1-5}$$

where *K* is a constant, m is the strain rate sensitivity, n is the work hardening exponent. With a higher m, the necking growth rate will be slowed down so that a higher elongation can be obtained. For most superplastic alloys, the m-values are usually higher than 0.3. For glass above the glass-transformation temperature T_g, it even has the maximum m-value of 1, which is referred as the Newtonian viscous flow.

The temperature, grain size and stress level are important parameters that significantly affect the superplastic deformation. The deformation behavior of materials at elevated temperatures can be represented by a constitutive equation which combines an activation energy term as given by [21]

$$\dot{\varepsilon} = \frac{AEb}{kT} D_0 \left(\frac{b}{d}\right)^{p} \left(\frac{\sigma - \sigma_{th}}{E}\right)^{n} \exp\left(-\frac{Q_t}{RT}\right), \tag{1-6}$$

where A is a dimensionless constant, E is the elastic constant, k is the Boltzmann’s constant, T is the temperature in Kelvin, D_0 is a related diffusion coefficient, b is the Burgers vector, d is the grain size, σ_{th} is the threshold stress, Q_t is the true activation energy for superplastic flow, R is the gas constant, p is the grain size exponent ranging 2-3, and n is the stress exponent around 2 for superplastic flow.

Normally, superplasticity can be classified into the following groups [28]:

(1) Internal stress superplasticity (ISS): ISS is usually generated by internal stresses accumulated under a low applied stress which involved a slip-controlled process to induce superplasticity. Internal stresses are generated in several ways: (i) polycrystalline materials which involve a phase transformation during a thermal cycling or a pressure cycling; (ii) composite materials that have different thermal expansion coefficients due to their different constituents during a thermal cycling; (iii) thermal cycling of pure metals or single-phase alloys, which have anisotropic thermal expansion coefficients. ISS takes place in materials which exhibit Newtonian viscous behavior (i.e. m~1). For such materials, fine grain sizes are not needed.

(2) Fine structure superplasticity (FSS): Grain boundary sliding (GBS) is usually the rate-controlling process for elevated temperature deformations in fine-grained metals. According to Eq. (1-6), the strain rate is inversely proportional to the grain size. The strain rate for optimum superplasticity increases with decreasing grain size when GBS is the dominant rate-controlling process. Consequently, grain-size refinement presents a powerful method in increasing the strain rate for superplastic forming of materials. In order to avoid rapid grain growth at elevated temperatures, a fine dispersion of second phase particles which act as a grain refiner are usually needed for pseudo-single phase materials. In addition, high energy (i.e., high angle, or disordered) boundaries will more readily slide. It usually needs to convert the low-angle boundaries to high-angle boundaries by proper thermomechanical treatments. FSS often occurs at temperatures about 0.8 T_m and can be regarded as high temperature superplasticity (HTSP).

(3) High strain rate superplasticity (HSRSP): Conventionally, the optimum superplastic strain rates are approximately 10^{-3}-10^{-4} s^{-1}. However, it has been observed that the superplastic

strain rates are raised up to 10^{-2}-10^{-1} s^{-1} or above, which are termed HSRSP [29,30]. The strain rate of 10^{-2} s^{-1} is generally regarded as the lower bound of HSRSP. The faster strain rates are of great interest for industrial applications due to the apparent reduction of forming time. According to Eq. (1-6), HSRSP is regarded as the extension of FSS. With decreasing grain size, the strain rate can increase. In order to reach HSRSP, grain size is generally reduced to about less than 5 μm or even less than 1 μm. In addition, liquid phases at high temperatures are often present at grain or interface boundaries during superplastic deformation for HSRSP.

(4) Low temperature superplasticity (LTSP): Conventional superplasticity is found at relatively higher temperatures, typically around or greater than 0.7 or 0.8 T_m. For industry applications, it is attractive to lower the superplastic deformation temperatures into the temperature ranges below 0.7 T_m. There has not any rigid definition for the upper bound temperature for LTSP, but generally 0.6 T_m seems to be a reasonable cut line. General speaking, ultrafine grain structures are necessary to promote LTSP, which were usually produced by various thermomechanical processes. A number of materials such as Al alloys, Mg alloys, Ti alloys, composites, and intermetallic compounds [31-35] have been developed for LTSP. The temperature of 0.36 T_m (450°C) of the nanocrystalline Ni_3Al, reported by McFadden et al. [36], is the lowest normalized superplastic temperature reported for all crystalline materials until now. Furthermore, Lu et al. [37] published that a bulk nanocrystalline (d~30 nm) pure copper fabricated by electrodeposition exhibited an extreme extensibility of elongation ~5100% as the pure copper was rolled at room temperature (0.22-0.24 T_m) with rolling strain rates of $1x10^{-3}$-$1x10^{-2}$ s^{-1}. The combinations of low temperature and high strain rate superplasticity are attractive subjects in the recent years. An intermetallic Ti-12Co-5Al alloy has been reported to exhibit superplastic elongation higher than 2000% occurring at a relatively low temperature of 700°C and

relatively higher strain rate faster than 3×10^{-2} s^{-1} [38].

(5) Other mechanisms: For example, coarse-grained class I solid solution alloys exhibit high elongations at low strain rates through Coble creep (grain boundary diffusion controlled), Nabarro-Herring creep (lattice diffusion controlled), Harper-Dorn creep (slip controlled), and solute drag dislocation creep [28].

1.3.2 Deformation mechanisms

Various superplastic deformation mechanisms occur in different materials under different conditions and are complicated processes. There are several theories that have been developed. Among them, grain boundary sliding with an accommodation process is the most commonly considered mechanism. If there is only GBS without any accommodation process, cavitations and grain overlapping will be present in the neighboring grains. Hence, the accommodation process is necessary to avoid premature fracture of superplastically loaded specimens. The main accommodation processes (see Table 2 [39-54]) are diffusion flow, dislocation deformation, grain-boundary migration, accommodational sliding, and emergence of grains from neighboring layers and combinations of these processes.

The models that consider the rearrangement of grains and changes in grain shape can be divided into two groups: GBS of individual grains and cooperation grain boundary sliding (CGBS). CGBS is a group of grains shearing slides as an entity in a cooperative manner. To make CGBS occur continuously, a rotation of grain groups and cooperative grain boundary migration can be considered as the accommodation process. Moreover, a heterophase boundary (a boundary between two grains with different crystal structures or chemical compositions) slides more readily than a homophase boundary (a boundary between two grains with similar crystal structures or chemical compositions). Since a homophase boundary slides more difficultly, a grain of one phase meets another grain of the same phase through CGBS would not slide readily and then a stringer of grains of the same phase might be formed. Table 3 lists the models of CGBS, which can be divided into two groups [55-64].

(1) Rigid CGBS [54-60]: All grains of the rigid grain block shear simultaneously along the shear surface. It often involves elastic and diffusional accommodation. Raj and Ashby [55] claimed that the rigid shear of two blocks of grains was accommodated by elastic or diffusional accommodation of skidding grains. In the case of elastic accommodation that the GBS is the rate controlling process, it allows only a small extent of sliding before internal stresses develop which oppose further sliding. In diffusional accommodation, the GBS rate depends linearly upon the applied shear stress. Nix [56] suggested a non-linear stress dependence on the GBS rate in the profile of bumps at a shear surface under traction of shear stress. Barret [57] demonstrated that diffusion controlled GBS accompanied by grain boundary migration caused the rigid CGBS. Cannon and Nix [58] considered that sliding grains are accommodated by intragranular dislocation and the accommodation process is the rate controlling process. Cannon and Nix [58] and Novikov and Portnoy [59] suggested that accommodation for GBS is not necessary for the case of square grains. Partridge et al. [60] considered CGBS in two phase materials that rigid shear would take place along the variant types of grain boundaries to cause a string of continuous phase. Considered the grain emergence, Hazzedine and Newbury [61] claimed that the trajectories of grain movement while CGBS could be determined. But details of accommodation for GBS are not considered.

(2) Sequential CGBS [56,62-64]: It can be treated as a sequential shear of grains along the sliding surface, which can be considered as a propagation of localized grain shear. The

glide of cellular dislocations is usually considered but this modal is only suitable for single phase materials. Morral and Ashby [62] suggested that the movement of cellular dislocations might accommodate the sequential shear of grains. The cellular dislocations as a topological defects exist in the regular array of grains with a cell structure. Nix [56] proposed the concept of deformation induced cellular dislocations. The deformation induced cellular dislocations can be considered as an extrinsic dislocation in the grain structure. The elastic strain around the cellular dislocations is extremely high. The model claimed by Sato et al. [63] has been developed to explain grain growth during superplastic deformation in terms of climb of cellular dislocations. Kamijo et al. [64] considered the sliding of grain group in three-dimension. In a regular hexagonal grain structure, the sliding grains remain their original shape with a six-sided grain structure during CGBS. Sequential CGBS can be treated as a penetration of shear from one side of a specimen to the other as a propagation of a percolation process.

1.4 Superplastic behavior in Ti_3Al alloys

1.4.1 HTSP in Ti_3Al alloys

To date, there have been a number of reports claiming the superplastic behavior of Ti_3Al based alloys [12,15,18,65,67-72]. It has also been reported that the Ti_3Al based alloys exhibited admirable superplasticity of elongation greater than 1200% [18,69,70,72]. In general, most Ti_3Al based alloys [15,18,65,67-72] exhibited superplastic behavior at temperatures between 960-1000^{o}C and strain rates between 10^{-4}-10^{-5} s^{-1}. It could thus be said that the optimum superplastic deformation conditions could take place at relatively higher temperatures and lower strain rates.

The study of superplasticity in Ti_3Al based alloys was first investigated by Miyazaki et al. [14] and Dutta and Banerjee [15] in 1990, individually. Miyazaki et al. [14] published that the important superplastic parameter, m-value, in a Ti_3Al alloy was determined to be ~0.44 at 900^{o}C. Dutta and Banerjee [15] published that a Ti-24Al-11Nb alloy showed an elongation of 520% at 980^{o}C and $3.3x10^{-4}$ s^{-1}. Microstructure revealed that this regular α_2 alloy consisted of a dual phase (α_2+β) and the ordered α_2 phase acted as the continuous matrix.

Yang et al. [65-67] (1991) reported the superplastic behavior in the regular α_2 and the super α_2 Ti_3Al based alloy. The maximum elongation of 810% was obtained for the regular α_2 alloy at 980^{o}C and $5x10^{-5}$ s^{-1} and 570% for the super α_2 alloy at 980^{o}C and $1.5x10^{-4}$ s^{-1}. They also related the microstructure with the superplastic deformation process. From microstructural observations, strain induced morphological change of α_2 and β during superplastic defromation were observed in both the super α_2 and regular α_2 alloys. Strings of α_2 grains were orientated at 30-60^{o} to the tensile axis and intersecting strings could be seen. Surface irregularities, which were related to the intersection of strings, were formed. In addition, the initial lath-like α_2 phase was seen to break up into more equiaxed morphology during superplastic deformation in the super α_2 alloy. According to the above phenomena, it could be attributed to the CGBS as the dominating deformation process. The activation energies of superplasticity in these two Ti_3Al based alloys have been calculated, being 182 and 308 kJ/mol for the regular α_2 and super α_2 alloys, respectively.

Ghosh and Cheng [68] (1991) published that superplasticity could be obtained in both the regular and super α_2 alloys. The optimum superplastic temperature was about 950-1050^{o}C. Elongations of 500 and 800% could be obtained at 950^{o}C and $8x10^{-5}$ s^{-1} for the regular and super α_2 alloy, respectively. The continuous strain hardening, which was due to the gradual grain growth, has been observed for the regular α_2 alloy. In contrast, the continuous strain softening, which was due to the breaking-up of the elongated structure, was observed for the super α_2 alloy.

Wu et al. [71] (1997) published that the Ti_3Al-Nb (Ti-25Al-10Nb) alloy showed a maximum elongation of 1083% at a higher superplastic deformation temperature of 1000^oC and a strain rate of $2x10^{-4}$ s^{-1}. The m-values were between 0.4-0.83 at deformation temperatures of 925-1000^oC and strain rates of 10^{-4}-10^{-3} s^{-1}. They also studied that the relationship with the flow stresses, the microstructure evolution, and the deformation temperatures. Under a strain rate of $2x10^{-4}$ s^{-1}, strain hardening occurred at superplastic deformation temperatures within 975-1025^oC, while a steady-state flow occurred over 925-950^oC. Strain hardening might occur, since dynamic grain growth might increase the deformation stress. However, strain softening might occur since the dynamic recrystallization might decrease the deformation stress. The steady-state flow, which took place at 925-950^oC, might be a result of the balance between dynamic recrystallization and dynamic grain growth. The strain hardening which occurred at 975-1025^oC might be a result of dynamic grain growth.

The superplastic elongation of 1350% was obtained at 960^oC and an initial strain rate of $1.7x10^{-3}$ s^{-1} using constant crosshead speed tests of the 3 mm thick super α_2 sheets, as investigated by Ridley et al. in 1991 [69]. Moreover, Fu and Huang [70] (1998) in National Sun Yat-Sen University demonstrated that similar materials of the 1 and 2 mm thick sheets could exhibit elongations of about 600 and 1500%, respectively, at 960^oC and a constant strain rate of $2x10^{-4}$ s^{-1}. The m values were around 0.4-0.6 for the strain rate range about 10^{-4} s^{-1}. With increasing superplastic strain, three stages of deformation behavior could be seen. For $\varepsilon<0.5$, the thermally activated dislocation slip process controlled the deformation, with m~0.33 and Q_t~400-500 kJ/mol [70]. For $0.5<\varepsilon<0.8$, grains became more equiaxed and GBS started to be the rate-controlling mechanism, with m~0.5 and Q~270 kJ/mol. For $\varepsilon>0.8$, GBS and associated accommodation mechanisms continuously operated [70].

After that, Kim et al. [18] (1999) examined a two-phase ($\alpha_2+\beta$) Ti_3Al-Nb alloy which showed an elongation of 1280% at 970°C and an initial strain rate of 10^{-3} s^{-1}. They suggested that GBS together with PBS (phase boundary sliding) were largely accommodated via dislocation motion inside the α_2 and β phases. In addition, it was observed that the softer β phase deformed more heavily than the α_2 phase. The optimum β volume fraction to achieve maximum elongation was about 20%. However, this result was much different from other two-phase Ti alloys such as TiAl and Ti-6Al-4V, in which the maximum elongation occurred with equal phase proportions [53]. Fu and Huang [70] also found that the Ti_3Al base alloy exhibited the maximum elongation as the volume fraction of the α_2 and β phase being nearly 50% to 50%, which would help to suppress severe grain growth. The unusual conclusion suggested by Kim et al. [18] inferred that it might be a result of the boundary properties as well as the deformation behavior in the β phase. In other words, the sliding resistance against α_2/β PBS was smaller than that of α_2/α_2 GBS, leading to a dominant phase boundary sliding during superplastic deformation. In addition, the smaller β grain size would lead to homogeneous deformation rather than planar slip in the β phase. However, the grain size of the β phase increased with increasing β volume fraction. As a result, the optimum β volume fraction was about 20% to achieve homogeneous deformation without local stress concentration at grain boundaries.

The Ti-24Al-14Nb-3V-0.5Mo alloy investigated by Zhu et al. [72] (2001) exhibited good superplasticity at temperatures between 960-980°C and strain rates between 3.5×10^{-4}-4×10^{-3} s^{-1}, the m-value was greater than 0.5. Moreover, the maximum m-value of

0.76 was obtained at 960°C and a strain rate of $1.5x10^{-3}$ s^{-1}, while the elongation was 1240%. The apparent activation energy in the superplastic regime was determined about 162.5 kJ/mol, which was close to the lattice diffusion on the β-Ti of 150 kJ/mol. The values of A and n in Eq. (1-6) were determined to be 2818 and 2.39, respectively. Strings of α_2 phase were revealed to form during superplastic deformation, while the α_2 volume fraction increased with increasing superplastic strain. On the base of the n-value, activation energy value, and the microstructural observation, the major superplastic deformation mechanism was believed to be GBS.

A summary of the HTSP and the related processes in Ti_3Al based alloys is present in Table 4.

1.4.2 LTSP in Ti_3Al alloys

In view of the above mentioned results, the optimum superplastic deformation temperatures were approximately between 960-980°C (~0.64 T_m, where T_m for Ti_3Al is 1953 K). However, superplastic forming at these temperatures requires expensive tooling and leads to oxidation during long superplastic forming time. Therefore, reduction in the temperature range to <0.6 T_m would be attractive. However, there have been very limited studies reporting the superplasticity in Ti_3Al alloys at low temperatures.

Imayev et al. [17] reported in 2000 that Ti_3Al alloys with a submicrocrystalline structure exhibited superplasticity at relatively low temperatures over 700-900°C, even at high strain rates. The deformation temperatures became significantly lower as the grain size was reduced to the submicrocrystalline values. The grain sizes of 0.1, 0.3, and 0.8 μm with no porosity were produced by dynamic recrystallization during isothermal forging. During dynamic recrystallization, superplastic deformation proceeded with extensive grain boundary diffusion and sliding and resulted in improving microstructural homogeneity as well as increased ductility. The elongation of 680% could be obtained at a low temperature of 600^oC (0.45 T_m) and a strain rate of $6.4x10^{-4}$ s^{-1} with the grain size of 0.1 µm. In addition, the elongation of 780% could be obtained at 700^oC (0.50 T_m) and $6.4x10^{-4}$ s^{-1} with the grain size of 0.3 µm.

The true stress-strain curves of microcrystalline (d=8.5 µm) and submicrocrystalline (d=0.8 µm) Ti_3Al specimens were studied by Imayev et al. [73]. It should be noted that the appearance of steady-state flow implied the operation of superplastic flow in Ti_3Al alloys [74]. The steady-state flow stage usually began after a hardening stage in the Ti_3Al alloys. This hardening stage was connected with a gradual accumulation of defects and a growth of initial grains. The accumulation of defects would be restricted by the occurrence of grain boundary sliding. Moreover, a structural recovery process was usually accompanied with grain boundary sliding. As the hardening stage was transformed into the steady-state flow stage, grain boundary sliding and dynamic recrystallization proceed, retarding the accumulation of defects. The microcrystalline specimen showed a steady-state flow at 1000^oC, while the submicrocrystalline specimen at 800^oC. That is to say, Ti_3Al alloys with grain size of 0.8 µm exhibited superplastic behavior at temperatures lowered to 800^oC and the m-value was determined to be 0.8. In addition, high strain rate but not low temperature superplasticity at $1.3x10^{-1}$ s^{-1} was also displayed in the Ti_3Al alloys with a grain size of 0.8 µm. An elongation of 190% could be obtained at 950^oC and a high strain rate of $1.3x10^{-1}$ s^{-1} and the m-value was determined to be 0.31.

Imayev et al. [75] also investigated the effects of partial and full ordering on the ductility in Ti_3Al alloys. They claimed that superdislocations in fully ordered structures and ordinary dislocations in completely disordered structures experienced less resistance to glide than the dislocations in partially disordered structures, and the former lead to greater ductility. Ti_3Al alloys, which have a high ordering energy, would greatly decrease dislocation mobility with even light disordering, and resulted in reduced ductility at deformation temperatures lower than 400°C. However, the ductility of ordered and partially disordered Ti_3Al alloys was almost the same at temperatures higher than 500°C. In other words, the long-range ordering degree of Ti_3Al alloys was not an important affecting parameter for superplastic deformation temperature greater than 500°C. It should be noted that an initial fully ordered Ti_3Al alloys with d=0.3 μm and d=0.1 μm became partially disordered after superplastic deformation at 500 and 600°C. Nevertheless, larger grain sized Ti_3Al alloys did not decrease the long-range ordering degree after superplastic deformation. Imayev et al. [75] suggested that the transformation from a fully ordered structure into a partially disordered structure might be due to the extensive grain boundary sliding leading to disordering near the grain boundaries.

A summary of the LTSP and the related processes in Ti_3Al based alloys is present in Table 5 [17].

1.4.3 LTSP and HSRSP in other Ti based alloys

With respect to the TiAl based intermetallic compounds, Imayev et al. [76] (1992) reported the observation of superplasticity of ~225% with a grain size of ~0.4 μm in a Ti-50Al alloy at a low temperature of 850°C (~0.6 T_m, where T_m for TiAl is 1953 K) and a relatively higher strain rate of $8x10^{-4}$ s^{-1}. The cast Ti-50Al alloy was prepared by isothermal forging at 800-1100°C followed by annealing at 800-1130°C in air. Nieh et al. [77] (1997) studied Ti-47Al-2Cr-2Nb which was made by rapid solidification and subsequent powder extrusion at 1150°C followed by annealing at 900°C for 2 h. An elongation of 310% was obtained at 800^{o}C (0.58 T_m) and a strain rate of 2x10^{-5} s^{-1}. The microstructure consisted of coarser B2 grains of 4-5 μm and fine γ+α_2 grains of 0.5-1 μm. In the papers of Imayev et al. [73] (1999), they published that a number of TiAl alloys such as Ti-46Al, Ti-46Al-2Cr-2Nb-1Ta, and Ti-48Al-2Cr-2Nb with submicrocrystalline structures by multi-directional isothermal forging also exhibited low temperature superplasticity.

Huang et al. [78] (2000) also reported the low temperature and high strain rate superplasticity in TiAl based Ti-33Al-3Cr-0.5Mo alloys. The ultrafine-grained microstructure, which was produced by canned-forging to a total strain of 80%, resulted in superpasticity of 325% at 900^{o}C and 1x10^{-3} s^{-1}.

As for titanium alloys, Hofmann et al. [79] (1995) revealed that the ultrafine-grained Ti-10Co-4Al alloy exhibits high strain rate superplasticity. This alloy, consisting of α-Ti and intermetallic Ti_2Co compound, was prepared by hot rolling and then water quenching. Final processing was performed below the eutectoid transformation temperature in order to refine grain sizes. As a result, the α-Ti matrix of 0.5 μm and intermetallic particles less than 0.2 μm were produced. It showed that an elongation more than 1000% could be obtained at relatively low deformation temperatures (650-750^{o}C, 0.47-0.52 T_m) and high strain rates up to 5x10^{-2} s^{-1}.

Sergueeva et al. [80] (2000) have indicated high strain rate superplasticity in a Ti-6Al-4V alloy, which has duplex α_2+β phases. Superplasticity can proceed at lower temperatures (650-725^{o}C, 0.47-0.51 T_m) and higher strain rates (even at 10^{-1} s^{-1}) by high pressure torsion straining which is a kind of severe plastic deformation method, resulting in samples with no residual porosity and with a grain size as small as 0.1-0.2 μm. The hot rolled Ti-6Al-4V alloy was subjected to high-pressure torsion under 5 GPa to a true logarithmic strain of 7 at room temperature. The alloy exhibited a tensile elongation of 575% at a strain rate of 10^{-3} s^{-1} and a low temperature of 650°C. Moreover, this alloy showed an elongation of 215% at 10^{-1} s^{-1} and 725°C.

Based on the above reports, a reduction in grain size of TiAl and Ti based alloys seemed to be a promising method to enhance low temperature or high strain rate superplasticity. A summary of the LTSP or HSRSP associated with the related processes in other Ti based alloys is present in Table 6 [73,76-80].

1.5 Phase transformation phenomena

The phase transformation between the α (HCP) and β (BCC) phases have been studied in pure Ti or Ti based alloys [3,81-84], occurred during static heat treatment or dynamic deformation at elevated temperatures, as well as during cooling. Unlike the $\alpha \leftrightarrow \beta$ transformation that has been carefully examined, the transformation between the α_2 (DO_{19}) and β (BCC or B2) phases has rarely been reported, especially the transformation mechanism that occurs under tensile loading.

In Ti_3Al-Nb alloys, Strychor et al. [3] reported that the Ti_3Al-Nb alloys with low Nb contents less than 5 at%, the β phase would transform martensitically from the BCC β phase to the hexagonal α' phase during rapid cooling from the β phase field.

Banerjee et al. [8] indicated that the Ti-Al-Nb compounds undergo transformation mostly from a B2 into a hexagonal α_2 and/or derivative phase with orthorhombic O phase with the space group of *Cmcm*; depending on temperature and composition. Their coworkers

Muraleedharan et al. [4] also explored that a massive phase transformation from the B2 phase to the O phase in a Ti-24Al-15Nb alloy. In samples aged in the β phase field followed by quenching in water, the phase transformation occurred without change in composition. The O phase, which has a distorted DO_{19} α_2 structure based on the stoichiometry Ti_2AlNb, can form from the α_2 phase decomposition and also directly from the β phase. Based on the Ti-Al-Nb phase diagram, as shown in Fig. 4, the O phase appears in significant amounts at Nb content exceeding 12 at% [85].

Hsiung et al. [86] suggested the transformation sequence in a Ti-24Al-11Nb alloy under the isothermal condition between 450 to 850°C. The isothermal transformation path from the B2 to the final α_2 structure has found to follow the route of B2 ($Pm\overline{3}m$) →B19 (*Pmma*) →O" (*Cmcm*) →O'(*Cmcm*) →α_2 ($P6_3/mmc$) at temperatures above 500°C. Below the temperature, the O'→ α_2 reaction becomes very sluggish and the O' phase becomes kinetically stable. The O'' termed here is the DO_3-like phase and the O' phase is the ordered orthorhombic O phase.

The transformation mechanism and the influence on superplasticity in a Ti-22Al-27Nb alloy were investigated by Ren et al. [83]. They demonstrated that the B2 to α_2/O phase transformation was expected to be a pure diffusional process. If diffusion is possible, a diffusional-displacive transformation may occur with simultaneous lattice shuffle/shear and atomic migration. When temperature is high enough to allow diffusion occur, the B2 phase can transform into α_2 or O phase during superplastic deformation so as to accommodate strain. The stress-induced phase transformation could strengthen the high strain region and thus helps to maintain homogeneous deformation and prevent early necking formation.

In other Ti alloys, the deformation induced $\beta \rightarrow \alpha''$ martensitic transformation was observed in a Ti-Al-V-Fe alloy and the phase transformation is accompanied by a significant 2.8% volume increase [82]. The transformation surrounding the crack could give rise to a crack tip shielding effect. The transformation process, acting as an energy consuming process, would induce the ability of the material to absorb energy during fracture and increase the fracture toughening.

1.6 Anisotropy during superplastic deformation

The textured Ti_3Al-Nb alloy with anisotropic superplasticity at 925-1000^{o}C has been investigated by Wu et al. [71]. From the results of tensile tests along different directions, the superior superplasticity along the rolling direction was observed. They illustrated that the anisotropic behavior was caused by the relationship between the preferred orientation and the dislocations in the slip systems. However, there were conflicting reports in which the anisotropic superplasticity was suggested to be caused by the microstructure rather than the texture effect. Ghosh and Cheng [68] indicated that the super α_2 alloy showed superior superplasticity at 950^{o}C along the transverse direction. While superplastic loading, the rolling texture would gradually evolve into a more equiaxed form, especially in the transverse direction. For the Ti-6Al-4V alloy, McDarmaid et al. [87] also reported that such a stress and strain anisotropy at 880 and 928^{o}C was produced by the aligned equiaxed α grains which acted as barriers to grain boundary sliding, and the anisotropy was not dependent upon the texture. The superplastic deformation became less anisotropy with increasing superplastic strain due to the progressive breakdown of aligned microstructure by grain boundary sliding. However, room-temperature anisotropy was controlled by the original α-phase texture, which was still present even after superplastic strain of 1.48 (334%) at 928^{o}C.

The effects of temperature over 925-1000°C and strain rate of $5x10^{-4}$ s^{-1} on anisotropic superplasticity in the Ti-25Al-10Nb alloy have also been described by Wu et al. [71]. The degree of anisotropic superplasticity was reduced with increasing deformation temperature or decreasing deformation strain rate. During the superplastic deformation, the texture would change into a random distribution because of grain boundary sliding and grain rotation. Moreover, grain boundary sliding was easier to proceed at higher temperatures and lower strain rates. Thus, the degree of anisotropic superplasticity would be reduced under such conditions.

For conventional superplastic materials, the grain structures are equiaxed. It is expected that the deformation is more or less homogeneous, with no apparent anisotropy behavior. The limited reports on the anisotropic superplasticity might be either related to the grain or microstructure inhomogeneity, but might also result from the textures present in the processed materials. The texture evolution during processing and superplastic deformation at elevated temperatures in various superplastic Ti_3Al based alloys is reviewed below.

1.7 The texture analyses on Ti_3Al alloys

After thermomechanical processes over 900-1100°C, the Ti_3Al alloys usually exhibit a crystallographic texture [88-91]. Hon et al. [88] accounted that after two-step hot rolling process at 1000°C and 900°C and then annealed at 900°C for 48 h, a sharp (0001) basal plane texture was formed in the Ti-25Al-10Nb alloy. Knorr et al. [89] studied the influence of heat treatments after rolling on texture in the Ti-24Al-11Nb alloy. The as-received sheet in the as-hot-rolled condition, possessed the α_2 $\{11\bar{2}0\}$ texture and the β {200} cubic texture. Cross-rolling developed a similar texture component at 90° in the plane of the sheet, i.e.,

$\{11\bar{2}0\}<0001>$ and $\{11\bar{2}0\}<10\bar{1}0>$ texture components in the α_2 phase. After heat treatments, the original texture components were retained whereas the intensity and sharpness of texture components were altered. Annealing in the β field producing a *Widmanstätten* structure was found to sharpen both the α_2 and β textures. However, annealing in the $\alpha_2+\beta$ field producing equiaxed α_2 grains and the intergranular β phase had little modification.

Suwas et al. [90] studied the texture evolution of a Ti-24Al-11Nb alloy during thermomechanical processing which involved hot rolling at different temperatures and thickness reductions. The as-cast material which possessed a weak basal (0002) α_2 texture would undergo texture evolution under the influence of rolling temperature and thickness reduction percentage. The hot rolling processes were conducted at 900^{o}C and 1100^{o}C with reduction amounts ranging between 50 to 80% at each temperature. At 1100^{o}C, deformation in the α_2 phase was restricted and a weak basal (0002) texture was induced, since it mostly consisted of high temperature β phase with a volume percent of 85%. Furthermore, this alloy would undergo recrystallization at temperatures above 1000^{o}C. Hence, dynamic recrystallization took place during rolling at 1100^{o}C and resulted in some non-basal textures. In comparison, a strong basal (0002) α_2 texture was produced during rolling at 900^{o}C, where the α_2 phase comprised about 85%. It could also be found that the basal α_2 texture was strengthened with increasing deformation amount during deformation at both 900^{o}C and 1100^{o}C. The stability of the rolling texture during subsequent annealing was also examined by Suwas et al [91]. After rolling at 900^{o}C, isochronal and isothermal annealing at were performed to investigate texture stability. Isochronal annealing was carried out at 850, 900, 960, and 1020^{o}C for 1 h, as well as isothermal annealing was carried out at 900^{o}C for 15, 30, 120, and 720 min. It was showed that the basal (0001) α_2 rolling texture was always retained but the strength was changed during heat treatments involving recovery, recrystallization, and grain growth in the α_2 phase. From the results of both isochronal and isothermal annealing, the rolling texture was weakened somewhat during recovery, while it started regaining its strength in the recrystallization stage. However, the rolling texture became decreasing its strength with new non-basal orientations appeared during the grain growth stage; a strong $(\bar{1}2\bar{1}0)[60\bar{6}0]$ orientation was produced during isochronal annealing, while $(\bar{1}2\bar{1}3)[10\bar{1}0]$, $(\bar{1}2\bar{1}1)[10\bar{1}0]$, $(\bar{1}2\bar{1}4)[10\bar{1}0]$, and $(\bar{1}2\bar{1}0)[10\bar{1}0]$ orientations were produced during isothermal annealing.

The texture evolution in the β phase during thermomechanical processes with different rolling temperatures and rolling reductions were also investigated by Suwas et al. [92]. They focussed the texture characteristics from the influence of phase volume fraction. The as cast Ti-24Al-11Nb alloy possessed the weak β textures within {112}~{113}<uvw>, while the α_2 phase exhibited a strong (0002) basal texture. The volume fraction of the β phase increased with increasing rolling temperatures. At rolling temperature of 900°C in the 50% rolled specimen, multiple texture components were present, i.e. {001}<110>, {112}<110>, {112}<111>, and {013}<331>. The deformation was rather restricted due to the significant α_2 amount of 70% so that the rotation of the β phase became difficult. With increasing rolling reduction amount to 80%, the texture components remained almost the same but the intensity was strengthened since the rotation of the β phase became more sufficient and resulted in more well-defined textures. At rolling temperature of 1020°C, the strong β textures such as {001}<uvw>, {112}<uvw>, and {332}<uvw> were observed in specimens deformed to both 50 and 80%. The volume fraction of the β phase at this temperature was about 50%, which provided a sufficient amount of deformation in the β phase and resulted in clear and well-defined textures. Furthermore, the β phase did not undergo any kind of dynamic relaxation process, recovery or recrystallization at this temperature, and resulted in well-defined textures. In summary, as the temperature of rolling decreased, the deformation of the β phase becomes more and more constrained due to the simultaneous presence of progressively higher amounts of the α_2 phase, thereby influencing the texture of the β phase.

The relationship between superplasticity and texture in Ti alloys has been examined in the recent years. Kaibyshev et al. [93] considered the influence of texture on superplasticity of the titanium alloy VT6 (Ti-6.5Al-5.1V). The crystallographic texture of the α_2 (0002) basal texture formed during rolling strongly influenced the conditions of superplastic deformation. The presence of a strong initial texture enabled superplastic deformation to occur at lower temperatures and higher strain rates [93]. Under the superplastic flow at deformation temperature within 600-950°C, textures might influence plastic properties as a result of the change in the grain boundary structure. The role of grain boundary in deformation process, such as dislocation generation, dislocations climb and annihilation, grain boundary sliding, and grain boundary diffusion, increased in the ultrafine-grained materials. This grain boundary structure was connected with the misorientaion between grains and crystallographic texture. The relationship between the texture and the superplasticity in Ti_3Al alloys has been studied by Wu et al. [16]. The textured and non-textured Ti_3Al-Nb alloys were produced after thermomechanical processes at different rolling temperatures. They found that the superplasticity of the textured Ti_3Al-Nb alloy was better than that of the non-textured Ti_3Al-Nb alloy. Based on the above two reports, a textured alloy after thermomechanical treatments seemed to exhibit better superplasticity.

Fu and Huang [70] also dealt with the evolution of texture before and after superplastic deformation. The texture in the Ti_3Al alloy became much weaker with increasing superplastic strain. It was concluded that grain boundary sliding and grain rotation proceeded during superplastic loading. Thus, texture might influence tensile properties of Ti_3Al alloys as a result of changes in grain boundary structure.

In summary of the above literatures, both the textures formed during thermomechanical treatments and the effects of heat treatments on texture in Ti_3Al based alloys have been widely published. The texture evolution during the superplastic deformation at the optimum superplastic temperatures of $950 \pm 50^{o}C$ was also reported. However, there were very limited reports regarding on the texture evolution and anisotropic superplasticity at relatively lower temperatures. In addition, most reports on texture analyses were examined by X-ray pole figures. In fact, the conventional pole figure method is difficult to obtain local or quantitative information on the orientation distribution. The texture analyses using EBSD involving microtexture and quantitative information become an interesting technique for investigating the grain structure and texture evolution during superplastic deformation.

1.8 Introduction to electron back scattered diffraction (EBSD)

1.8.1 Advantages of EBSD

EBSD is a promising method in investigating grain misorientations, orientation distributions, and microtexture. By conventional texture analysis techniques, either microstructures or crystallographic information can be obtained. The common techniques for studying microtructures include optical microscopy (OM), scanning electron microscopy (SEM), and transmission electron microscopy (TEM), whereas crystallographic information can be obtained by X-ray pole figures and TEM diffraction patterns. For instance, although grain sizes and grain shapes could be revealed by OM or SEM, crystallographic information could not be obtained. Moreover, some low-angle grain boundaries and special boundaries could not be exposed since these boundaries are difficult to be etched. The X-ray method can only be suitable to macrotexture (macroscopic texture) measurements rather than microtexture (local texture) measurements. In contrast, the TEM method can measure the orientation of individual grain (local texture). However, the regions selected for examination are very limited. Therefore, EBSD is now acknowledged as an optimum technique for most applications not only microstructures and microtexture but also crystallographic information [94].

1.8.2 The basic principles and set-up of a typical EBSD system

A simplified explanation for the principle of EBSD is illustrated in Fig. 5 [95]. The optimum angle of incident electron beam and specimen normal needs to be up to approximately 70^{o}~80^{o}. Hence, the major fraction signal is backscattered rather than absorbed. As the incident electron beam bombards at crystal, inelastic scattering occurs. The Kikuchi lines are formed by Bragg diffraction of inelastic scattered electrons which will be able to be Bragg diffracted by the (hkl) planes. The parallel Kikuchi lines can be formed on the phosphor screen. From these parallel Kikuchi lines, crystallographic orientations can be obtained. The set-up of an EBSD system is illustrated in Fig. 6 [96]. EBSD can be added to most SEM instruments. These Kikuchi patterns, which can be considered as electron back-scattered patterns, will be detected by a phosphor screen and viewed with a low-light TV camera. The real-time picture of the diffraction pattern is viewed on a monitor and analyzed using a computer driven cursor and dedicated software [97].

There are several kinds of information which can be obtained from EBSD [97].

(1) Pole figure and inverse pole figure: The Miller indicates of the diffraction patterns will be inferred by a computer. A pole figure which consists of discrete datum points is the most direct and simple mean of displaying the statistics of orientations of individual grains. For

an inverse pole figure, the axes which are displayed in a reference direction in the specimen coordinate system, for example the normal direction (ND), the rolling direction (RD), or fiber axis.

(2) Orientation distribution functions (ODFs): Though pole figures can show orientations in two dimensions, orientations in three dimensions should rely on ODFs. From ODFs, a compelete texture determination might be obtained. Euler angles (φ_1, ϕ, φ_2) are usually used to describe an orientation as shown in Fig. 7 [97]. Euler angles could be plotted as polar coordinations in an Euler space, which constructs the ODFs.

(3) Orientation image: Grains can be shaded, colored, coded in the orientation image. It displays of orientation and spatial information. As grains have the same orientation, grains are able to show the same color in the orientation image. Therefore, an orientation image, which displays plentiful colors by various orientations, can show the distribution of grain boundary geometries in the analyzed region of microstructure.

(4) Misorientation distribution: Misorientation might describe the orientation between two grains. Once orientations of the two neighboring grains obtained, choosing a reference axis is needed. The external axis of the specimen is considered as the reference axes for the misorentation between two grains. The external axis can also act as a tilt axis which can tilt a minimum angle to reach the orientations of the two grains. This minimum angle is referred as the misorientation angle as illustrated in Fig. 8 [95]. A misorientation distribution is composed of widely misorientation angles which can help to obtain information of low, medium, and high misorientation angles.

1.9 Motive of the research

As mentioned above, the excellent superplastic behavior for Ti_3Al alloy in the temperature ranges of 920-1000^oC has been widely published. The development of low temperature superplasticity is intended. The combinations of reduction for fabrication energy and cost enhanced the research motive on low temperature superplasticity. It would be a breakthrough for Ti_3Al alloys to develop low temperature superplasticity since Ti_3Al based alloy is typically brittle and hard to deform. Although Imayev et al. [17,73] reported that superplasticity in TiAl and Ti_3Al based alloys with submicrocrystalline structure could occur at temperatures below 900^oC, their deformation mechanism, anisotropy behavior and texture evolution are still inadequately understood. In this research, the following works are aimed.

(1) To further study the optimum parameters for superplasticity at lower temperatures, from previous optimum superplastic deformation temperature range of 950 ± 50^oC (0.63 ± 0.02 T_m), down to temperatures below 900^oC, around 800 ± 100^oC (0.55 ± 0.05 T_m).

(2) To examine the stress or strain anisotropy in the current super α_2 Ti_3Al based alloy at higher (950 ± 50^oC) and lower (800 ± 100^oC) temperatures. And to compare the deformation anisotropic behavior at 950 ± 50^oC (under the optimum HTSP superplastic flow condition) and at 800 ± 100^oC (under the LTSP or dislocation creep condition).

(3) To reveal the microstructure evolution, texture evolution, grain boundary characteristics, and volume fraction change during lower temperature deformation, and to relate to the superplastic behavior. And to compare the microstructure and texture evolutions at 950 ± 50^oC under the HTSP condition and at 800 ± 100^oC under the LTSP or dislocation creep condition. The relationship between anisotropy and texture will be examined.

(4) To understand the phase transformation phenomena of β to α_2 in the two-phase (α_2+β) region during static annealing and superplastic straining at 700-1000°C.

(5) To establish the deformation models in consistence with the microstructure and texture evolution.

CHAPTER 2 Experimental Methods

2.1 Materials

The super α_2 material was supplied by Rockwell Internatioal, USA, originally fabricated by Timet, USA, with a nominal composition of Ti-25%Al-10%Nb-2%V-1%Mo (in at%), or Ti-13.6%Al-20.2%Nb-3.3%V-2.0%Mo (in wt%). The material has been double checked by ICP-OES in Materials Research Laboratory in Tsinchu which gave the composition of Ti-22.88%Al-10.48%Nb-3.07%V-1.01%Mo (in at%). The as-received Ti_3Al thin sheet specimen was 2 mm in thickness. The fabrication method in producing the fine-grained superplastic-grade materials is not fully provided due to the patent restriction. Based on literatures, the possible procedures might include homogenization at elevated temperatures and then followed by a series of hot rolling over the temperature range of 800-1100^{o}C (the two-phase region).

2.2 Mechanical tests

In order to study superplasticity, the mini tensile specimens with the tensile axis parallel to the rolling direction were machined from the as-received Ti_3Al thin sheet by wire cutting with a gauge length of 5.5 mm and gauge width of 3 mm for testing at elevated temperatures, as depicted in Fig. 9(a). Larger specimens were machined with a gauge length of 10 mm and a gauge width of 3 mm for applying an extensometer during loading at room temperature, as depicted in Fig. 9(b). Tensile tests were conducted in accordance with the constant-crosshead-speed (i.e. decreasing strain rate tests) method using an INSTRON 5582 universal testing machine equipped with a three-zone high-temperature furnace. The testing temperature was controlled to be within $\pm 3\,^{o}$C. The system was performed with purging argon at a flow of 3 *l*/min all over the heating and superplastic loading time. Furthermore, specimens were prior heated to 100^{o}C and then coated with special glass (Deltaglaze 347, obtained from Axhson, Japan) on the surface with sequential air cooling before tensile tests to suppress oxidation. Argon was a protective atmosphere rather than a back pressure that was usually used for suppressing cavitations during superplastic tensile loading or superplastic forming practices.

Systematic LTSP tensile tests were performed under the constant-crosshead-speed tests at 700-850^{o}C with initial strain rates of 8x10^{-5}, 2x10^{-4}, 5x10^{-4}, and 1x10^{-2} s^{-1}, respectively. It was usually taken about 60 min for the specimens to reach the set temperatures without thermal fluctuations. The tensile data were recorded with an on-line computer for further dealing with stress-strain curves. In addition, the heating curves were recorded by a Yukogawa μR 180 dot-printing micro recorder (model 4176) for each test.

2.3 Anisotropic tests

For studying the isotropic or anisotropic superplasticity, the tensile specimens were machined with the loading axis aligned along a direction parallel, perpendicular, or 45^{o} to the rolling directions, respectively. Note that the tensile specimens for anisotropic study machined with tensile axis parallel to the rolling direction are the same as the previous ones for tensile tests. Anisotropic tensile tests were performed at 25, 750, 850, and 920^{o}C.

2.4 Retention of microstructure for tensile specimens

To retain the microstructure of superplastically loaded specimens, the specimens should be rapidly cooled. However, to take account of safety and to prevent oxidation in air, high-temperature furnace could not be opened at temperatures above 500°C for allowing cooling by liquid nitrogen. To achieve rapid cooling, it was necessary to use a thin steel pipe to insert into the furnace close to the specimen so that nitrogen or liquid nitrogen, which would help rapid cooling, could be purged via the pipe. By purging nitrogen with a pressure of 2 kg/cm^2, the microstructure was retained. To increase the quenching rate, liquid nitrogen would be used. The design for quenching by liquid nitrogen is illustrated in Fig. 10. Liquid nitrogen is bottled into a washing bottle then injected to the specimen via the steel pipe.

2.5 Microstructure characteristics

2.5.1 OM and SEM observations

The as-received and superplastically loaded specimens were rough-polished using emery papers with water, and then polished using 0.1-0.3 μm Al_2O_3 suspensions. After that, specimens were etched with the Kroll's reagent (10% HF + 5% HNO_3 + 85% H_2O) for microstructural observation by optical microscopy (OM) or scanning electron microscopy (SEM).

To study whether deformation enhanced phase transformation has been induced during superplastic straining, static and dynamic loading experiments were conducted at higher temperatures (950 ± 50°C) and lower temperatures (800 ± 100°C). The specimens were statically annealed with different holding time for grain structure observations and compared to the dynamically superplastic-loaded specimens.

2.5.2 TEM observations

To observe dislocation structure and phase transformation during static annealing and superplastic deformation, the rolling planes of both the as-received and statically annealed specimens were examined by TEM for comparison. The as-received and statistically annealed specimens were punched to 3 mm disks before electrochemical polished. The TEM thin foils of the as-received and static annealed samples were thinned by using a twin-jet electrochemical polishing, carrying out in a solution consisting of 30 ml perchloric acid, 175 ml alcohol, and 300 ml methanol at -30^{o}C with an applied current of 70 mA, a voltage of 30 V, and a flow rate of 2.5 *l*/min. The thin foils were examined by a JEOL 3010 TEM operated at 300 kV and phase determination was done with the help of a commercial software "CaRIne crystallography" [98].

2.6 Volume fraction determinations

From the digital SEM images, the volume fractions of various phases are explored by using a computer program "Optimas" [99]. By adjusting brightness and contrast of the loaded image, the phase, which would like to be determined its volume fraction, could be selected. The volume fraction of each phase could be analyzed by a computer.

2.7 Texture analyses

In this study, microtextures of the rolling plane of both as-received and post-SP specimens were determined by EBSD techniques. Pole figures, inverse pole figures, and ODFs are used to investigate the texture change during superplastic deformation. Misorientation angle distributions could be obtained via mapping by EBSD. From these texture analyses and misorientation angle distributions associated with microstructural morphology, the deformation mechanisms under different superplastical loading conditions were determined.

The microtexture estimations were conducted by using an Oxford Instrument LinkOpal^{TM} EBSD system interfaced to a field emission gun JSM-6330TF SEM with an EBSD system. The lattice constants and atomic positions of the α_2 and β phase required for basic crystal information establishment are shown in Table 7. The lattice constants extracted from the X-ray experiment were determined by Fu [100]. The atom positions of Ti and Al of the α_2 DO_{19} structure and β BCC structure are indicated in Table 7 and Fig. 3. With the addition of Nb element, Nb atoms will randomly substitute in the Ti sites in the α_2 phase, forming a composition of $(Ti,Nb)_3Al$, phase. In the β phase, Ti and Al occupy the two separate primitive sublattices, Nb atoms will occupy the Al sublattice, forming a composition of Ti(Al,Nb).

The as-received and superplastically loaded specimens were rough-polished using emery papers with water to remove about 25% thick of the specimens, then using a colloidal silica polishing suspension for a long time polishing by taking more than one hour as best. If the specimen surface retains surface damage on a crystallographic scale, or has any surface contaminant, oxide, or reaction product layers left, the EBSD pattern formation may be suppressed. To enhance the pattern quality, the specimens were further electropolished with an electrolyte, the same as the twin-jet electrochemical polishing, prior to the establishment of Kikuchi patterns by EBSD. Crystal information is obtained from the "INCA" computer software connected to the Oxford Instrument. The image mapping which provided a crystallographic orientation in a specific region was performed by selecting the crystal map size of 256 referred to the division of the selected area or corresponding to the pixel area of 0.11 μm^2 was chosen. The texture determination was also done with the "CaRIne crystallography" computer software [98].

CHAPTER 3 Experimental Results

3.1 Microstructure characterization of the as-received materials

The three-dimensional SEM microstructure and OM microstructure of the as-received material are shown in Figs. 11 and 12, respectively. It could be seen from the SEM micrograph, the alloy consists of mixture of α_2 (the darker phase) and β (the lighter phase) phases. The coarse α_2 plates (measuring ~10x4x2 μm) and fine spherical α_2 particles (measuring ~2 μm) are nearly random dispersed within the β matrix. For some regions, the long axis of the lath-like α_2 grains appears to align along the two 45^o directions to the rolling direction, implying that cross-rolling was conducted during hot deformation. The grain structure of the coarser lath-like α_2 grains seen from the longitudinal and transverse planes are much flatter, suggesting that the coarser α_2 grains are present in a flat and long pancake-like form. Assuming that the α_2 grains are spherical particles, the average effective grain size of the α_2 grains is 2.2 μm. Judging from the grain size of ~2.2 μm, the LTSP performance may not be as satisfactory as those possessing submicrocrystalline grains around 0.1-0.3 μm [17,73,75,76].

A typical TEM micrograph taken from the as-received material is shown in Fig. 13, where a spherical α_2 grain is surrounded by the β matrix. Based on the diffraction pattern, the β phase is consistently the ordered BCC structure. Note the diffuse streaking contrast in the diffraction pattern in Fig. 13(c), originating from the tweed microstructure [3,4] and the "displacive wave" [83] along the <110> directions in the β grains. Some subgrains within the β matrix can be seen. Figure 14 indicates that planar slip is proceeded in the deformable β phase.

The fabrication method in producing the fine-grained superplastic-grade materials is not fully provided due to the patent restriction. Based on literatures, the possible procedures might include homogenization at elevated temperatures and then followed by a series of hot rolling over the temperature range of 800-1100°C (the two-phase region). As a result, the 2 mm thick sheet is produced. It is believed that the thermomechanical treatment was conducted mostly at ~1050°C, at which the more deformable β phase occupied around 75% in volume fraction. Finally, this material was annealed at 900-1100°C for 1-2 h, so as to fully recrystallize to achieve a final fine-grained two-phase (α_2+β) microstructure.

3.2 Mechanical tests

3.2.1 Room temperature properties

The engineering and true stress-strain curves of the as-received Ti_3Al alloy at room temperature and $3x10^{-3}$ s^{-1} are shown in Fig. 15. The elongation is ~5% at room temperature. In addition, the engineering yield strength (YS) and the ultimate tensile strength (UTS) was extracted to be 950 ± 30 MPa and 1100 ± 40 MPa, respectively.

3.2.2 Elevated temperature properties

The superplastic tensile tests were performed at temperatures over 700-850°C with initial strain rates from $8x10^{-5}$ to $1x10^{-2}$ s^{-1}. Table 8 summarizes the results of tensile mechanical properties at elevated temperatures together with some of the previous results for HTSP [100]. The dependences of superplastic elongations as a function of test temperature and initial strain rate are shown in Figs. 16 and 17. From these results, the reasonable superplastic elongation can be obtained at temperatures above 750°C. The highest LTSP elongation of ~333% was obtained at 850°C and an initial strain rate of $5\text{x}10^{-4}$ s^{-1}. However, the elongation decreases abruptly as loading temperatures fell below 750°C. Figure 18 shows the appearance of specimens before and after superplastic loading at 850°C and $5\text{x}10^{-4}$ s^{-1}. The gauge section of the post-superplastic (post-SP) loading specimen was fractured without pronounced local necking and deformed uniformly. With the prevention from oxidation, cavities, cracks and oxides formed on the surface could be reduced.

The true stress-strain curves transformed under the assumption of uniform deformation at various temperatures and initial strain rates are shown in Fig. 19. After rapid strain hardening, flow stresses reached the ultimate tensile strength and then subsequent strain softening occurred. The stress levels for superplastic straining increase with decreasing deformation temperatures or increasing strain rates. Figure 20 shows the UTS values, which are obtained from the engineering stress, as a function of loading temperatures from 700 to 1000°C. At loading temperatures below 900°C, UTS increases significantly. It is suggested that the rate-controlling mechanism below 900°C might be different from what occurred above 900°C at which GBS dominates the deformation mechanism.

3.3 Anisotropic tests

The optimum condition for LTSP takes place at 850°C and $5\text{x}10^{-4}$ s^{-1}. In order to demonstrate the influence of temperatures on anisotropic properties, different temperature ranges from room temperature (25°C), lower temperature (750°C), medium temperature (850°C), and higher temperature (920°C) are performed. The stress-strain curves of the anisotropic tests are shown in Fig. 21. The flow stresses depend upon strain in 0°, 45°, and 90° at room temperature and 750°C are quite different, while similar flow stresses behavior could be obtained at 850 and 920°C. The mechanical properties tested at room temperature under an initial strain rate of $3x10^{-3}$ s^{-1} are listed in Table 9. It could be found that the lower the yield stress is accompanied by a higher elongation at room temperature. The yield stress, which is the threshold stress for initiation of dislocation motions, is lowest in the 45° specimen. In addition, the tensile test results at 750 to 920°C under an initial strain rate of $5x10^{-4}$ s^{-1} are listed in Table 10. The higher elongations for the 45° specimens are obtained under the anisotropic tensile tests within the overall temperature range. Figure 22 represents the fracture morphology of the 920°C specimens with diffuse necking. Note that the 1910% occurred in the 45° specimen is even higher than the previously reported highest superplastic elongation of 1500% at 960°C for the Ti_3Al based alloy [100]. And the current temperature and strain rate of 920°C and $5x10^{-4}$ s^{-1} are also lower and faster than the previous one of 960°C and $2x10^{-4}$ s^{-1}.

3.4 Microstructure evolutions

3.4.1 Static annealing

To identify the stability of the two phase microstructure, representative SEM microstructures of samples statically annealed at various temperatures for 1.5 h and then water quenched are shown in Fig. 23. The grain size and shape of the α_2 (the darker phase) and β (the brighter one) phases remain highly stable with increasing annealing temperatures up to 960°C, and the α_2 grain size is still around 3 μm except for few elongated 10 μm grains. In specimens annealed at temperatures between 750 and 900°C, a fine lenticular phase was observed to form inside the lighter β phase (most clearly observed in Fig. 23(d)). This lenticular lath semi-coherent phase is termed here as the α_2' phase and is a result of transformation from β to α_2' during annealing. The α_2' phase has the same crystal structure as the original α_2 phase, as confirmed by TEM diffraction as well as high temperature and room temperature X-ray diffraction, but with different shapes; no diffraction peak was found other than those from the α_2 and β phases. The transformed volume fraction for the α_2' phase $V_f(\alpha_2')$ values were at most ~20%. The reason for terming this transformed lath phase as α_2' is to differentiate it from the original spherical α_2 grains. Both the α_2 and α_2' phases are determined in this study to be of the same DO_{19} crystal structure. The measurements of the grain sizes and relative volume fractions for the α_2, β, and α_2' phases in the statically annealed specimens are summarized in Table 11.

At the lowest annealing temperature of 700°C, no evidence of transformation was observed due to sluggish diffusion rates, and the relative V_f values remained the same as the as-received starting specimens. The driving force based on thermodynamics was high, but the kinetic transformation rate was too low. Transformation in the intermediate temperature range of 750-900°C, but not at 960 or 1000°C is consistent with stronger thermodynamic driving forces and sufficient diffusion rates, to promote transformation to α_2' so as to approach the equilibrium V_f values shown in the phase diagram data in Fig. 2.

A typical TEM micrograph taken from the sample statically annealed at 850°C for 1.5 h and then water quenched is shown in Fig. 24. The remarkable feature not observed in the starting material is the lath-like α_2' phase. The selected area diffraction analysis confirmed that the crystalline structure of α_2' is the same as the starting α_2 phase, though the ordering degree in α_2' is less complete than that observed in Fig. 13(b) for the equilibrium α_2 phase. In addition, severely dislocation activities are observed, as shown in Fig. 25, that dislocation structures could be seen in the α_2 and β phases.

The typical microstructures observed in isothermal static annealing at 800 and 850°C for different periods of time are shown in Fig. 26. The size and thickness of the α_2' laths increased with increasing annealing time for 3 min to 1 h, as tabulated in Table 12. The α_2' volume fraction also increased initially. For the later stage at 850°C, the transformed α_2' tended to merge with the α_2 grains, leading to a lower reading in $V_f(\alpha_2')$ and a higher reading of $V_f(\alpha_2)$. The overall volume fraction of $\alpha_2+\alpha_2'$ remained fixed at 65-70%.

In order to determine whether the $\beta\rightarrow\alpha_2'$ phase transformation proceeded primarily during either annealing or cooling, one specimen was annealed at 1000°C for 1.5 h and then water quenched. No transformed α_2' lath inside the β grain was found in this annealed and quenched specimen. Since the starting α_2 and β phases and their relative populations were stable at 1000°C, no $\beta\rightarrow\alpha_2'$ transformation should take place during annealing. The absence of transformed α_2' lath in this very specimen means that no apparent transformation occurred during water quenching as well. The same results were also obtained in our previous annealing experiments at 1050-1200°C followed by water quenching [7]. This confirmed that the $\beta\rightarrow\alpha_2'$ transformation, observed in specimens annealed at all temperatures, occurred during annealing, not water quenching, as discussed further in Sec. 4.2.

In addition, specimens annealed at 850°C for 1.5 h were subjected to furnace cooling, water quenching, and liquid nitrogen quenching. With increasing cooling rate, the morphology of the α_2' phase became slightly sharper and the α_2' volume fraction also slightly decreased, as listed in Table 13. There is an 8% difference in $V_f(\alpha_2')$ between the furnace cooled and liquid nitrogen quenched specimens. This result also indicates that the transformation did take place primarily during annealing. However, continuous α_2' evolution during prolonged furnace cooling would also contribute minor coarsening and thickening, slightly increasing the α_2' volume fraction.

3.4.2 The crystal relationship between β and α_2'

The relationship between the adjacent β and α_2' phases was determined by both EBSD and TEM diffraction analyses. Typical indexed EBSD Kikuchi patterns of the β and α_2' grains are shown in Figs. 27(a) and 27(b). The orientation of the β grain with respect to the rolling plane and direction is about $(4\bar{3}1)[340]$, and the orientation of the α_2' grain is about $(0\bar{2}23)[1\bar{1}01]$. Figure 27(c) shows the overlap of {001} and {0001} pole figures for the β and α_2' grains. It can be readily seen from Fig. 27(c) that the $(011)_\beta$ and $\{0001\}_{\alpha2'}$ poles and $[\bar{1}11]_\beta$ and $[\bar{2}110]_{\alpha2'}$ directions overlap, indicating that the relationship between the orientation of $(4\bar{3}1)\ [340]_\beta$ and $(0\bar{2}23)[1\bar{1}01]_{\alpha2'}$ satisfies the Burgers relationship, namely, $\{011\}_\beta$ // $\{0001\}_{\alpha2'}$ and $<111>_\beta$ // $<11\bar{2}0>_{\alpha2'}$.

As seen in Fig. 13(c), the diffuse streaking along the <110> directions in the β grains reflects the existence of tweed or mottled microstructure and displacive waves on the {110} planes [3,4,94]. The nucleation of the α_2' lath would start on the β {011} planes, with the help of local shear along the <110> directions coupled with atom diffusion [94]. As a result, the basal planes of the α_2' lath tend to lie on the β {011} plane. The habit planes of the α_2' phase are nearly the {011} planes of the β grain. It can be seen in Fig. 24(a) that there are two variants of the α_2' laths, forming on the (110) and $(1\bar{1}0)$ planes of the β grains.

The same orientation relationship was consistently observed in a number of the β grains containing the α_2' phase, as also confirmed by TEM diffraction with the help of commercial software Crystallography [98]. In diffraction pattern simulation and comparison for the ordered BCC crystal structure, the Ti atoms were assigned to occupy the corner sites and the rest Al and Nb (with minor V and Mo) took the body center sites, forming a Ti(Al,Nb) (or more precisely, Ti(Al,Nb,Mo,V) phase (Table 7). However, the precise composition of the B2 phase has not been clarified until now. The Ti_2AlNb composition was first suggested by Banerjee et al. in 1990 [101], but another one also suggested by Banerjee et al. in 1992 [4] proposed the TiAl(Nb) composition. For the α_2 (or α_2') DO_{19} structure, the Ti occupied 6 out of the 8 sites in the 1/3 of the hexagonal volume, and the rest took the other 2 sites, forming a $(Ti,Nb,Mo,V)_3Al$ phase (Table 7). It is apparent that there would be extensive atom relocations during the $\beta \rightarrow \alpha_2$' transformation. Atom diffusion is necessary.

The interface or the habit plane is a low-energy boundary and it normally does not move during the growth of a α_2' lath. On the other hand, the boundary at the end or edge of α_2' lath is expected to be a non-coherent and high-energy boundary in agreement with its observed mobility. On this basis, one would expect that a lath should only grow in length but not in thickness. However, the thickening of the laths from 0.05 μm to 0.50 μm, which has been observed experimentally, would be a result of the lateral movement of small ledges or steps along the coherent faces of the α_2' laths.

3.4.3 Microstructural evolution during superplastic loading

To study the microstructural change after superplastic loading, microstructures in the gauge and grip sections of the post-tension samples at different superplastic temperatures and strains were compared. The grip section exhibited the similar microstructure as those subjected to static annealing. Note that the gauge sections were taken from the maximum strain section near the failure tip after removal of the surface layer. The relative volume fractions in the gauge section of the post-tension specimens are listed in Table 14. The time exposed during tensile loading is also included in Table 14, from which it can be seen that the time duration is comparable to that received during static annealing.

Typical microstructures in the gauge and grip sections of the post-tension specimens, strained at 700 and 800°C and $2x10^{-4}$ s^{-1}, are shown in Fig. 28. The grain structures are quite similar between the gauge and grip sections of samples loaded at 700°C (with <30% elongation), as shown in Fig. 28(a). As with the statically annealed samples, the loaded specimens at 700°C also showed similar relative volume fractions as the as-received one, due to the slow transformation rate at this low working temperature. At 800°C, the grain size became smaller and appreciable phase transformation from β to α_2' was observed (Fig. 28(d) and Table 14). The α_2' occupied ~40% volume, much higher than that in the statically annealed one (~20%) at the same temperature, as compared in Fig. 29. Deformation-enhanced phase transformation is apparent.

Figure 30 shows the grain evolution observed from the gauge section of specimens loaded to true strains of 0.3 (33%), 1.0 (165%), 1.2 (223%), 1.4 (300%), and 1.5 (333%) at 850°C and $5x10^{-4}$ s^{-1} and then stopped and rapidly quenched by blowing liquid nitrogen. In the grip sections, both the α_2 and β grains remained the original morphology and the grain sizes were still 2-3 μm, independent of the strain levels in the gauge sections. The volume fractions of the α_2, β, and α_2' phases in the grip sections for all gauge strain levels were consistently around 45%, 30%, and 25%, respectively. However, the microstructure in the gauge sections becomes quite different. With increasing strain to 0.3, the original lath-like α_2 grains changed their shape into equiaxed grains (Fig. 30(b)), implying the occurrence of dynamic recrystallization during the initial strain hardening stage of superplastic loading. Furthermore, as shown in Table 15, the α_2' phase increased significantly with strain up to 1.2, and V_f(α') finally reached ~35% at a strain of 1.5. The stress level is about the same over

ε=0.5-1.5 in Fig. 30(a), suggesting that the continuous $V_f(\alpha_2')$ enhancement was not stress driven. The variation of α_2' volume fraction as a function of strain level can also be visualized from the microstructures near and away from the fracture tip. For example, in a fractured specimen loaded at 900°C, $V_f(\alpha_2')$ was observed to decrease appreciably with increasing distance from the fracture tip; there was hardly any transformed α_2' near the grip section. It can also be seen from Table 15 that the α_2' lath thickness in the loaded specimen is also much higher than that of the statically annealed ones at the same temperature of 850°C.

The increment ratio of $V_f(\alpha')$ during tensile loading and static annealing was more pronounced with increasing temperature (the last column of Table 14), since the total strain (and thus the exposure time duration) is higher at higher temperatures. There seemed no simple relationship between the enhancement of $V_f(\alpha')$ with stress. The enhancement was mostly strain driven.

3.5 Texture analyses

3.5.1 The as-received materials

The macrotexture revealed by X-ray pole figures of the as-received material taken from the α_2 $(11\bar{2}0)$ planes and β (200) planes and is shown in Fig. 31 [100]. There is a strong {100} texture with a maximum intensity contour of 40 existing in the β phase, while there appears a weaker $\{11\bar{2}0\}$ texture with a maximum intensity contour of 10 existing in the α_2 phase. It could be concluded that the preferred orientation in the β matrix was resulted from the previous thermomechanical treatments, while the α_2 grains were more randomly dispersed in the continuous β matrix. Note that crystal orientations are usually described in the from of {ND}<RD>. However, the orientation distribution stated by X-ray pole figures displays an incomplete examining range from 0^o to $\sim 70^o$ due to the restriction of the X-ray diffraction instrument. Hence, it is difficult to determine the orientation direction <RD> from the X-ray pole figures.

The microtexture of the as-received material was also examined by EBSD for comparisons. Pole figures, inverse pole figures, and ODFs are helpful to establish the texture information. The semi-quantitative information could be obtained from the pole figures and inverse pole figures. In a pole figure, the poles, i.e. the normal to a lattice plane for a chosen family of planes, are plotted relevant to the sample reference axes. The sample reference axes can be the longitudinal or rolling direction, the transverse direction, and the normal direction. The plot can be made for different families of poles. It is common to plot {100}, {110} and {111} pole figures for a cubic system. Crystal orientations based on pole figures could be determined by the follow steps. For instance, from the texture present in Fig. 32(a) and associates with Fig. 33 for texture determination.

(1) Choose one common pole figure, i.e. {100}, {110}, or {111}. For instance, choose the {100} pole figure and the {100} family poles are projected (see Fig. 33(a)).

(2) Find a standard projection and rotate it, to make all the {hkl} pole families lie on the same position in the standard projection. For instance, select the {100} standard projection (in Fig. 33(b)) to make the intensity maxima (in Fig. 33(a)) coincide with the {100} plane family pole positions in the standard projection.

(3) Then, crystal orientation could be read from the standard projection and represent in the form of {ND}<RD>. For instance, {100}<011> could be identified (Fig. 33(c)).

(4) Choose other pole figures to make sure that all the poles are coincided in the standard projection.

One might further check the crystal orientation from the inverse pole figures. From Fig. 32(b), the crystals orientated <001> direction parallel to the sample normal and <101> direction parallel to the rolling direction, implying the {001} plane parallel to the rolling plane and the <101> direction parallel to the rolling direction. Hence, the {100}<011> could be further confirmed.

In addition, the three dimensional orientation spaces could be obtained from the Euler space. In general, the Euler space could be described by the angles ψ, θ, and φ; or φ_1, ϕ, and φ_2 that correspond to a rotation about Z-Y-Z axes in the Roe system [102] or Z-X-Z in the Bunge system, respectively [103]. By using the Bunge system, the rotation g would be represented by the three Euler angles φ_1, ϕ, and φ_2, and usually represented by g={hkl}<uvw>. Euler angles are a sequence of three angles which describe the rotation of a crystal with reference to the crystal axes, as shown in Fig. 6. The first is a rotation of φ_1 about the crystal [001] (Z), then ϕ about the [100] (X), and finally φ_2 about [001] (Z). Crystal orientations could be obtained from the calculation of the rotation matrix or by using a standard projection. In Fig. 32(c), the intensity maximum is appeared to be $\varphi_1=45^o$, $\phi=0^o$, and $\varphi_2=90^o$, i.e. {100}<011> texture.

In a cubic system, the relationship between the orientation g{φ_1, ϕ, φ_2} and {hkl}<uvw> in the Bunge system can be expressed by

$$\begin{bmatrix} h \\ k \\ l \end{bmatrix} = \begin{bmatrix} \sin j_2 \sin f \\ \cos j_2 \sin f \\ \cos f \end{bmatrix}, \qquad (3\text{–}1)$$

and?

$$\begin{bmatrix} u \\ v \\ w \end{bmatrix} = \begin{bmatrix} \cos j1 \cos j\,2 - \sin j1 \sin j\,2 \cos f \\ -\cos j1 \sin j\,2 - \sin j1 \cos j\,2 \cos f \\ \sin j1 \sin f \end{bmatrix}. \qquad (3\text{-}2)$$

In a cubic system, the [100], [010] and [001] directions are parallel to the X, Y, and Z reference axis, respectively. In the case of the hexagonal system, the $[10\bar{1}0]$, $[\bar{1}2\bar{1}0]$ and [0001] directions are parallel to the X, Y, Z reference axis. The hexagonal system represented by $\{OX_1X_2X_3\}$ and the cubic system represented by {OXYZ} are shown in Fig. 34. The matrix T_{ij} that relates both systems is expressed by [104]

$$\begin{bmatrix} X_1 \\ X_2 \\ X_3 \end{bmatrix} = \begin{bmatrix} 2/\sqrt{3} & 0 & 0 \\ 1/\sqrt{3} & 1 & 0 \\ 0 & 0 & 1 \end{bmatrix} \begin{bmatrix} x \\ y \\ z \end{bmatrix}. \qquad (3\text{-}3)$$

From Eq. (3-3), the [hkil] directions parallel to Z axis and the [uvtw] directions parallel to the X axis can be expressed by

$$\begin{bmatrix} h \\ k \\ l \end{bmatrix} = \begin{bmatrix} 2/3 & -1/3 & 0 \\ -1/3 & 2/3 & 0 \\ 0 & 0 & 1 \end{bmatrix} \begin{bmatrix} 2/\sqrt{3} & 0 & 0 \\ 1/\sqrt{3} & 1 & 0 \\ 0 & 0 & a/c \end{bmatrix} \begin{bmatrix} \sin j_2 \sin f \\ \cos j_2 \sin f \\ \cos f \end{bmatrix}, \qquad (3\text{-}4)$$

and

$$\begin{bmatrix} u \\ v \\ w \end{bmatrix} = = \begin{bmatrix} 2/3 & -1/3 & 0 \\ -1/3 & 2/3 & 0 \\ 0 & 0 & 1 \end{bmatrix} \begin{bmatrix} 2/\sqrt{3} & 0 & 0 \\ 1/\sqrt{3} & 1 & 0 \\ 0 & 0 & a/c \end{bmatrix} \begin{bmatrix} \cos j1 \cos j2 - \sin j1 \sin j2 \cos f \\ -\cos j1 \sin j2 - \sin j1 \cos j2 \cos f \\ \sin j1 \sin f \end{bmatrix}. \tag{3-5}$$

Since the plane (hkil) is not perpendicular to the [hkil] direction, the plane perpendicular to a [hkil] direction is given by (hkiλ^2l). Where λ^2 is 2/3(c/a)^2. Thus, the {hkil} perpendicukar to the <uvtw> can be expressed by

$$\begin{bmatrix} h \\ k \\ i \\ l \end{bmatrix} = \begin{bmatrix} \sqrt{3}/2 & -1/2 & 0 \\ 0 & 1 & 0 \\ -\sqrt{3}/2 & -1/2 & 0 \\ 0 & 0 & c/a \end{bmatrix} \begin{bmatrix} \sin j_2 \sin f \\ \cos j_2 \sin f \\ \cos f \end{bmatrix}, \tag{3-7}$$

and

$$\begin{bmatrix} u \\ v \\ t \\ w \end{bmatrix} = \begin{bmatrix} 2/3 & -1/3 & 0 \\ 0 & 2/3 & 0 \\ -2/3 & -1/3 & 0 \\ 0 & 0 & c/a \end{bmatrix} \begin{bmatrix} \cos j1 \cos j2 - \sin j1 \sin j2 \cos f \\ -\cos j1 \sin j2 - \sin j1 \cos j2 \cos f \\ \sin j1 \sin f \end{bmatrix}. \tag{3-8}$$

Figures 32 and 35 show the EBSD results of the β and α_2 phases in the as-received specimen, respectively. It demonstrates that multiple textures are existed in both two phases, strong {100}<011> and the weak {111}<$1\bar{2}1$> textures in the β phase, as well as strong {$11\bar{2}0$}<0001>, weak {$11\bar{2}0$}<$\bar{1}100$> and {0001}<$\bar{1}100$> textures in the α_2 phase. The intensity is divided into eight levels and the black color implies that there is no orientation present. The results are consistent with the X-ray results in Fig. 31. Furthermore, the resulting recrystallization orientations of {$11\bar{2}0$} texture in the α_2 phase and {100} texture in the β phase are in agreement with the report by Knorr et al. [89].

The orientation data could be displayed in the form of pole figure, inverse pole figure or Euler Angle. It could be further displayed in an orientation image map (OIM) with different colors by various orientations, which provide the information connected to the microstructure. Figure 36 displays the OIMs in the normal, transverse, and longitudinal directions in the β and α_2 phases. By using color keys in Figs. 36(e) and (i) for the cubic β and hexagonal α_2 phases, respectively, the orientation distribution cloud be roughly determined; for instance, the {100}<011> orientation in ND-β in red and RD-β in green. A strong preferred orientation is present in the β phase with almost a single color, while multiple preferred orientations are present in the α_2 phase with plentiful colors.

In order to ensure the homogeneous sampling, five regions were randomly selected, and the EBSD results of the two phases are shown in Figs. 37 and 38. It could be concluded that in the AR state, strong textures of {100}<011> rotated cube and {111}<$2\bar{1}\bar{1}$>, plus weak {110}<001> Goss texture, are co-present in the β phase. In the α_2 phase, the strong {$11\bar{2}0$}<0001>, as well as the weak {0001} fiber, {$11\bar{2}0$}<$\bar{1}100$>, {0001}<$\bar{1}100$>, and {0001}<$11\bar{2}0$>, are consistently present in the α_2 phase under the AR state. The orientation components are slightly shifted for a few degrees to the main texture components, since the grains after the thermomechanical treatment tend to align along toward such texture components but with slightly deviations.

3.5.2 Texture evolution during anisotropic tensile straining

It is well known that GBS is the main deformation mechanism for superplastic deformation, so grains would gradually become randomly oriented after superplastic deformation. The misorientation angle distributions and texture evolutions would reflect the operation of GBS. The current alloys exhibit admirable superplasticity at 920^{o}C, however, the elongations decreased abruptly at 750°C. For comparison, specimens after the anisotropic tensile tests along the three directions, which are carried out at 750°C and 920°C with an initial strain rate of 5×10^{-4} s^{-1}, are examined systematically by EBSD. The textures examinations are illustrated separately in these sub-sessions.

3.5.2.1 Lower temperature at 750°C

For the 0° specimen loaded at 750°C to a total failure strain of 0.33 (or 39% elongation), the EBSD results of the β and α_2 phases at the fracture tip of the post-SP specimen are shown in Figs. 39 and 40. From Fig. 39, the original $\{111\}\langle 2\bar{1}\bar{1}\rangle$ texture is significantly present, while the {100}<011> rotated cube becomes extremely weak in the β phase. From Fig. 40, the strongest texture $\{11\bar{2}0\}$<0001> present in the AR state became extremely weak. It also reveals that the strongest texture becomes nearly the $\{0001\}\langle \bar{1}100\rangle$ orientation, or precisely $\{0001\}\langle \bar{4}130\rangle$ orientation, with the weak {0001} fiber texture in the α_2 phase. That is to say the α_2 grains rotate and slide and have a tendency to align the {0001} planes parallel to the rolling plane during loading, whereas the β grains concentrate into $\{111\}\langle 2\bar{1}\bar{1}\rangle$ orientation.

The EBSD results of the 45° specimen to a total failure strain of 0.94 (or 155% elongation) are shown in Figs. 41 and 42. From Fig. 41, it could be clearly seen that the {001}<100> texture retained from the as-received state is strongly present and the $\{111\}\langle 3\bar{2}1\rangle$ and $\{111\}\langle 2\bar{1}\bar{1}\rangle$ and other multiple components are also be seen in the β phase. From Fig. 42, the {0001} fiber, $\{0001\}\langle \bar{4}130\rangle$, and $\{0001\}\langle 11\bar{2}0\rangle$ textures with a deviation angle are shown. The texture intensity of the β phase is weaker than the α_2 phase. It indicated that grain rotations in the α_2 grains are more difficult than in the β grains.

For the 90° specimen to a total failure strain of 0.32 (or 38% elongation), the EBSD results are shown in Figs. 43 and 44. The strong $\{111\}<0\bar{1}1>$, which is the $\{111\}<2\bar{1}\bar{1}>$ orientation originally present in the AR specimen rotated about 90^{o}, is present in the β phase (Figs. 43 and 45(a)). The strong $\{0001\}<11\bar{2}0>$, $\{11\bar{2}0\}<\bar{1}100>$, and $\{0001\}$ fiber, which are as a result of 90^{o} rotation from the $\{0001\}<\bar{1}100>$, $\{11\bar{2}0\}<0001>$, and $\{0001\}$ fiber textures originally present in the AR state, are also present in the α_2 phase (Figs. 44 and 45(b)).

3.5.2.2 Higher temperature at 920^{o}C

As for the 0^{o} specimen loaded at 920^{o}C to a true strain of 2.9 (or 1680% elongation) at the fracture tip, multiple orientations are present in the β and α_2 phases and the texture intensities are greatly decreased (Figs. 46 and 47). Poles are distributed uniformly over the projections for the β phase, as shown in Fig. 46, and there is almost no apparent preferred orientation. In contrast, multiple orientations are present in the α_2 phase even the poles are nearly randomly distributed over the $(11\bar{2}0)$ and $(10\bar{1}0)$ projections, the remained textures are similar to those at the lower temperature, e.g. the extremely weak $\{0001\}<\bar{4}130>$ and strong $\{0001\}$ fiber textures, as shown in Figs. 47 and 48. In addition, It implies that the α_2 grains have rotated and slid to render $\{0001\}$ lying parallel to the rolling plane in the initial stage, and then the extensive GBS continuously operated until failure.

For the 45^{o} specimen with a true strain of 3.0 (or 1910% elongation) at the fracture tip, the β grains become almost in random distribution and textures are difficult to define (Fig. 49), while the α_2 grains rotate and slide to result in the weak $\{0001\}$ fiber and othe extremely weak textures (Fig. 50). Texture intensities are significantly weakened in both of the two phases, due to the notable GBS and the optimum elongation of 1910%. Similar results are obtained in the 90^{o} specimen (true strain of 3.0 or 1880% elongation), as shown in Figs. 51

and 52. The orientation distribution becomes almost random in the β phase with very weak $\{111\}<0\bar{1}1>$ occasionally observed and very weak {0001} fiber and $\{0001\}<10\bar{1}0>$ textures are present in the α_2 phase.

It could be concluded that grain rotations have operated at 750^{o}C, through the dislocation activities and dynamic recrystallization for all of the 0^{o}, 45^{o} and 90^{o} specimens. In addition, the shorter c-axis of the DO_{19} structure would further enhance the alignment of the {0001} plane to lie parallel to the rolling plane in the α_2 phase. Under the severe dislocation actions, some of the β grains concentrate into $\{111\}<2\bar{1}\bar{1}>$ orientation during loading at lower temperatures. At 920^{o}C, the textures have become much more weakened in the two phases after SP deformation, and the elongations can be obtained more than 1600% due to the extensive operation of GBS. It could be more readily seen from the pole figures expressed by the datum points for the 0^{o} specimens loaded at 750 and 920^{o}C, as shown in Fig. 53, where the orientation distribution appears to be more uniform at 920^{o}C.

3.5.2.3 Grain misorientation distributions at 750^{o}C and 920^{o}C

The grain orientation distribution could be further clarified from the misorientation angle distribution, which provides overall angle distribution information. In addition, higher proportion of high angle boundary (high energy boundary) is more suitable for GBS. Hence, it is interesting to know the distribution of the angle distribution after thermomechanical treatments. In common, the range of low angle boundary (LAB), medium angle boundary (MAB), and high angle boundary (HAB) in the cubic system are often defined to be 0-10^{o}, 10-30^{o}, and over than 30^{o}, respectively. However, the boundary definition has not been well defined in the hexagonal system. The simulated random distributions in the cubic and hexagonal systems are shown in Fig. 54 [105,106]. Assuming that the areas of LAB, MAB, and HAB occupied the same area proportion in the cubic and hexagonal systems, the LAB, MAB, and HAB could be roughly assigned to be 0-13^o, 13^o-35^o, and over 35^o, respectively, in the hexagonal system.

The misorientation angle distributions in the α_2 and β phases in the AR alloy, and the post-SP 0^o specimen at the fracture tip loaded at 750 and 920^{o}C are shown in Fig. 55. The occurrence fractions of LAB, MAB, and HAB are listed in Table 16. The data under the theoretically random case are obtained by calculating the integrated area under the misorientation curve from Fig. 54. In the AR alloy, the bimodal distribution is displayed and much higher proportion of HAB is existed in the α_2 phase due to the presence of multiple textures (Fig. 55(a) and Table 16), while LAB occupied a significant amount in the β phase (Fig. 55(b) and Table 16). It implies that α_2/α_2 is more available than β/β for grain boundary sliding.

In the post-SP 0^o specimen loaded at 750^{o}C, with the extensive dislocation motion, α_2 grains rotates to the align the {0001} planes parallel to the rolling plane during loading, and the bimodal distribution is more weakened in the α_2 phase than that in the AR state (Fig. 55(c)). Even though a large amount of the β grains concentrate into the $\{111\}<2\bar{1}\bar{1}>$ orientation and results in the increment of MAB and LAB, the LAB is still dominated (Fig. 55(d) and Table 16). In the post-SP 0^o specimen loaded at 920^{o}C, dynamic recrystallization occurred and both the α_2 and β grains break into nearly equiaxed grains during loading, as shown in Fig. 56. Phase boundary sliding and grain boundary sliding have pronouncedly proceeded to yield the equiaxed shape and results in a basically random distribution in both two phases (Fig. 55(e)(f) and Table 16). Even we have mentioned that α_2/α_2 is more available than β/β for grain boundary sliding, the misorientation distribution is quite similar in both phases. This is because the α_2/β phase boundary sliding is more readily than the α_2/α_2 or β/β

grain boundary sliding. In addition, the volume fraction of the deformable β phase increases to 50%, increasing the occurrence of β/β grain boundary sliding. It could also be seen that with the break-up of the grains, HAB in the β phase increases rapidly, leading the continuous GBS.

3.5.2.4 Texture evolution as a function of superplastic strain

The orientation evolution during superplastic deformation under the optimum LTSP condition of 850^{o}C and 5x10^{-4} s^{-1} is investigated. Various locations with true strains of ε~0.3, 1.0, 1.2 and 1.5 in the post-SP 0^{o} specimens are examined, as shown in Figs. 57 and 58, respectively. Figure 57 shows the texture evolution in the β phase. In the initial stage of loading with a true strain of 0.3, the {111}$<2\bar{1}\bar{1}>$ and {100}<011> with a slight deviation of around $\pm 10^{o}$, which are remained from the as-received state, are strongly present (Fig. 57(a)). At a true strain of 1.0, some of the orientations are concentrated at {111}$<2\bar{1}\bar{1}>$, and the intensity is weakened (Fig. 57(b)). With increasing true strain to 1.2, the {111}$<2\bar{1}\bar{1}>$ and the {100}<011> rotated cube are still remained with some other minor components accompanied, but the intensity is weakened. The β orientation continuously becomes more random due to the minor operation of GBS (Fig. 57(c)). At a true strain of 1.5, some other minor components appear but weak {100}<011>, {111}$<2\bar{1}\bar{1}>$, and {110}$<\bar{1}10>$ are still seen, and the β orientation becomes much more random (Fig. 57(d)).

In the initial stage at a true strain of 0.3, the orientation in the α_2 phase firstly concentrated at $\{11\bar{2}0\}<\bar{1}100>$, but weak {0001}$<\bar{1}100>$ and {0001}$<11\bar{2}0>$ texture components are still remained (Fig. 58(a)). At a true strain of 1.0, the $\{11\bar{2}0\}<\bar{1}100>$ texture is weakened and some of the {0001}$<\bar{1}100>$ and {0001}$<11\bar{2}0>$ textures are combined (Fig. 58(b)). With increasing true strain to 1.2, the {0001}$<\bar{1}100>$ and

$\{0001\}<11\bar{2}0>$ textures are combined to form the {0001} fiber texture. In addition, with the appearance of other weak texture components, the intensity of texture is weakened (Fig. 58(c)). At the fracture tip with a true strain of 1.5, multiple weak texture components are simultaneously present, and the {0001} fiber orientation is no longer distinctly dominant. Orientation distributions become much more random (Fig. 58(d)). In comparison, the original textures present in the β phase of the AR specimen appear to be easier to be retained than those in the α_2 phase.

Figure 59 shows the misorientation angle distribution in the α_2 and β phases at various true strain locations of ε~0.3, 1.0, 1.2 and 1.5; the fractions of LAB, MAB, and HAB are listed in Table. 17. In the initial stage of ε~0.3, the misorientation distribution became more random since some α_2 grains rotate to concentrate at $\{11\bar{2}0\}<\bar{1}100>$. However, the bimodal distribution in the α_2 phase is still retained but the distribution with a slightly scattering due to the occurrence of grain rotation. Grain rotation also leads the HAB to significantly increase even the LAB still occupies a large amount in the β phase during this stage. With increasing superplastic strain to 1.0 and 1.2, the α_2 grains concentrate to the {0001} fiber, while the β grains concentrate to $\{111\}<2\bar{1}\bar{1}>$, and the misorientation distribution becomes more random in both phases. With further increasing strain to failure, the misorientation distribution became more and more random, indicating that GBS accommodated by grain rotation has occurred extensively, especially at the high strain level greater than 1.2. But some of the original textures present in the AR state are still retained even with grain boundary and phase boundary sliding. The significant strain enhanced phase transformation of the α_2' phase could not be ignored. The rigid α_2' phase occupies a large amount of volume fraction and would impede the GBS operation at certain locations. The textures sharpness present in the AR and the superplastic specimens are listed in Table 18.

CHAPTER 4 Discussions

4.1 Deformation mechanisms

4.1.1 Apparent strain rate sensitivity (m_a)

The true stress-strain curves at 700-850°C under initial strain rates from 8x10^{-5} to 5x10^{-4} s^{-1} have been shown in Fig. 19. To select the flow stress value for extracting the apparent strain rate sensitivity m_a-value, it is necessary to choose a fixed strain level from the true stress-strain curves, and is usually selected at the balance stage between strain hardening and strain softening. In the current case, the balance stage or the plateau region at the true stress-strain curves occurred approximately at ε=0.25 at 800 and 850°C, while the balance stage could not be located at 700 and 750°C, only the maximum stress is chosen. According to Eq. (1-4), the m_a-value could be extracted from the slope of the double logarithm plot of the flow stress versus the strain rate, as demonstrated in Fig. 60. The values are 0.11, 0.16, 0.27, and 0.27 at 700, 750, 800, and 850°C, respectively.

4.1.2 Apparent activation energy (Q_a)

The apparent activation energy Q_a could be established from the expression,

$$\dot{e} = A' s^{n_a} \exp(\frac{-Q_a}{RT}), \tag{4-1}$$

where A' is a coefficient. It follows from Eq. (4-1) that the apparent activation energy, Q_a, could be written as,

$$Q_a = -R\frac{\partial(\ln \dot{e})}{\partial(1/T)}\Big|_s \ , \qquad (4\text{-}2)$$

and

$$Q_a = n_a R\frac{\partial(\ln s)}{\partial(1/T)}\Big|_{\dot{e}} \ . \qquad (4\text{-}3)$$

The Q_a-value for superplastic flow would be determined under either the constant stress or constant strain conditions. The Q_a-value under the constant stress condition is estimated from a slope of a double-linear plot of $\ln\dot{e}$ against 1000/RT. Similarly, under the constant strain rate condition, Q_a is estimated from a slope of $\ln\sigma$ against 1000/ n_aRT, where n_a is the inverse of m_a. Note that the Q_a-values determined from these two methods should be consistent.

As shown in Fig. 61, at loading temperatures over 700-750°C, the Q_a-values are ~392 and 346 kJ/mol under the constant stress and constant strain rate conditions, respectively. Similarly, over 800-850°C, the Q_a-values are ~271 and 264 kJ/mol, respectively, as shown in Fig. 62. The average Q_a-values are ~370 kJ/mol at 700-750°C and ~270 kJ/mol at 800-850°C.

4.1.3 Threshold stress (σ_{th}), true strain rate sensitivity (m_t), and true activation energy (Q_t)

The threshold stress σ_{th} could be extracted from the plot of σ versus $\dot{e}^{1/n_t}$. By substituting appropriate true n-values into $\dot{e}^{1/n_t}$, where n_t is the inverse of m_t, various plots are made. Extending the fitted lines to $\dot{e}^{1/n_t} = 0$, the threshold stresses can be obtained. Furthermore, the threshold stress decreases with increasing temperature and it is obtained from the best precision value (R-value) of the linear lines in the plots. It should be further satisfied the equation proposed by Park and Mohamed [107],

$$\frac{n_a}{n_t} = \frac{s}{s - s_{th}}, \qquad (4\text{-}4)$$

or

$$\frac{m_t}{m_a} = \frac{s}{s - s_{th}}. \qquad (4\text{-}5)$$

Figures 63 and 64 show the plots of σ versus $\dot{e}^{1/n_t}$ at 700-750°C and 800-850°C, respectively. The best precision R-values could be obtained for substituting n_t=6 and 3.5 at 700-750°C and 800-850°C, respectively. However, in order to satisfy Eqs. (4-4) and (4-5), and the smaller threshold stress at higher temperatures, n_t=5 and 3 are selected for overall consistency. The threshold stress could be thus determined to be 149 and 134 MPa at 700 and 750°C, respectively, with m_t=0.2 (n_t=5); and to be 85 and 69 MPa at 800 and 850°C, respectively, with m_t=0.33 (n_t=3).

By taking into account the threshold stress, Eq. (4-1) could be written to be Eq. (4-6), hence the true activation energy (Q_t) can be obtained.

$$\dot{e} = A'(s - s_{th})^{n_t} \exp(\frac{-Q_t}{RT}). \qquad (4\text{-}6)$$

The Q_t-value would be determined under either the constant stress or constant strain rate conditions, similar to the extraction of Q_a-value. As shown in Fig. 65, at loading temperatures over 700-750°C, the Q_t-values are ~377 and 339 kJ/mol under the constant stress and constant strain rate conditions, respectively. Similarly, over 800-850°C, the Q_t-values are ~209 and 225 kJ/mol, respectively, as shown in Fig. 66. The average Q_t-values are ~350 kJ/mol at 700-750°C and ~215 kJ/mol at 800-850°C. The extracted m-values and the

Q-values at 700-850^{o}C are listed in Tables 19 and 20, respectively.

4.1.4 Deformation mechanisms during LTSP

At loading temperatures over 700-750^{o}C, the true strain rate sensitivity, m_t, is determined to be ~0.2, which is consistent with the dislocation power law creep during which the deformation mechanism is mainly controlled by dislocation glide plus climb. From the true stress-strain curves, as shown in Figs. 19(a) and (b), there is almost no steady- state flow stage, especially at lower temperature (lower than 700^{o}C) and higher strain rates (higher than 5x10^{-4} s^{-1}). Grain boundary sliding cannot operate smoothly due to the insufficient accommodation; diffusion process is also sluggish, leading to a decrease in ductility at this temperature range. The true activation energy, Q_t, is determined to be ~350 kJ/mol over 700-750^{o}C. This value can be compared with the Q-value of about 290-350 kJ/mol with the n-value within 4-7 in a Ti-27Al-25Nb alloy by Nandy and Banerjee [108], who suggested that dislocation climb controlled the deformation. This result is also close to the interdiffusion of Ti-Al of 312 kJ/mol in the Ti_3Al alloy suggested by Nakajima et al. [109]. The self-diffusion of Ti and Al in Ti_3Al has been demonstrated by Rusing and Herzig [110], suggesting the value is 288 kJ/mol and 394 kJ/mol, respectively. On the other hand, the diffusion path might be the self-diffusion of Ti-Ti or Al-Al, or interdiffusion in Ti-Al in the ordered α_2 phase. This implies that the controlling deformation mechanism at 700-750^{o}C is mainly the dislocation glide plus climb in the ordered α_2 phase, and the climb step is governed by the lattice diffusion in the α_2 phase.

At loading temperatures over 800-850^{o}C, the true strain rate sensitivity, m_t, is determined to be ~0.33, the rate controlling mechanism is the viscous glide of dislocations. A narrow plateau of steady-state flow can be found in the true stress-strain curves, as shown in

Figs. 19(c) and (d), implying minor GBS operation.

The activation energy of Ti self-diffusion in the β phase suggested by Brown and Ashby was ~270 kJ/mol [112] and the diffusion along the α_2/β interface should be lower to ~250 kJ/mol. The true activation energy, Q_t-values, is determined to be ~215 kJ/mol over 800-850°C, which is close to the diffusion along the α_2/β interface or the pipe diffusion in the β phase. It should be noted that this value is lower than the Q_t-value of 270 kJ/mol (m_t-value of 0.5) over 900-960°C in our previous study [70,100].

As a result, in our study, even viscous glide dominated the deformation mechanism over 800-850°C, the minor contribution of GBS is still operating. The Q_t-value of 215 kJ/mol might be related to the β phase grain boundary diffusion or dislocation pipe diffusion, or α_2/β interphase diffusion at 800-850°C, which acts as the controlling step for dislocation slip plus climb in the β phase (the latter is in turn acts as the accommodation step for GBS).

4.2 Phase transformation characteristics

4.2.1 β to α_2 transformation behaviors

The phase transformation between the BCC β phase and HCP α phase in numerous Ti base alloys has been widely studied. For most cases, the α phase was formed martensitically from the high temperature β phase during rapid cooling [3,83]. In the Ti_3Al base alloy, Strychor et al. [3] reported that the Ti_3Al-Nb alloys with the Nb content less than 5 at% would also transform martensitically from the BCC β phase to the hexagonal DO_{19} α_2 phase during rapid cooling from the β phase field.

In this study, the super α_2 Ti_3Al base alloy contains much higher solute amounts, with 10%Nb, 2%V and 1%Mo. The starting alloy consisted of 60% β and 40% α_2 in volume percentage, which is an equilibrium phase partition resulting from the previous heat treatment at ~1000^{o}C. Upon subsequent static annealing and superplastic loading at 700-960^{o}C, the existing phase proportion became unstable, and the alloy tended to undergo phase evolution, approaching the equilibrium phase partition at the respective temperature. The phase transformation was seen to take place predominantly at the holding temperature, rather than a result from rapid or slow cooling. In other words, the current phase evolution is not considered to be a result of martensitic diffusionless transformation. The growth of the transformed α_2' lath is diffusion-controlled.

The difference in equilibrium volume fractions at the post-rolling annealing temperature (~1000^{o}C) and subsequent holding temperatures (700-960^{o}C) acts as the driving force for the transformation of $\beta \rightarrow \alpha_2$'. However, although there exists a relatively higher driving forcer at lower temperatures (700~750^{o}C), the slower diffusion kinetics suppresses the phase transformation development for the annealing times used in this study. At higher temperature (900~960^{o}C), a relatively lower driving forcer also restrains the phase transformation development in spite of higher diffusion rates. Therefore, a maximum degree of transformation was obtained at intermediate holding temperatures (800-850^{o}C) for both static annealing and dynamic loading, as illustrated in Fig. 24. This characteristic of phase transformation is consistent with the common diffusion-controlled transformation [114].

Based on the static annealing experiments at 800, 850 and 900^{o}C for different periods of time, as well as with different subsequent cooling rates, the $\beta \rightarrow \alpha_2$' transformation was seen to follow the diffusion-controlled process. The thickening of the α_2' laths is a direct function of annealing time t, following the $t^{1/2}$ diffusion rule (Fig. 67(a)). Using the slope K in Fig.

67(a), the activation energy for the diffusivity D can be roughly evaluated, using the relationship,

$$h \propto K\sqrt{t} \propto \sqrt{Dt}\,, \tag{4-4}$$

and

$$\ln D = \ln(K^2) = A - \frac{Q}{RT}\,, \tag{4-5}$$

where A is a constant, Q the activation energy involved the α_2' growth kinetics, and RT the general meaning. Although there are only two datum points, the extracted Q in Fig. 67(b) is 200 kJ/mol, which is in reasonable agreement with the activation energy for solute element diffusion in the β phase (200-250 kJ/mol) [115,116]. This value is also in fair agreement with the activation energy extracted from our previous analyses on the HTSP deformation mechanisms (~270 kJ/mol) [70] and the current LTSP deformation mechanisms over 800-850°C (~215 kJ/mol).

At 850°C, some large α_2' plates would merge with existing α_2 grains at later stages, making the measurement of α_2' volume fraction inside the β grains more difficult. This problem was not pronounced at 800°C, since the α_2' size was much finer. Figure 68(a) shows the limited data on V_f' (=$V_f/V_{f,saturation}$, where the latter means the α_2' volume fraction for complete transformation, ~21% for the current case) versus the annealing time, basically following the S-curve. By plotting the lnln(1/(1-V_f')) versus lnt, as shown in Fig. 68(b), the extracted slope is the transformation characteristic exponent n, following the Avrami's equation [83].

$$V_f' = 1 - \exp(-kt^n)\,, \tag{4-6}$$

and $$\ln \ln\left(\frac{1}{1-V_f'}\right) = k' + n(\ln t)\,. \tag{4-7}$$

The obtained n is 0.93 (close to 1), suggesting the transformation is diffusion controlled for plate growth mechanism [114]. This is consistent with the α_2' lath shape.

Recent studies on the $\alpha-\gamma$ transformation in the Ti-Al base alloys upon intermediate cooling rate of 10^2-10^3 K/s [117-119] have shown the massive transformation characteristics, i.e., (i) with crystalline structure change but no composition changes, (ii) the interfacial controlled behavior, (iii) not necessarily fixed orientation relationship, etc. The current $\beta \rightarrow \alpha_2$ transformation in the two-phase region during isochronal or isothermal annealing or loading correlated well with traditional diffusion controlled transformation (with $t^{1/2}$ dependence, rational activation energy, reasonable n-value, fixed Burgers orientation relationship). It did not behave as the massive transformation.

Also, once the α_2' phase is formed inside the β grain during annealing or superplastic loading, there will be minimal martensitic $\beta \rightarrow \alpha_2$' transformation occurred during subsequent cooling. Since the α_2 phase in the current alloy is more complicated in crystal structure and since there are more atom relocations required (Ti, Al, Nb, V, and Mo) between β and α_2, as described in Sec. 3.4.2, the $\beta \rightarrow \alpha_2$ transformation is unlikely to be completed during rapid cooling through a diffusionless martensitic transformation.

4.2.2 Deformation enhanced transformation

There is a volume change upon $\beta \rightarrow \alpha_2$ transformation. According to high temperature X-ray diffraction, the lattice constants were determined to be a=3.24 Å for the β phase and

a_1=5.86 Å and c=4.74 Å for the α_2 phase at ~900°C [100]. Given that there are 2 atoms in the β unit cell and 8 atoms in the α_2 unit cell (see Fig. 69), and with the assumption of equivalent packing density, the volume change from β to α_2 can be calculated to be +3.6% based on the equation,

$$\Delta V = \frac{V_{a_2'} - V_b}{V_b} x100\% = \frac{a_1^{\,2} \sin 60^o c - 4 \cdot a^3}{4 \cdot a^3} x100\% = +3.6\% . \qquad (4\text{-}8)$$

When deformed in tension at high temperatures, the tensile stress might impose a positive factor on the phase transformation with volume expansion. This might be the reason that the volume fraction of the transformed α_2' phase was higher under tension loading.

Another aspect that might cause the strain enhanced $\beta \rightarrow \alpha_2$ transformation is the kinetic factor. The higher defect concentrations of vacancies and dislocations in the superplastically strained specimens with increasing strain would enhance diffusion, directly promoting the diffusion-controlled phase transformation. Thus under the similar period of time, there appeared more transformed α_2' in the tension loaded specimens; and the increment ratio is higher with increasing strain level or loading temperature as shown in Table 14.

In fine-grained alloys, grain boundary sliding (GBS) with accommodation processes is usually the rate-controlling mechanism for high temperature deformation. The main accommodation processes can be diffusional flow or dislocation activities. It has been shown above that the β? α_2' phase transformation is a diffusional process. The atoms in β need to rearrange or interdiffuse so as to form α_2'. The defects or vacancies generated from the operation of GBS and accommodation might be partially consumed by such atom rearrangement and interdiffusion. In other words, GBS might also be partly accommodated by the deformation enhanced β? α_2' phase transformation, similar to the thinking in ref. [94].

On the thermodynamic view, the total Gibbs free energy term, ΔG_t, expressed as

$$DG_t = Ag + V(DG_v + DG_e)\,, \tag{4-9}$$

where A and V represent the surface and volume, and γ, ΔG_v and ΔG_ε are the surface energy, bulk Gibbs free energy and strain energy terms, respectively, which could be lowered since the positive strain energy ΔG_ε induced by β? α_2' could be relieved by tensile loading. Thus the phase transformation can be more readily proceed under tensile deformation.

4.2.3 Relationship between microstructure transformation and superplastic performance

At high temperatures above 900°C, the phase volume fractions initially present in the tensile specimens were close to the equilibrium values, so that there was minimum phase transformation inside the β grains during the heating stage. Upon subsequent superplastic loading, there will be minor deformation-enhanced α_2' (~10-15% in volume fraction) transformed from β. Such a low α_2' volume fraction would not be able to behave as obstacles against dislocation slip across the β grains (the major accommodation process for GBS), but can contribute some positive effects in accommodation as described above. Under such conditions, the alloy undergoes smooth grain boundary sliding and exhibits superior superplastic elongations greater than 500%.

In contrast, appreciable $\beta \rightarrow \alpha_2$' transformation (~40% in volume fraction) occurred during the heating stage as well as during tensile straining at loading temperatures below 900°C, thus the numerous α_2' laths inside the β grains would impede the major dislocation-slip accommodation, leading to premature failure and lower tensile elongations. The minor positive effect due to volume expansion would not able to compensate the major negative influence from the impedance against dislocation slip. At 850°C, a higher superplastic elongation was obtained at a higher strain rate of $5x10^{-4}$ s^{-1} (compared with $2x10^{-4}$ and $8x10^{-5}$ s^{-1}), presumably due to the shorter transformation time and thus a smaller amount of α_2' and hence more effective operation of accommodation. It is also possible that the $\beta \rightarrow \alpha_2$' transformation that occurred during the heating stage before tensile loading might induce microcracks at the α_2'/β interface. These microcracks would be detrimental to the subsequent superplastic deformation, resulting in degraded elongations.

4.3 The relationship among texture, mechanical anisotropy and superplasticity

4.3.1 Texture evolution during thermomechanical treatment

It is suggested that the thermomechanical treatment for the current super α_2 alloy was conducted mostly at ~1050°C, and then annealed at 900-1100°C for 1-2 h to fully recrystallize and to achieve a fine-grained two-phase (α_2+β) microstructure in the as-received material [100]. From literatures [80-84], it was suggested that the rolling texture in the α_2 phase is mainly the basal {0001} fiber texture. In addition, it has been shown that, in order to enhance ductility, a basal fiber texture is desired [91].

The stability during subsequent annealing has been investigated in details by Suwas et al. [91], which aimed the annealing temperatures at 850-1020°C. The texture characteristics are approximately the same to our current result only with the intensity difference, especially at annealing temperatures of 850 and 900°C (see Fig. 70 [91] and Fig. 38). In the study of

Suwas et al. [83], during 850^{o}C annealing, a number of orientations along [0001]//ND, $[10\bar{1}0]$//ND and $[10\bar{1}0]$//TD fibers are present. Furthermore, the intensity of near basal fiber is decreased as compared to that in the hot rolling condition. During 900^{o}C annealing, the basal texture offsets 6^{o} away from the perfect (0001)<uvtw>. Furthermore, the $(0001)[\bar{1}100]$, $(0001)[1\bar{2}10]$, $(0001)[4\bar{3}\bar{1}0]$, and $(01\bar{1}6)[2\bar{4}21]$ appear. Similarly, in our current study, the basal texture is also retained from the rolling texture and deviated the perfect (0001)<uvtw> within 10^{o}. Furthermore, the $\{0001\}<11\bar{2}0>$ and $\{0001\}<\bar{1}100>$ basal textures as well as $\{11\bar{2}0\}$<0001>, $\{11\bar{2}0\}<\bar{1}100>$, and other multiple non-basal textures are coexisted in our starting material. It could be believed that the {0001} basal fiber texture was formed during hot rolling. Under subsequent recovery and recrystallization process, $\{11\bar{2}0\}$<0001>, $\{11\bar{2}0\}<\bar{1}100>$ are evolved in this stage. The other multiple components are developed during the limited grain growth stage [91].

The rolling texture in the β phase was also investigated by Suwas et al. [92] but the stability during subsequent annealing was not clearly reported. The as-cast Ti_3Al rolled at 1100^{o}C possessed a strongest {011}<100> texture. The {011}<011> and {013}<110> texture components were also strong. A number of other orientations like {112}<111>, {112}<110>, {011}<110>, and {001}<230> are also present. Knorr et al. [89] reported that the {200} cubic texture is present after heat treatments, retaining from the original texture components whereas the intensity were altered. In our study, the strong {100}<011> rotated cube and $\{111\}<2\bar{1}\bar{1}>$, and weaker {110}<001> Goss texture are observed in the β phase in the starting material. Hence, textures present in the β phase could not be clarified whether the developed texture is a result of the rolling texture or recrystallization texture. It is postulated that the current super α_2 alloy has been cross-rolled during the TMT process, and this would complicate the resulting texture of the continuous β matrix.

4.3.2 Texture evolution during superplasticity

After superplastic loading at 750 to 920^{o}C, the $\{11\bar{2}0\}$<0001> texture present in the starting material become extremely weak and the α_2 grains have a tendency to lead the (0001) plane parallel to the rolling plane parallel to the tensile direction and the $\{0001\}<\bar{1}100>$ orientation, or more precisely $\{0001\}<\bar{4}130>$ orientation, but the intensities are greatly decreased in specimens at 920^{o}C (Figs. 40 and 47). Hon et al. [88] demonstrated that the existence of the basal texture in Ti_3Al alloys would give rise to ductility, which is agreed with our current results. It could be found that the grains rotation behavior already occurred at 750^{o}C, even though the elongation was not high. Moreover, during tensile loading in the early stage (Fig. 58(b)), the α_2 grains have been rotated to lead [0001]//ND for the subsequent deformation. Hence, the ductility would be enhanced in the dislocation creep domainating deformation stage (n~3-5). Once the (0001) plane parallel to the rolling plane is formatted, dislocations would readily slip along the <a> directions. Note that twinning is restricted in Ti_3Al alloys due to the ordered structure [120,121]. At 920^{o}C, in the subsequent grain boundary sliding stage with n~2, the rotation of α_2 grains is continuously operating and the orientations are distributed more and more random.

In comparison, the orientation distributions in the β phase are overall more random than those in the α_2 phase during LTSP, and some of the β grains concentrate into the $\{111\}<2\bar{1}\bar{1}>$ orientation after superplastic loading. During the dislocation creep dominating deformation stage at 750^{o}C with n~3-5, several slip systems act simultaneously in the β phase due to the BCC structure. Subsequently, the β grains concentrate into the $\{111\}<2\bar{1}\bar{1}>$ orientation. In the following grain boundary sliding stage at 920^{o}C with n~2, the intensity of the $\{111\}<2\bar{1}\bar{1}>$ orientation is decreased, indicating the severe grain boundary sliding and grain rotation in the β phase.

4.3.3 Influence from textures on the mechanical anisotropy

4.3.3.1 Microstructure effects on the mechanical anisotropy

Grains with equiaxed shape are suitable for grain boundary sliding and would not give rise to pronounced superplastic anisotropy. However, the elongated hard grains acting as barriers to grain boundary sliding would give rise to superplastic anisotropy [87]. In the as-received state, the coarse lath-like α_2 plates and the fine spherical α_2 particles are nearly randomly dispersed within the β matrix. Hence, the effect from microstructure grain shape is postulated to be minor.

4.3.3.2 Texture effects on the mechanical anisotropy

Dislocation mobility would significantly affect the ductility at temperatures below 750°C (under the dislocation creep condition), and during the initial stage of the deformation at higher temperatures (under the superplastic flow condition). To consider about the dislocation mobility in the β and α_2 phases, the Schmid factor is an important indication [16]. As the TEM microstructure shown in Figs. 13(a) and 14, the subgrains formation and the planar slip phenomena within the β grains, indicating the significance of dislocation activities during deformation.

Dislocations would tend to slip along the system with the higher Schmid factor. The β phase which has the BCC crystal structure is more deformable than the hexagonal α_2 phase. The dislocation motion and dislocation accommodation process would be operative more readily in the β phase. In addition, the Schmid factor effect on the β phase may be more important than that on the α_2 phase due to the higher initial volume fraction (~60%) of the β phase. For the BCC β phase, the Schmid factor analysis was only carried out on the dislocations acting on the main $\{110\}<\bar{1}11>$ slip system. Several slip systems i.e. $\{211\}<\bar{1}11>$ and $\{321\}<\bar{1}11>$ could also offer dislocations slip, but they are usually less favorable than the main slip system. For the major texture existed in the β phase, when the stress is acted to the 45^{o} to the RD direction, the Schmid factors are highest (in Table 21). There are 12 slip systems of the kind existed in the β phase. If one set of the dislocation is blocked during loading, dislocations would easily continue to cross slip into another set of slip systems.

The main slip systems in the α_2 phase mainly includes (i) basal $\{0001\}<11\bar{2}0>$, (ii) prismatic $\{10\bar{1}0\}<11\bar{2}0>$ and (iii) pyramidal $\{10\bar{1}\bar{1}\}<11\bar{2}0>$. In the Ti_3Al alloy, the primary slip system is the <a> type dislocation acting on the prism plane, i.e. $\{10\bar{1}0\}<11\bar{2}0>$ since the c/a ratio is less than the ideal value [12,113]. In average, the Schmid factor is also highest in the α_2 phase of the 45^{o} direction, leading to a highest elongation (in Tables 9, 10, and 22). It could be seen that the Schmid factors in the major textures in the 0^{o} specimen are zero. As a result, dislocation motions could only occur in grains of the minor textures or after the α_2 grains rotate into a position with the (0001) plane parallel to the rolling plane.

The {0001} basal texture formation during tensile loading might be similar to that in the basal rolling texture. The <a> type dislocation slips on the {0001}, $\{10\bar{1}0\}$, and $\{10\bar{1}\bar{1}\}$ planes, leading to the formation of the basal texture [121]. After the α_2 grains rotate into the {0001} <uvtw> orientation, the Schmid factors increases, as tabulated in Table 18. The Schmid factors of $<11\bar{2}0>$ dislocations acting on the three main slip systems in the basal $\{0001\}<\bar{1}100>$ and $\{0001\}<11\bar{2}0>$ orientations are greater than those in the

$\{11\bar{2}0\}$<0001> and $\{11\bar{2}0\}<\bar{1}100>$ orientations. Consequently, dislocation glide and climb could proceed further until fracture in the dislocation creep dominating stage (n~3-5) at 700-850^{o}C.

The Schmid factors of the 90^{o} direction are higher than that of the 0^{o} direction in the α_2 phase, and hence dislocations can glide and cross slip in both the major and minor textures. However, due to the highly dislocation motion acting on the $\{11\bar{2}0\}$ planes, the tendency of the formation in {0001} basal texture is decreased. The insufficient slip systems of the <a> type dislocation acting on the $\{11\bar{2}0\}$ planes, leading to the inferior ductility.

At 900-1000^{o}C under the smooth grain boundary sliding stage with n~2, the rotation of α_2 grains are continuously operating and the orientations are distributed more and more randomly. At higher temperatures, the texture effects decrease since the volume fraction of the ductile β phase increases to 50% at 960^{o}C. However, the texture effects should still be considered even in the superplastic flow condition [16,74]. The textured Ti alloys showed the greater ductility compared with the textureless alloy with the same microstructure, and with the same GBS as the rate controlling mechanism. It should be also noted that the texture intensity decreases significantly at temperatures above 850^{o}C. Both the α_2 and β phases break into more equiaxed grains upon loading, allowing the operating of grain rotations and grain boundary sliding.

CHAPTER 5 Conclusions

(1) Although the super α_2 alloy exhibited superior superplastic elongations of 1500% at 960^{o}C, the elongation dropped appreciably to 600% at 900^{o}C, 330% at 850^{o}C and 140% at 750^{o}C.

(2) At loading temperatures over 700-750^{o}C, the true strain rate sensitivity, m_t, is determined to be ~0.2, suggesting that dislocation slip plus climb creep is the rate-controlling mechanism. The true activation energy, Q_t, is determined to be ~350 kJ/mol, implying the diffusion path may be the self-diffusion of Ti-Ti or Al-Al, or interdiffusion in Ti-Al in the ordered α_2 phase.

(3) At loading temperatures over 800-850^{o}C, the true strain rate sensitivity, m_t, is determined to be ~0.33, or the rate controlling mechanism is the viscous glide of dislocations. The true activation energy, Q_t-values, is determined to be ~215 kJ/mol, which is close to the activation energy for the diffusion along the α_2/β interface.

(4) During static annealing, $\beta \rightarrow \alpha_2$' transformation occurred in accordance with the equilibrium phase diagram, and the maximum transformation rate occurred at the intermediate temperatures of 800-850^{o}C.

(5) There exists a fixed Burgers-typed orientation relationship between the β and α_2' phases, namely, $\{011\}_\beta$ // $\{0001\}_{\alpha 2'}$ and $<111>_\beta$ // $<11\bar{2}0>_{\alpha 2'}$.

(6) Based on the analyses on the thickening of the α_2' laths and the increment of α_2' volume

fraction, the $\beta \rightarrow \alpha_2$' transformation in the Ti_3Al base alloy is diffusion controlled, and not a massive or martensitic mechanism. The activation energy for transformation is ~200 kJ/mol and the transformation exponent for the Avrami equation is ~1.

(7) During tensile loading, the α_2 and β phases were gradually broken into smaller and equiaxed grains with increasing strain. The $\beta \rightarrow \alpha_2$' transformation was observed to be enhanced during tensile straining. The volume increase due to the $\beta \rightarrow \alpha_2$' transformation may help accommodate the tensile loading state.

(8) With abundant α_2 laths inside the β grains, the major accommodation process via dislocation slip across the β grains is impeded, leading to premature failure and lower tensile elongations (even with the refined grain size and a minor positive effect from $\beta \rightarrow \alpha_2$' volume expansion).

(9) In the as-received alloy, strong {100}<011> rotated cube, strong $\{111\}<2\bar{1}\bar{1}>$, and weaker {110}<001> Goss textures are present in the β phase; strong $\{11\bar{2}0\}<0001>$ and the minor {0001} fiber, $\{11\bar{2}0\}<\bar{1}100>$, $\{0001\}<\bar{1}100>$, and $\{0001\}<11\bar{2}0>$ are present in the α_2 phase.

(10) After superplastic loading at 750 to 920°C, the $\{11\bar{2}0\}<0001>$ texture present in the α_2 phase of the starting material becomes extremely weaker, and the (0001) plane tends to lie parallel to the rolling plane and $<\bar{2}110>$, $<\bar{4}130>$ or $<\bar{1}100>$ directions tent to align along the tensile direction.

(11) After LTSP straining, the orientations in the β phase are distributed more randomly than

the α_2 phase and some of the β grains tend to concentrate into the $\{111\}<2\bar{1}\bar{1}>$ orientation.

(12) Higher elongations are obtained in the 45^o specimens as tensile loaded at 25 to 960^oC.

(13) The microstructure effects to the mechanical anisotropy appear to be minor due to the equiaxed and some randomly dispersed elongated α_2 grains in the as-received specimen.

(14) The Schmid factors for the 45^o specimens are highest in the α_2 and β phases. It provides the reasonable origin for the mechanical anisotropy.

REFERENCES

1. C. H. Ward, Int. Mater. Rev., 38 (1993) 79.
2. H. Hino, T. Miyashita, and S. Minakata, Light Metals (Japan), 43 (1993) 545 (in Japanese).
3. R. Strychor, J. C. Williams, and W. A. Soffa, Metall. Trans., 19A (1988) 225.
4. K. Muraleedharan, T. K. Nandy, D. Banerjee, and S. Lele, Metall. Trans., 23A (1992) 401.
5. W. A. Baeslack III and T. Broderick, Scripta Metall. Mater., 24 (1990) 319.
6. M. Long. and H. J. Rack, Mater. Sci. Technol., 11 (1995) 150.
7. C. S. Liauo, H. C. Fu, I. C. Hsiao, and J. C. Huang, Mater. Sci. Eng., A271 (1999) 275.
8. D. Banerjee, Prog. Mater. Sci., 42 (1997) 135.
9. D. Banerjee, T. K. Nandy, and A. K. Gogia, Scripta Metall., 21 (1987) 597.
10. D. S. Xu, Y. Song, D. Li, and Z. Q. Hu, Mater. Sci. Eng., A234-236 (1997) 230.
11. D. G. Konitzer, I. P. Jones, and H. L. Fraser, Scripta Metall., 20 (1986) 265.
12. H. A. Lipsitt, D. Shechtman, and R. E. Schafrik, Metall. Trans. A, 11A (1980) 1369.
13. 吳易座，“ Ti_3Al-Nb 鈦鋁介金屬合金之超塑性研究 ”，國立台灣大學材料科學與工程研究所博士論文，1998。
14. A. Miyazaki, M. Tokizane, and T. Inaba, J. Japan Inst. Metals, 54 (1990) 1279.
15. A. Dutta and D. Banerjee, Scripta Metall. Mater., 24 (1990) 1319.
16. Y. T. Wu and C. H. Koo, Intermetallics, 5 (1997) 29.
17. G. A. Salishchev, R. M. Imayev, O. N. Senkov, V. M. Imayev, N. K. Gabdullin, M. R. Shagiev, A. V. Kuznetsov, and F. H. Froes, Mater. Sci. Eng., A286 (2000) 236.
18. J. H. Kim, C. G. Park, T. K. Ha, and Y. W. Chang, Mater. Sci. Eng., A269 (1999) 197.
19. J. W. Zang, S. Q. Li, D. X. Zou, W. Q. Ma, and Z. Y. Zhong, Intermetallics, 8 (2000)

699.

20. T. G. Langdon, Superplasticity in Advanced Materials, S. Hori, M. Tokizane, and N. Furushiro (eds.), Osaka, JSRS, 1991, p. 3.
21. O. D. Sherby and J. Wadsworth, Prog. Mater. Sci., 33 (1989) 169.
22. N. Ridley, Mater. Sci. Tech., 6 (1990) 1145.
23. A. H. Chokshi, A. K. Mukherjee, and T. G. Langdon, Mater. Sci. Eng., R10 (1993) 1.
24. S. Primdahl, A. Thölén, and T. G. Langdon, Acta Metall. Mater., 43 (1995) 1211.
25. J. W. Edington, Metall. Trans. A. 13A (1982) 703.
26. M. Kawazoe, T. Shibata, T. Mukai, and K. Higashi, Scripta Mater., 36 (1997) 699.
27. G. E. Dieter, Mechanical Metallurgy, McGraw-Hill Book Co., (1988) 289.
28. T. G. Nieh, J. Wadsworth, and O. D. Sherby, Superplasticity in Metals and Ceramics, Cambridge University Press, Cambridge, New York, 1997, p. 22.
29. M. Mabuchi, K. Higashi, Y. Okada, S. Tanimura, T. Imai, and K. Kubo, Scripta Metall. Mater., 25 (1991) 2517.
30. T. G. Nieh and J. Wadsworth, Mater. Sci. Eng. A, 147 (1991) 129.
31. S. J. Hales, T. R. McNelley, and H. J. McQueen, Metall. Trans. A, 22A (1991) 1037.
32. M. Mabuchi, H. Iwasaki, K. Yanase, and K. Higashi, Scripta Metall. Mater., 36 (1997) 681.
33. E. Girault, J. J. Blandin, A. Varloteaux, M. Suery, and Y. Combres, Scripta Metall. Mater., 29 (1993) 503.
34. D. R. Lesuer, C. K. Syn, O. D. Sherby, J. Wadsworth, J. J. Lewandowski, and W. H. Hunt, Inter. Mater. Rev., 41 (1996) 169.
35. T. G. Nieh and J. Wadsworth, Mater. Sci. Eng., A239-240 (1997) 88.
36. S. X. McFadden. R. S. Mishra, R. Z. Valiev, A. P. Zhilyaev, and A. K. Muherjee, Nature, 398 (1999) 684.
37. L. Lu, M. L. Sui, and K. Lu, Science, 287 (2000) 1463.

38. Q. Liu, W. Yang, and G. Chen, Acta Metall. Mater., 43 (1995) 3571.

39. D. Lee, Metall. Trans., 1 (1970) 309.

40. K. Holm, J. D. Embury, and G. R. Purdy, Acta Metall., 25 (1977) 1191.

41. M. F. Ashby and R. A. Verrall, Acta Metall., 21 (1973) 149.

42. M. F. Ashby, G. H. Edward, J. Davenport, and R. A. Verrall, Acta Metall., 26 (1978) 1379.

43. T. E. Chung and T. J. Davies, Acta Metall., 27 (1979) 627.

44. D. S. Wilkinson, B. Wilshire and D. R. J. Owen (eds.), Creep and Fracture of Engineering Materials and Structures, Pineridge, Swansea, 1982, p. 223.

45. T. L. Spingarn and W. D. Nix, Acta Metall., 26 (1978) 1389.

46. T. Kamijo, T. Furakama, and H. Fukutori, J. B. BildeSorensen, N. Hansen, D. J. Jensen, et al. (eds.), Materials Architecture, Proc. 10th Riso Int. Symp. on Metallurgy and Materials Science, 1989, p. 429.

47. R. C. Gifkins, Metall. Trans. A., 7 (1976) 1225.

48. R. Z. Valev and T. G. Langdon, Acta Metall., 41 (1993) 949.

49. B. Baudelet, Scripta Metall. Mater., 27 (1992) 745.

50. K. Matsuki, H. Morita, M. Yamada, and Y, Murakami, Met. Sci., 11 (1977) 156.

51. R. C. Gifkins, J. Mater. Sci., 13 (1978) 1926.

52. T. G. Langdon, Met. Forum, 4 (1981) 14.

53. A. E. Geckinli, Met. Sci., 17 (1983) 12.

54. R. C. Gifkins, N. E. paton and C. H. Hamiton (eds.), Superplastic Forming of Structural Alloys, Metallurgical Society of AIME, New York, 1982, p. 3.

55. R. Ray and M. F. Ashby, Metall. Trans. A, 2 (1971) 1113.

56. W. D. Nix, J. C. M. Li and A. K. Mukherjee (eds.), Rate Processes in Plastic Deformation of Materials, Vol. 4, American Society of Metals Park, OH, 1975, p. 384.

57. C. G. Barret, J. G. Rasmussen (ed.), High Temperature Materials Phenomena, Vol. 1,

Polytecknisk Forlag, 1973, p. 79.

58. W. R. Cannon and W. D. Nix, Phil. Mag., 27 (1973) 9.
59. I. I. Novikov and V. K. Portnoy, Superplasticity in Alloys with Ultrafine Grain Structure, Metallurgia, Moscow, 1984, (in Russian).
60. P. G. Partridge, D. S. MacDarmaid, and A. W. Bowen, Acta Metall., 33 (1985) 571.
61. P. M. Hazzeldine and D. E. Newbury, Proc. ICSMA3, Cambridge, 1 (1973) 202.
62. J. E. Morral and M. R. Ashby, Acta Metall., 22 (1974) 567.
63. E. Sato, K.Kuribayshi, and R. Horiuchi, M. J. Mayo, M. Kobayashi and Wadsworth (eds.), Superplasticity in Metals, Ceramics, and Intermetallics, Materials Research Society, Pittsburgh, PA, 1990, p. 27.
64. T. Kamijo, T. Furakama, and H. Fukutori, J. B. BildeSorensen, N. Hansen, D. Jucel Jensen, et al. (eds.), Materials Architecture, Proc. 10th Riso Int. Symp. on Metallurgy and Materials Science, 1989, p. 429.
65. H. S. Yang, P. Jin, E. Dalder, and A. K. Mukherjee, Scripta Metall., 25 (1991) 1223.
66. H. S. Yang, M. G. Zelin, R. Z. Valiev, and A. K. Mukherjee, Scripta Metall. Mater., 26 (1992) 1707.
67. H. S. Yang, M. G. Zelin, and A. K. Mukherjee, Proc. Conf. High Temp. Ordered Intermetallic Alloys V, Boston, Mass, USA, 1992, p. 879.
68. A. K. Ghosh and C. H. Cheng, Superplasticity in Advanced Materials, S. Hori, M. Tokizane and N. Furushiro (eds.), Osaka, JSRS, 1991, p. 299.
69. N. Ridley, D. W. Livesey, and M. T. Salehi, Proceedings of the International Conference on High Temperature Intermetalics, London, UK, 1991, p. 198.
70. H. C. Fu, J. C. Huang, T. D. Wang, and C. C. Bampton, Acta Mater., 46 (1998) 465.
71. Y. T. Wu and C. H. Koo, Scripta Mater., 38 (1998) 267.
72. H. Zhu, Z. Li, B. Shang, W. Mao, and C. Wang, J. Mater. Sci. Technol., 17 (2001) 119.
73. R. Imayev, N. Gabdullin, and G. A. Salishchev, Intermetallics, 5 (1997) 229.

74. O. A. Kaibyshev, Superplasticity of Commercial Alloys, Moscow, Russian, 1984, p. 263.
75. R. M. Imayev, N. K. Gabdullin, G. A. Salishchev, O. N. Senkov, V. M. Imayev, and F. H. Froes, Acta Mater., 47 (1999) 1809.
76. R. M. Imayev, V. M. Imayev, and G. A. Salishchev, J. Mater. Sci., 27 (1992) 4465.
77. T. G. Nieh, J. N. Wang, L. M. Hsiung, J. Wadsworth, and V. Sikka, Scripta Metall., 37 (1997) 773
78. B. Huang, Z. Deng, Y. Liu, X. Qu, and Y. He, Intermetallics, 8 (2000) 559.
79. H.Hofmann, G. Frommeyer, and W. Herzog, Mater. Sci. Eng., A203 (1995) 128.
80. V. Sergueeva, V. V. Stolyarov, R. Z. Valiev, and A. K. Mukherjee, Scripta Mater., 43 (2000) 819.
81. T. Ahmed and H. J. Rack, Mater. Sci. Eng., A243 (1998) 206.
82. M. Grujicic and P. Dang, Mater. Sci. Eng., A224 (1997) 187.
83. X. Ren and M. Hagiwara, Acta Mater., 49 (2001) 3971.
84. J. Koike, Y. Shimoyama, I. Ohnuma, T. Okamura, R. Kainuma, K. Ishida, and K. Maruyama, Acta Mater., 28 (2000) 2059.
85. K. Mualeedharan, T. K. Nandy, and D. Banerjee, Intermetallics, 3 (1995) 187.
86. L. M. Hsiung and H. N. G. Wadley, Mater. Sci. Eng., A192/193 (1995) 908
87. D. S. McDarmaid, A. W. Bowen, and P. G. Partridge, J. Mater. Sci., 19 (1984) 2378.
88. W. P. Hon, S. K. Wu, and C. H. Koo, Mater. Sci. Eng., A131 (1991) 85.
89. D. B. Knorr and N. S. Stoloff, Mater. Sci. Eng., A123 (1990) 81.
90. S. Suwas, A. K. Singh, R. K. Ray, and S. Bhargava, Scripta Mater., 35 (1996) 897.
91. S. Suwas and R. K. Ray, Acta Mater., 47 (1999) 4599.
92. S. Suwas and R. K. Ray, Metall. Trans., 31A (2000) 2339.
93. O. A. Kaibyshev, I. V. Kazachkov, and R. M. Galeev, J. Mater. Sci., 16 (1981) 2501.
94. **廖忠賢，黃志青，科儀新知，第十九卷，第五期，**1998，43 **頁。**
95. Link Opal Operater's Guide, Opalman 3.0, Issue 1, Oxford Instruments plc,

Buckinghamshire, UK, 1997.

96. V. Randle, Oxford Guide Book Series, Electron Backscatter Diffraction, 1996, p. 3.
97. V. Randle, Microtexture Determination and Its Applications, Institute of Materials, London, 1992, p. 20.
98. CaRIne Crystallography version 3.1, 17 rue du Moulin du Roy F-60300 SENLIS FRANCE, (c) 1989-1998 C. Boudias & D. Monceau.
99. OPTIMAS version 6.1, Copyright (c) 1995 - 1999 Media Cybernetics Inc. 8484 Georgia Avenue, Silver Spring, MD 20910, USA.
100. 伏和中，“Ti_3Al 基介金屬合金超塑性薄板之顯微組織變化與變形機構分析”，國立中山大學材料科學研究所博士論文，1998。
101. A. K. Gogia, D. Banerjee, and T. K. Nandy, Metall. Trans. A, 21A (1990) 609.
102. R. J. Roe, J. Appl. Phy., 36 (1965) 2024.
103. H. J. Bunge, Texture Analysis in Material Science, Butterworths, London, Boston, 1982, p. 22.
104. G. Garces, M. C. Cristina, M. Torralba, and P. Adeva, Journal of Alloys and Compounds 309 (2000) 229
105. J. Wheeler, D. J. Prior, Z. Jiang, R. Spiess, P. W. Trimby, Contribution to Mineralogy and Petrology, 141 (2001) 109.
106. N.Gey and M. Humbert, Acta Mater., 50 (2002) 227.
107. K. T. Park and F. A. Mohamed, Metall. Mater. Trans., 26A (1995) 3119.
108. T. K. Nandy and D. Banerjee, Intermetallics, 8 (2000) 915.
109. H. Nakajima, W. Sprengel, and K. Nonaka, Intermetallics, 4 (1996) s17.
110. J. Rusing and Chr. Herzig, Intermetallics, 4 (1996) 647.
111. T. G. Nieh, J. Wadsworth, and O. D. Sherby, Superplasticity in Metals and Ceramics, Cambridge University Press, Cambridge, New York, 1997, p. 223.
112. A. M. Brown and M. F. Ashby, Acta Metal., 28 (1980) 1085.

113. V. M. Imayev, G. A. Salishev, M. R. Shagiev, A. V. Kuznetsov, R. M. Imayev, O. N. Senkov, and F. H. Foes, Scripta Mater., 40 (1999) 183.

114. J. W. Christian, The Theory of Transformations in Metals and Alloys, Pergamon Press, Oxford, New York, 1975. p. 489.

115. R. S. Mishra and D. Banerjee, Mater. Sci. Eng. A, 130 (1991) 151.

116. C. Huang and M. H. Lorretto, Mater. Sci. Eng. A, 192 (1995) 722.

117. T. B. Massalski, Metall. Trans., 33A (2002) 2277.

118. P. Wang, D. Veeraraghavan, M. Kumar, and V. K. Vasudevan, Metall. Trans., 33A (2002) 2353.

119. J. M. Howe, W. T. Reynolds, and V. K. Vasudevan, Metall. Trans., 33A (2002) 2391.

120. D. Banerjee, J. H. Wetbrook and R. L. Fleischer (eds.), Intermetallic Compounds, Vol. 2, John Wiley, New York, 1994, p. 91.

121. B. Bai, H. S. Yang, N. Chen, and A. K. Mukherjee, Scrip. Mater., 40 (1999) 1079.

122. D. R. Thornburg and H. R. Piehler, R. I. Jaffee and H. M. Burte (eds.), Titanium Science and Technology, Plenum Press, New York, 1973, p. 1187.

Table 1 Summary of typical intermetallic compounds [2]

Materials	d (g/cm^3)	E (GPa)	T_m (^oC)	Max. Temp. (for creep) (^oC)	Max. Temp. (oxidation) (^oC)	Elong. (at RT) (%)	Structure
Ti_3Al	4.2	140	1700	815	649	2-5	DO_{19}
TiAl	3.8	170	1500	1038	1038	1-2	$L1_0$
Ti alloys	4.5	100	1670	583	593	20	HCP/BCC
Superalloys	8.3	206	1453	1093	1093	3-5	FCC
Ni_3Al	7.5	180	1390	-	-	-	$L1_2$
NiAl	5.9	290	1640	-	-	-	B2
Fe_3Al	6.7	140	1400	-	-	-	DO_3
FeAl	5.6	260	1250	-	-	-	B2

Table 2 The main accommodation processes accommodated for GBS [39-54]

Accommodation mechanism/ Ref.	Schematic presentation
Grain boundary migration	
Lee [39]	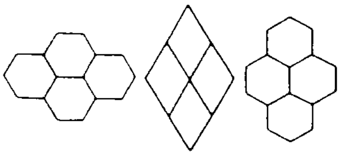
Holm et al. [40]	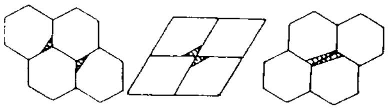
Diffusion accommodation	
Ashby and Verral [41]	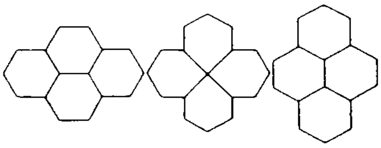
Ashby et al. [42]	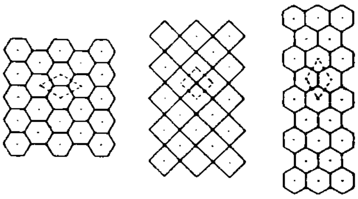
Chung and Davies [43]	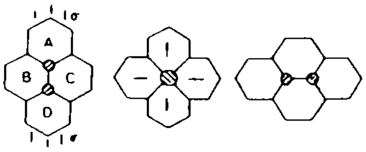
Pundy and Embury [44]	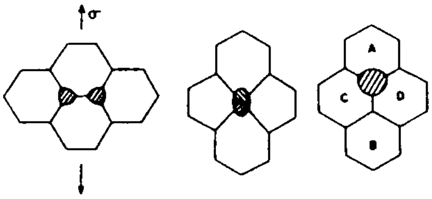
Spingarn and Nix [45]	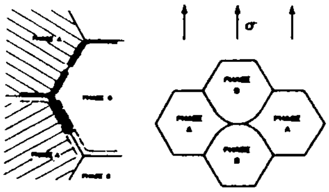
Kamijo et al. [46]	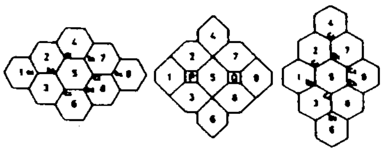

Dislocation accommodation

Gifkin [47]

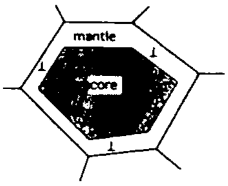

Valiev and Langdon [48]

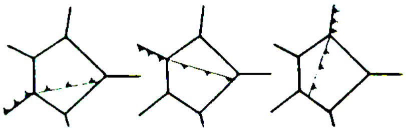

Baududelet [49]

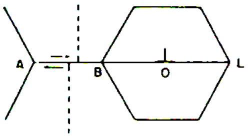

Matsuki et al. [50]

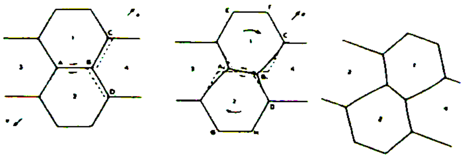

Grain emergence

Gifkins [51]

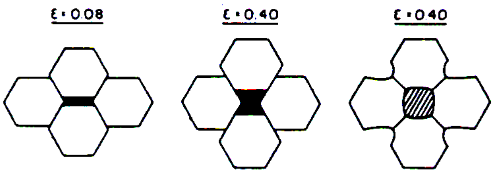

Langdon [52]

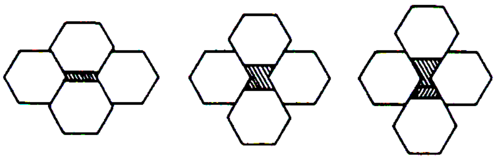

Geckinili [53]

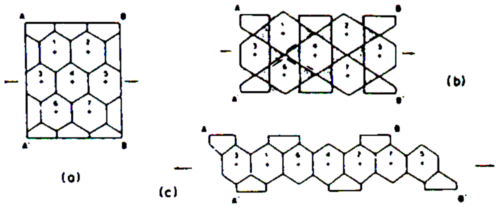

Combination of accommodational mechanisms

Gifkins [54]

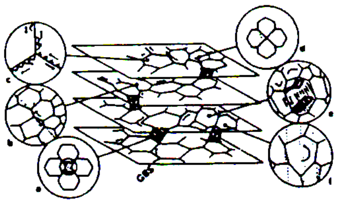

Table 3 Models of CGBS [55-64]

Deformation mechanism/Ref.	Schematic presentation
Rigid shear Raj and Ashby [55]	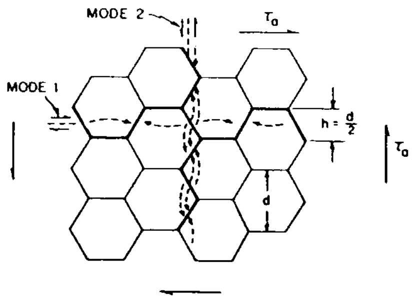
Nix [56]	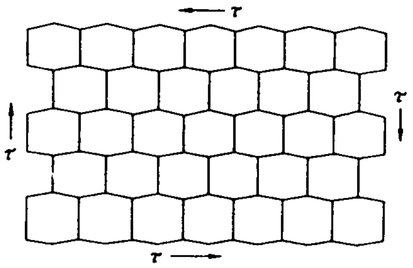
Barret [57]	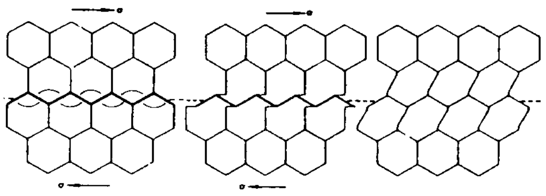
Cannon and Nix [58]	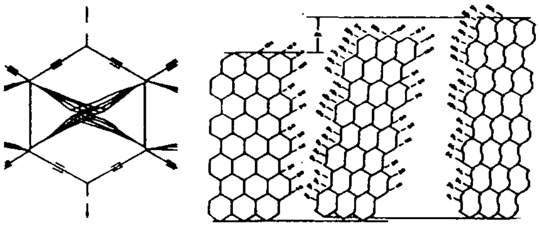
Cannon and Nix [58] Novikov and Portnoy [59]	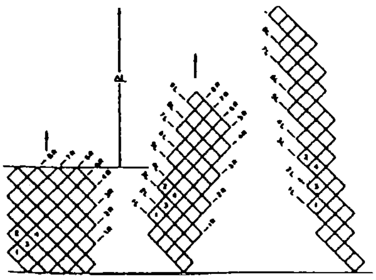
Partridge et al. [60]	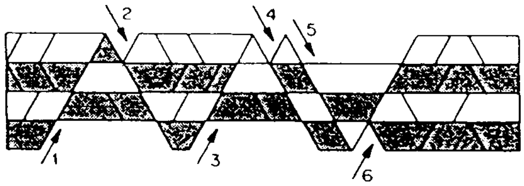

Hazzeldine and Newbury [61]	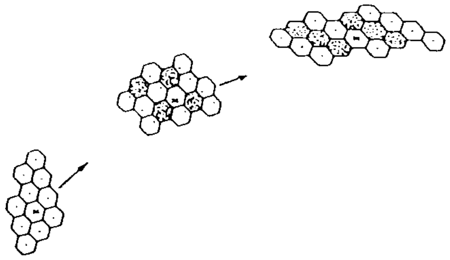
Sequential shear Morral and Ashby [62]	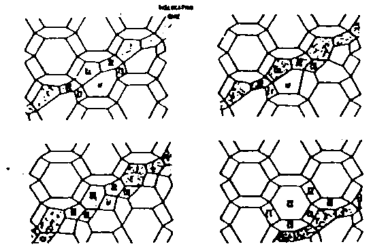
Nix [56]	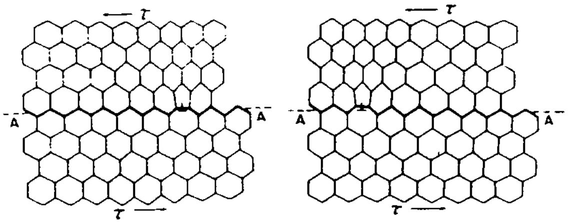
Sato et al. [63]	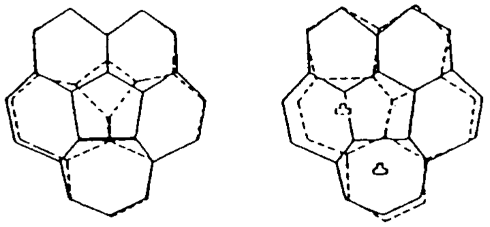
Kamijo et al. [64]	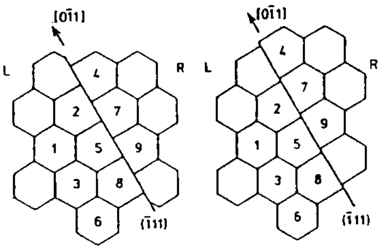

Table 4 Summary of HTSP in Ti_3Al base alloys [14,15,18,65,67-72]

Materials	Process	d (μm)	Temp. (^oC)	Strain rate (s^{-1})	Elong. (%)	Author	Year	Ref.
Ti_3Al	Hot press	1.5	900	-	-	Miyazaki et al.	1990	14
Ti-24Al-11Nb	Hot forging+ hot rolling	-	980	$3.3x10^{-4}$	520	Dutta and Banerjee	1990	15
Ti-25Al-10Nb -3V-1Mo	-	-	980	$5x10^{-5}$ $1.5x10^{-4}$	810 570	Yang et al.	1991	65,67
Ti-25Al-10Nb -3V-1Mo	-	10.2	950	$8x10^{-5}$	-	Ghosh and Cheng	1991	68
Ti-25Al-10Nb -3V-1Mo	-	-	960	$1.7x10^{-3}$	1350	Ridley	1991	69
Ti-25Al-10Nb	Hot rolling+ annealing	4.5	1000	$2x10^{-4}$	1083	Wu et al.	1997	71
Ti-25Al-10Nb -3V-1Mo	-	2-3	960	$2x10^{-4}$	1500	Fu and Huang	1998	70
Ti-24Al-11Nb	Cross-rolling+ annealing	3.6	970	10^{-3}	1280	Kim et al.	1999	18
Ti-24Al-14Nb -3V-0.5Mo	-	2	960	$1.5x10^{-3}$	1240	Zhu et al.	2001	72

Table 5 Summary of LTSP in Ti_3Al base alloys [17]

Materials	Process	d (μm)	Temp. (°C)	Strain rate (s^{-1})	Elong. (%)	Author	Year	Ref.
Ti-25Al	Multi-directional isothermal forging+ annealing	0.1	500 600	$6.4x10^{-4}$ $6.4x10^{-4}$	120 680	Imayev et al.	2000	17
		0.3	600 700	$6.4x10^{-4}$ $6.4x10^{-4}$	300 780			
		0.8	600 800 800	$6.4x10^{-4}$ $1.3x10^{-4}$ $6.4x10^{-4}$	170 640 580			

Table 6 Summary of LTSP or HRSP in other Ti based alloys [73,76-80]

Materials	Process	d (μm)	Temp. (^oC)	Strain rate (s^{-1})	Elong. (%)	Author	Year	Ref.
Ti-50Al	Isothermal forging+ Annealing	0.4	850	$8x10^{-4}$	225	Imayev et al.	1993	76
Ti-47Al-2Cr-2Nb	Extrusion+ Annealing	4-5	800	$2x10^{-5}$	310	Nieh et al.	1997	77
Ti-46Al	Isothermal forging+ Annealing	0.2	800	$6.4x10^{-4}$	415	Imayev et al.	1999	73
Ti-46Al-2Cr-2Nb-1Ta	Isothermal forging+ Annealing	0.3	750 800	$6.7x10^{-4}$	310 520	Imayev et al.	1999	73
Ti-48Al-2Cr-2Nb	Isothermal forging+ Annealing	0.3	750 800 850	$8.3x10^{-4}$	195 355 270	Imayev et al.	1999	73
Ti-33Al-3Cr-0.5Mo	Canned-forging	-	900	$1x10^{-3}$	325	Huang et al.	2000	78
Ti-10Co-4Al	Hot rolling	-	1000	$5x10^{-2}$	650-750	Hofmann et al.	1995	79
Ti-6Al-4V	Hot rolling+ high-pressure torsion	0.1-0.2	650 725	$1x10^{-3}$ $1x10^{-1}$	575 215	Sergueeva et al.	2000	80

Table 7 The crystal parameters of the Ti_3Al-Nb alloy

	Crystal structure	Lattice constants (nm)		Atomic positions		
		a	c	Ti	Al	Nb
α_2 phase $(Ti,Nb)_3Al$	Hexagonal, DO_{19}	0.579	0.468	1/2, 0, 0 0, 1/2, 0 1/2, 1/2, 0 5/6, 1/6, 1/2 5/6, 2/3, 1/2 1/3, 2/3, 1/2	0,0,0 1/3, 1/6, 1/2	Randomly occupies the Ti sites
β phase Ti(Al,Nb)	BCC or B2	0.317	-	0, 0, 0	1/2, 1/2, 1/2	1/2, 1/2, 1/2

Table 8 Summary of tensile properties at different strain rates and temperatures. The elongations listed here are subjected to ± 10% uncertainty

Temperature (°C)	Strain rate (s^{-1})	Elongation (%)	UTS (MPa)
700	$8x10^{-5}$	28	526
	$2x10^{-4}$	20	594
	$5x10^{-4}$	26	855
	$1x10^{-2}$	16	917
750	$8x10^{-5}$	141	346
	$2x10^{-4}$	131	379
	$5x10^{-4}$	39	480
	$1x10^{-2}$	28	737
800	$8x10^{-5}$	80	214
	$2x10^{-4}$	130	269
	$5x10^{-4}$	123	305
	$1x10^{-2}$	84	553
850	$8x10^{-5}$	186	114
	$2x10^{-4}$	200	183
	$5x10^{-4}$	333	178
	$1x10^{-2}$	145	395
900*	$8x10^{-5}$	643	39
	$2x10^{-4}$	595	64
	$5x10^{-4}$	451	105
920*	$2x10^{-4}$	853	63
940*	$8x10^{-5}$	873	23
	$2x10^{-4}$	892	11
	$5x10^{-4}$	588	40
960*	$8x10^{-5}$	690	7
	$2x10^{-4}$	1413	13
	$5x10^{-4}$	683	30
980*	$8x10^{-5}$	729	6
	$2x10^{-4}$	726	11
	$5x10^{-4}$	646	20
1000*	$8x10^{-5}$	684	6
	$2x10^{-4}$	875	7
	$5x10^{-4}$	610	17

* Data obtain in ref. [100].

Table 9 Anisotropic tensile test results performed at room temperature and an initial strain rate of $3x10^{-3}$ s^{-1}

Orientation to RD	Yield stress (MPa)	Ultimate tensile strength (MPa)	Elongation (%)
0^o	950 ± 30	1100 ± 40	5
45^o	900 ± 40	1020 ± 50	6
90^o	1150 ± 30	1220 ± 50	2

Table 10 Anisotropic tensile test results performed at elevated temperatures and an initial strain rate of $5x10^{-4}$ s^{-1}

Orientation to RD	Elongation (%)			
	Decreasing strain rate condition			Constant strain rate condition [100]
	750^oC	850^oC	920^oC	960^oC
0^o	39	333	1680	1200
45^o	155	380	1910	1290
90^o	38	310	1880	1130

Table 11 The grain sizes and volume fractions in specimens statically annealed for 1.5 h and then water quenched

Annealing temp.	$d(\alpha_2)$	$V_f(\alpha_2)$	$V_f(\beta)$	$V_f(\alpha_2')$	$V_f(\alpha_2+\alpha_2')$	V_f(α_2 in Fig.2(b))
As-received	2.2 μm	40%	60%	0%	40%	--
700°C	3.0 μm	40%	60%	0%	40%	80%
750°C	3.0 μm	45%	45%	10%	55%	76%
800°C	3.0 μm	47%	32%	21%	68%	72%
850°C	3.7 μm	45%	35%	20%	65%	67%
900°C	3.9 μm	54%	42%	4%	58%	62%
960°C	4.0 μm	47%	53%	0%	47%	50%
1000°C	5.0 μm	40%	60%	0%	40%	40%

Table 12 Measurement of the α_2' thickness, h, and the relative volume fractions in specimens statically annealed at 800 and 850^{o}C for different periods of time and then water quenched

Annealing time	h (μm)		$V_f(\alpha_2)$		$V_f(\beta)$		$V_f(\alpha_2')$		$V_f(\alpha_2+\alpha_2')$	
	800^{o}C	850^{o}C	800^{o}C	850^{o}C	800^{o}C	850^{o}C	800^{o}C	850^{o}C	800^{o}C	850^{o}C
3 min	0.025	0.100	40%	40%	57%	53%	3%	7%	43%	47%
10 min	0.045	0.100	48%	48%	47%	35%	7%	17%	55%	65%
0.5 h	0.080	0.130	48%	45%	40%	33%	12%	22%	60%	67%
1.0 h	0.095	0.150	45%	45%	35%	35%	20%	20%	65%	65%
2.5 h	0.105	0.220	48%	52%	31%	34%	21%	14%	69%	66%
4.0 h	0.120	0.230	50%	56%	29%	30%	21%	14%	71%	70%

Table 13 The relative volume fractions in specimens statically annealed at 850^{o}C for 1.5 h and then cooled under different conditions

Cooling condition	$V_f(\alpha_2)$	$V_f(\beta)$	$V_f(\alpha_2')$	V_f $(\alpha_2+\alpha_2')$
Furnace cooling	45%	32%	23%	68%
Water cooling	45%	35%	20%	65%
Liquid nitrogen cooling	45%	40%	15%	60%

Table 14 The α_2 grain size and relative volume fractions in the tensile loaded specimens deformed to failure

Loading	Elongation	Strain	Time	Stress	$d(\alpha_2)$	$V_f(\alpha_2)$	$V_f(\beta)$	$V_f(\alpha_2')$	$V_f(\alpha_2+\alpha_2')$	$\frac{V_f(a_2)_{loading}}{V_f(a_2)_{annealing}}$
temperature		ε		σ, MPa	μm					
As-received	--	--	--	--	2.2	40%	60%	--	40%	--
700°C	25%	0.2	17 min	700	2.9	45%	55%	0%	45%	0%/0%
750°C	131%	0.8	67 min	450	2.0	45%	40%	15%	60%	15%/10%=1.5
800°C	130%	0.8	67 min	300	0.9	40%	20%	40%	80%	40%/21%=1.9
850°C	333%	1.5	50 min	225	1.4	40%	20%	35%	75%	35%/20%=1.8
900°C	600%	2.0	2.8 h	150	1.2	55%	30%	25%	70%	25%/ 4%=6.3
960°C	1500%	2.8	3.9 h	50	4.0	40%	50%	10%	50%	10%/0%
1000°C	875%	2.3	3.2 h	40	5.5	40%	60%	0%	40%	0%/0%

Table 15 Measurement of the α_2' thickness, h, and the relative volume fractions in specimens tensile loaded at 850°C and $5x10^{-4}$ s^{-1} to different engineering elongations or true strains ε

Elongation	ε	h	$V_f(\alpha_2)$	$V_f(\beta)$	$V_f(\alpha_2')$	$V_f(\alpha_2+\alpha_2')$
0%	0	0.15 µm	45%	35%	20%	65%
33%	0.3	0.29 µm	45%	33%	22%	67%
165%	1.0	0.33 µm	44%	32%	24%	68%
223%	1.2	0.38 µm	43%	28%	30%	73%
300%	1.4	0.45 µm	41%	25%	31%	71%
333%	1.5	0.56 µm	40%	20%	35%	75%

Table 16 The misorientation angle distribution in the theoretically random case, the as-received alloy, and the 0^o post-SP specimens at 750 and 920^oC

	α_2 phase			β phase		
	LAB	MAB	HAB	LAB	MAB	HAB
Random distribution	0.80%	17.50%	81.70%	0.80%	17.50%	81.70%
AR alloy	28.50%	25.50%	46.00%	69.20%	18.00%	12.80%
Post-SP at 750^oC	29.07%	27.58%	43.29%	52.73%	14.56%	30.74%
Post-SP at 920^oC	18.75%	13.46%	67.74%	12.00%	20.56%	67.41%

Table 17 The misorientation angle distribution in the theoretical randomly case, and the post-SP 0^o specimen performed at 850^oC and $5x10^{-4}$ s^{-1} to different true strains ε

	α_2 phase			β phase		
	LAB	MAB	HAB	LAB	MAB	HAB
Random distribution	0.80%	17.50%	81.70%	0.80%	17.50%	81.70%
$\varepsilon=0.3$	19.37%	31.63%	49.12%	56.25%	6.25%	37.50%
$\varepsilon=1.0$	20.00%	26.66%	53.31%	27.03%	29.73%	43.24%
$\varepsilon=1.2$	28.26%	17.10%	54.20%	21.51%	8.61%	69.94%
$\varepsilon=1.5$	22.67%	23.99%	53.34%	21.62%	18.01%	60.32%

Table 18 The textures sharpness measured from the AR alloy and the post-SP specimens

		Contour level in average	
		α_2 phase	β phase
As-received alloy		Sharp	Extremely sharp
Post-SP specimens at 750°C	0°	Sharp	Sharp
	45°	Sharp	Highly sharp
	90°	Sharp	Sharp
Post-SP specimens at 920°C	0°	Highly flat	Extremely flat
	45°	Highly flat	Extremely flat
	90°	Highly flat	Extremely flat
Post-SP specimens at 850°C	ε=0.3	Sharp	Highly sharp
	ε=1.0	Sharp	Sharp
	ε=1.2	Flat	Flat
	ε=1.5	Flat	Flat

Table 19 The apparent m_a-values and the true m_t-values at 700-850°C

Temperature (°C)	Apparent m_a-values	True m_t-values
700	0.11	0.2
750	0.16	
800	0.27	0.33
850	0.27	
900*	0.48-0.57	
920*	0.48	
940*	0.69-0.86	
960*	0.61-0.72	
980*	0.54-0.68	
1000*	0.61-0.72	

*The m-values were extracted by the jump-strain-rate method [100].

Table 20 The apparent Q_a-values and the true Q_t-values at 700-850°C

Temperature (°C)	Apparent Q_a-values		True Q_t-values	
	Constant stress condition	Constant strain rate condition	Constant stress condition	Constant strain rate condition
700-750	392	346	377	339
800-850	271	264	209	225

Table 21 Schmid factors calculated for the β phase

Orientation to rolling direction	Schmid factors of the β phase		
	Major textures		Minor texture
	{100}<110>	{111}<$2\bar{1}\bar{1}$>	{$0\bar{1}1$}<100>
	Acting on the {110}<$\bar{1}11$> slip system		
0°	0.14	0.18	0.27
45°	0.27	0.17	0.17
90°	0.14	0.14	0.14

Table 22 Schmid factors calculated for the α_2 phase

Orientation to rolling direction	Schmid factors of the α_2 phase											
	Major texture			Minor textures								
	$\{11\bar{2}0\}<0001>$			$\{0001\}<\bar{1}100>$			$\{0001\}<11\bar{2}0>$			$\{11\bar{2}0\}<\bar{1}100>$		
	Acting on the main slip systems											
	$\{10\bar{1}0\}<11\bar{2}0>$	$\{0001\}<11\bar{2}0>$	$\{10\bar{1}\bar{1}\}<11\bar{2}0>$	$\{10\bar{1}0\}<11\bar{2}0>$	$\{0001\}<11\bar{2}0>$	$\{10\bar{1}\bar{1}\}<11\bar{2}0>$	$\{10\bar{1}0\}<11\bar{2}0>$	$\{0001\}<11\bar{2}0>$	$\{10\bar{1}\bar{1}\}<11\bar{2}0>$	$\{10\bar{1}0\}<11\bar{2}0>$	$\{0001\}<11\bar{2}0>$	$\{10\bar{1}\bar{1}\}<11\bar{2}0>$
0^o	0	0	0	0.29	0	0.20	0.29	0	0.20	0.29	0	0.20
45^o	0.15	0.29	0.21	0.33	0	0.23	0.33	0	0.23	0.15	0.29	0.21
90^o	0.29	0	0.20	0.29	0	0.20	0.29	0	0.20	0	0	0

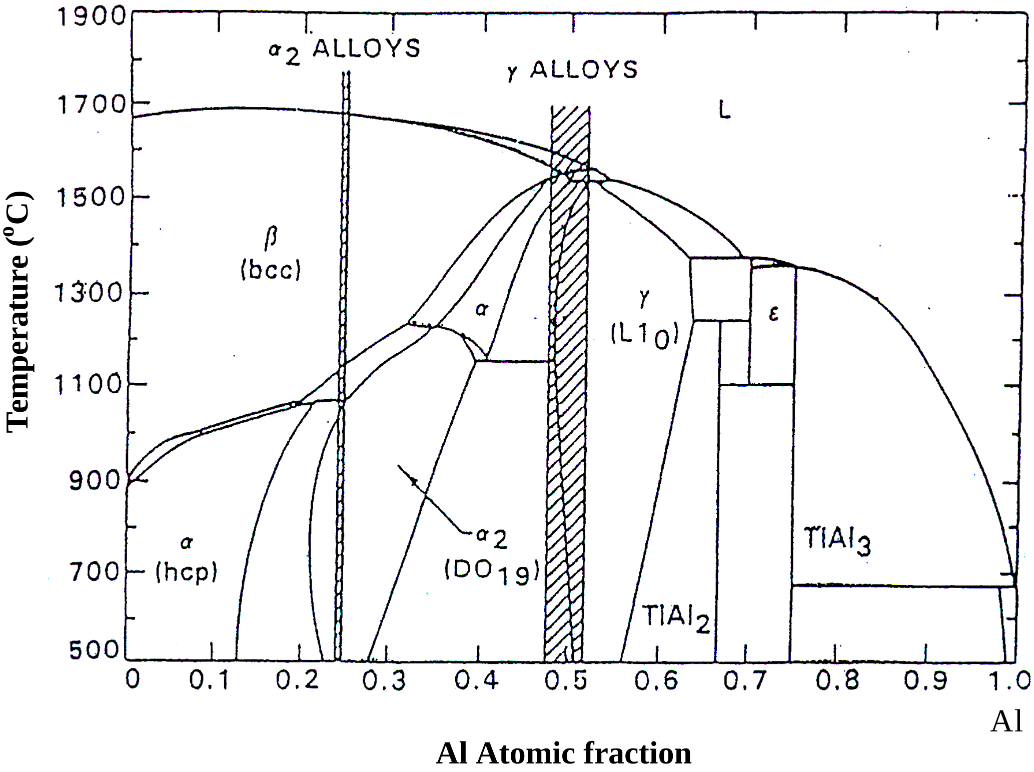

Fig. 1 Ti-Al binary equilibrium phase diagram [1].

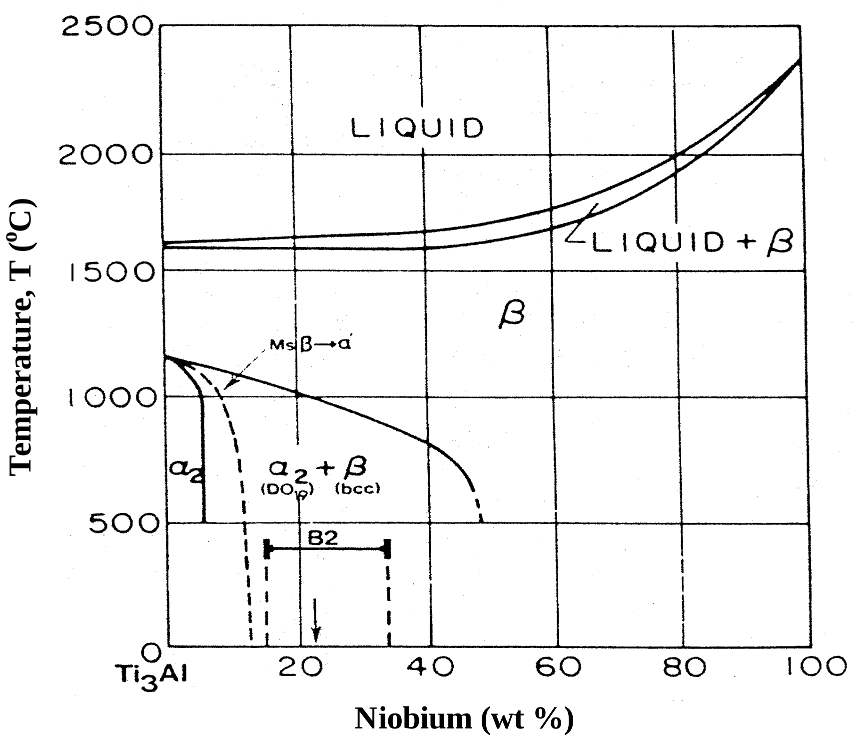

(a)

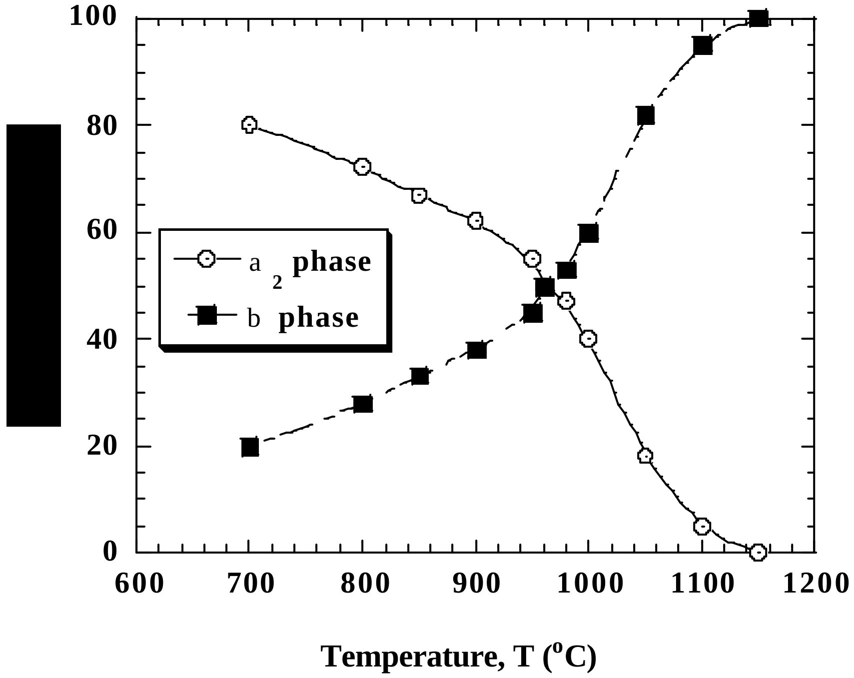
[redacted]

(b)

Fig. 2 (a) Phase diagram of the Ti_3Al-Nb system [3], and (b) relative volume fractions of the α_2 and β phases in accordance with the equilibrium phase diagram.

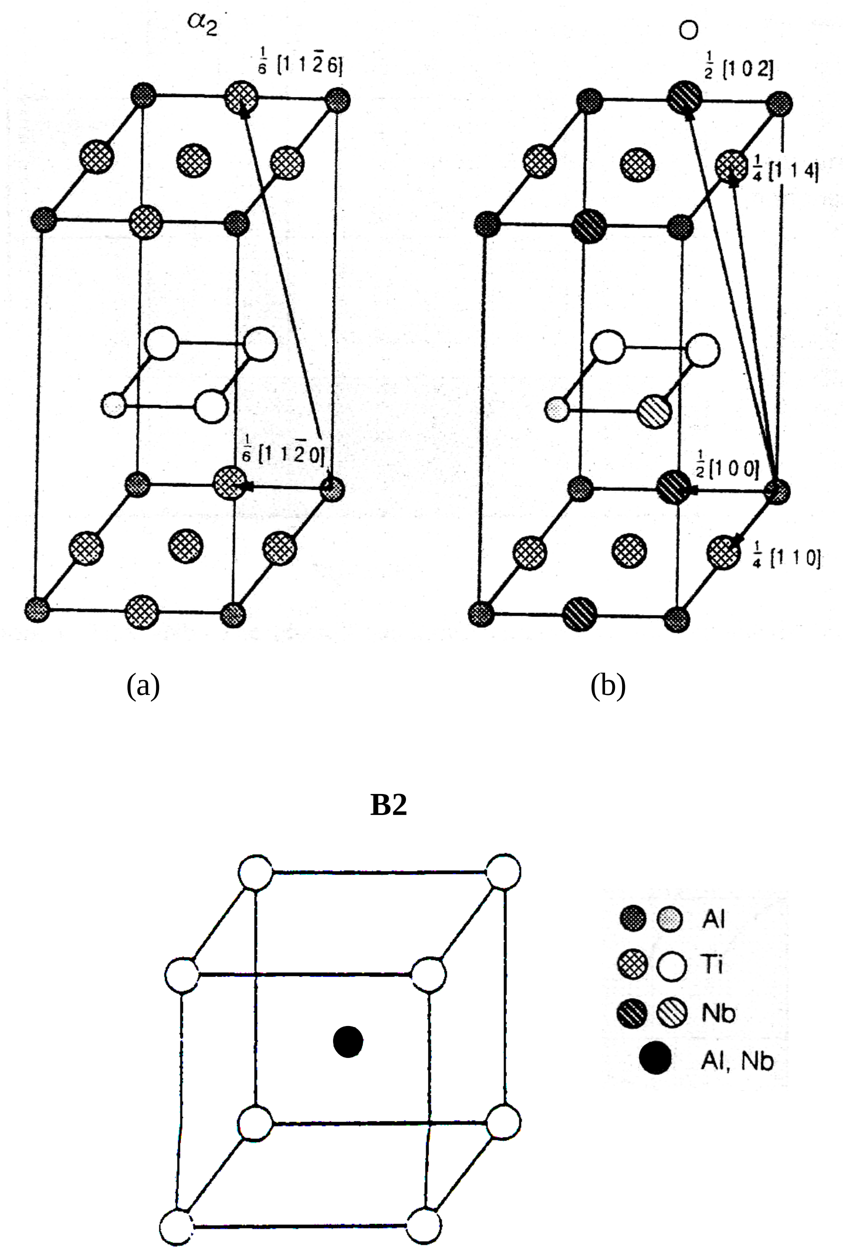

(a) (b) (c)

Fig. 3 The crystal structures of the (a) α_2, (b) O, and (c) β phases [8,9].

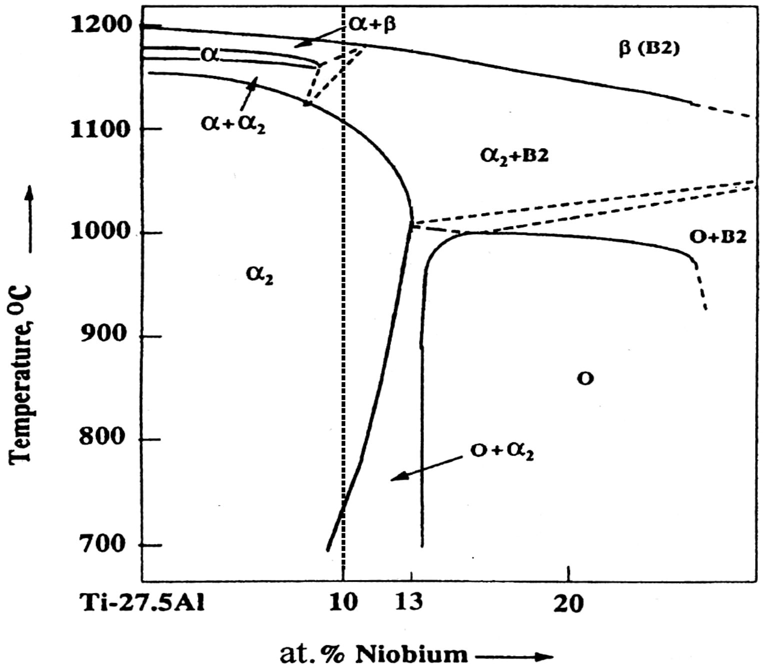

Fig. 4 A vertical section along the Ti-27.5Al-Nb for the Ti-Al-Nb system [85]. For Ti_3Al with the Nb content ~10 at%, the stable phases at the TMT processing temperature of ~1000-1200°C are only α_2 and B2.

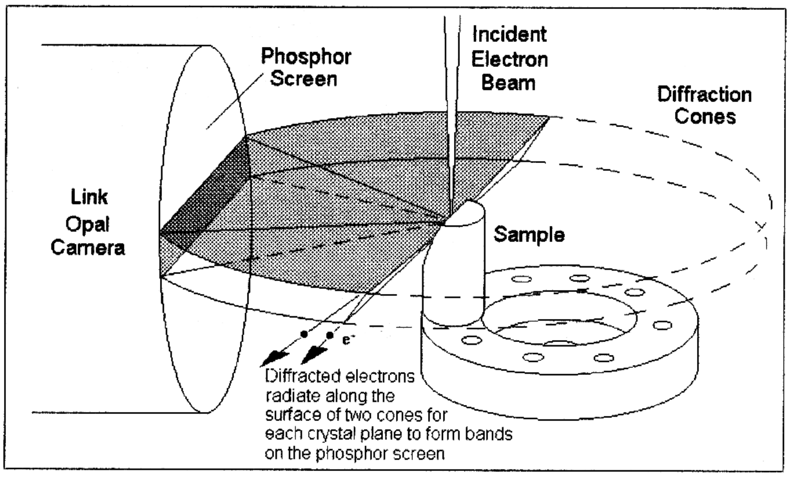

Fig. 5 Illustration of the principle of an EBSD system [95].

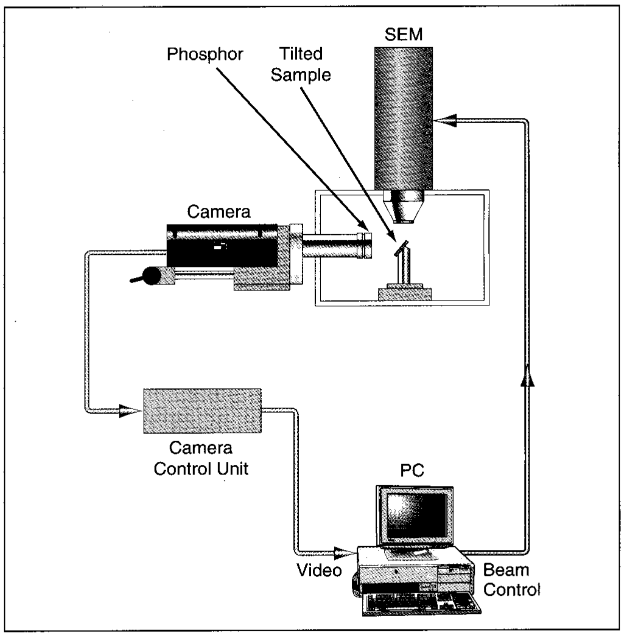

Fig. 6 Illustration of the set-up of an EBSD system [96].

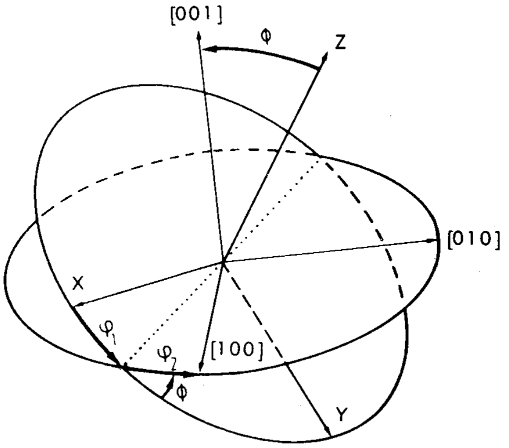

Fig. 7 Schematic Euler angles (φ_1, ϕ, φ_2), which would specify an orientation [97].

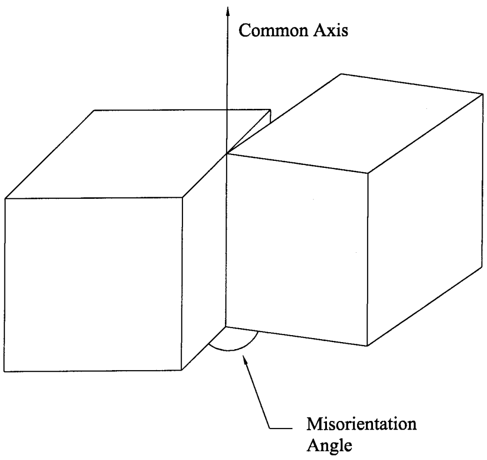

Fig. 8 Schematic illustration of the misorientation angle between two grains [95]

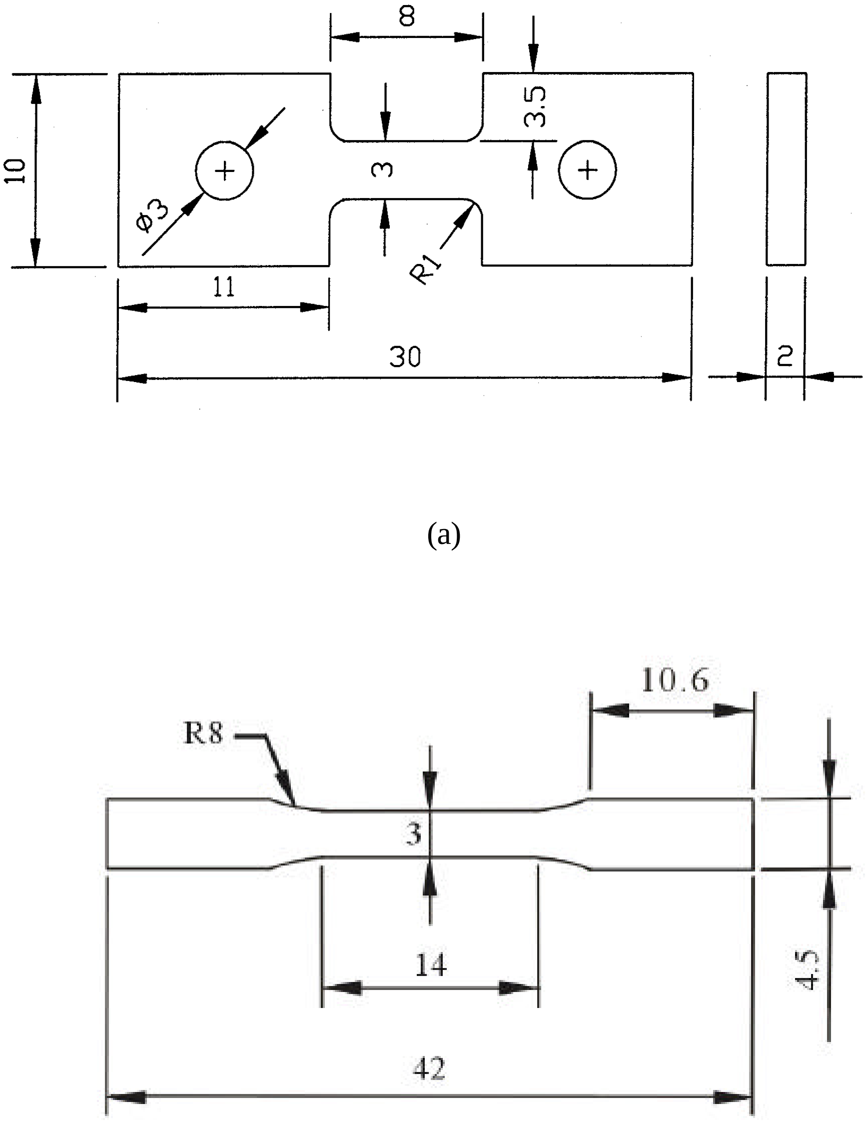

(a)

(b)

Unit: mm

Fig. 9 Schematic drawing of the specimen dimension for tensile tests at (a) elevated temperatures (with a gauge length of 5.5 mm), and (b) room temperature (with a gauge length of 10 mm).

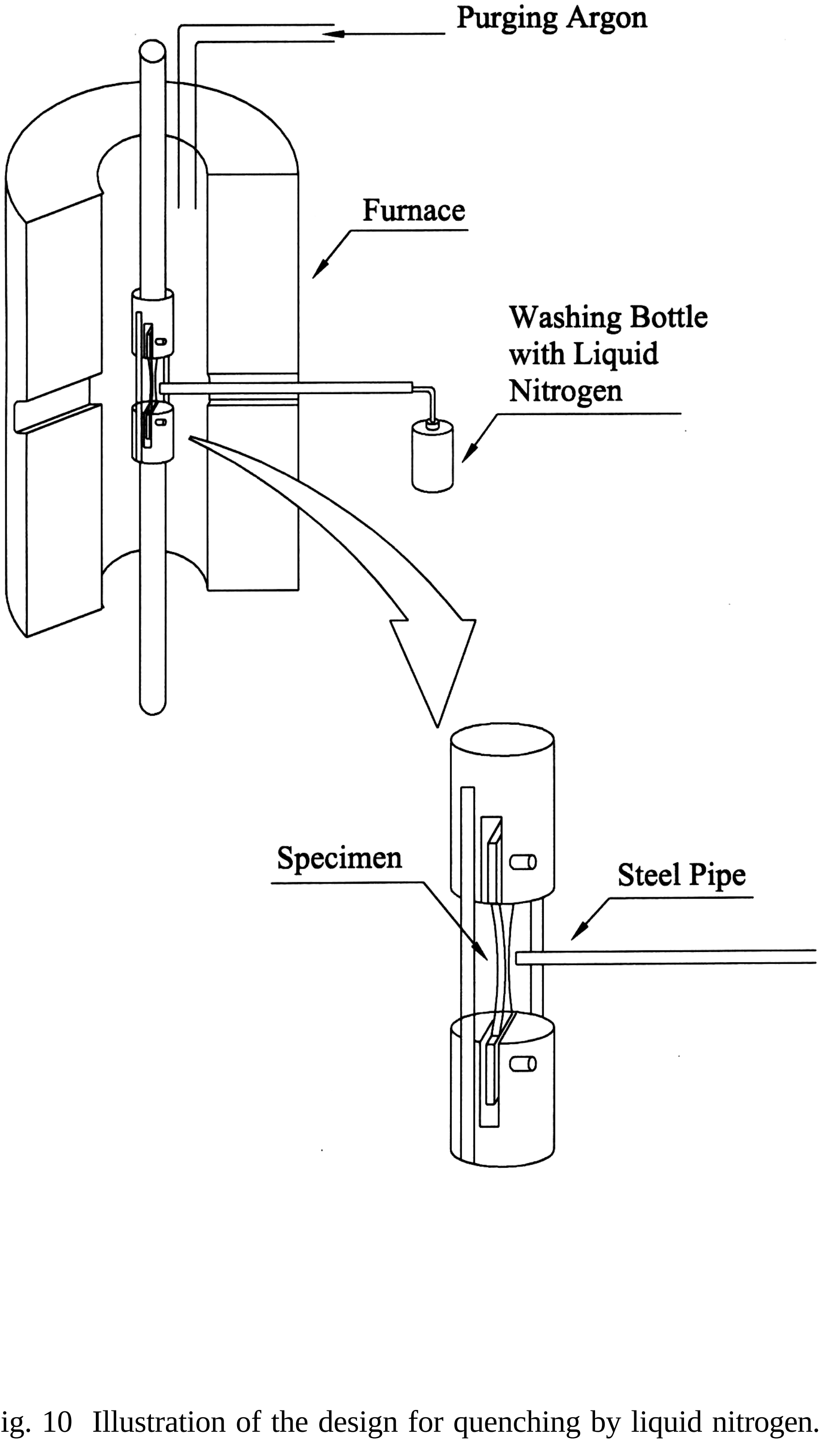

Fig. 10 Illustration of the design for quenching by liquid nitrogen.

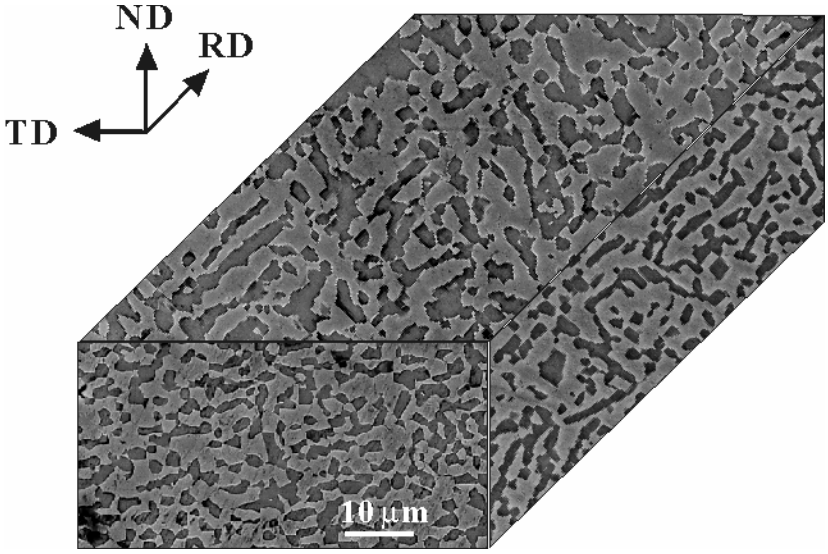

Fig. 11 SEM micrograph showing the three-dimensional microstructure of the as-received material (the darker phase is the α_2 phase and the lighter one is the β phase).

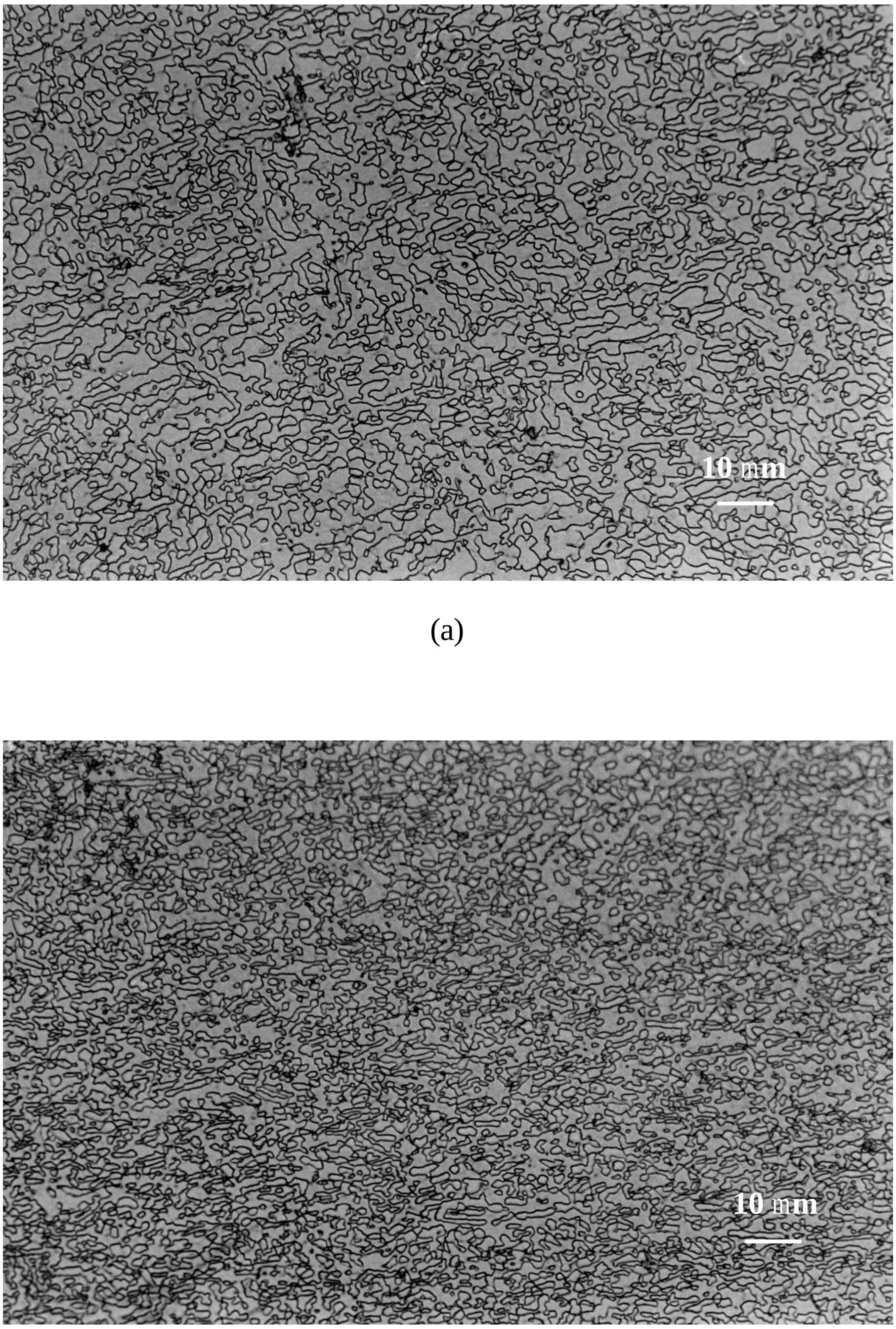

(a)

(b)

Fig. 12 OM micrographs of the as-received material taken from the (a) rolling plane, (b) longitudinal plane, and (c) transverse plane.

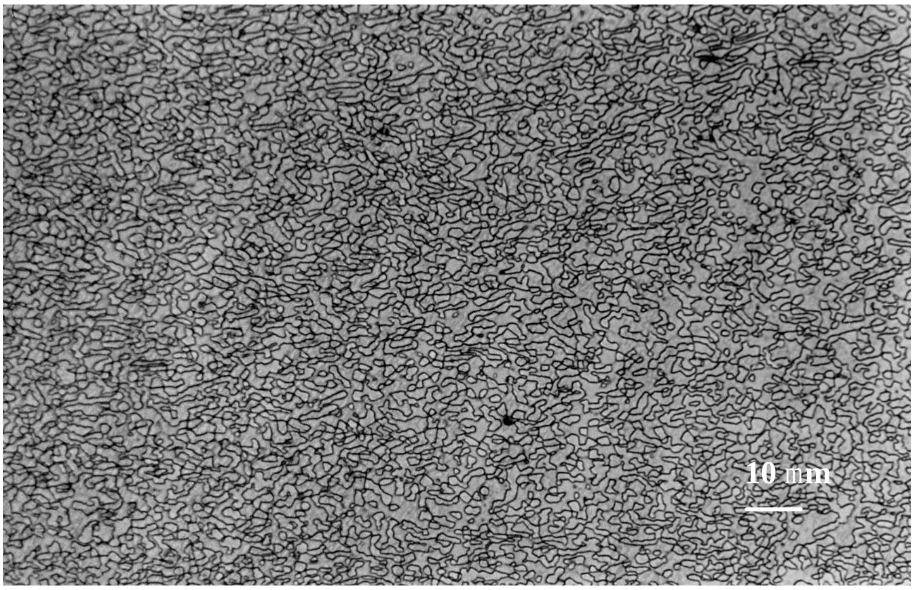

(c)

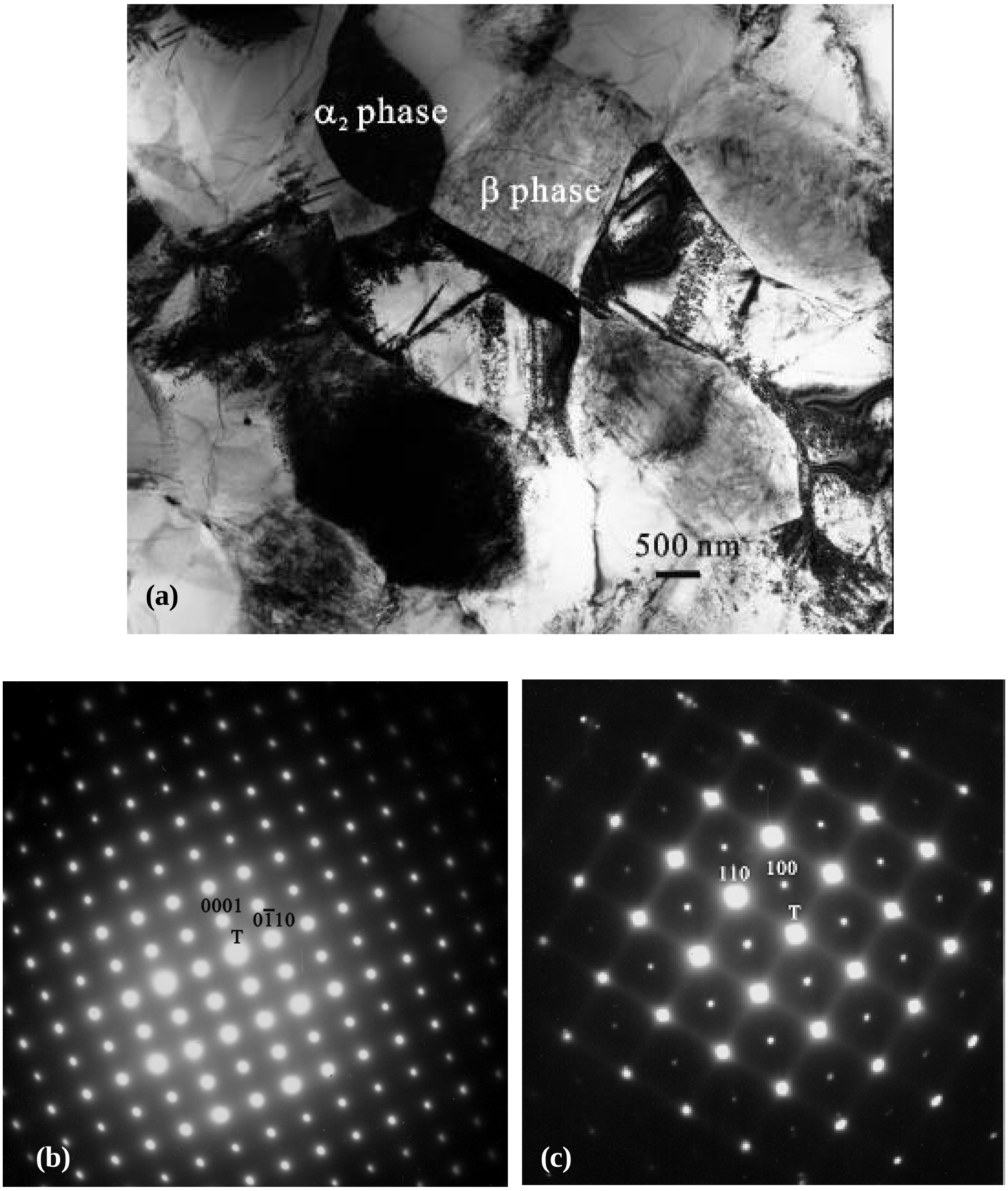

Fig. 13 (a) TEM micrograph of the as-received super α_2 sheet, with the diffraction patterns taken from the (b) α_2 $[2\bar{1}\bar{1}0]$ and (c) β [001] zones.

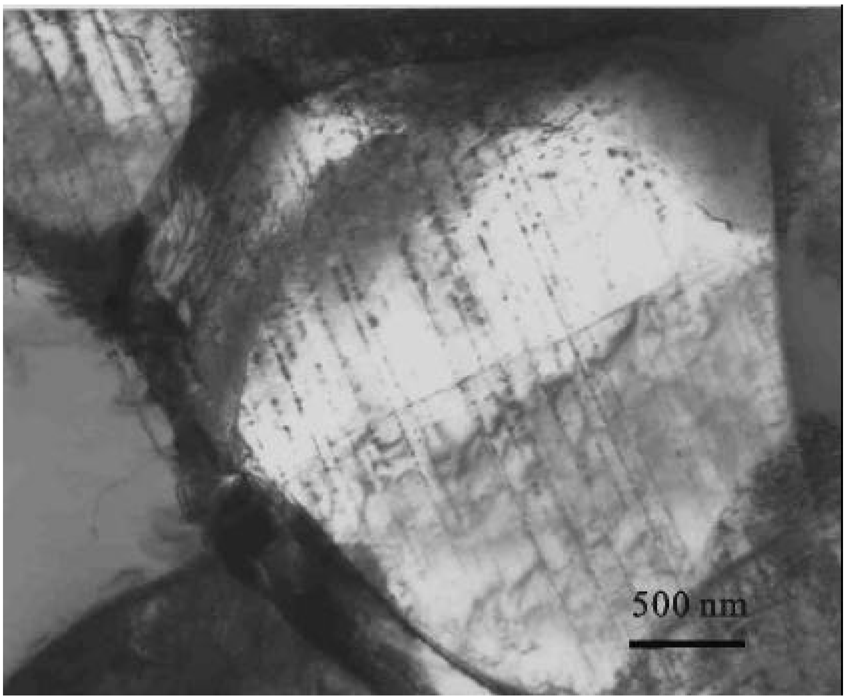

Fig. 14 Representative planer slip in the β phase.

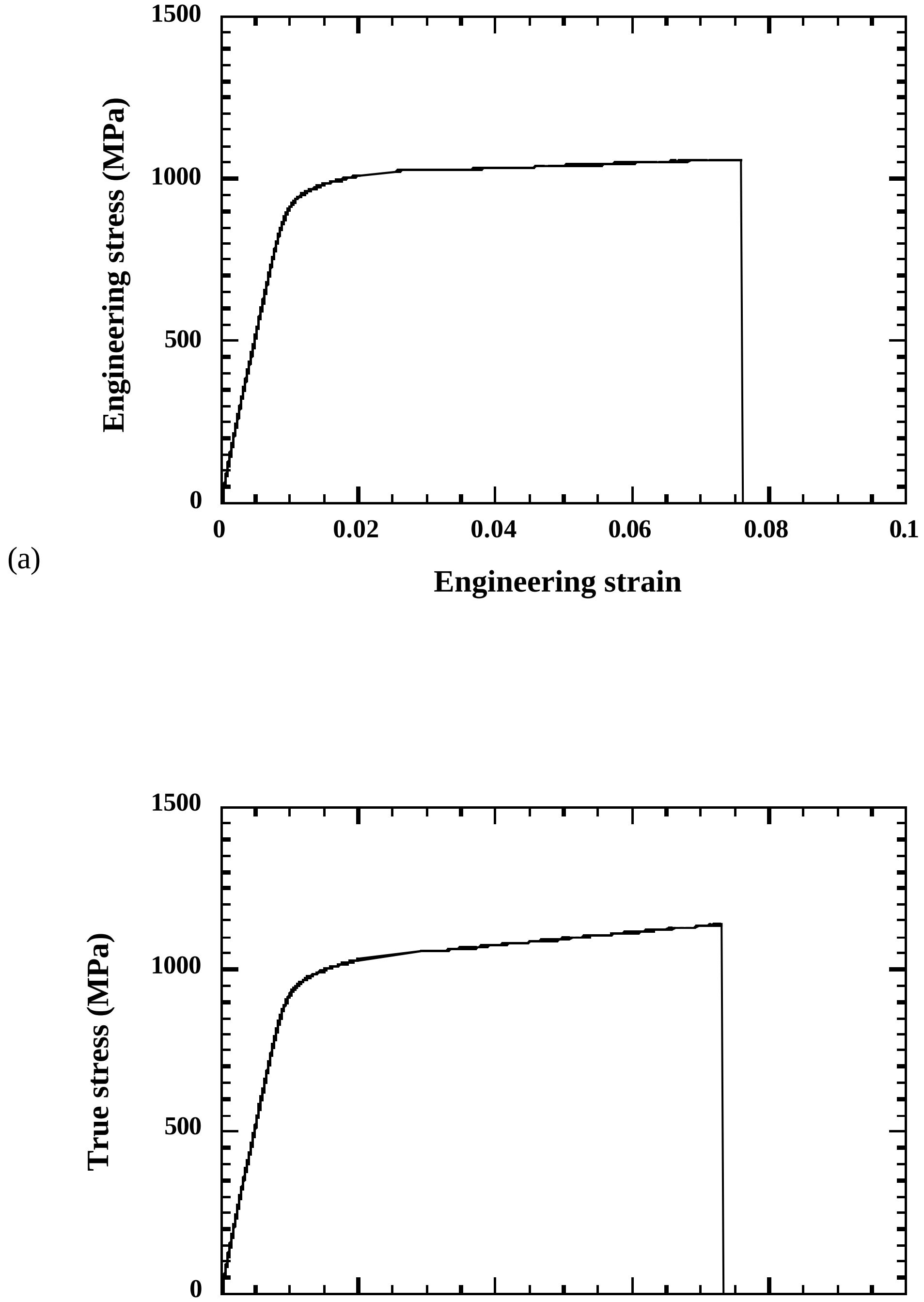

Fig. 15 The (a) engineering and (b) true stress-strain curves recorded from tensile tests performed at room temperature (25°C) and an initial strain rate of $3\text{x}10^{-3}$ s^{-1}.

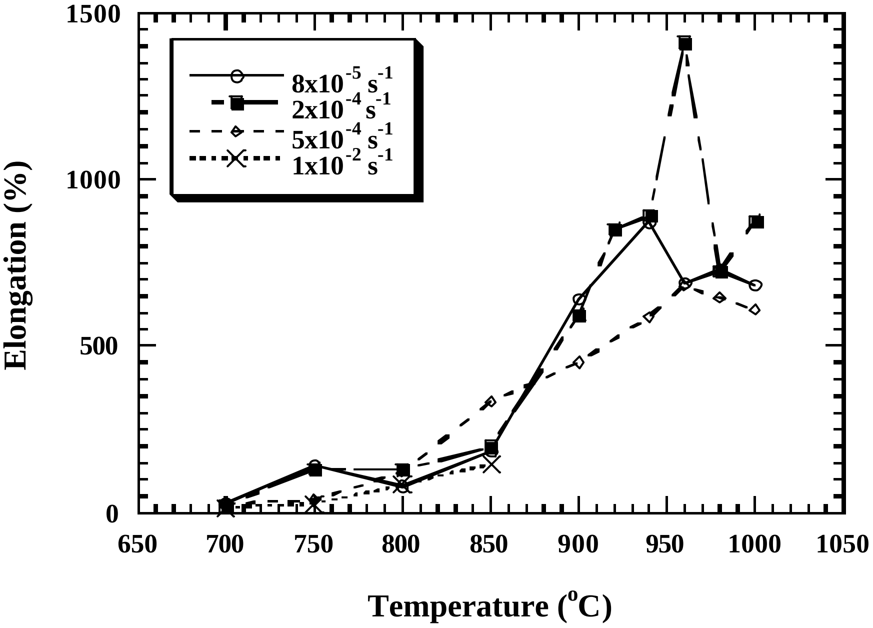

Fig. 16 The dependence of superplastic elongations as a function of loading temperature at four different initial strain rates.

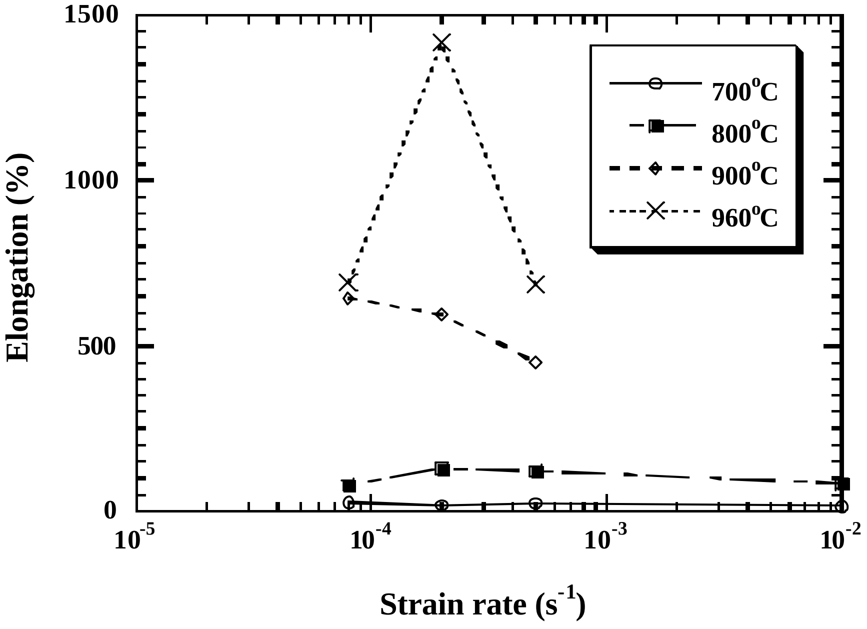

Fig. 17 The dependence of superplastic elongations as a function of strain rate at representative temperatures.

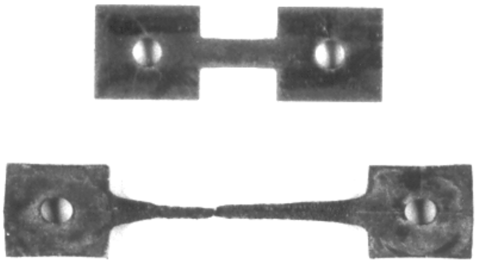

Maximum elongation= 333%

Testing temperature= 850°C

Initial strain rate= $5x10^{-4}$ s^{-1}

Fig. 18 The appearance of specimens before and after superplastic loading at 850°C and $5x10^{-4}$ s^{-1}.

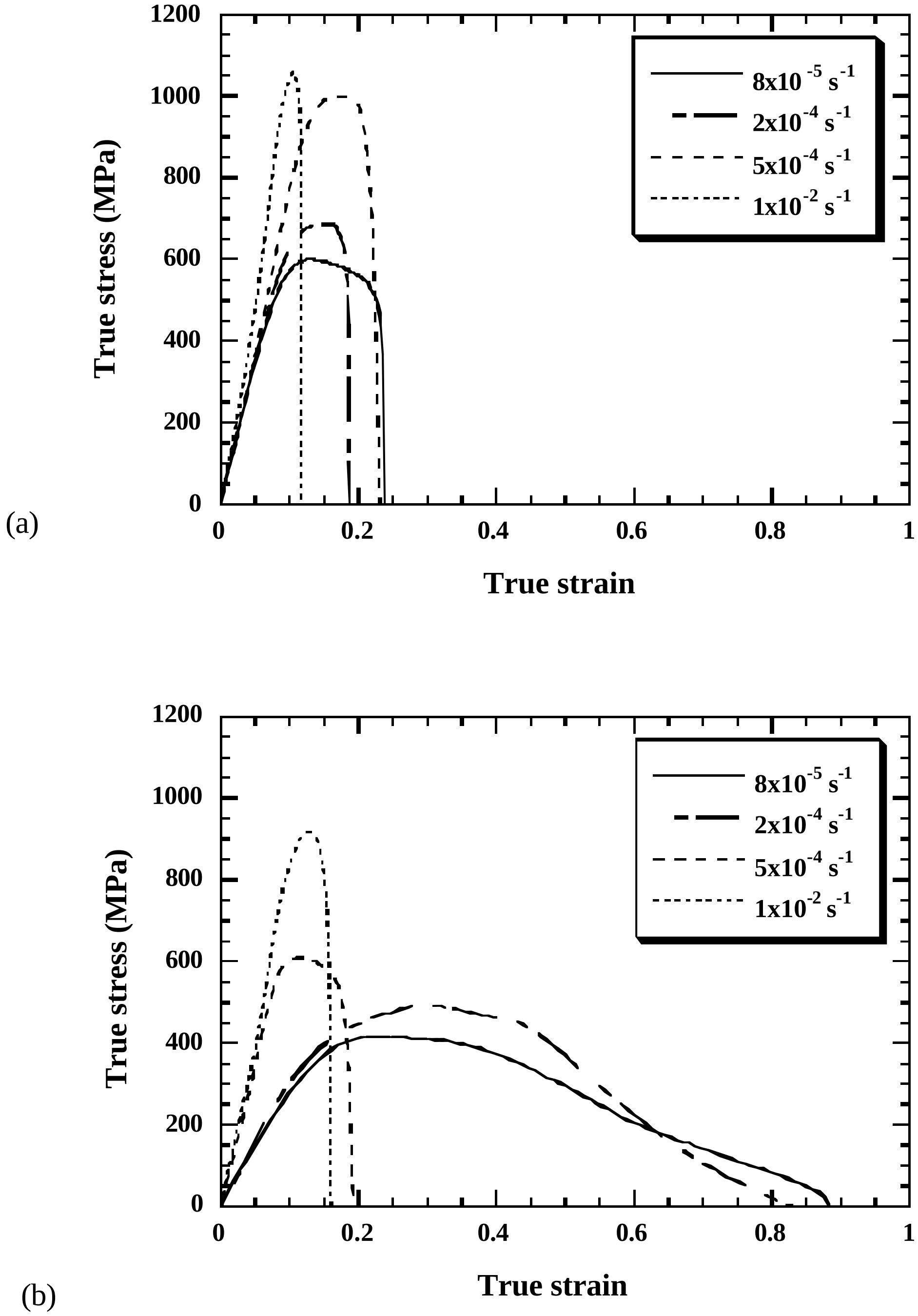

Fig. 19 Typical true stress-strain curves recorded from tensile tests at different initial strain rates for the loading temperatures of (a) 700°C, (b) 750°C, (c) 800°C, and (d) 850°C.

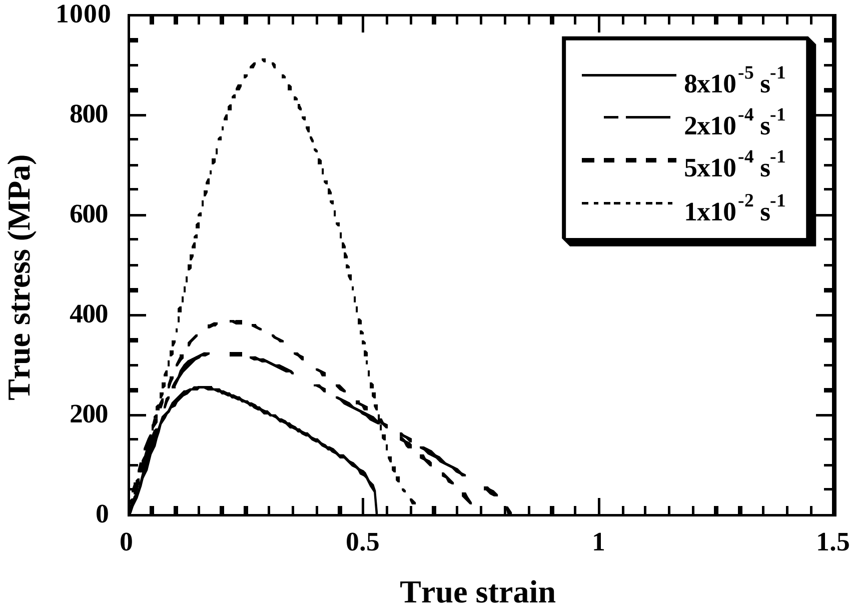
1000
800
600
400
200
0
True stress (MPa)
0
0.5
1
1.5
True strain
$8x10^{-5}$ s^{-1}
$2x10^{-4}$ s^{-1}
$5x10^{-4}$ s^{-1}
$1x10^{-2}$ s^{-1}

(c)

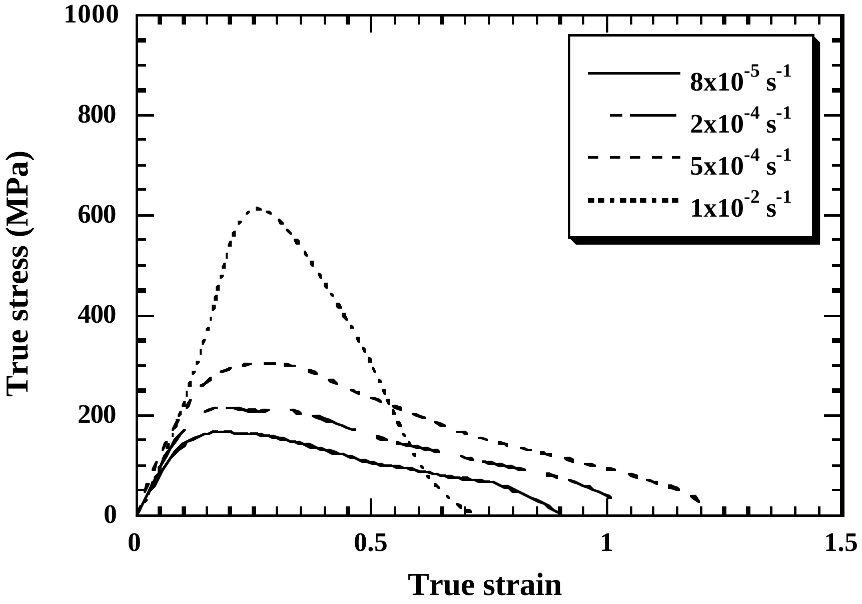
1000
800
600
400
200
0
True stress (MPa)
0
0.5
1
1.5
True strain
$8x10^{-5}$ s^{-1}
$2x10^{-4}$ s^{-1}
$5x10^{-4}$ s^{-1}
$1x10^{-2}$ s^{-1}

(d)

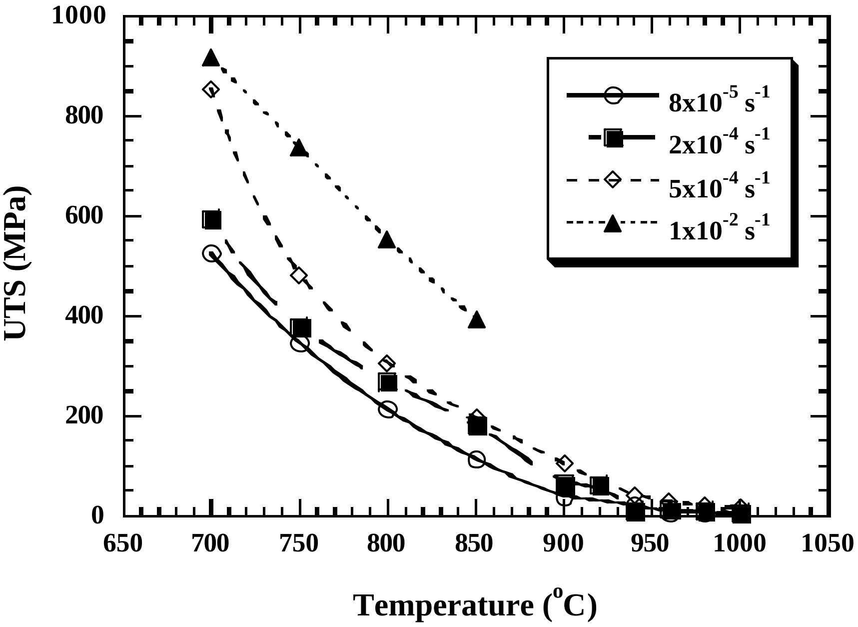

Fig. 20 The variation of engineering UTS as a function of loading temperature at 700-1000^{o}C.

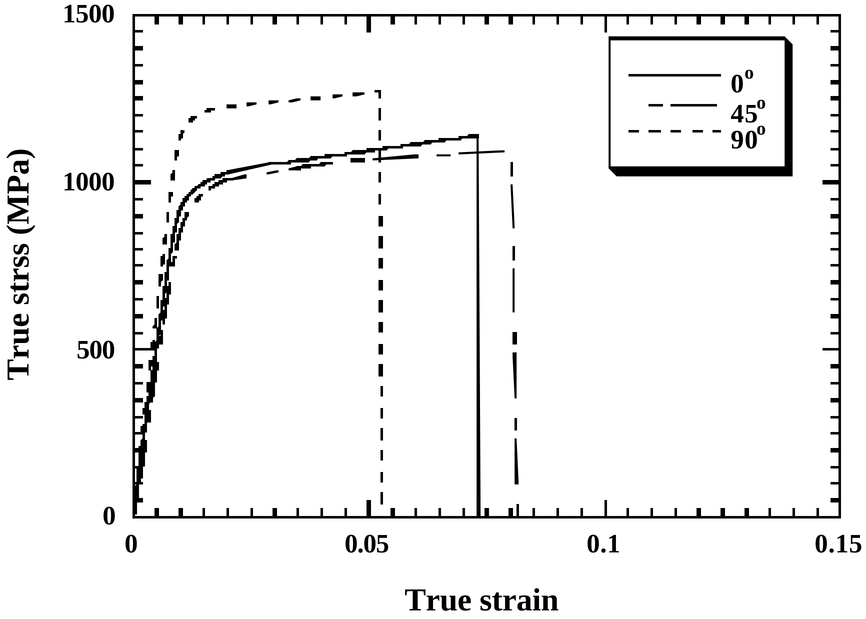

(a)

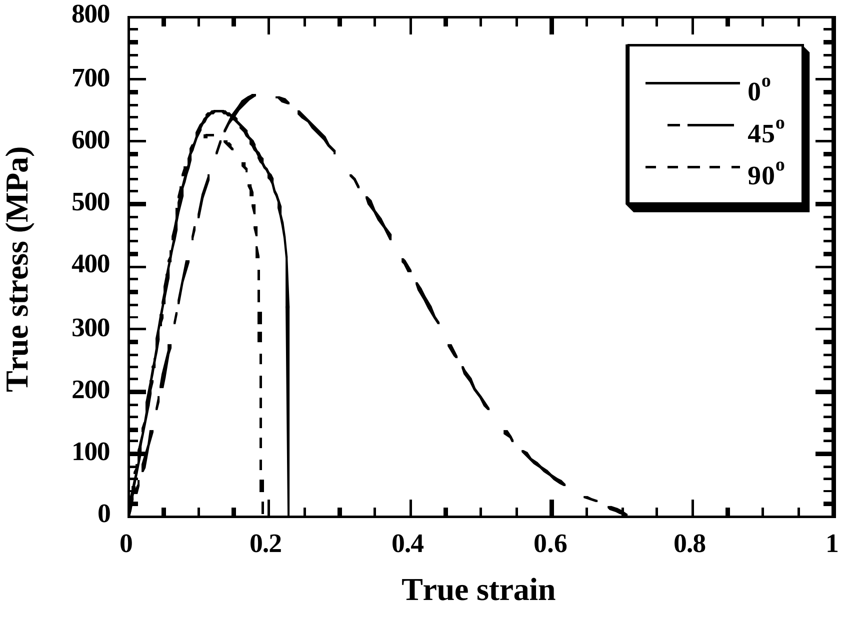

(b)

Fig. 21 The stress-strain curves recorded from the anisotropic tests under an initial strain rate of $3x10^{-3}$ s^{-1} performed at (a) room temperature, and under an initial strain rate of $5x10^{-4}$ s^{-1} performed at (b) 750°C, (c) 850°C, and (d) 920°C.

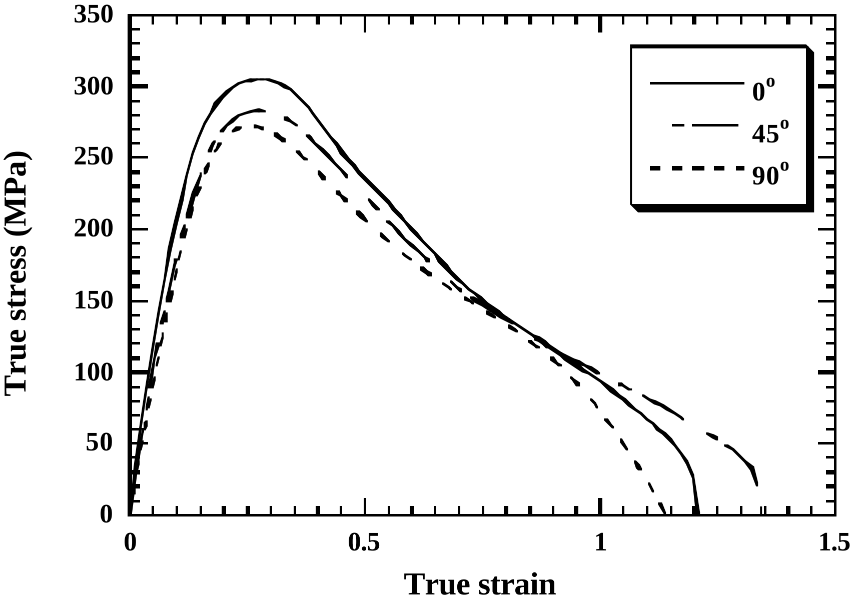
350
300
250
200
150
100
50
0
0
0.5
1
1.5
True stress (MPa)
True strain
0^o
45^o
90^o

(c)

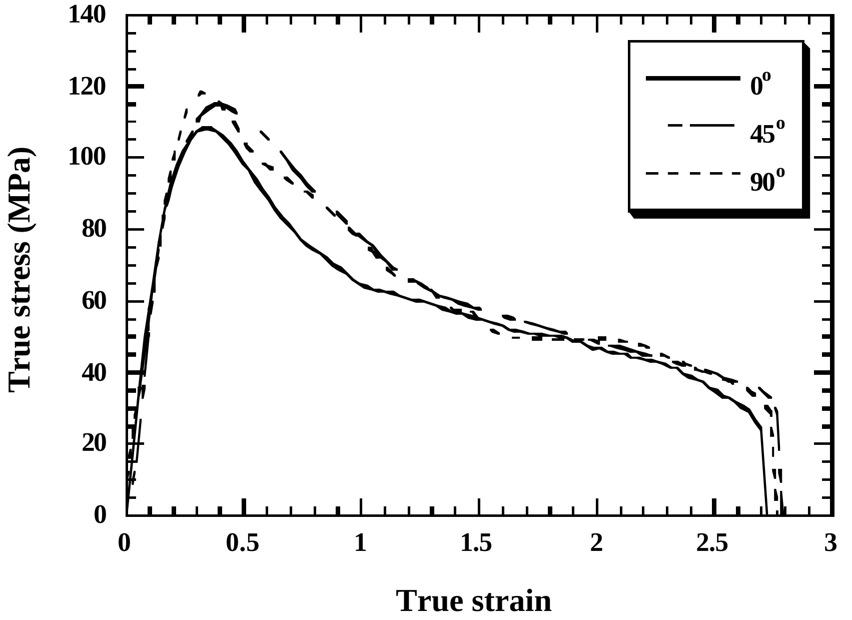
140
120
100
80
60
40
20
0
0
0.5
1
1.5
2
2.5
3
True stress (MPa)
True strain
0^o
45^o
90^o

(d)

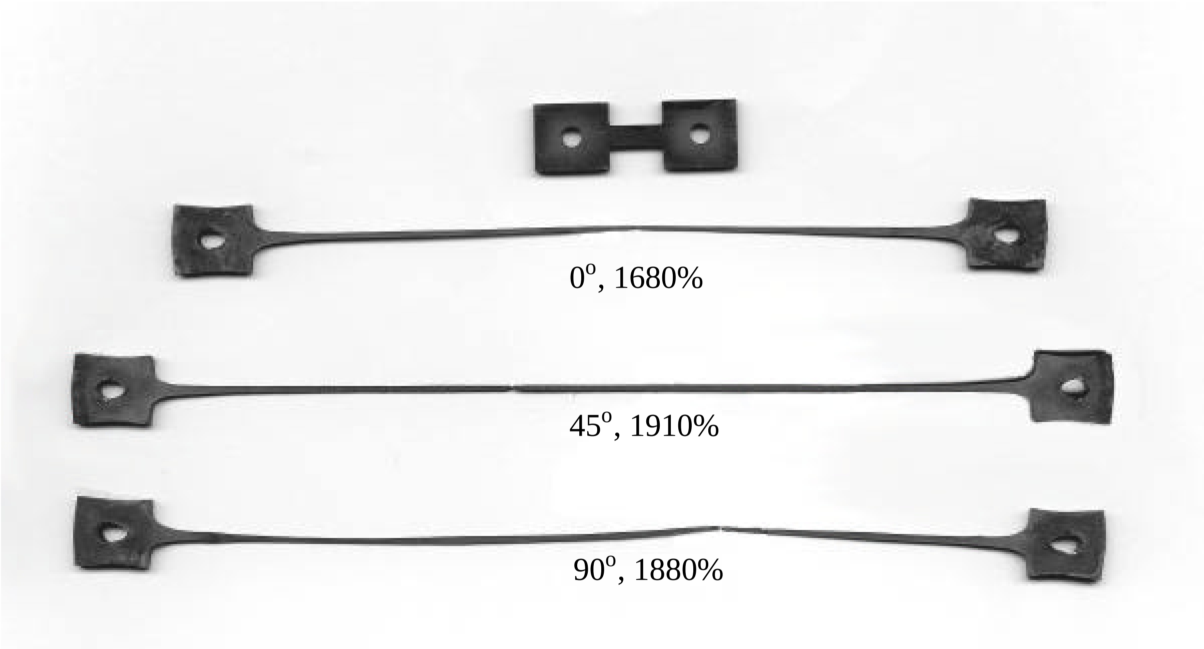

Fig. 22 Representative anisotropic tensile specimens loaded at 920°C and $5x10^{-4}$ s^{-1}.

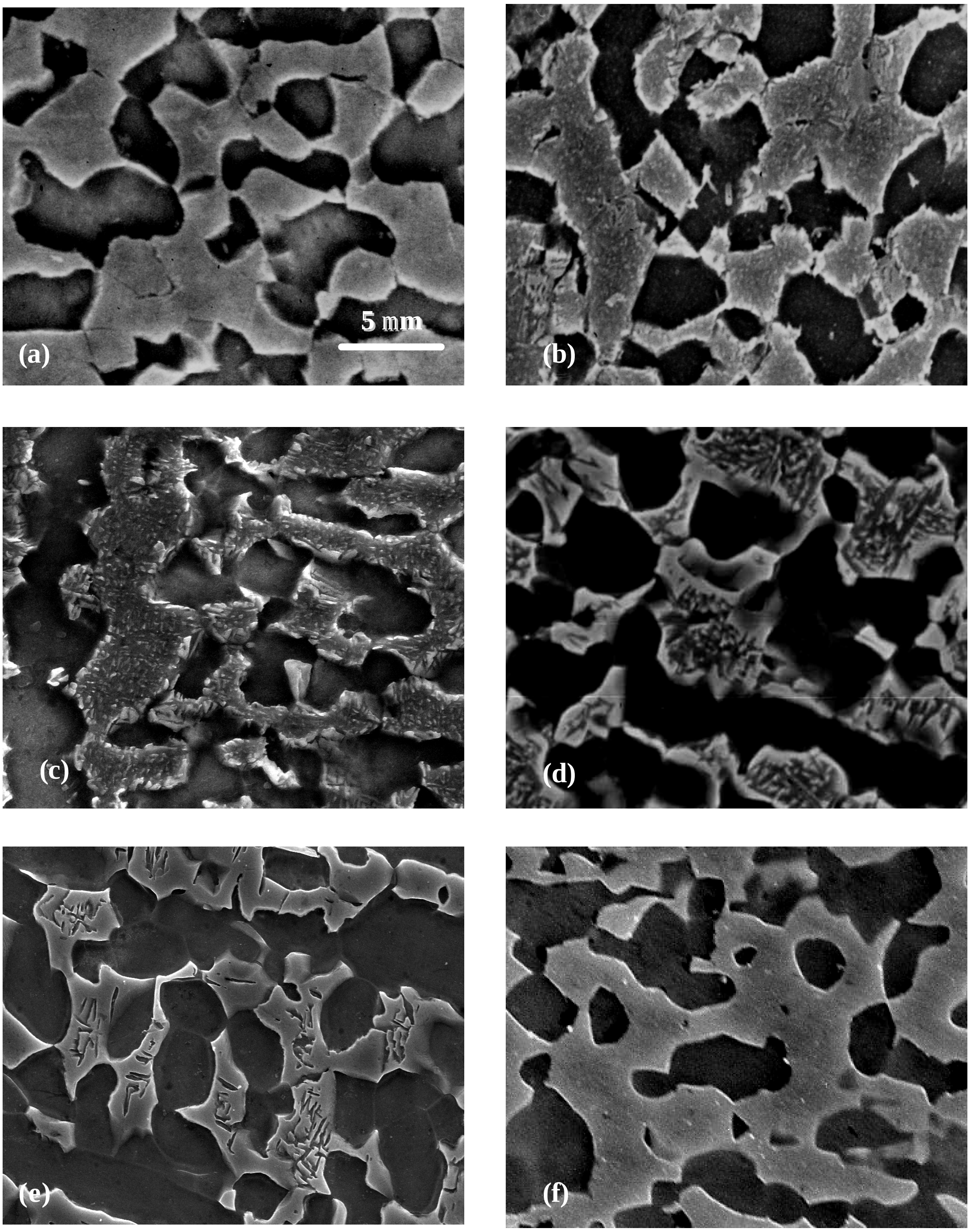

Fig. 23 Representative SEM micrographs showing the microstructures in the statically annealed specimens for 1.5 h for (a) 700°C, (b) 750°C, (c) 800°C, (d) 850°C, (e) 900°C, and (f) 960°C.

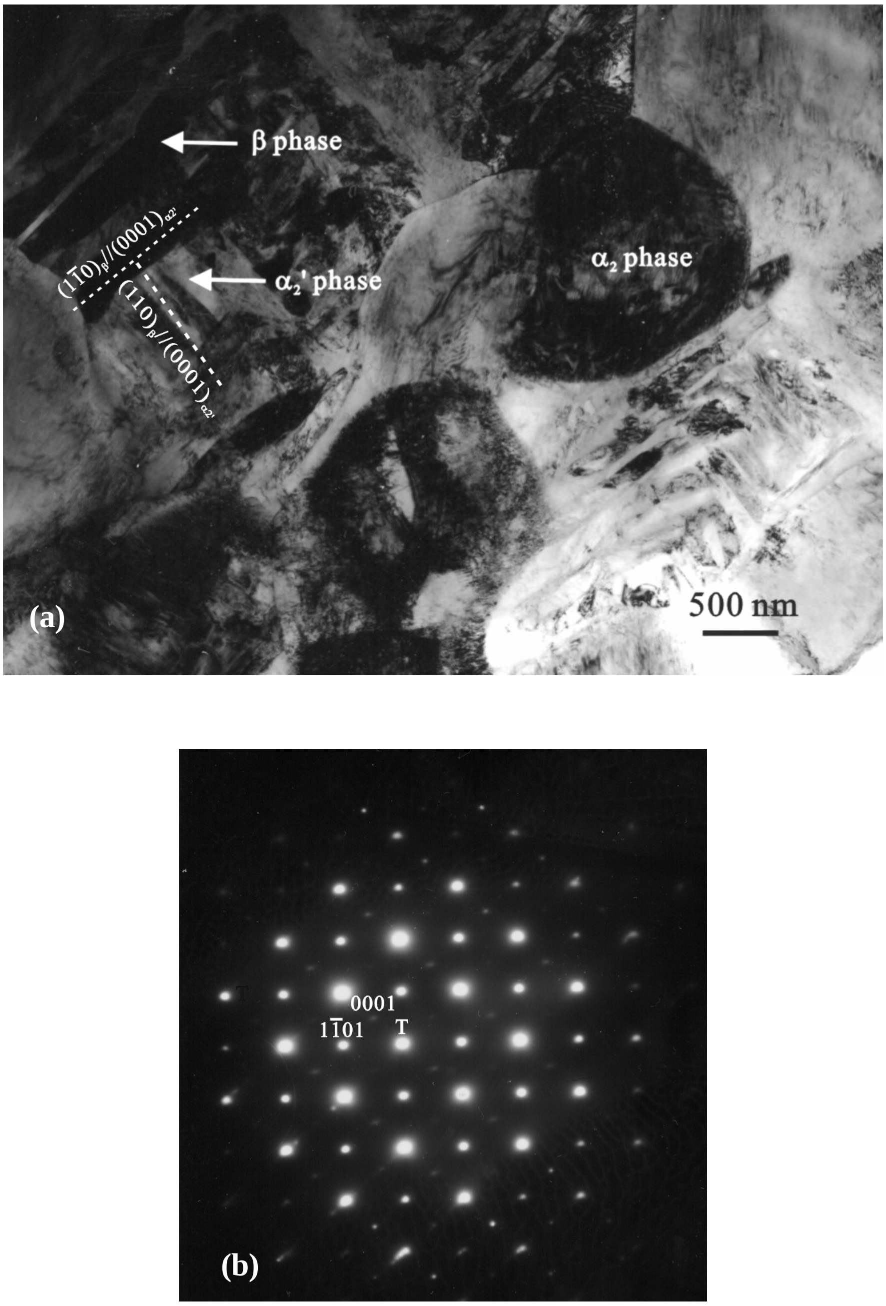

Fig. 24 TEM micrograph of the specimen statically annealed at 850°C for 1.5 h, with the diffraction pattern taken from the $[11\bar{2}0]$ zone of the transformed α_2’ phase.

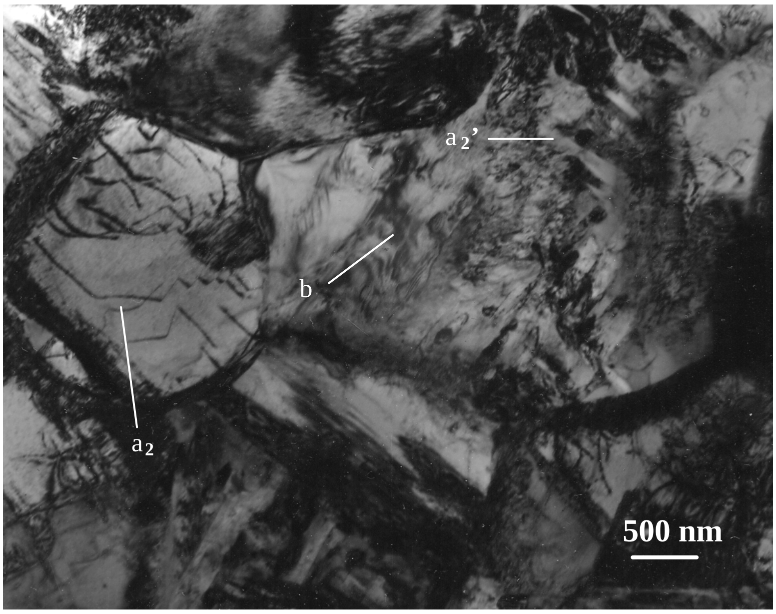

(a)

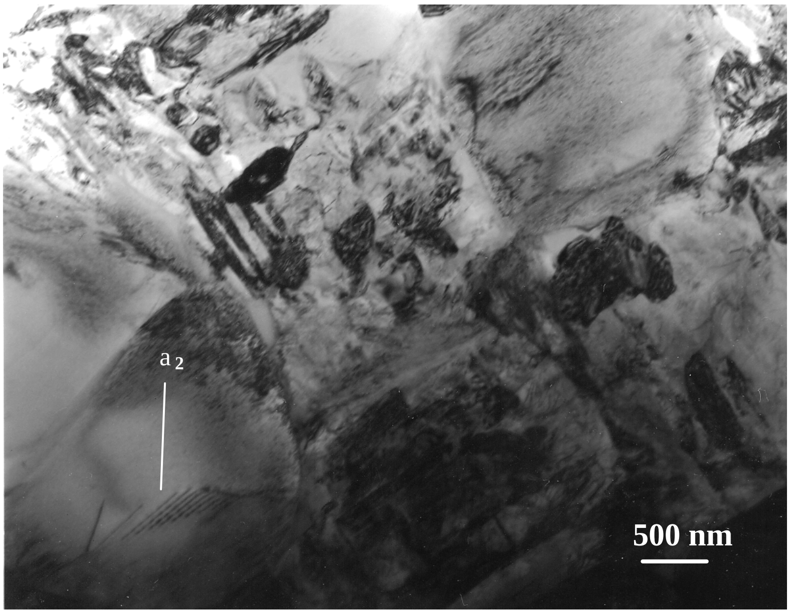

(b)

Fig. 25 TEM micrographs showing dislocation structures in the α_2 and β phases in the sample annealed at 850°C for 1.5 h and then water quenched.

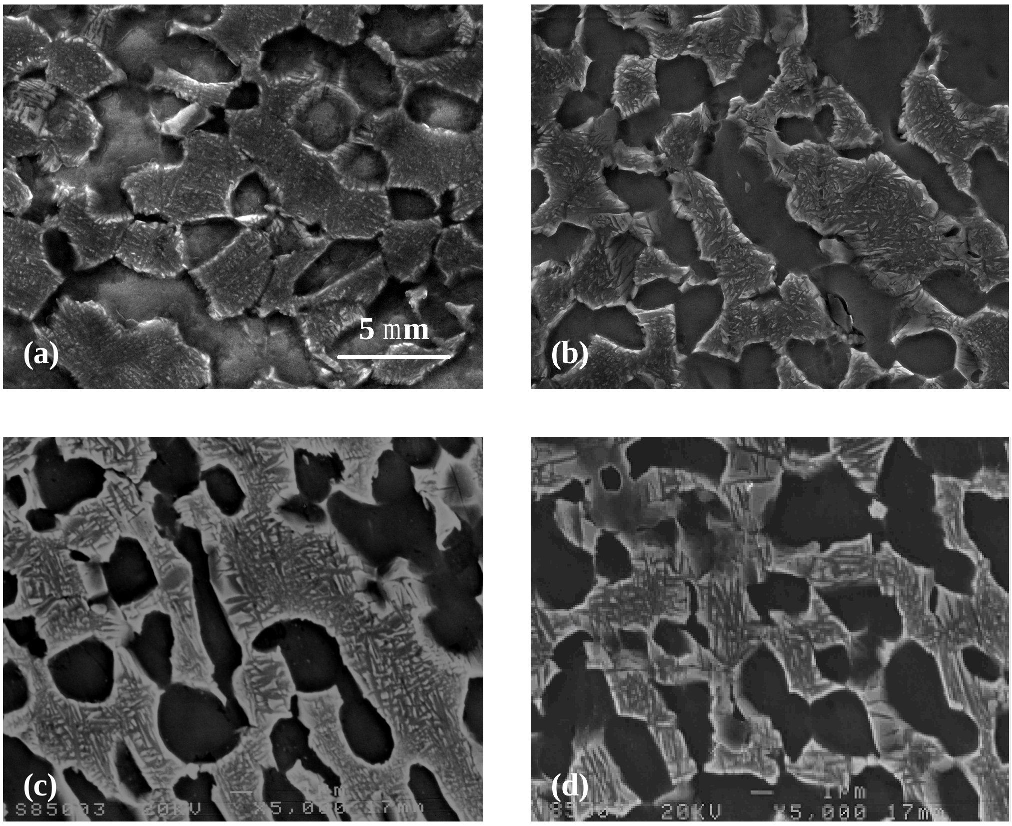

Fig. 26 Typical SEM micrographs showing the microstructures evolution during static annealing at (a) 800^{o}C for 30 min, (b) 800^{o}C for 2.5 h, (c) 850^{o}C for 3 min, and (d) 850^{o}C for 1.5 h.

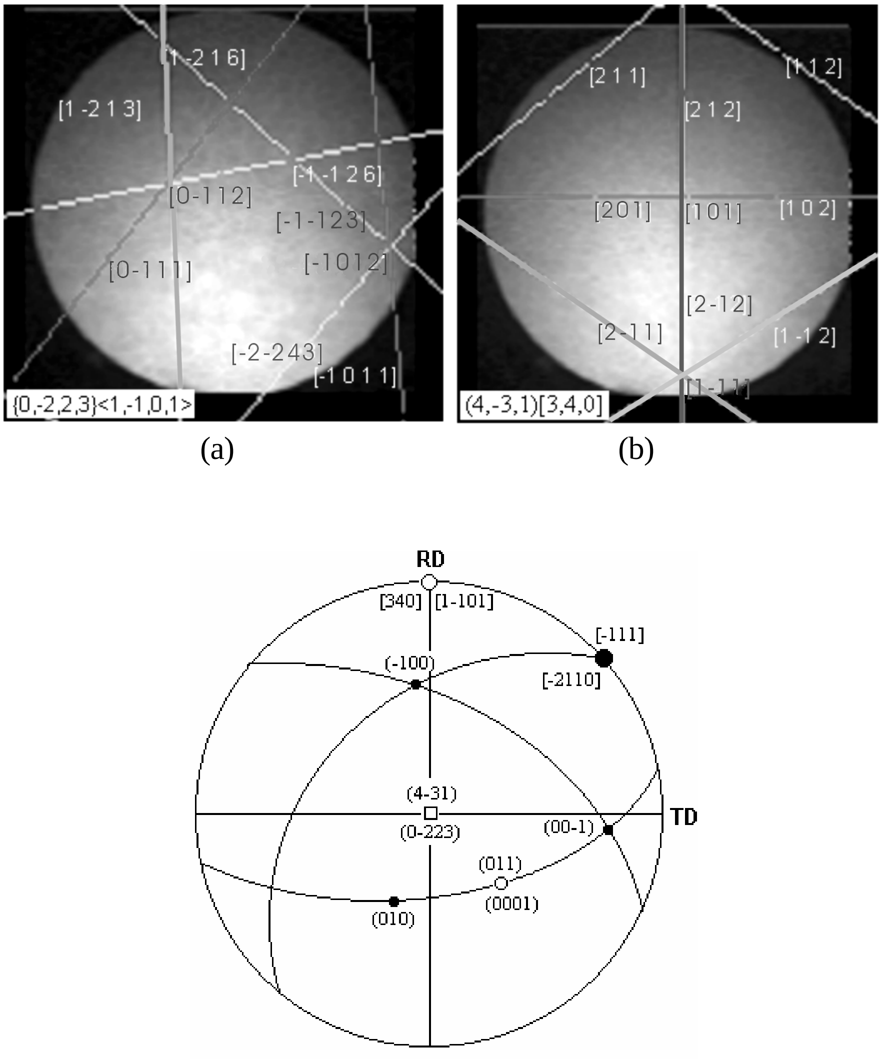

(a) (b)

(c)

Fig. 27 EBSD patterns taken from the (a) α_2' grain and (b) β grain. The overlapped stereographic projections in (c) shows the orientation relationship between the α_2' and β phases.

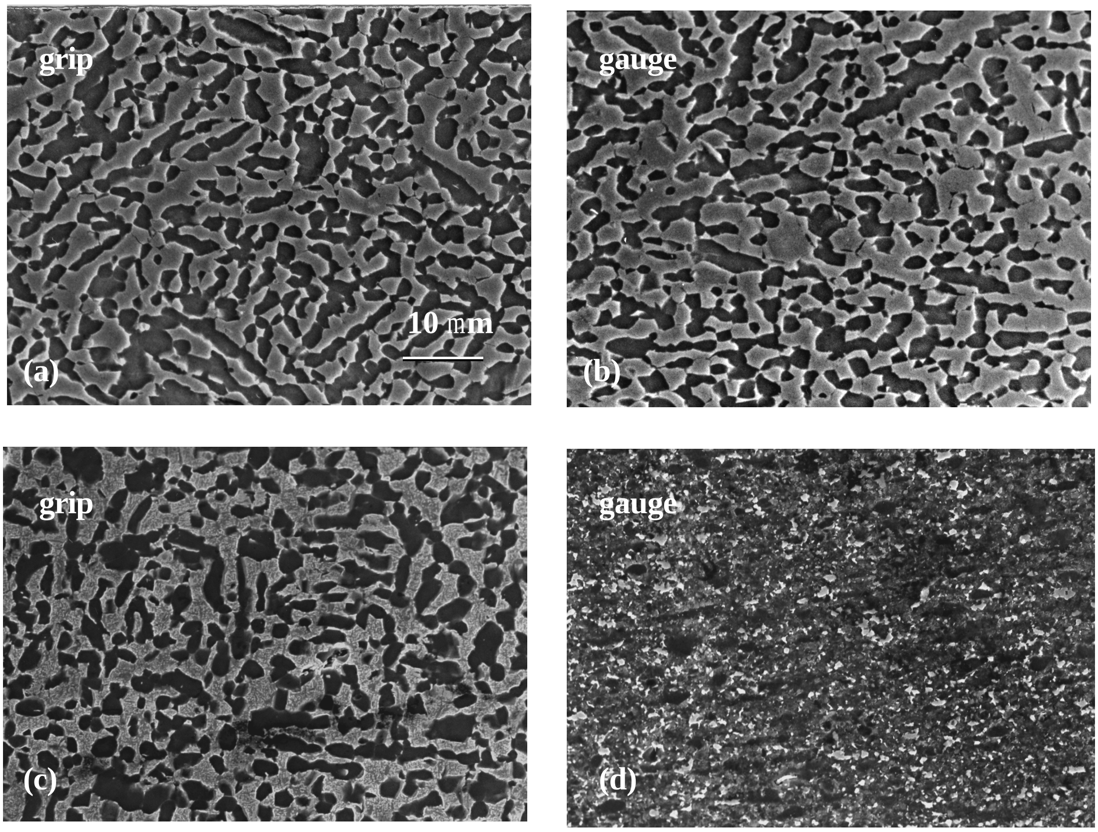

Fig. 28 SEM micrographs showing the microstructures in the superplastically loaded specimens: (a) grip, 700°C, (b) gauge, 700°C, (c) grip, 800°C, (d) gauge, 800°C.

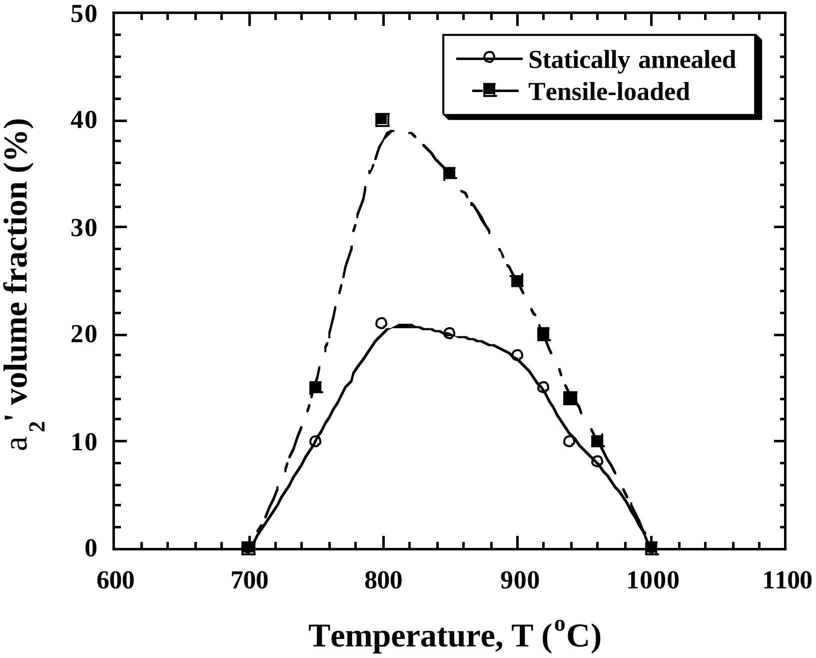

Fig. 29 Variation of the α_2' volume fraction as a function of the annealing or loading temperature.

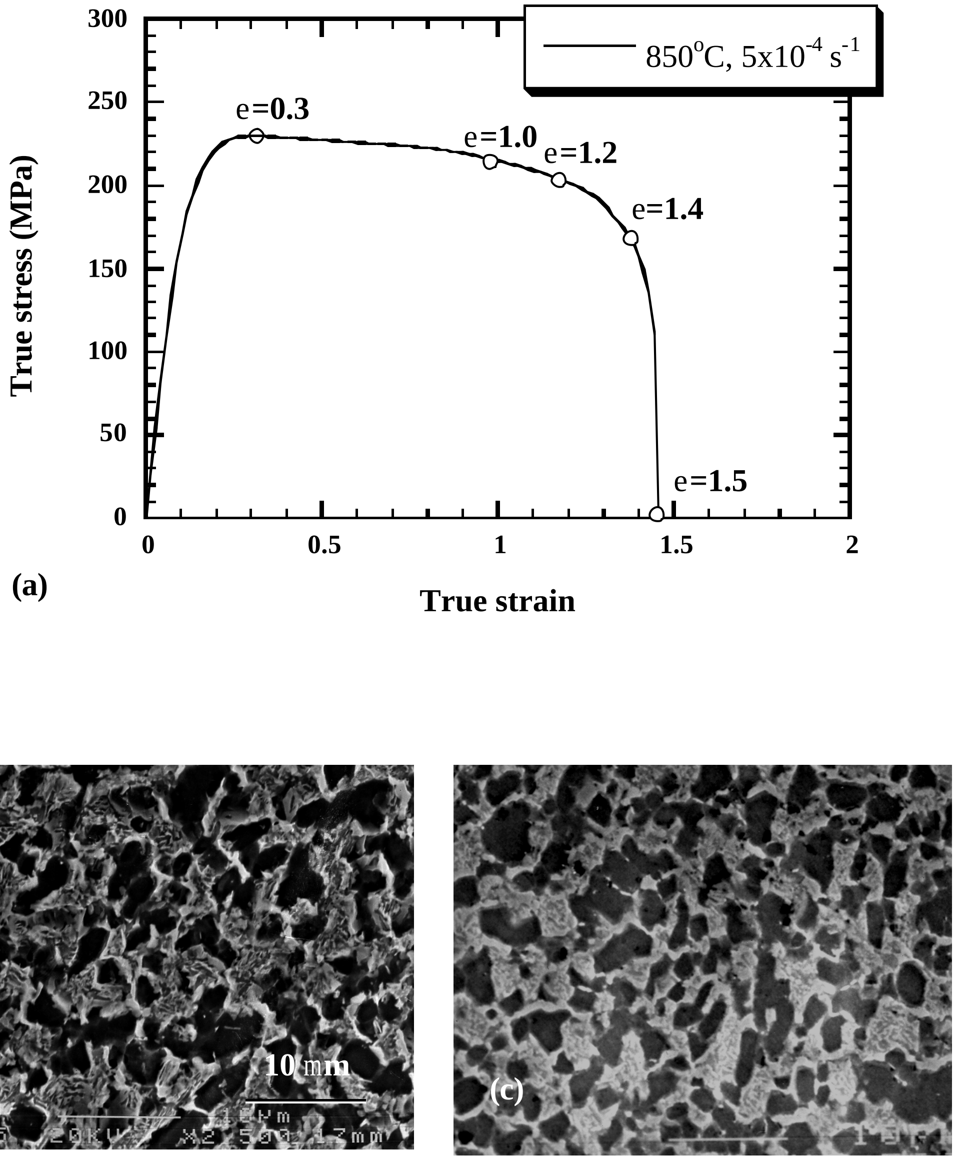

Fig. 30 SEM micrographs showing the microstructures in the gauge sections of the specimens loaded at 850°C and $5x10^{-4}$ s^{-1} to a true strain of (b) $\varepsilon=0.3$, (c) $\varepsilon=1.0$, (d) $\varepsilon=1.2$, (e) $\varepsilon=1.4$, (f) $\varepsilon=1.5$ (failure), and then stopped and rapidly quenched by blowing liquid nitrogen. The true stress and strain curve is shown in (a), which is plotted from the measurements of these stopped specimens.

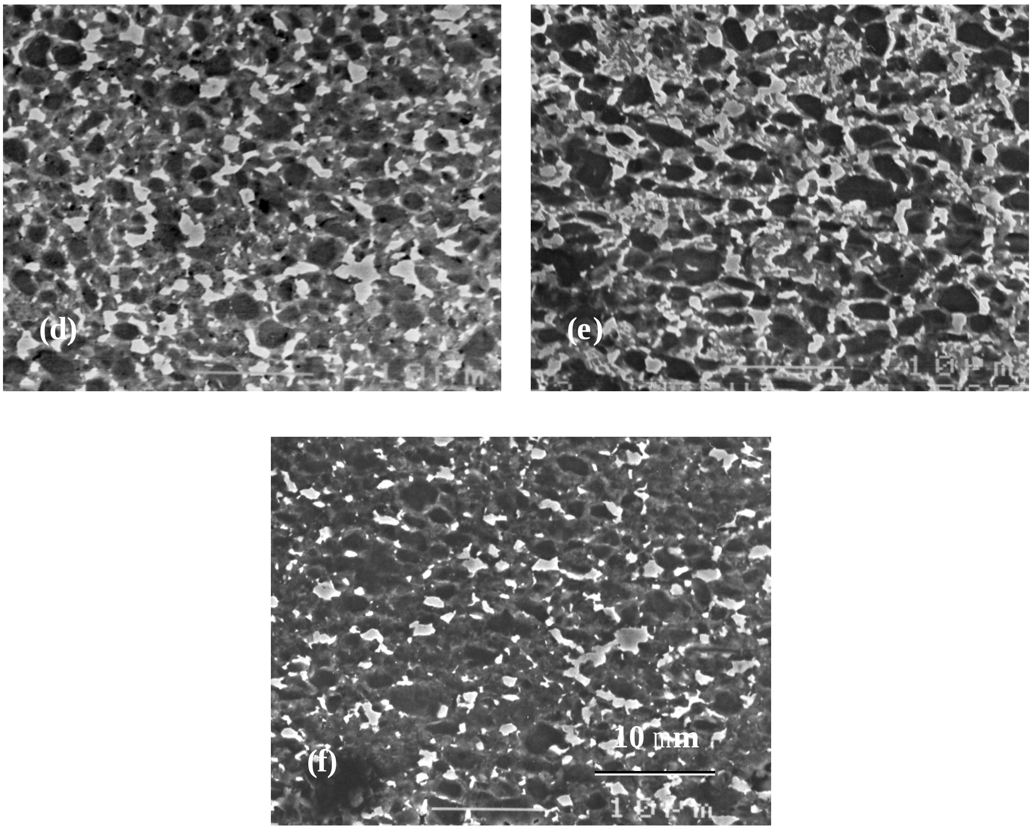
(d)
(e)
(f)
10 mm

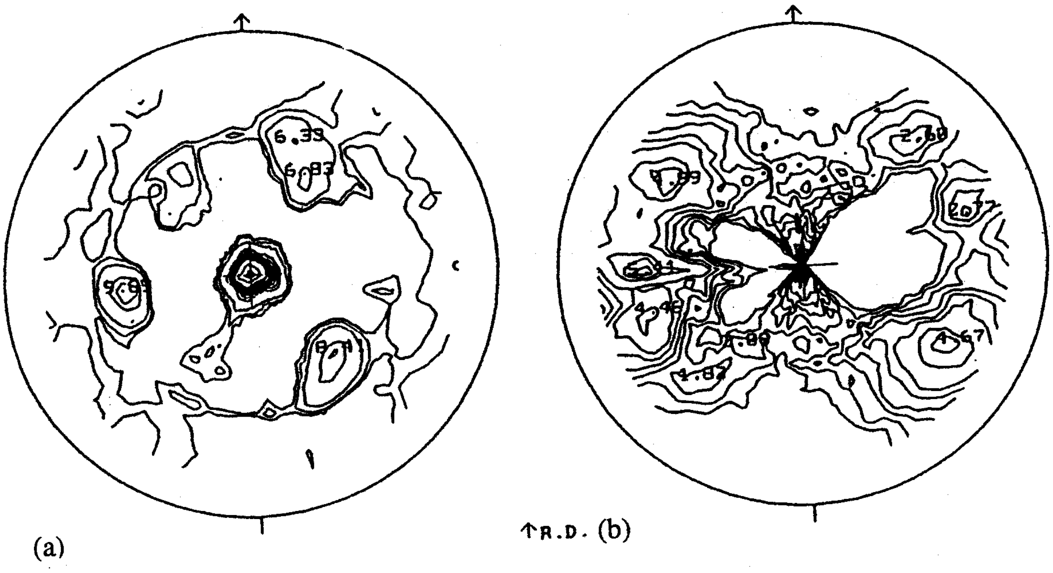

Fig. 31 X-ray pole figures of the as-received material: (a) the β phase (200) plane with the maximum intensity contour level of 40, and (b) the α_2 phase $(11\bar{2}0)$ plane with maximum contour of 10 [100].

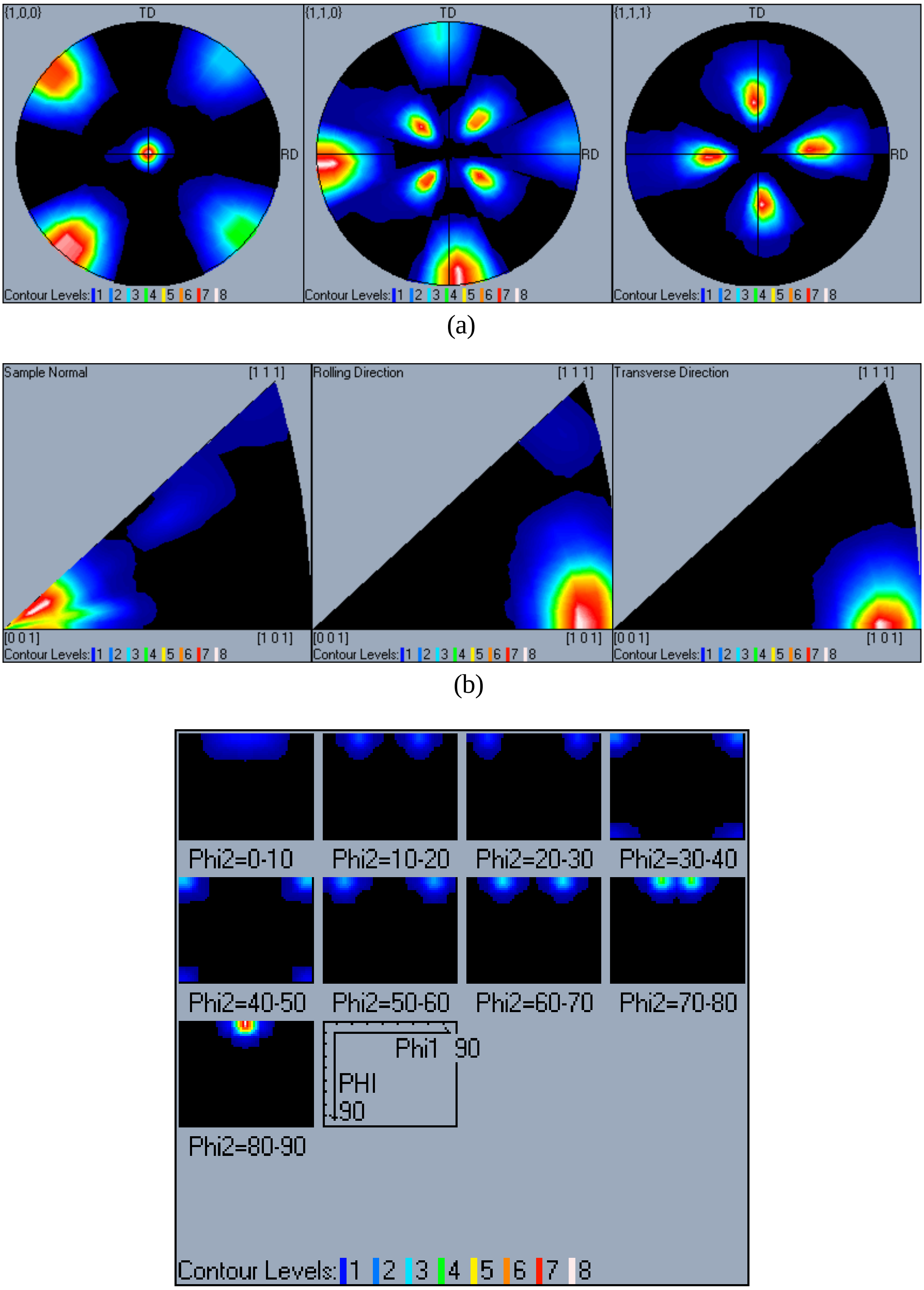

(a)

(b)

(c)

Fig. 32 (a) Pole figures, (b) inverse pole figures, and (c) ODF of the β phase in the as-received specimen.

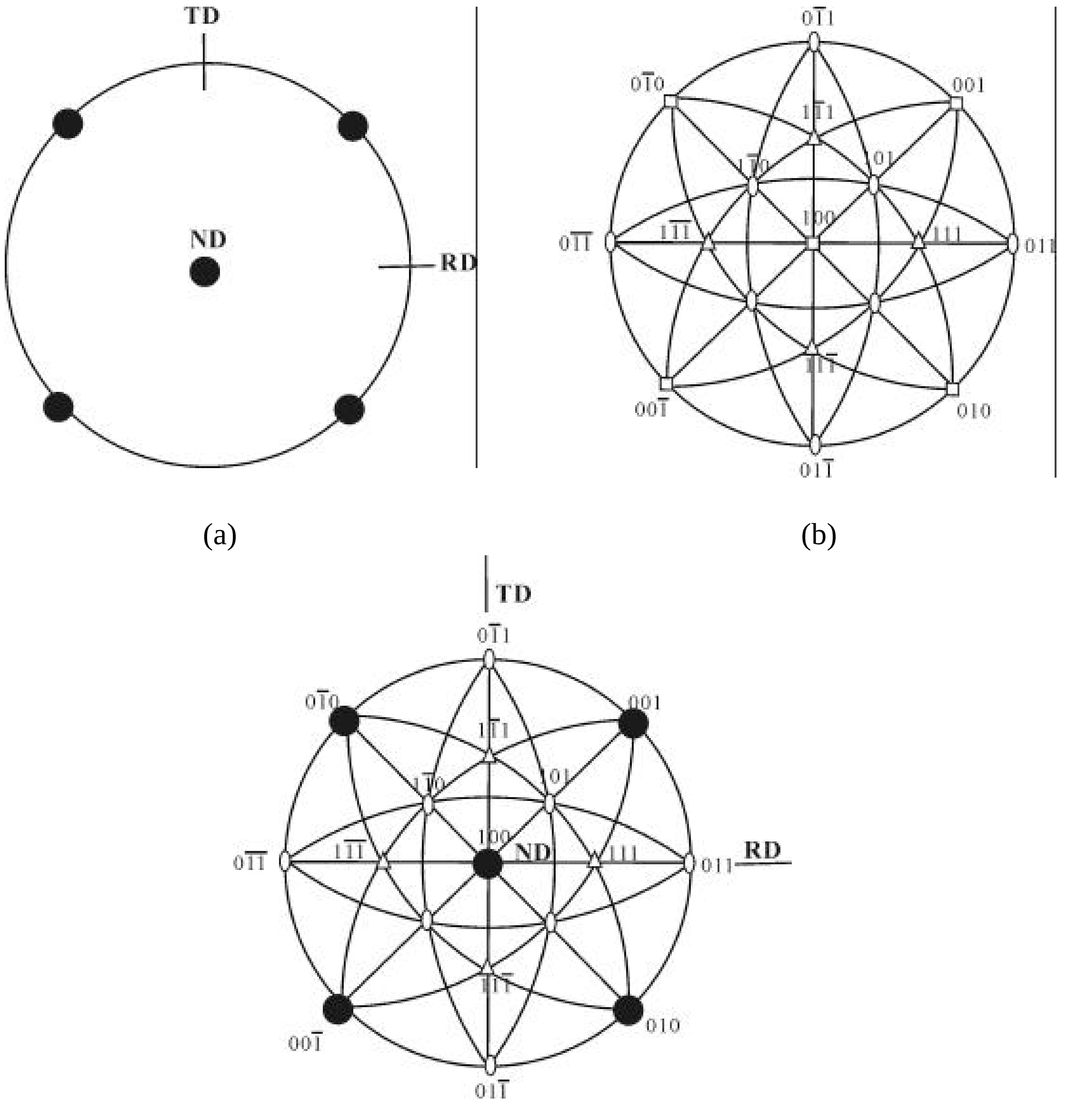

(a) (b)

(c)

Fig. 33 The sequence for texture determination: (a) a {100} pole figure; (b) choose a standard projection to make all the {100} poles in (a) occupy the {100} pole family in (b); (c) {ND}<RD> could be identified.

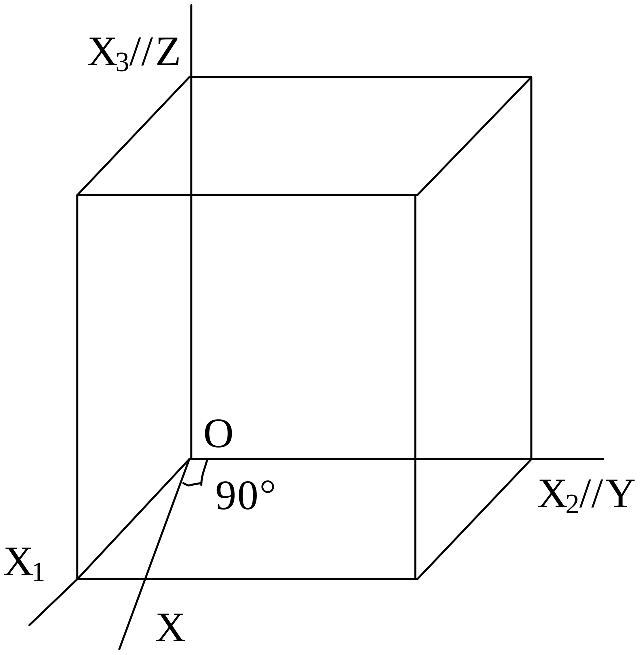

Fig. 34 Schematic illustration of the hexagonal system represented by $\{OX_1X_2X_3\}$ and the cubic system represented by $\{OXYZ\}$.

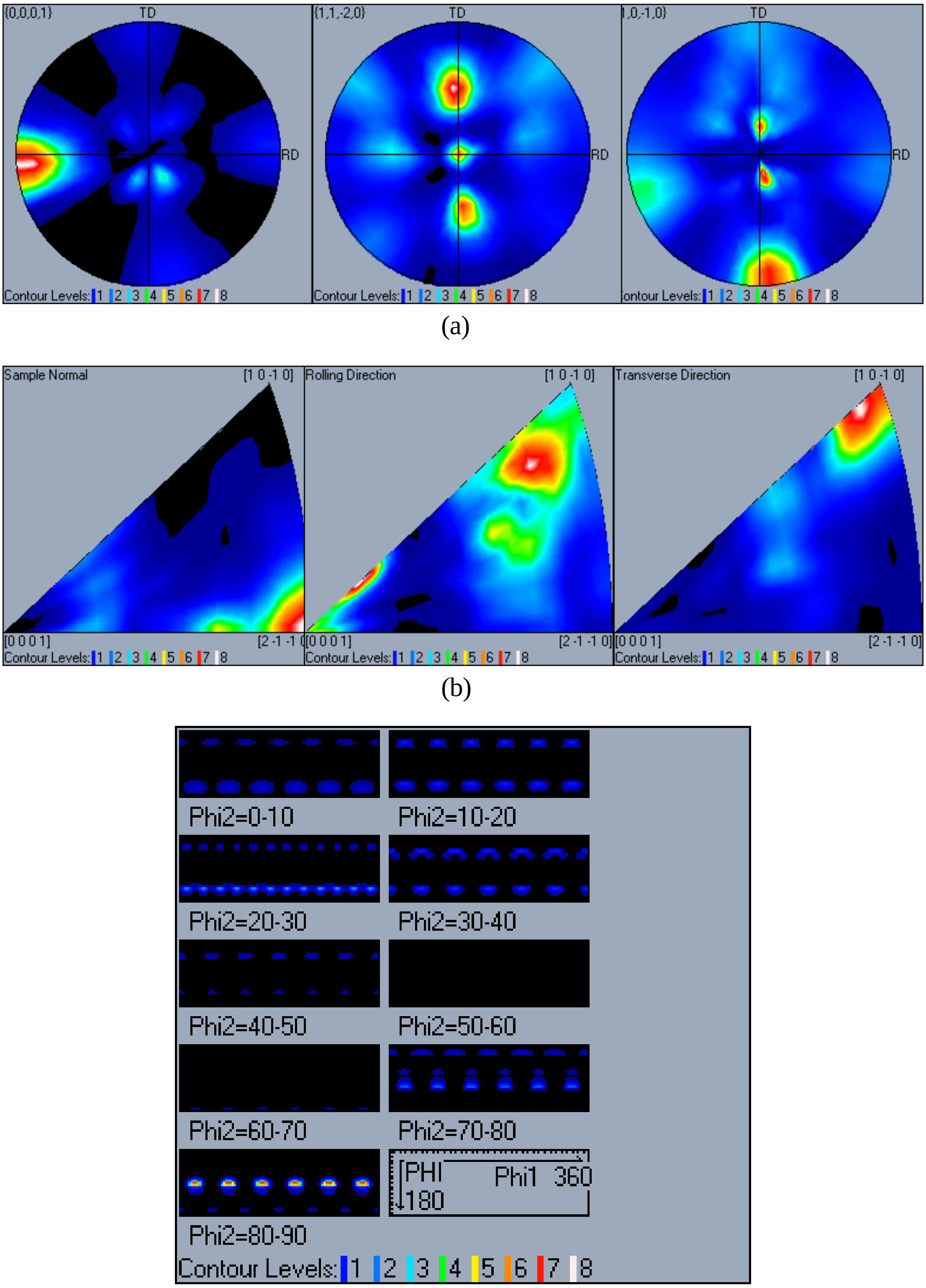

(a)

(b)

(c)

Fig. 35 (a) Pole figures, (b) inverse pole figures, and (c) ODF of the α_2 phase in the as-received specimen.

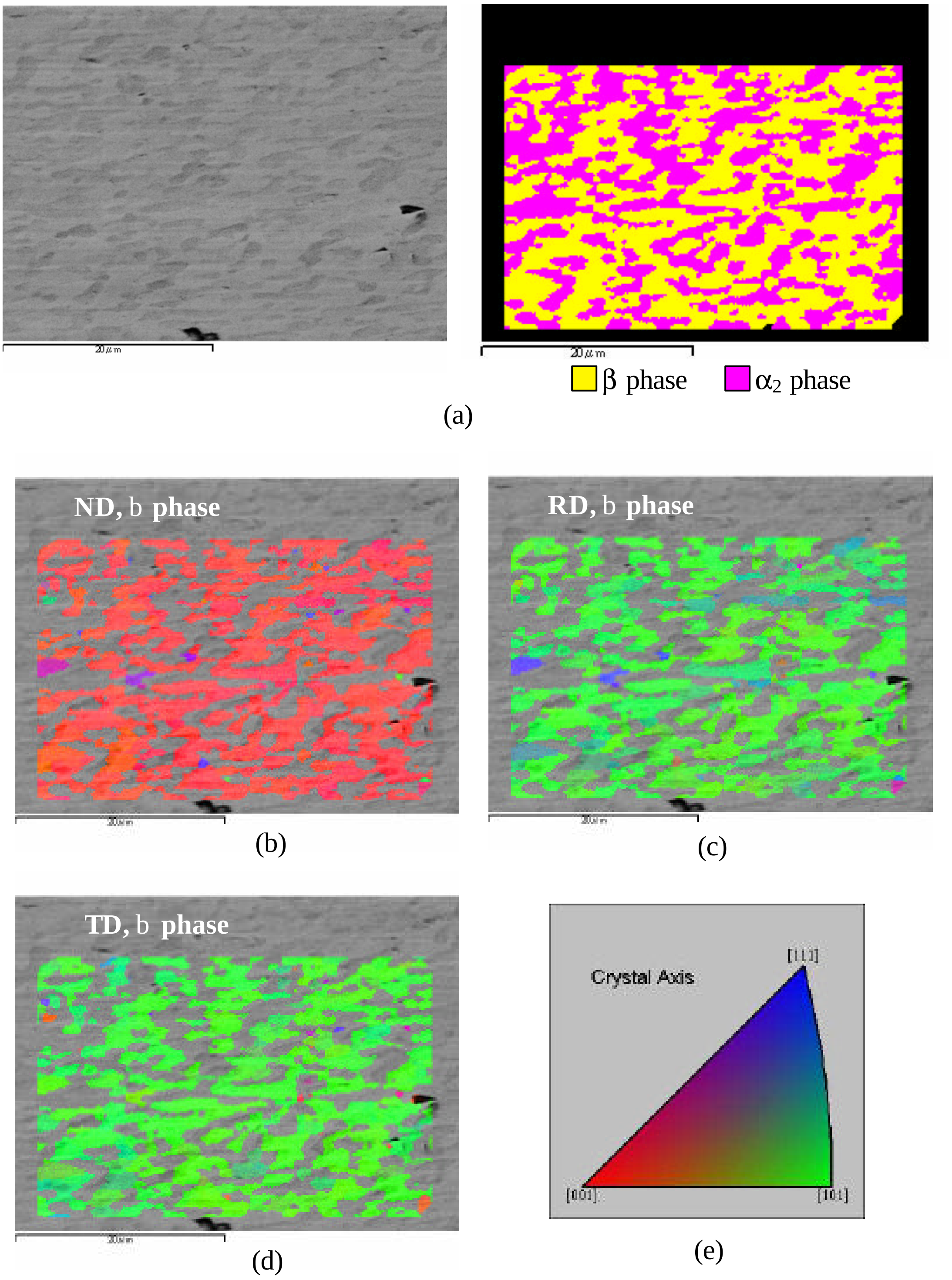

(a)

(b)

(c)

(d)

(e)

Fig. 36 (a) The SEI image and phase map in the as-received specimen. The OIMs displace the orientation distribution of (b)-(d) in the β phase and (f)-(h) in the α_2 phase. By using the orientation color key (e) and (i), orientation in the β and α_2 phases are visualized, respectively.

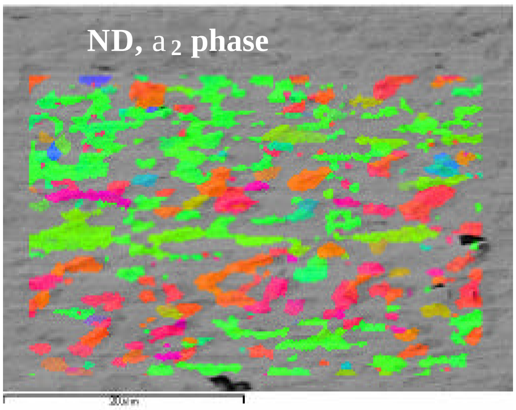
ND, a 2 phase

(f)

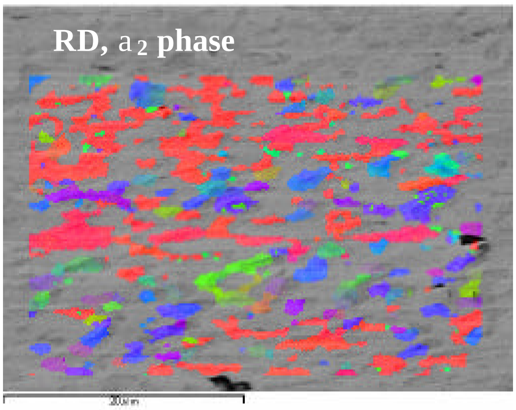
RD, a 2 phase

(g)

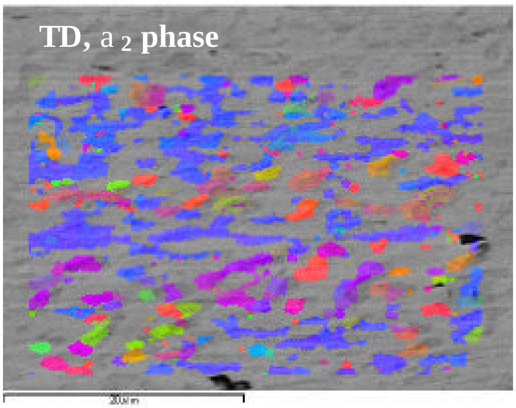
TD, a 2 phase

(h)

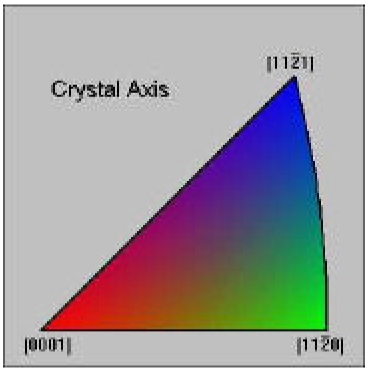
Crystal Axis
[11$\bar{2}$1]
[0001]
[11$\bar{2}$0]

(i)

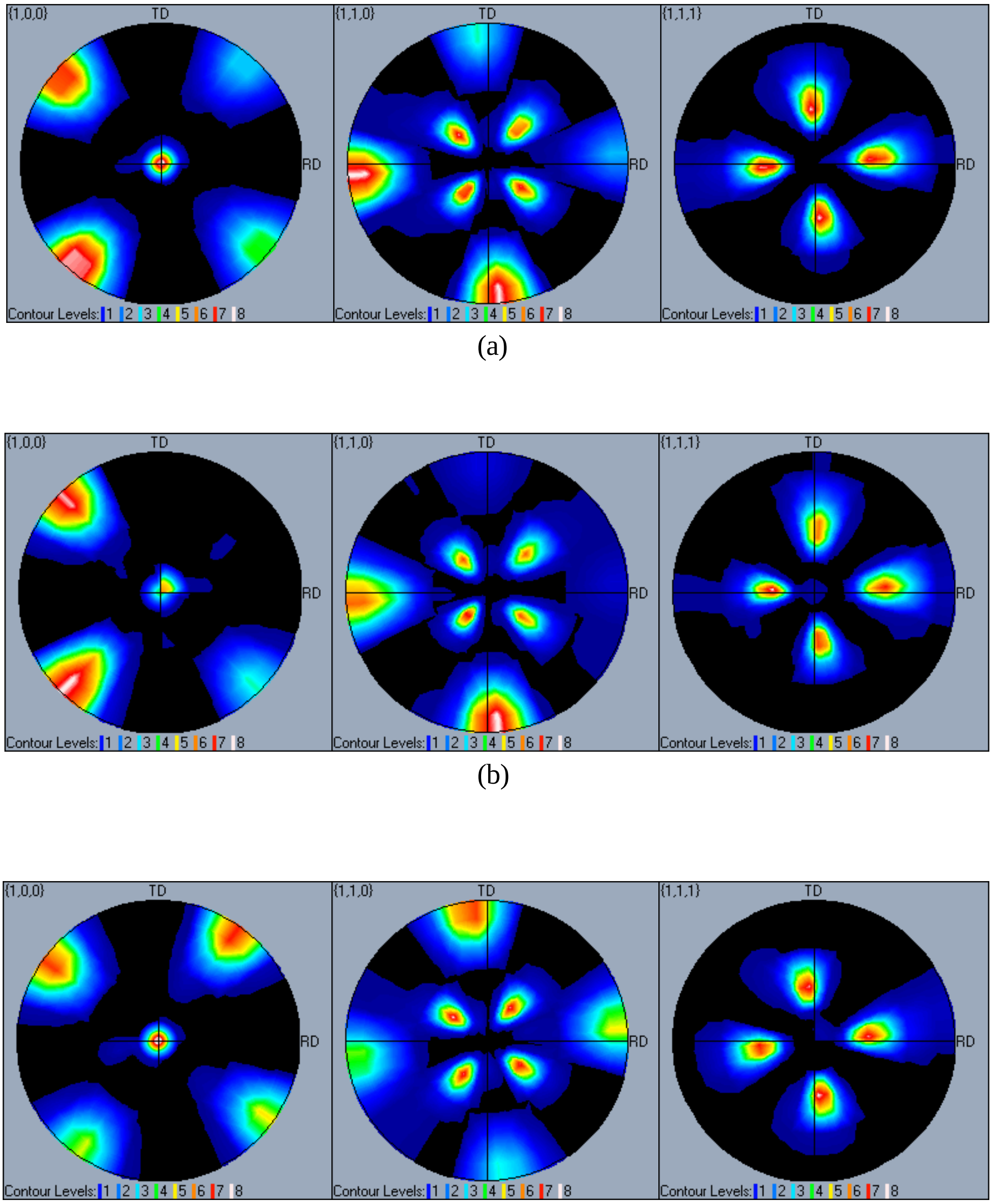

(a)

(b)

(c)

Fig. 37 Five regions sampled from the β phase in the as-received specimen: strong {100}<011> rotated cube and weak $\{111\}<1\bar{2}1>$ textures are present in (a), (b), and (c); occasional strong {110}<001> Goss in (d); and strong $\{111\}<2\bar{1}\bar{1}>$ in (e).

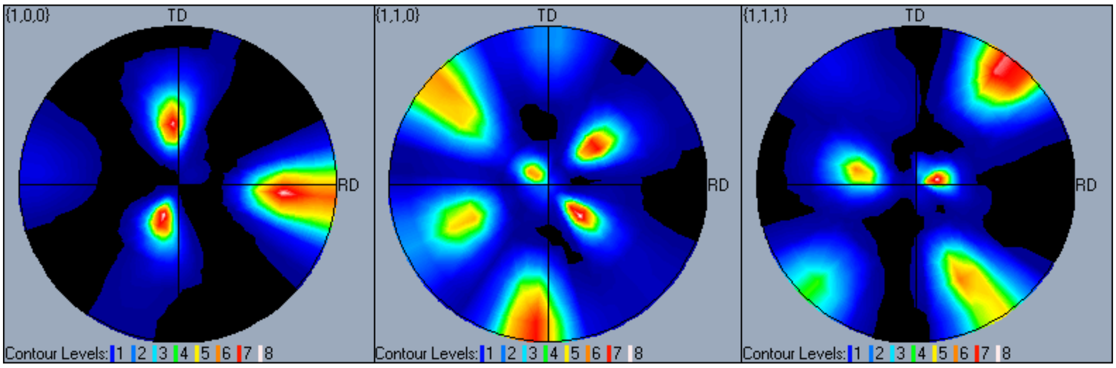
{1,0,0}
TD
RD
Contour Levels: 1 2 3 4 5 6 7 8
{1,1,0}
TD
RD
Contour Levels: 1 2 3 4 5 6 7 8
{1,1,1}
TD
RD
Contour Levels: 1 2 3 4 5 6 7 8

(d)

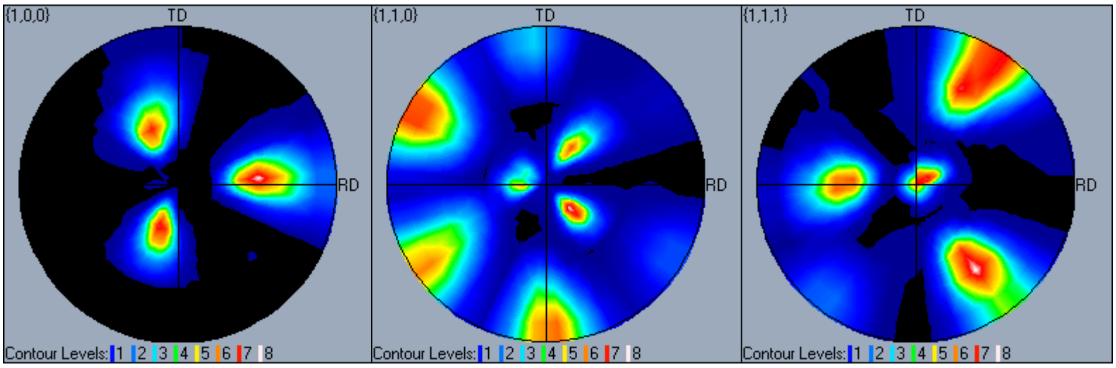
{1,0,0}
TD
RD
Contour Levels: 1 2 3 4 5 6 7 8
{1,1,0}
TD
RD
Contour Levels: 1 2 3 4 5 6 7 8
{1,1,1}
TD
RD
Contour Levels: 1 2 3 4 5 6 7 8

(e)

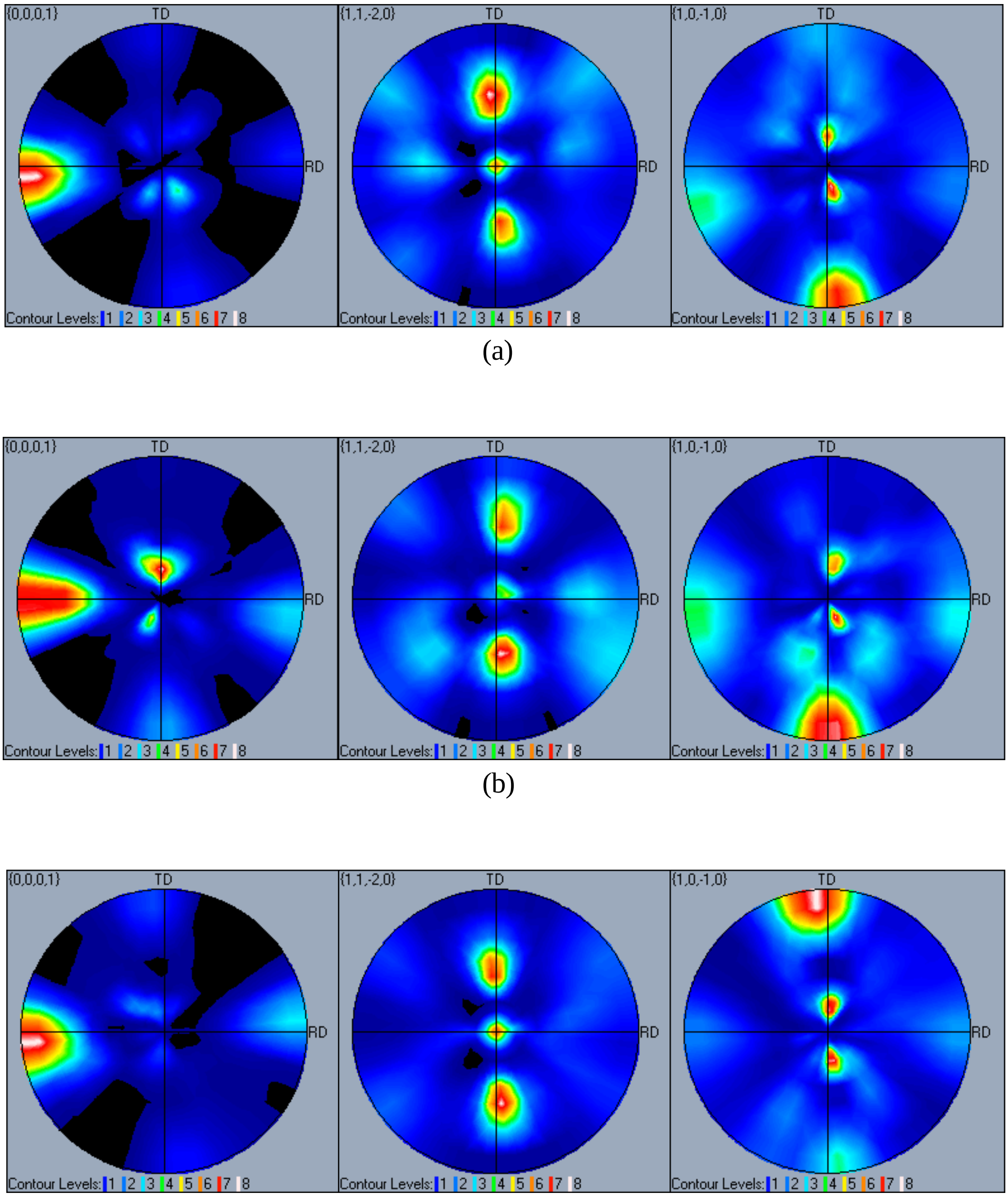

(a)

(b)

(c)

Fig. 38 Five regions sampled from the α_2 phase in the as-received specimen: strong $\{11\bar{2}0\}\langle 0001\rangle$ and weak $\{0001\}\langle\bar{1}100\rangle$ and $\{11\bar{2}0\}\langle\bar{1}100\rangle$ are present in (a), (b), and (c); strong $\{11\bar{2}0\}\langle 0001\rangle$ and weak $\{0001\}\langle 11\bar{2}0\rangle$ and $\{0001\}$ fiber in (d); strong $\{0001\}\langle 11\bar{2}0\rangle$ and weak $\{0001\}\langle\bar{1}100\rangle$ and $\{0001\}$ fiber in (e).

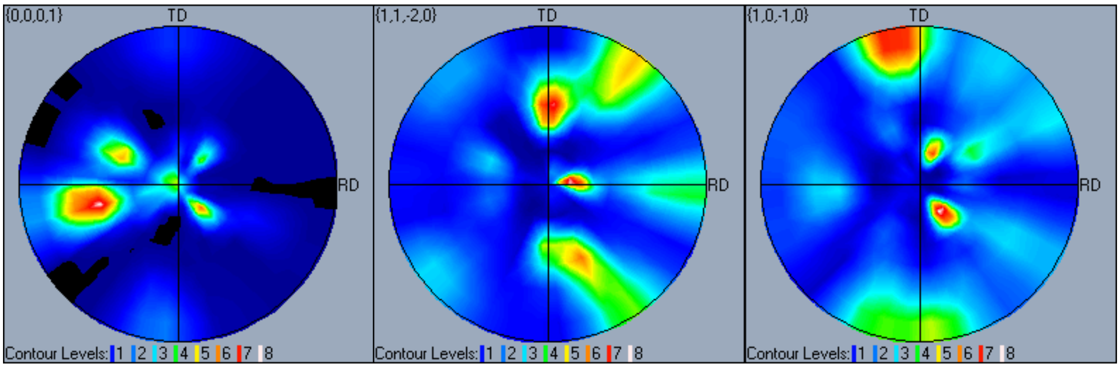
{0,0,0,1}
TD
RD
Contour Levels: 1 2 3 4 5 6 7 8
{1,1,-2,0}
TD
RD
Contour Levels: 1 2 3 4 5 6 7 8
{1,0,-1,0}
TD
RD
Contour Levels: 1 2 3 4 5 6 7 8

(d)

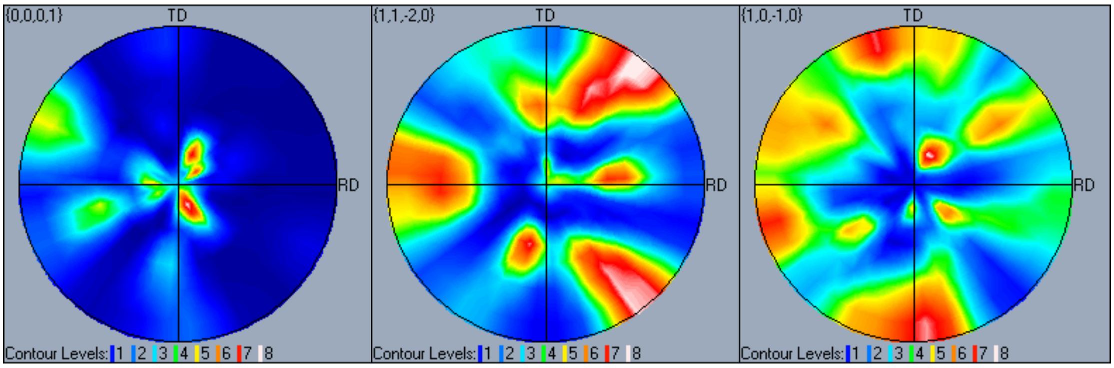
{0,0,0,1}
TD
RD
Contour Levels: 1 2 3 4 5 6 7 8
{1,1,-2,0}
TD
RD
Contour Levels: 1 2 3 4 5 6 7 8
{1,0,-1,0}
TD
RD
Contour Levels: 1 2 3 4 5 6 7 8

(e)

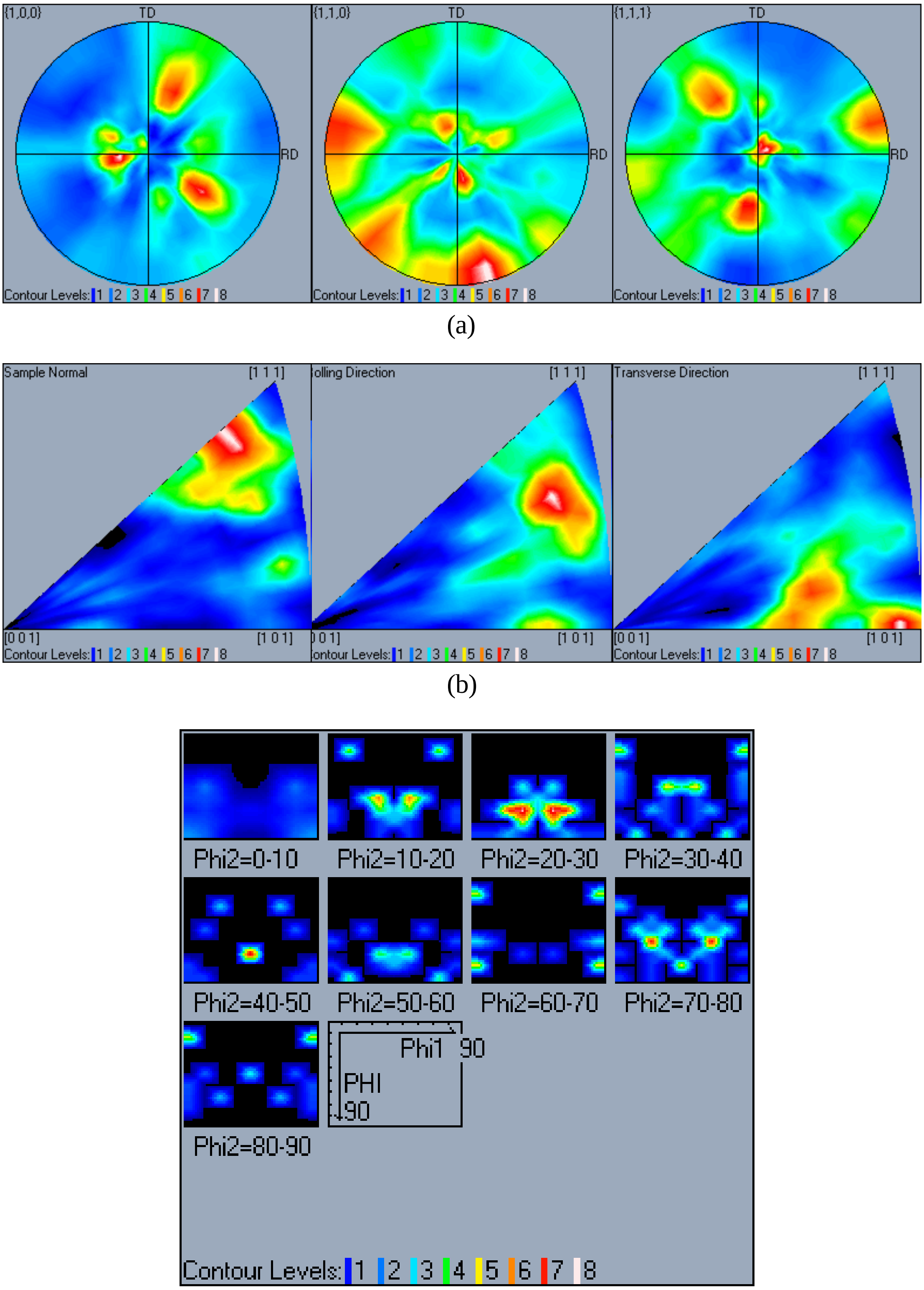

(a)

(b)

(c)

Fig. 39 (a) Pole figures, (b) inverse pole figures, and (c) ODF of the β phase in the 0^o specimen loaded at 750°C and $5x10^{-4}$ s^{-1}.

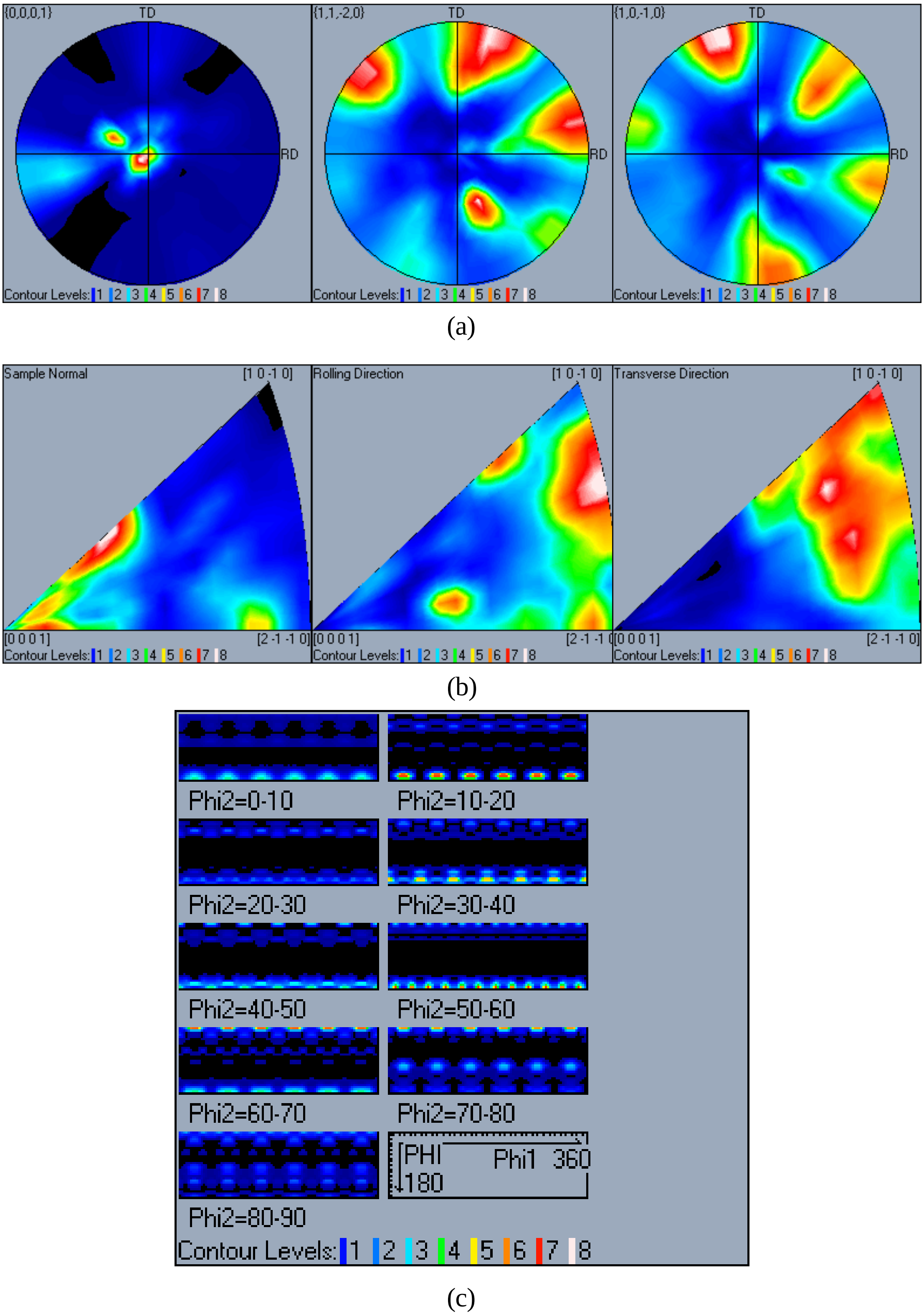

(a)

(b)

(c)

Fig. 40 (a) Pole figures, (b) inverse pole figures, and (c) ODF of the α_2 phase in the 0^o specimen loaded at 750^oC and $5x10^{-4}$ s^{-1}.

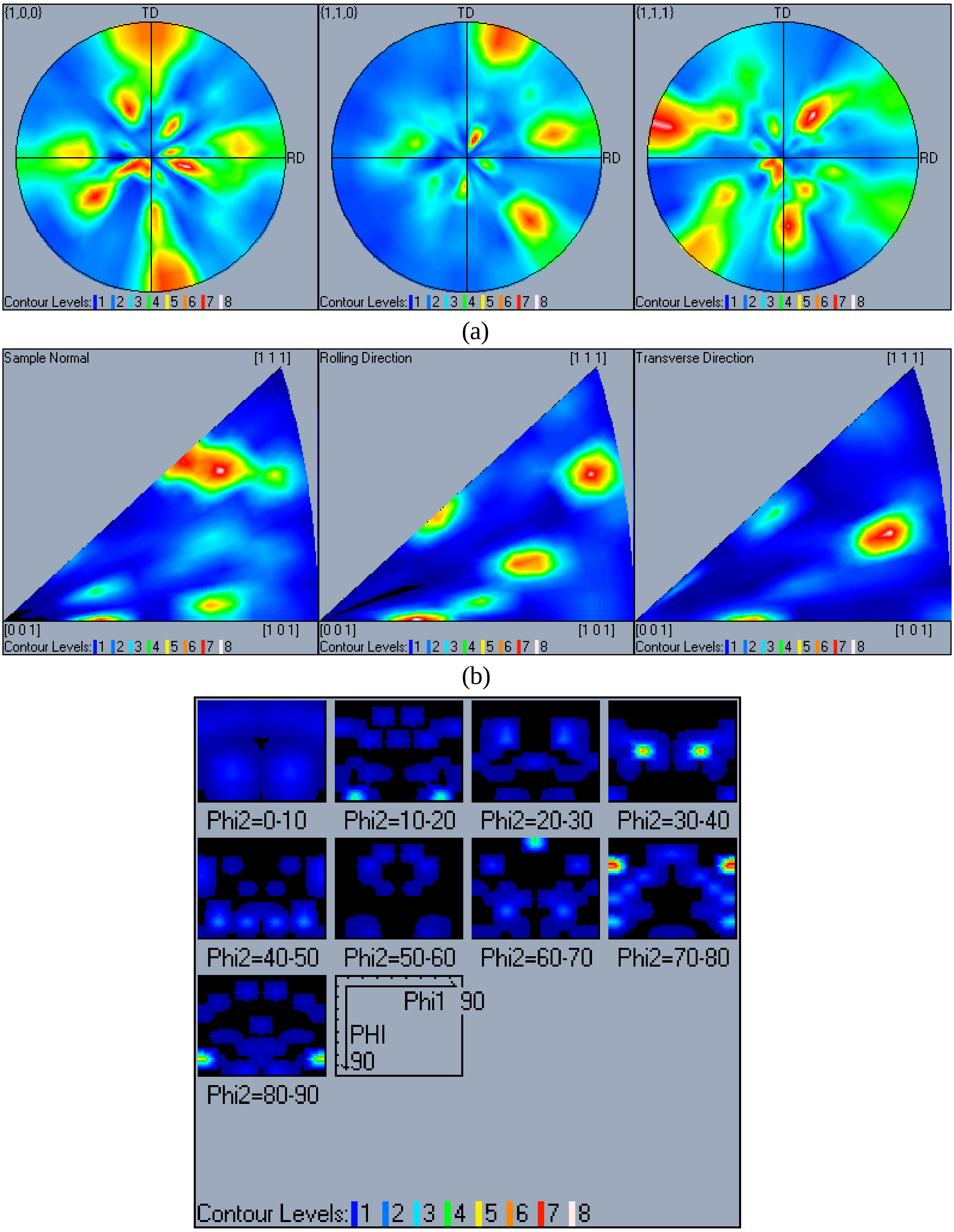

(c)

Fig. 41 (a) Pole figures, (b) inverse pole figures, and (c) ODF of the β phase in the 45° specimen loaded at 750°C and 5×10^{-4} s^{-1}.

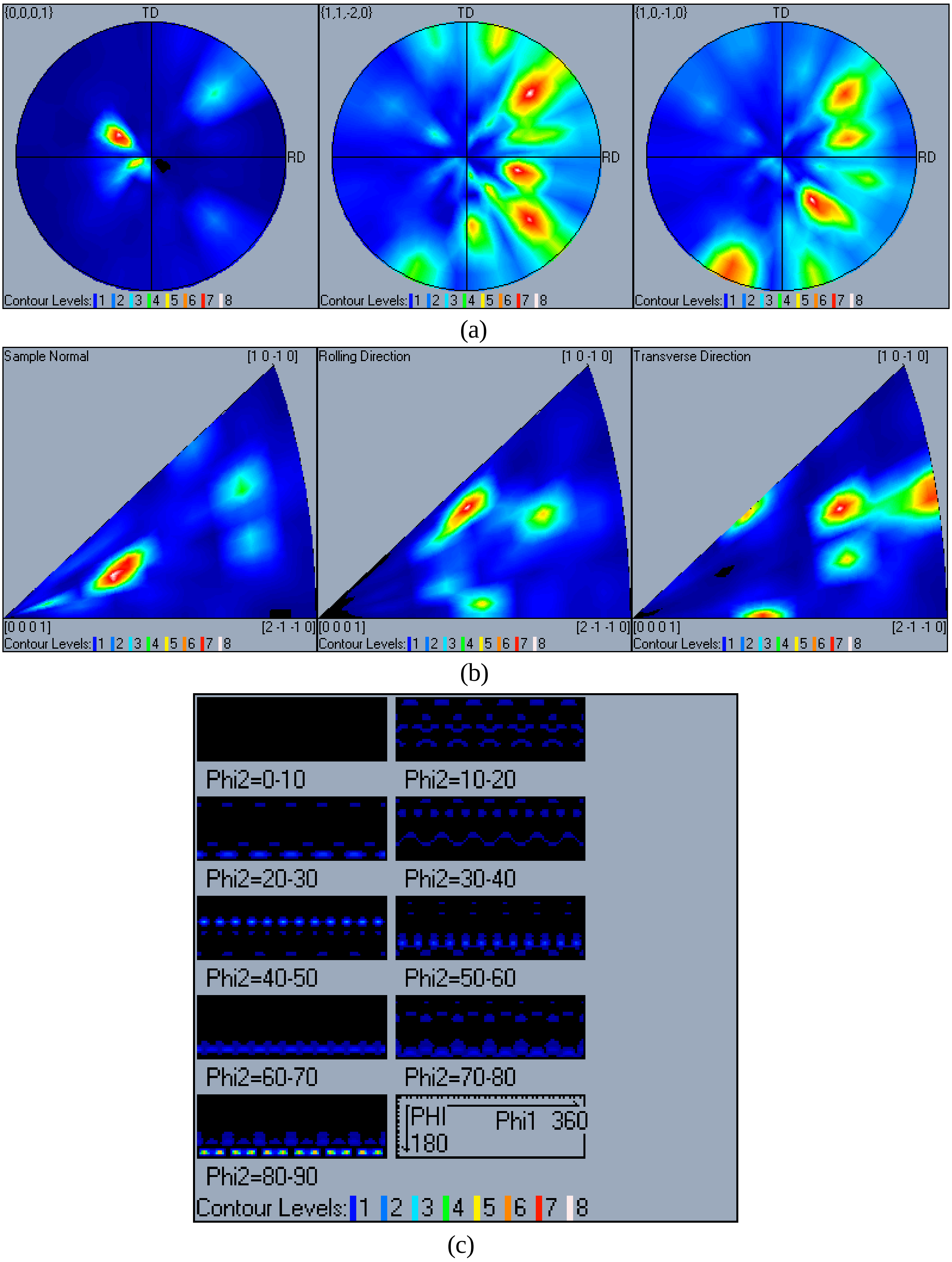

Fig. 42 (a) Pole figures, (b) inverse pole figures, and (c) ODF of the α_2 phase in the 45° specimen loaded at 750°C and $5\text{x}10^{-4}$ s^{-1}.

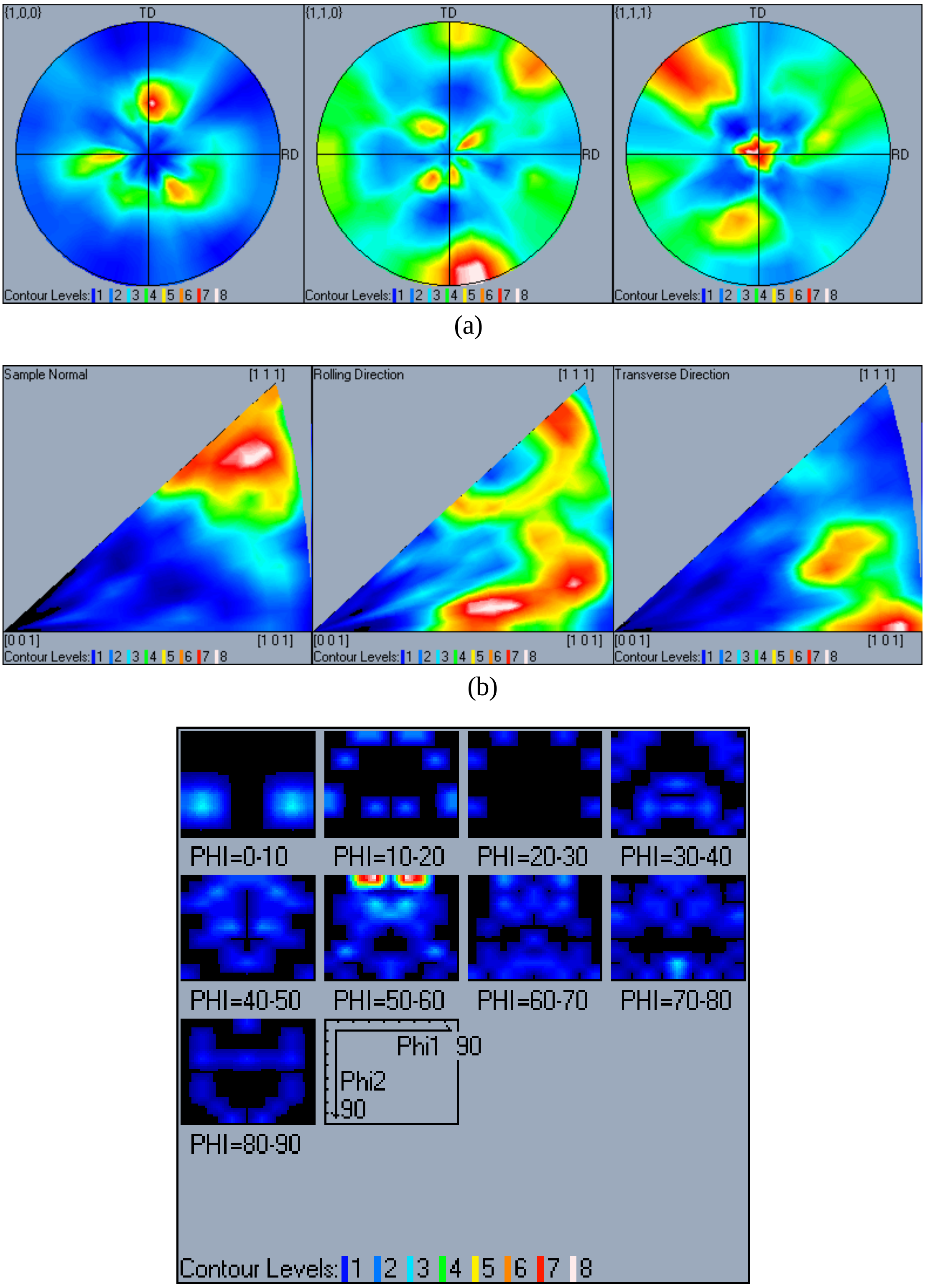

(a)

(b)

(c)

Fig. 43 (a) Pole figures, (b) inverse pole figures, and (c) ODF of the β phase in the 90° specimen loaded at 750°C and $5x10^{-4}$ s^{-1}.

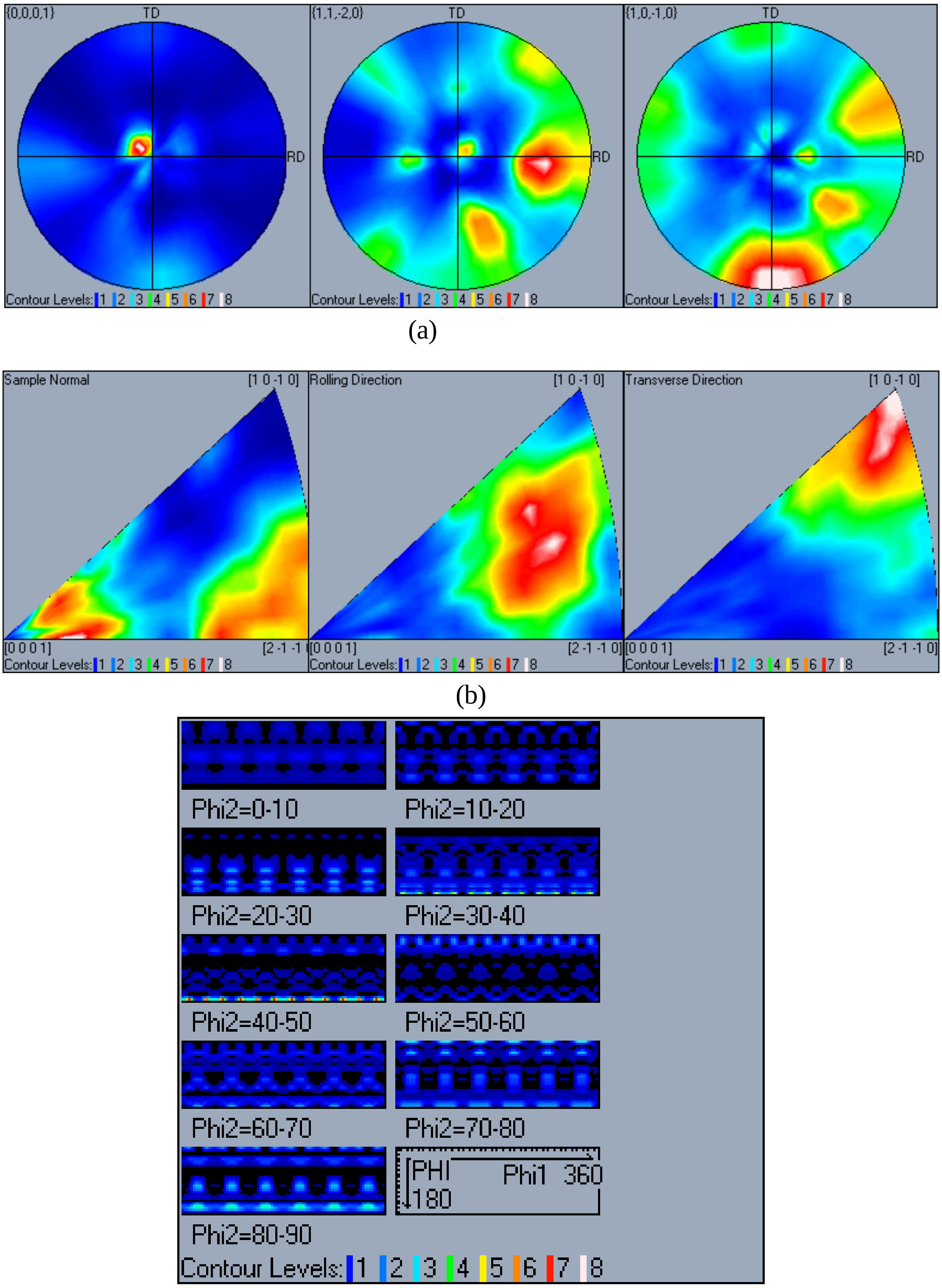

(a)

(b)

(c)

Fig. 44 (a) Pole figures, (b) inverse pole figures, and (c) ODF of the α_2 phase in the 90^o specimen loaded at 750^oC and $5x10^{-4}$ s^{-1}.

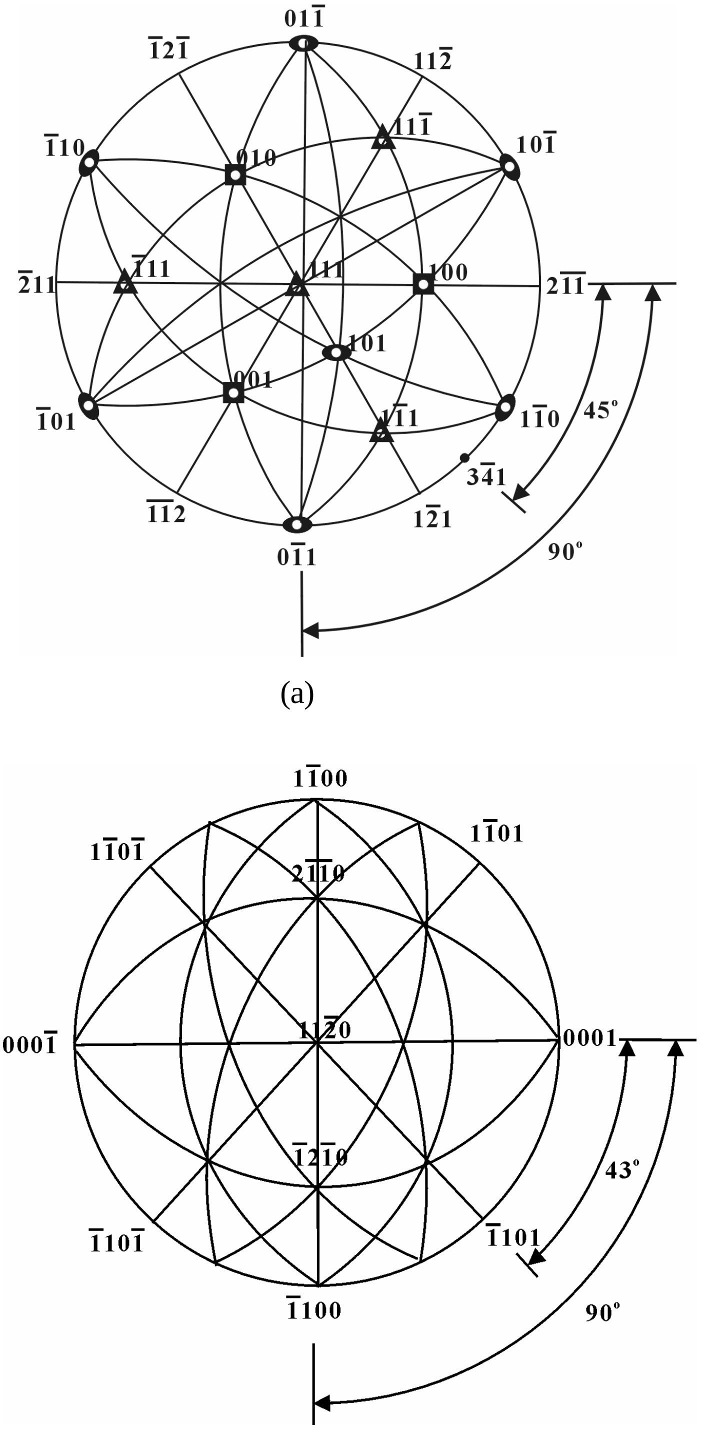

(a)

(b)

Fig. 45 (a) {111} and (b) $\{11\bar{2}0\}$ standard stereographic projections.

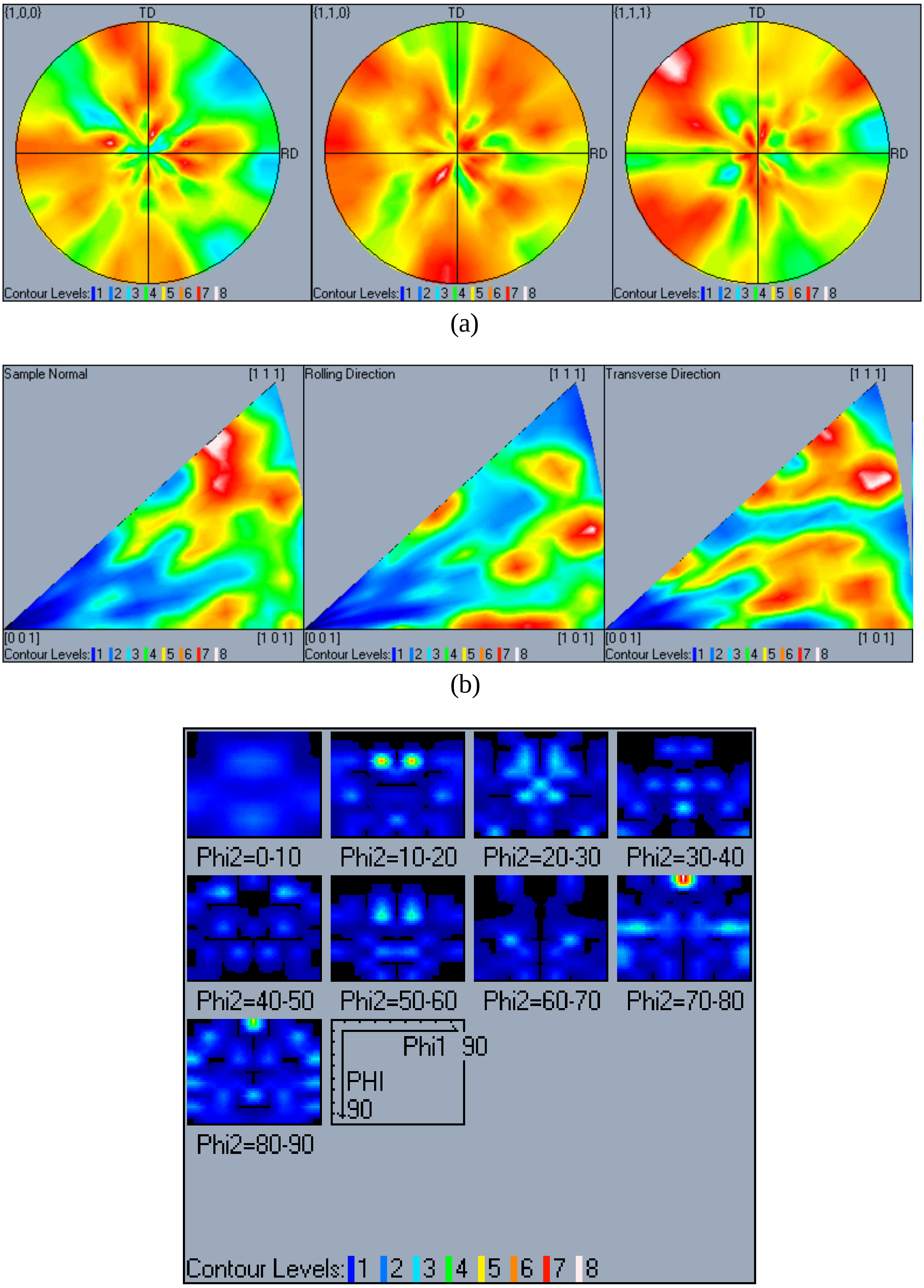

(a)

(b)

(c)

Fig. 46 (a) Pole figures, (b) inverse pole figures, and (c) ODF of the β phase in the 0° specimen loaded at 920°C and 5x10^{-4} s^{-1}.

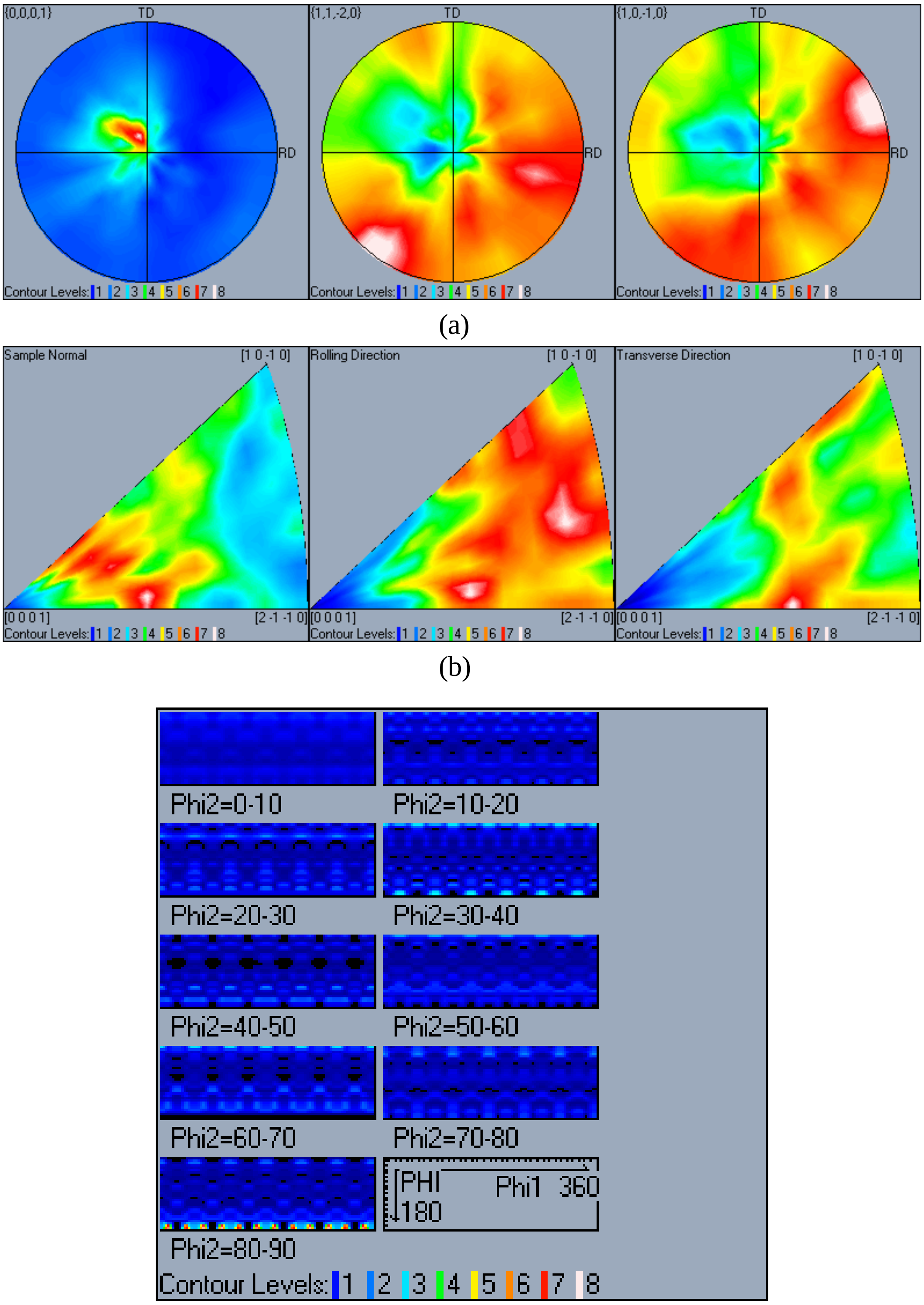

(a)

(b)

(c)

Fig. 47 (a) Pole figures, (b) inverse pole figures, and (c) ODF of the α_2 phase in the 0^o specimen loaded at 920°C and $5x10^{-4}$ s^{-1}.

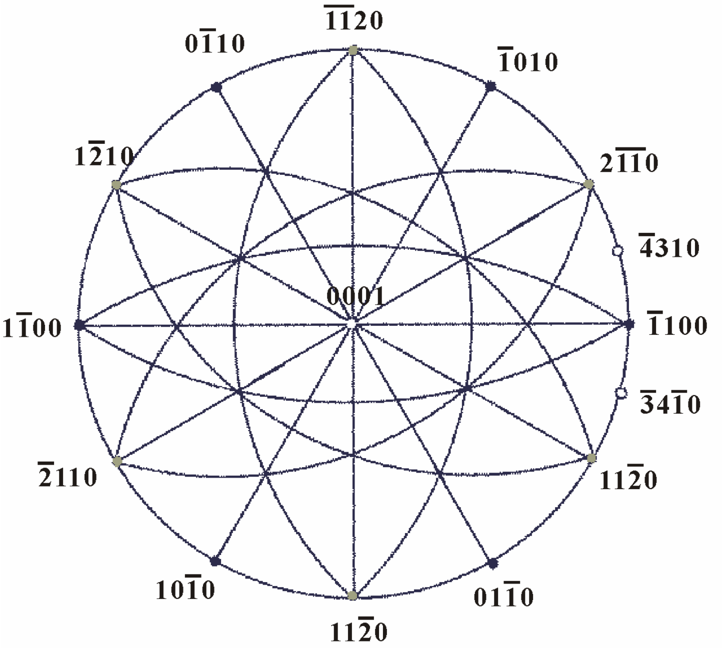

Fig. 48 Standard {0001} stereographic projection. After superplastic loading, the {0001}< $\bar{4}310$ > texture is present in the α_2 phase in the 0^o specimens loaded at 750 and 920^oC.

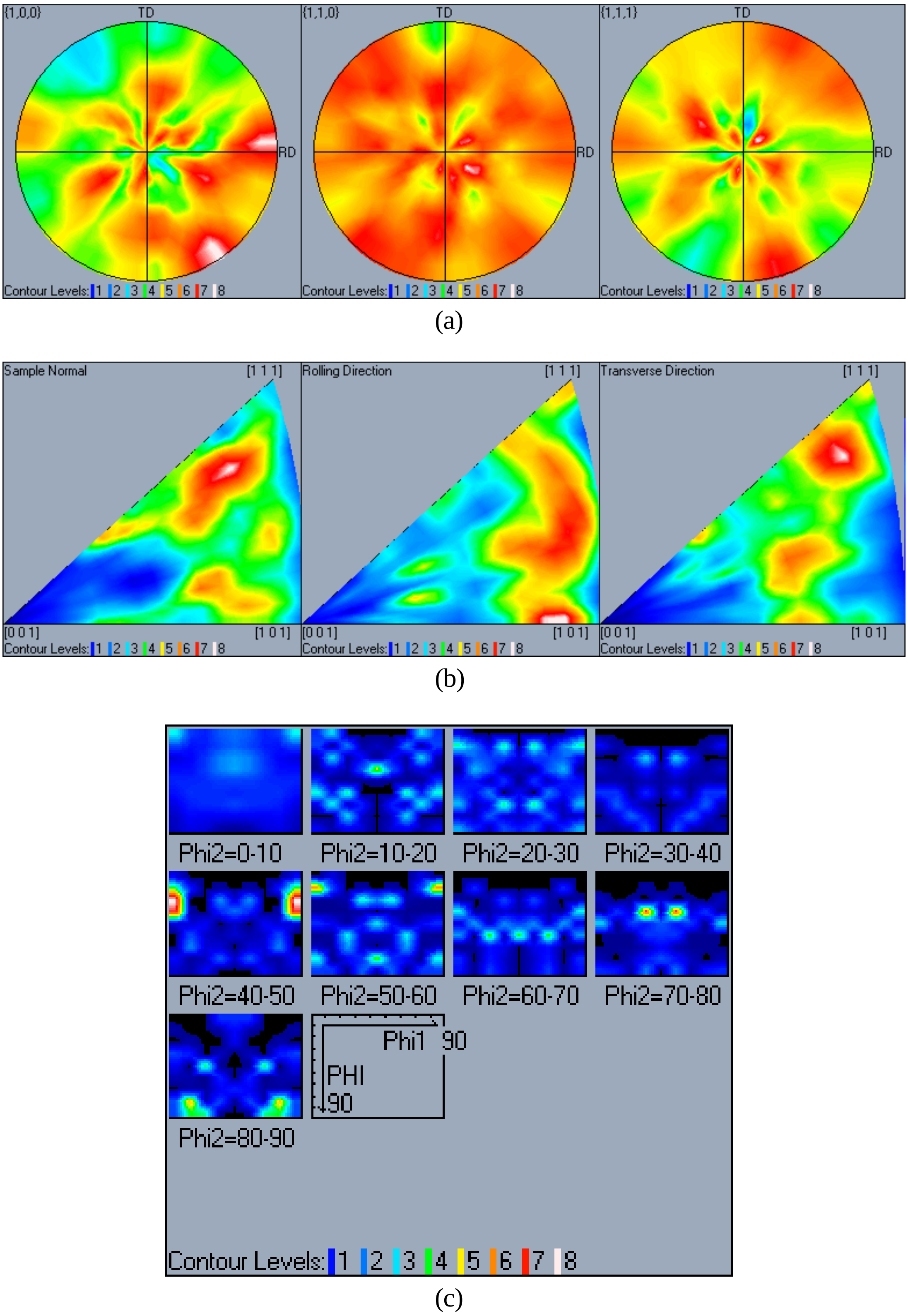

(a)

(b)

(c)

Fig. 49 (a) Pole figures, (b) inverse pole figures, and (c) ODF of the β phase in the 45° specimen loaded at 920°C and 5×10^{-4} s^{-1}.

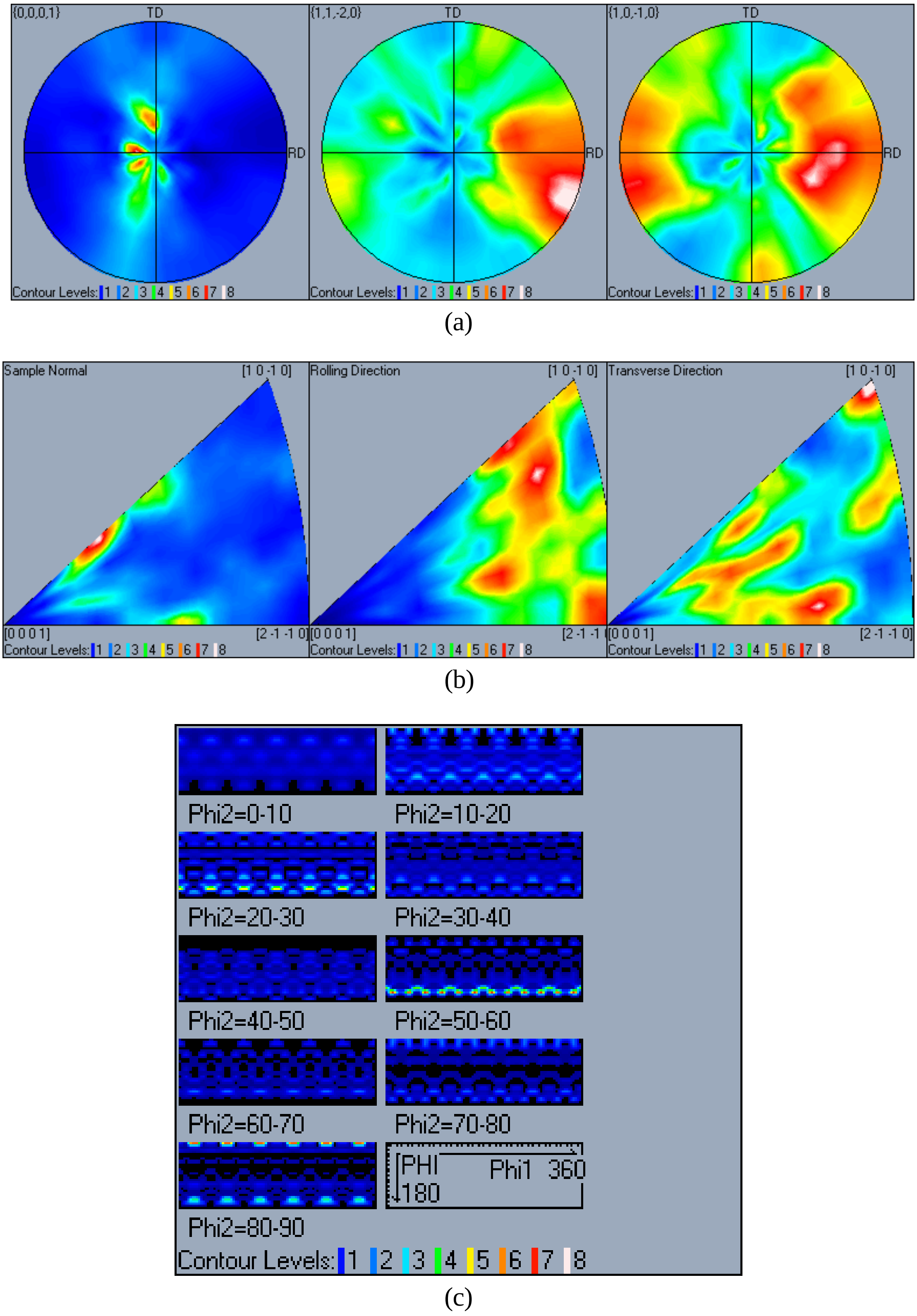

(a)

(b)

(c)

Fig. 50 (a) Pole figures, (b) inverse pole figures, and (c) ODF of the α_2 phase in the 45° specimen loaded at 920°C and 5×10^{-4} s^{-1}.

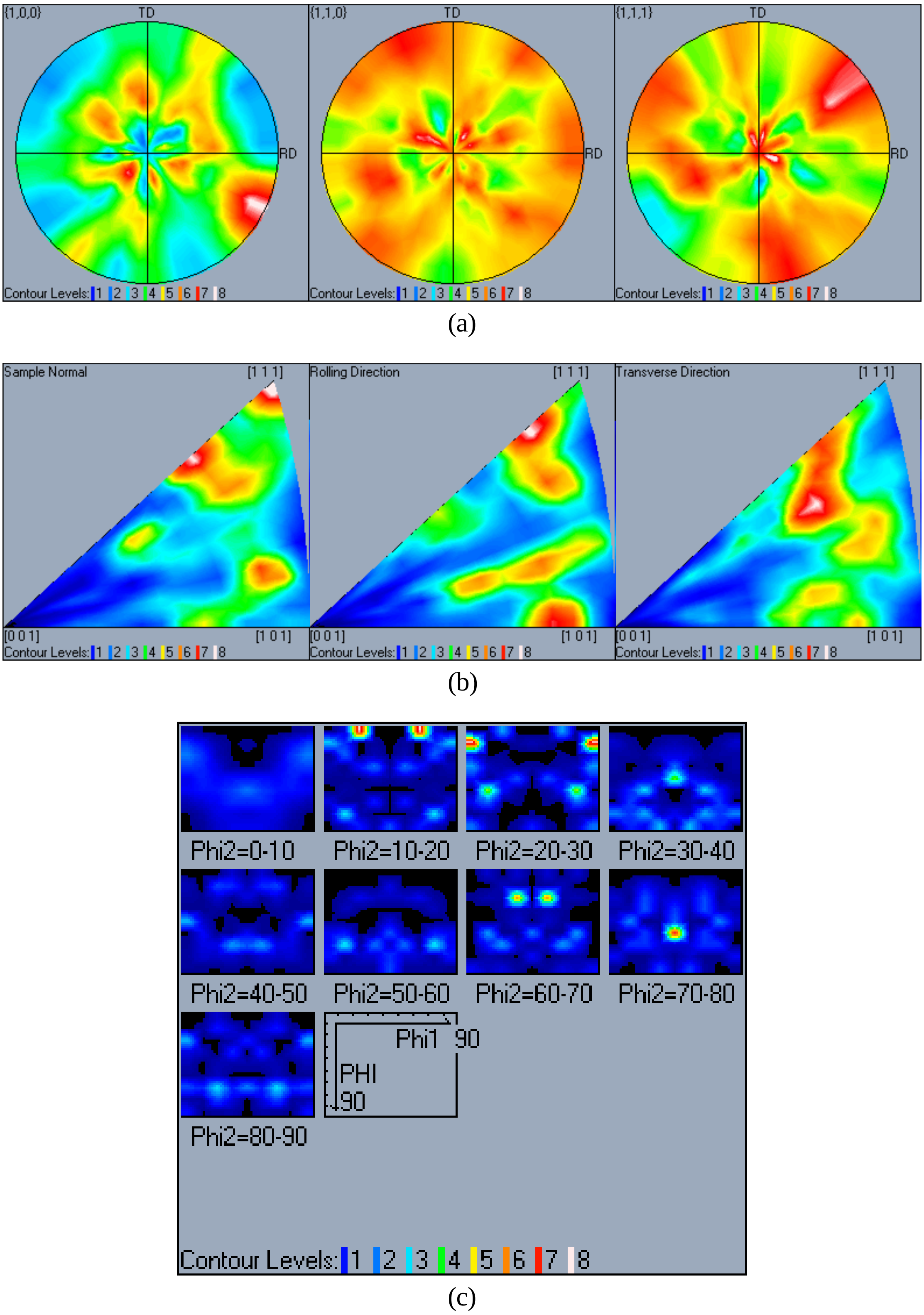

Fig. 51 (a) Pole figures, (b) inverse pole figures, and (c) ODF of the β phase in the 90° specimen loaded at 920°C and 5x10^{-4} s^{-1}.

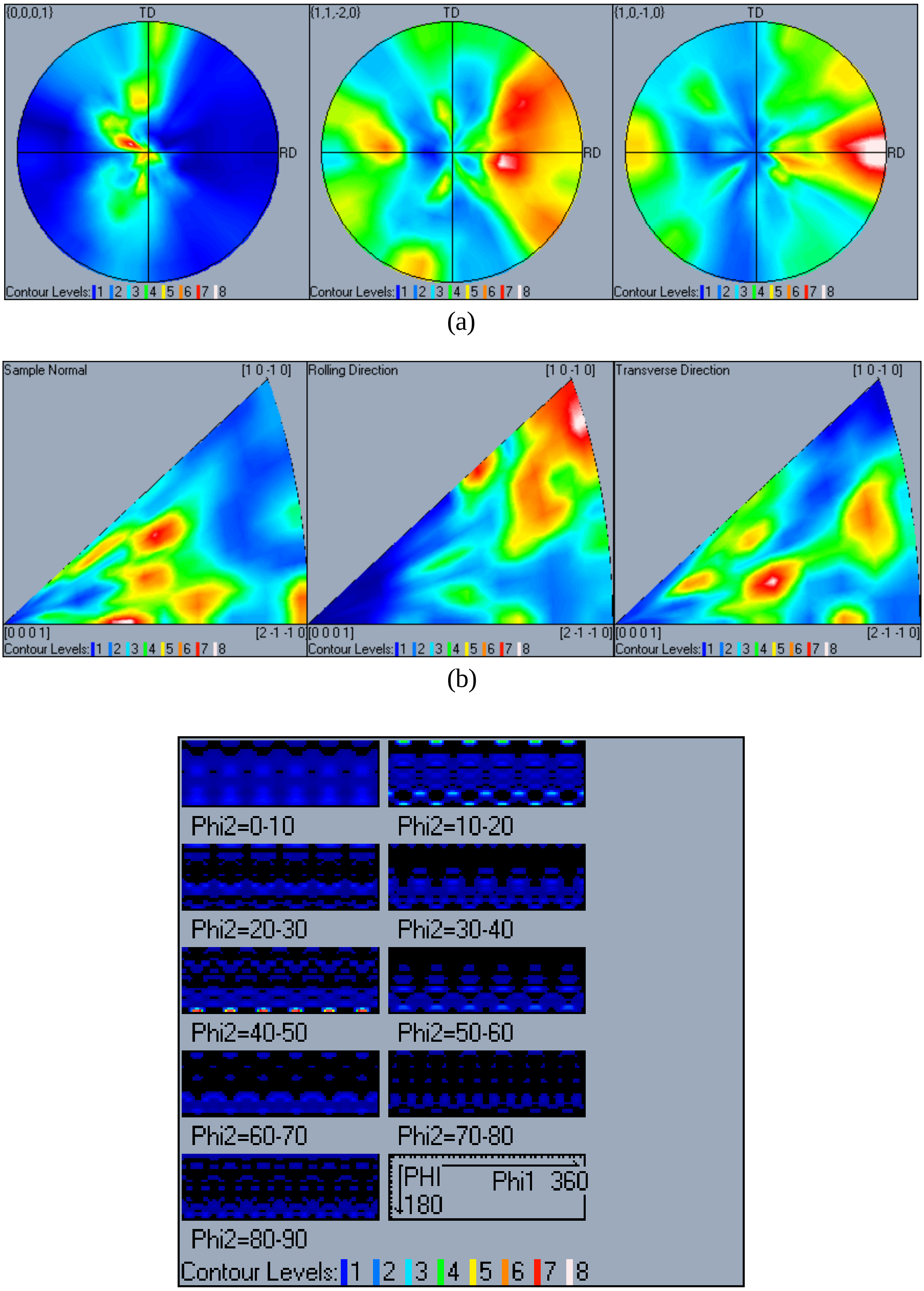

(a)

(b)

(c)

Fig. 52 (a) Pole figures, (b) inverse pole figures, and (c) ODF of the α_2 phase in the 90° specimen loaded at 920°C and $5x10^{-4}$ s^{-1}.

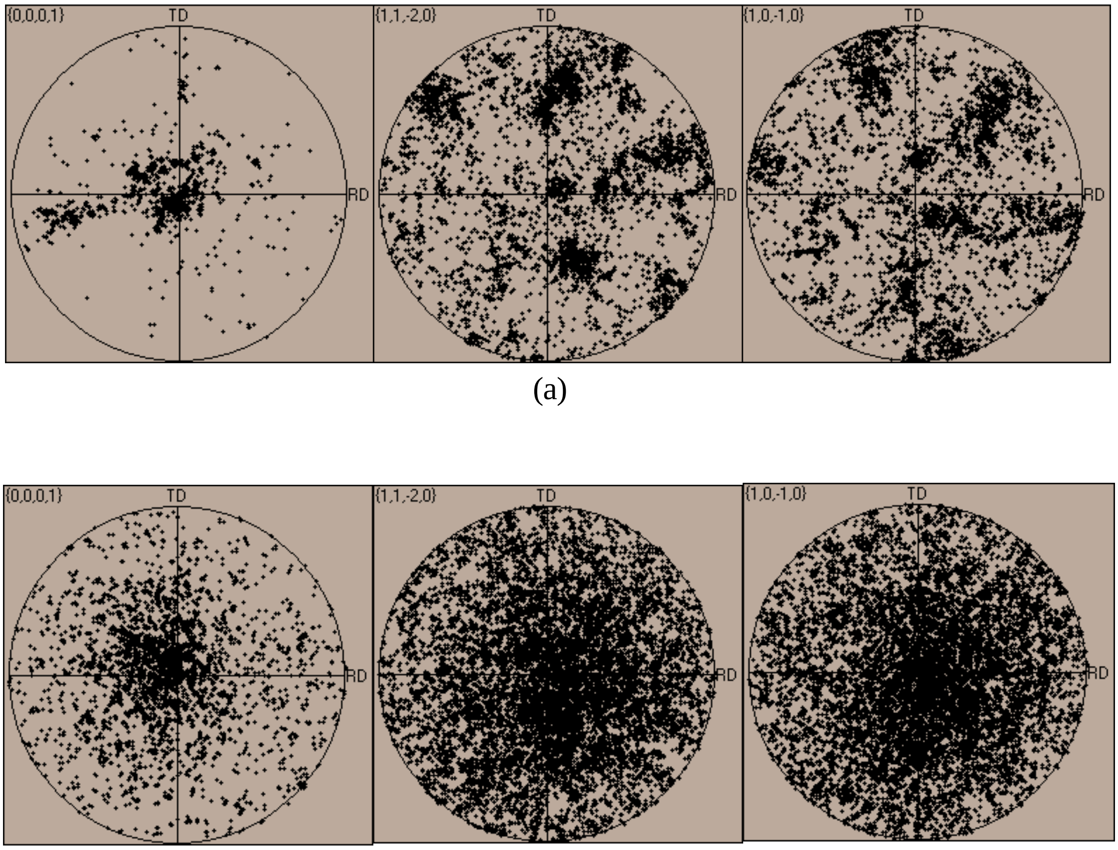

(a)

(b)

Fig. 53 Pole figures obtained from the 0^{o} specimens loaded at (a) 750^{o}C and (b) 920^{o}C. Orientation distributions become much more random at higher temperatures.

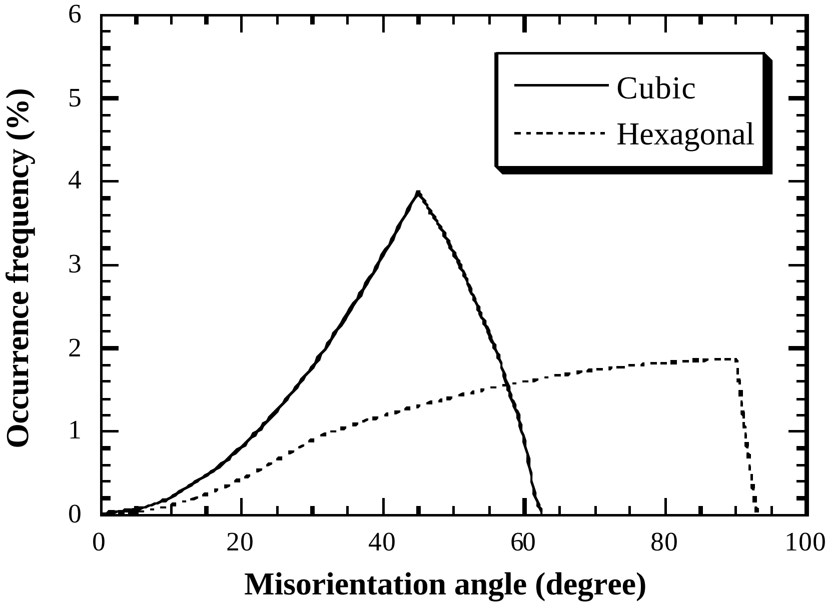

Fig. 54 The random grain misorientation distribution in the cubic and hexagonal systems. Redrawn from ref. [105,106].

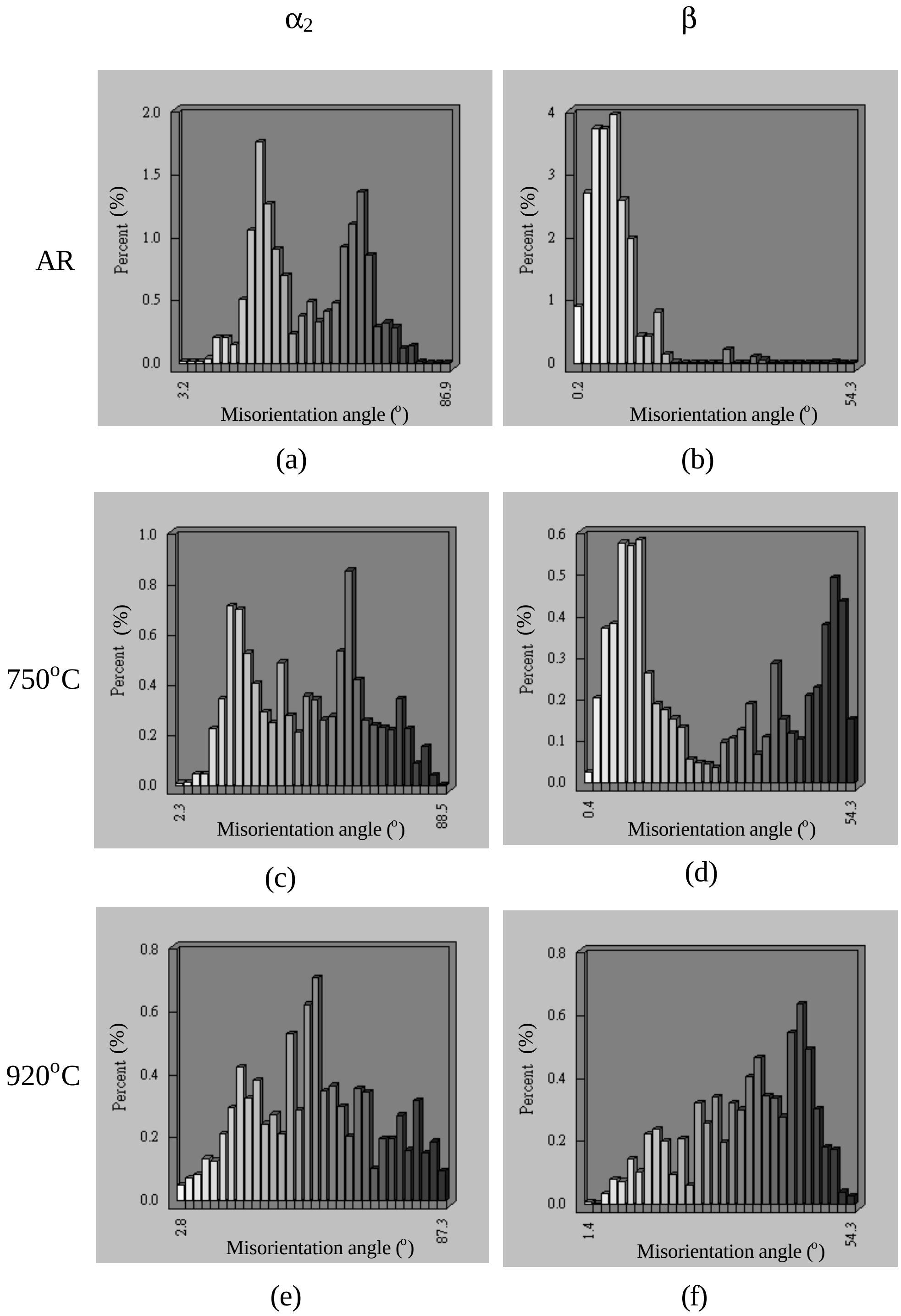

Fig. 55 Misorientation angle distributions of the (a) α_2 and (b) β phases in the AR alloy, (c) α_2 and (d) β phases in the post-SP 0° specimens at 750°C, (e) α_2 and (f) β phases in the post-SP 0° specimens at 920°C.

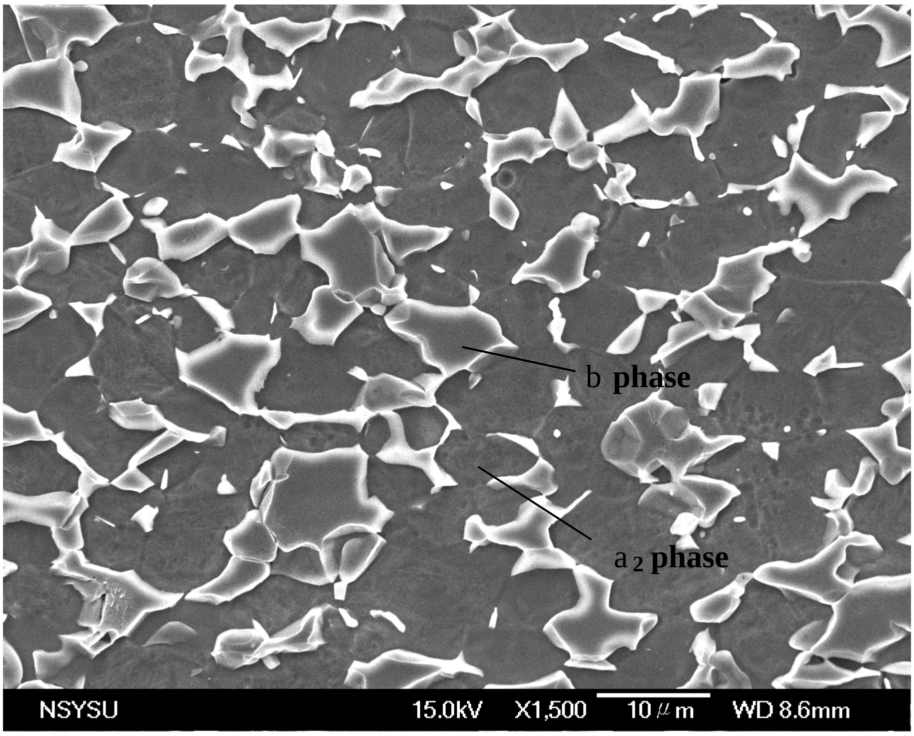

Fig. 56 SEM micrograph showing the microstructure at the fracture tip of the post-SP specimen loaded at 920^{o}C and 5x10^{-4} s^{-1}. The volume fraction of the light β phase and the darker α_2 phase are nearly 50% to 50%.

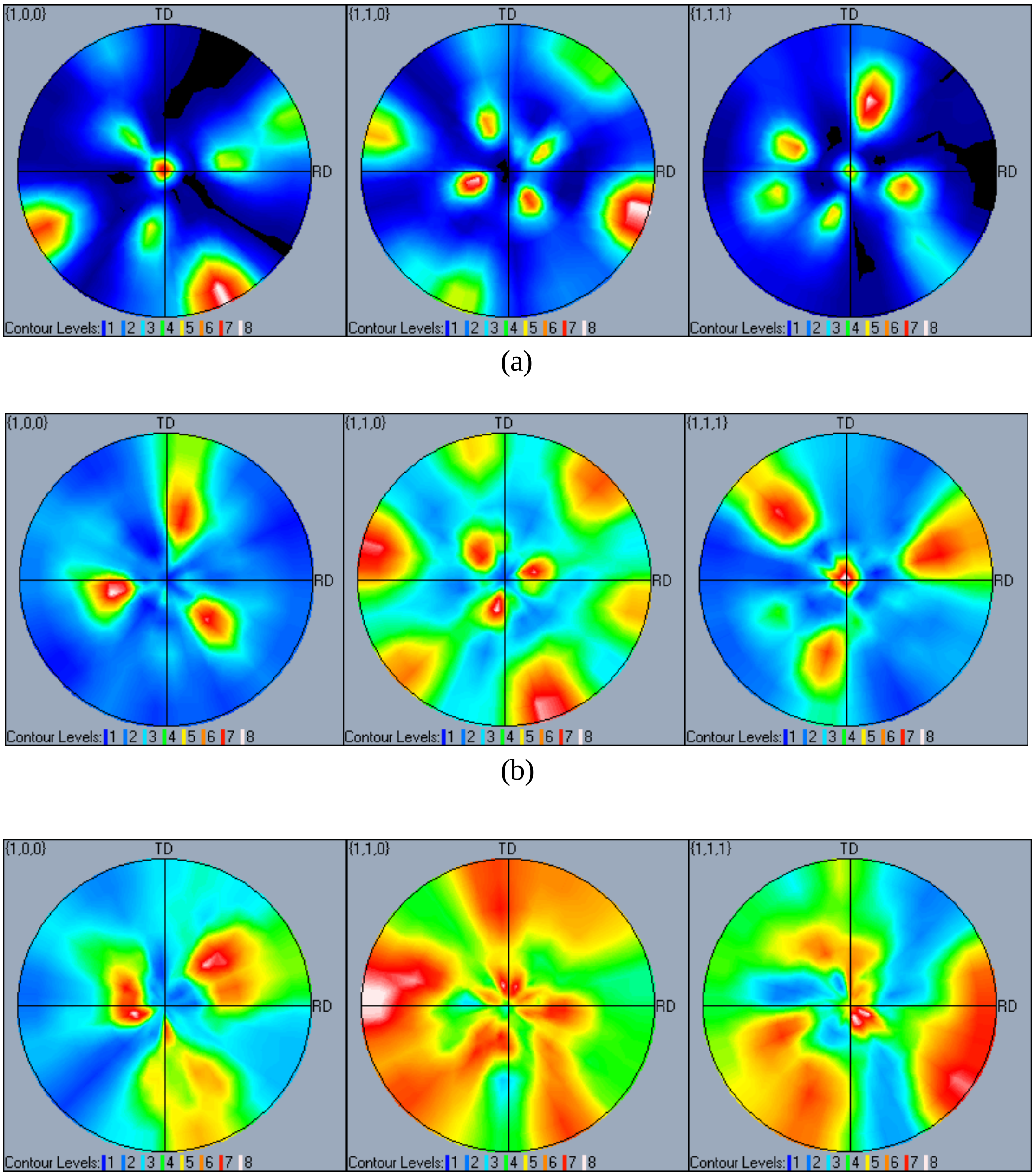

(a)

(b)

(c)

Fig. 57 Texture evolution while superplastic loading at 850°C and $5\text{x}10^{-4}$ s^{-1} to a true strain of (a) $\varepsilon=0.3$, (b) $\varepsilon=1.0$, (c) $\varepsilon=1.2$, (d) $\varepsilon=1.5$ (failure) in the β phase.

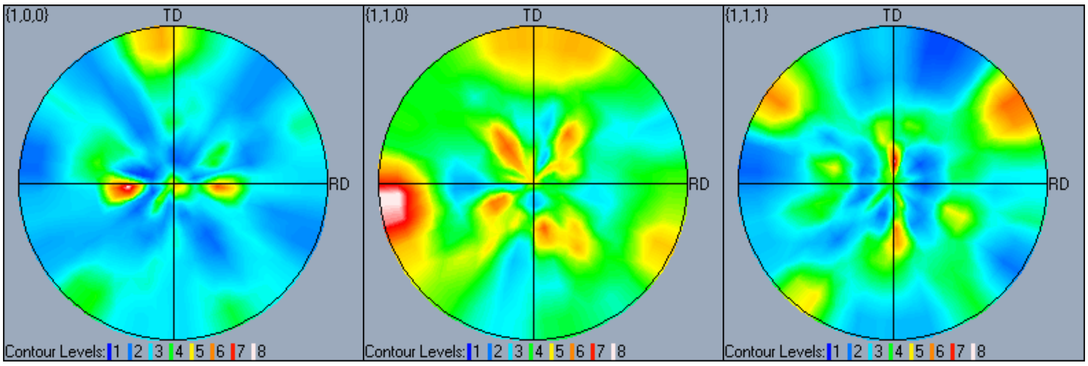
{1,0,0}
TD
RD
Contour Levels: 1 2 3 4 5 6 7 8
{1,1,0}
TD
RD
Contour Levels: 1 2 3 4 5 6 7 8
{1,1,1}
TD
RD
Contour Levels: 1 2 3 4 5 6 7 8

(d)

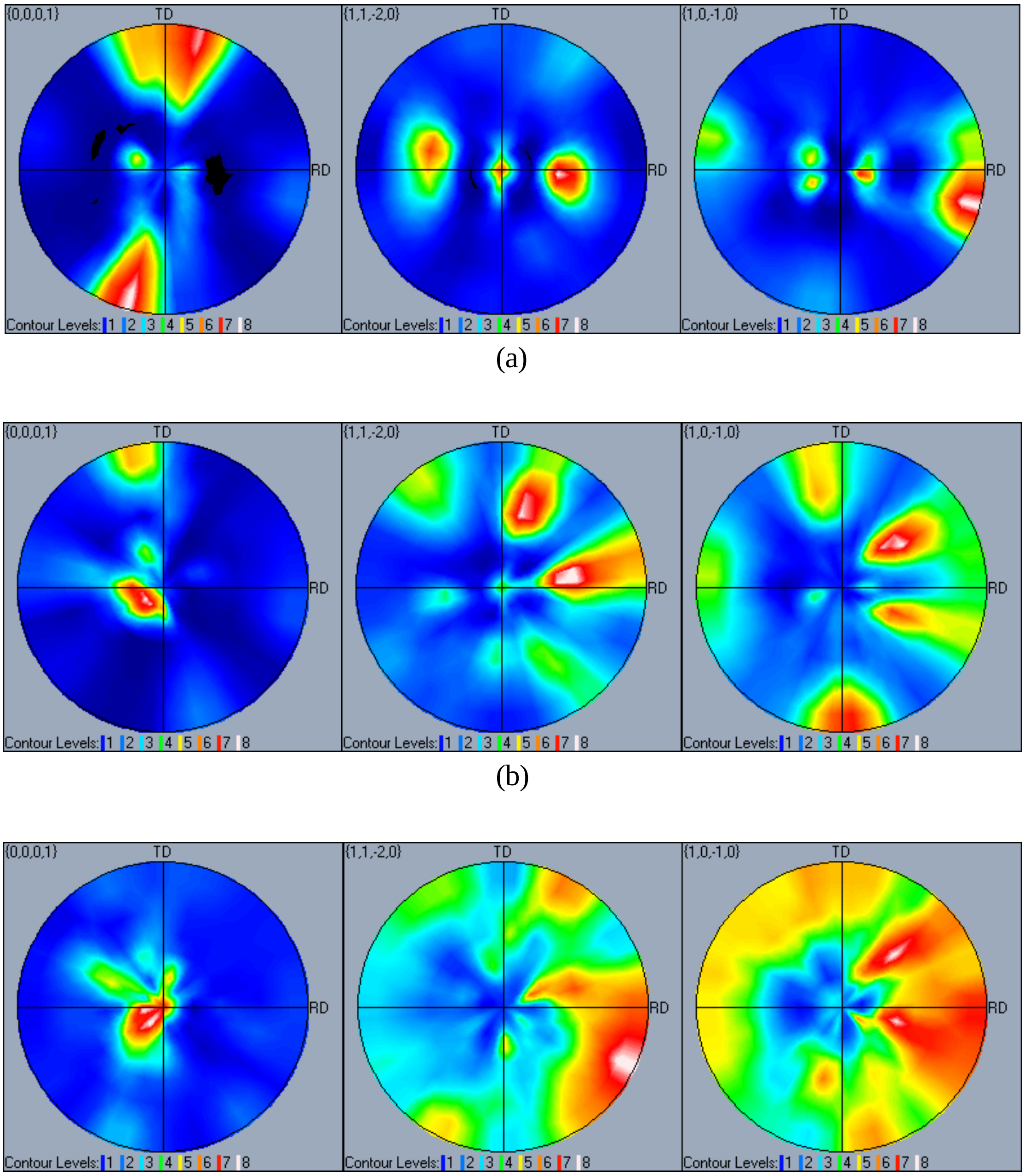

(a)

(b)

(c)

Fig. 58 Texture evolution while superplastic loading at 850^{o}C and 5x10^{-4} s^{-1} to a true strain of (a) ε=0.3, (b) ε=1.0, (c) ε=1.2, (d) ε=1.5 (failure) in the α_2 phase.

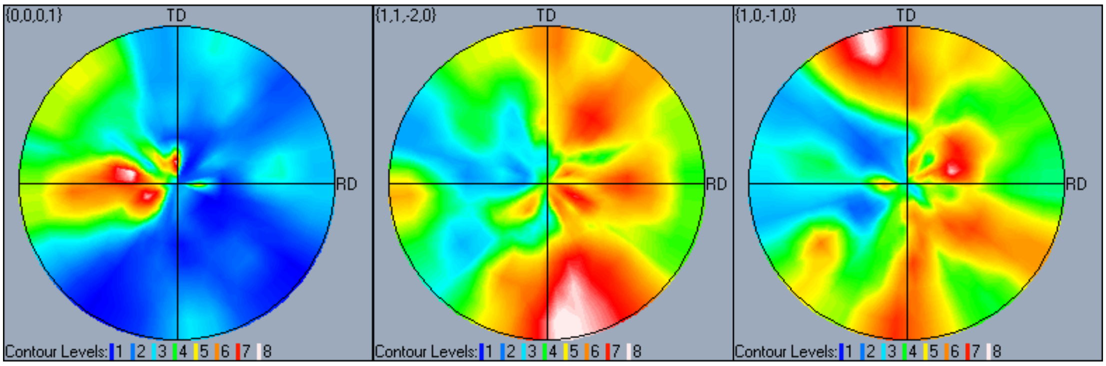
{0,0,0,1}
TD
RD
Contour Levels: 1 2 3 4 5 6 7 8
{1,1,-2,0}
TD
RD
Contour Levels: 1 2 3 4 5 6 7 8
{1,0,-1,0}
TD
RD
Contour Levels: 1 2 3 4 5 6 7 8

(d)

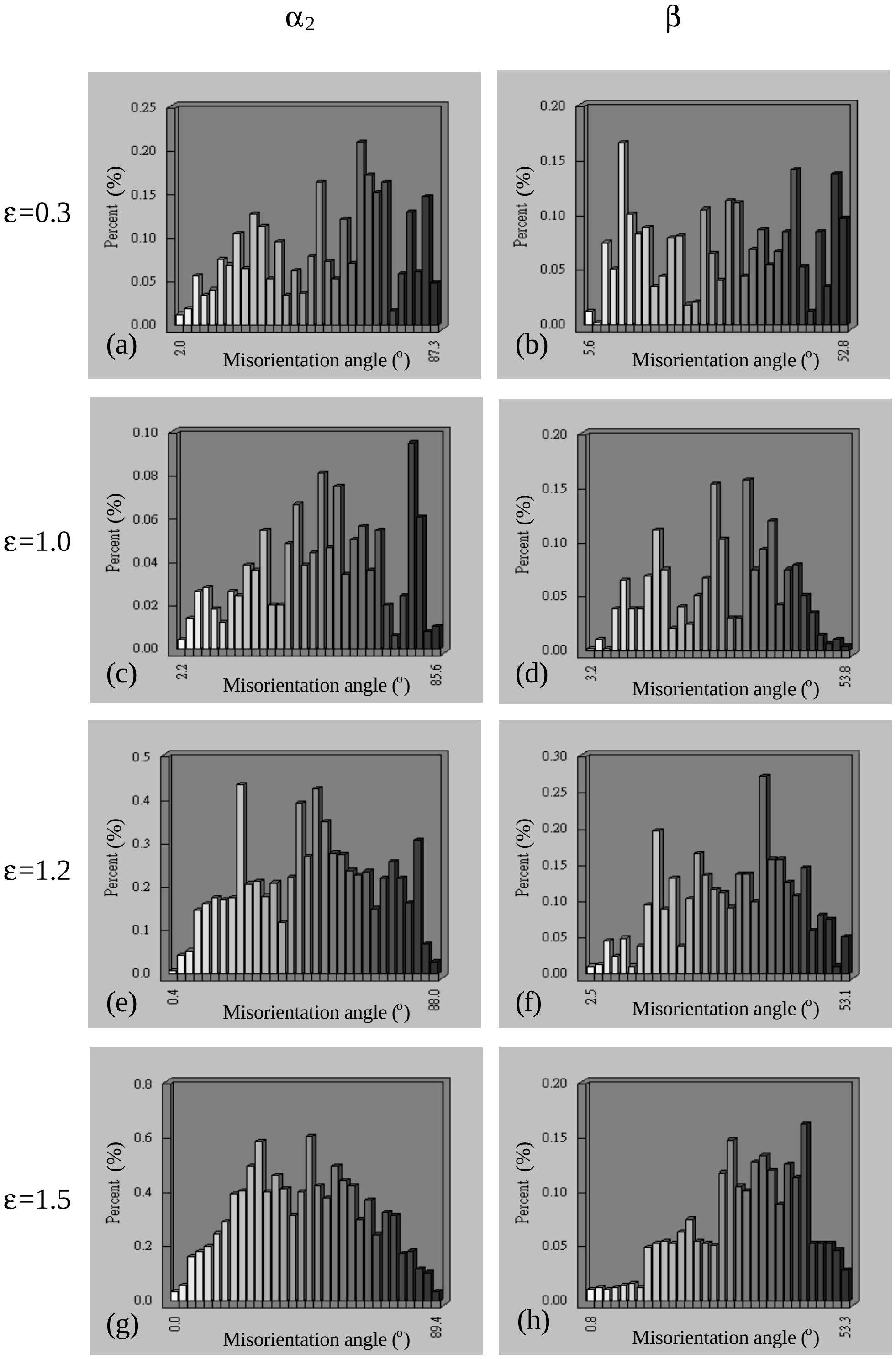

Fig. 59 Misorientation angle distribution of the α_2 and β phases at various true strain locations with ε~0.3, 1.0, 1.2 and 1.5 in the post-SP 0° specimen performed at 850°C and $5\text{x}10^{-4}$ s^{-1}: (a) ε=0.3, α_2 phase, (b) ε=0.3, β phase, (c) ε=1.0, α_2 phase, (d) ε=1.0, β phase, (e) ε=1.2, α_2 phase, and (f) ε=1.2, β phase, (g) ε=1.5, α_2 phase, and (h) ε=1.5, β phase.

(a)

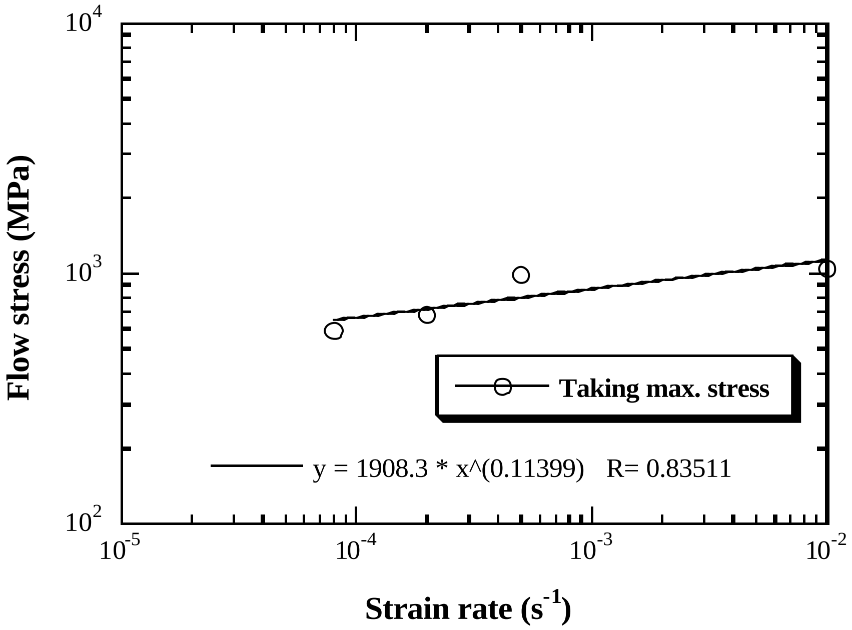

(b)

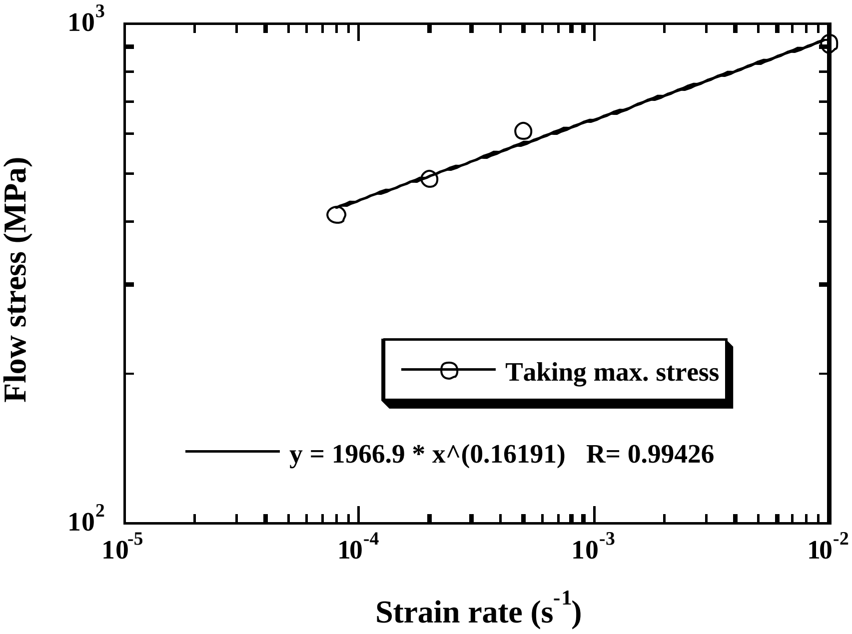

Fig. 60 The dependence of the flow stress versus the strain rate for (a) 700, (b) 750, (c) 800, and (d) 850°C, from the slope the m_a-value can be extracted.

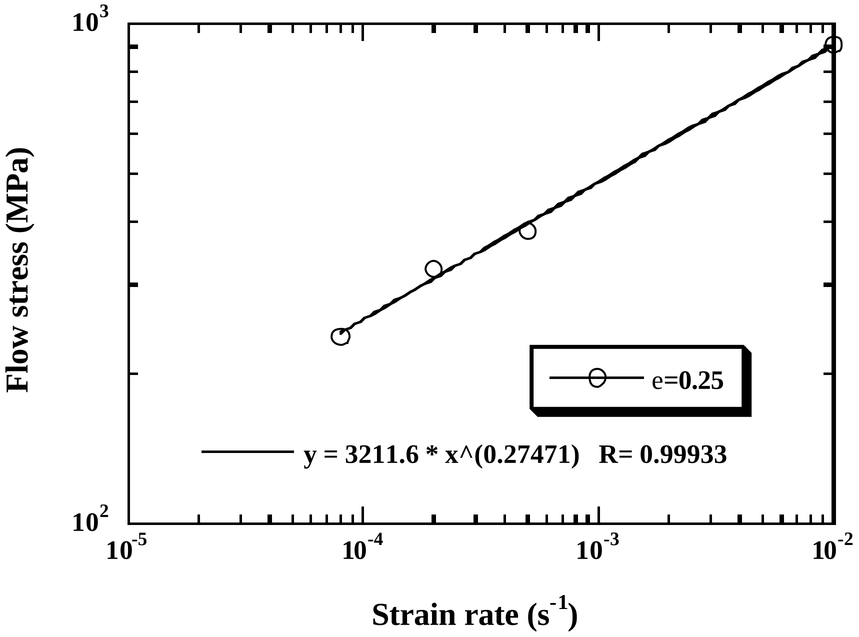
Flow stress (MPa)
10^3
10^2
10^{-5}
10^{-4}
10^{-3}
10^{-2}
Strain rate (s^{-1})
e=0.25
y = 3211.6 * x^(0.27471)   R= 0.99933

(c)

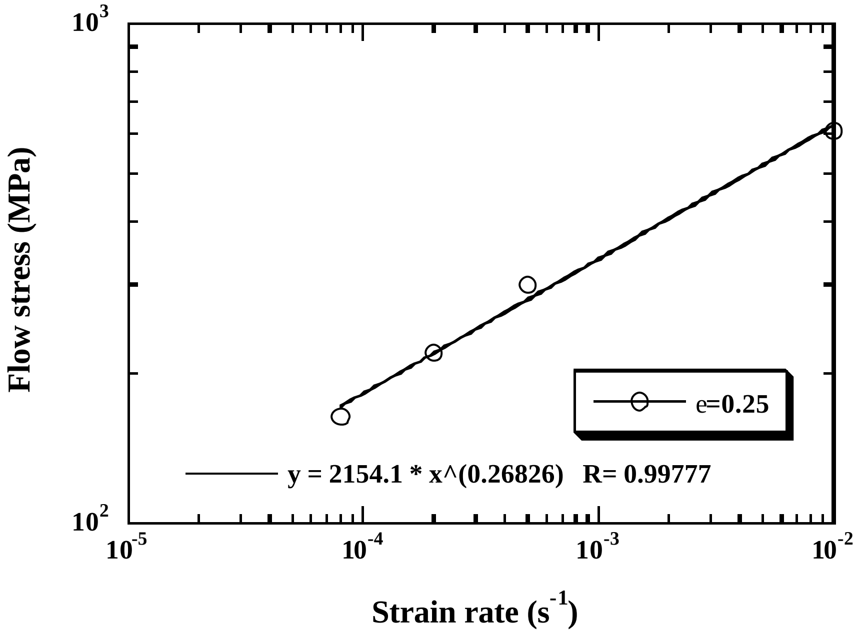
Flow stress (MPa)
10^3
10^2
10^{-5}
10^{-4}
10^{-3}
10^{-2}
Strain rate (s^{-1})
e=0.25
y = 2154.1 * x^(0.26826)   R= 0.99777

(d)

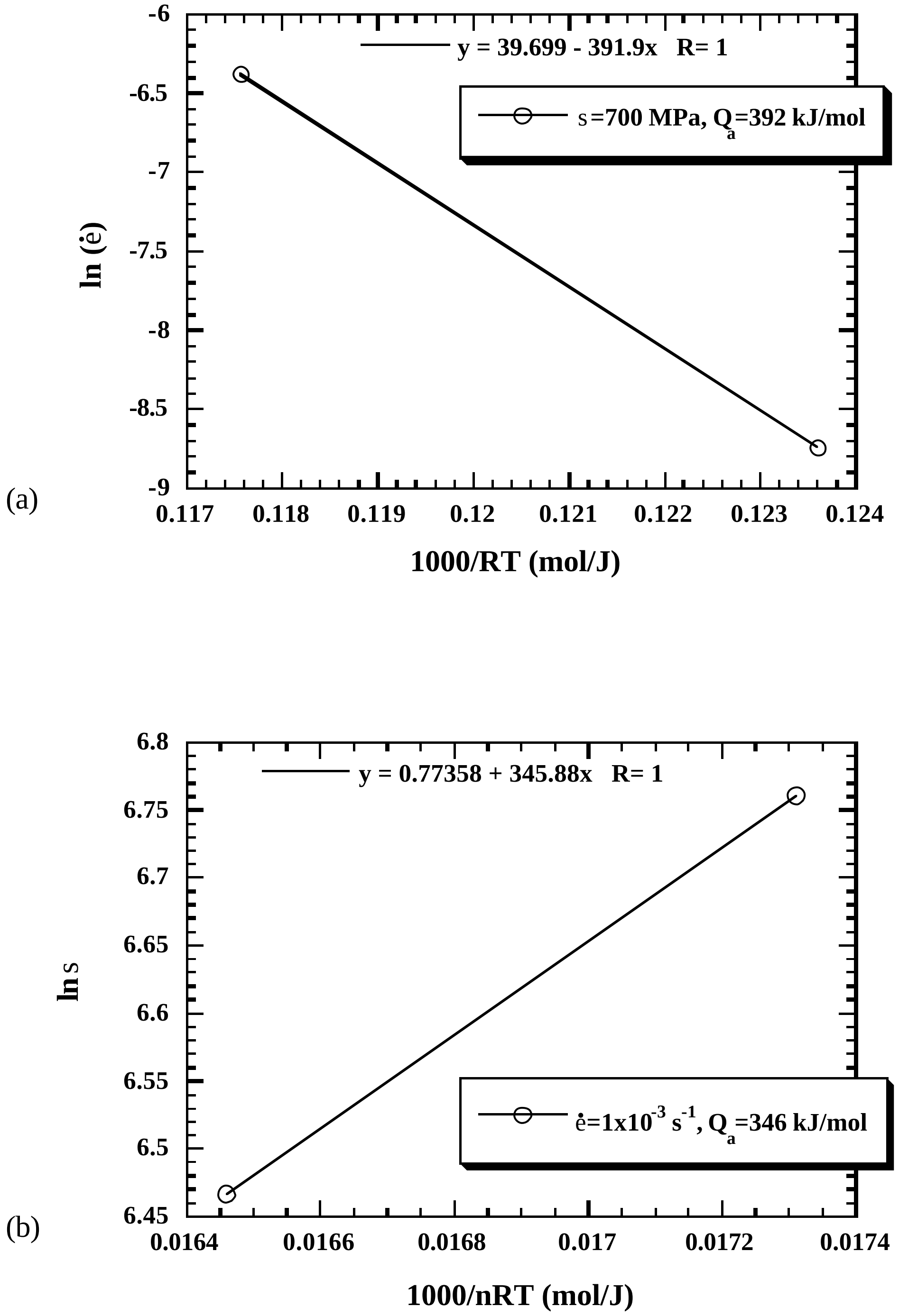

Fig. 61 Dependence on (1/T) for (a) ln ($\dot{e}$) under a fixed stress condition, and (b) ln (σ) under a fixed strain condition for 700-750^{o}C. From the slope, the apparent activation energy can be extracted.

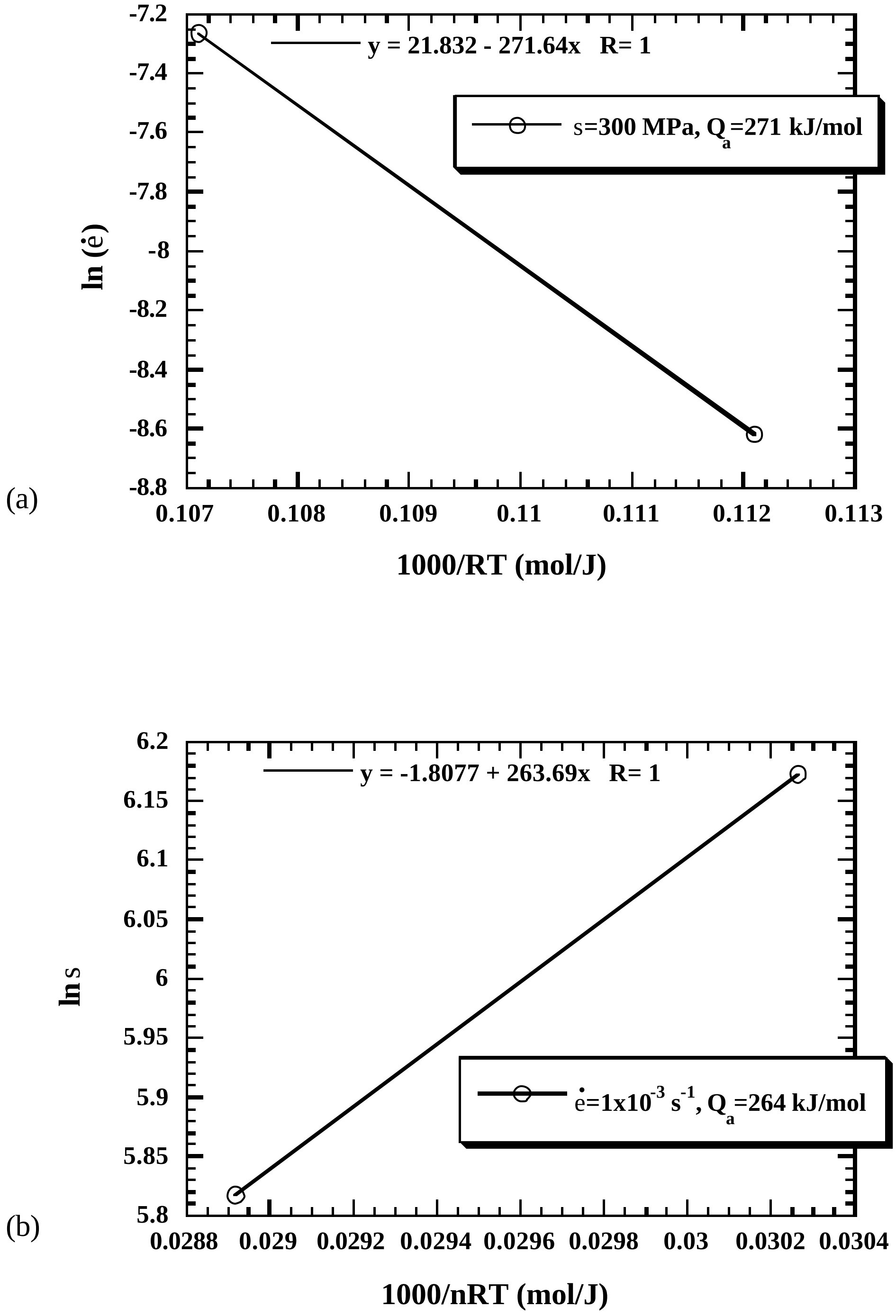

Fig. 62 Dependence on (1/T) for (a) ln ($\dot{e}$) under a fixed stress condition, and (b) ln (σ) under a fixed strain condition for 800-850°C. From the slope, the apparent activation energy can be extracted

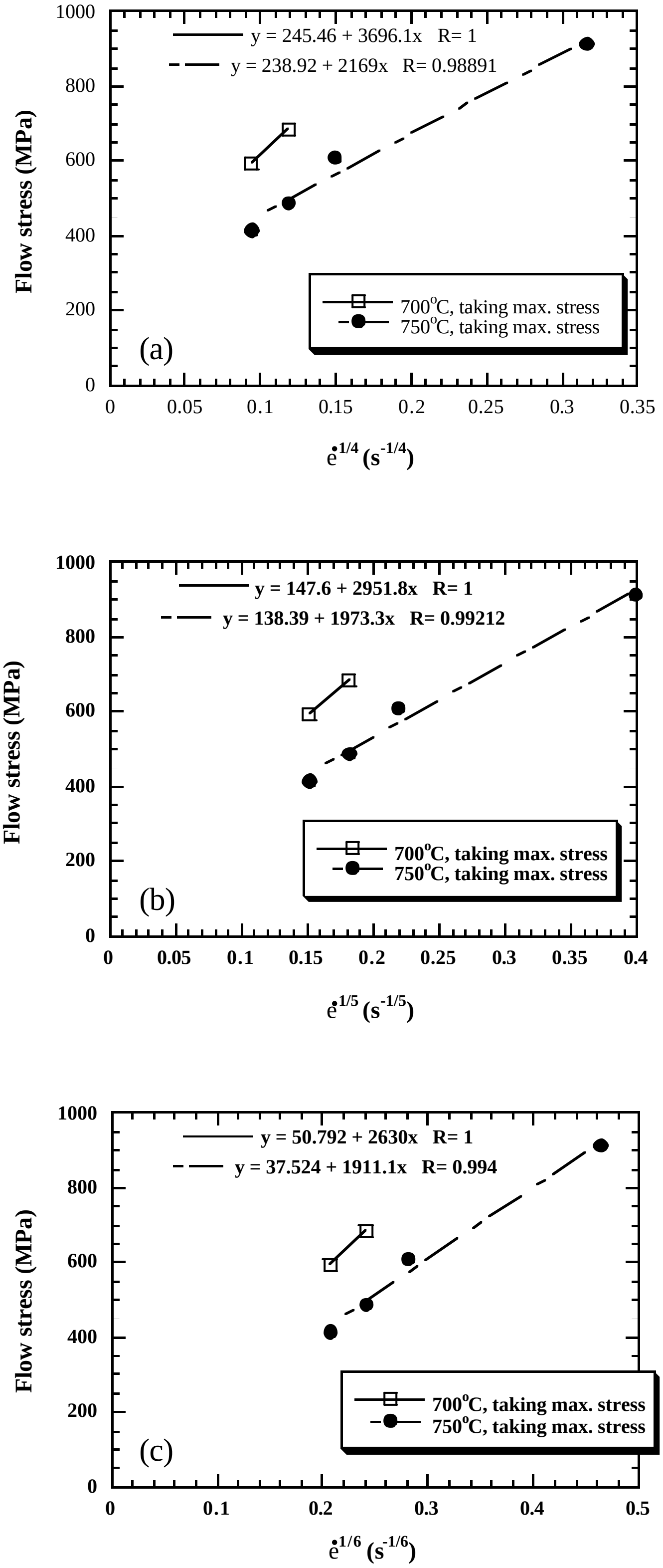

Fig. 63 The plot for extracting the threshold stress σ_{th} at 700-750°C by substituting n_t=4, 5, and 6.

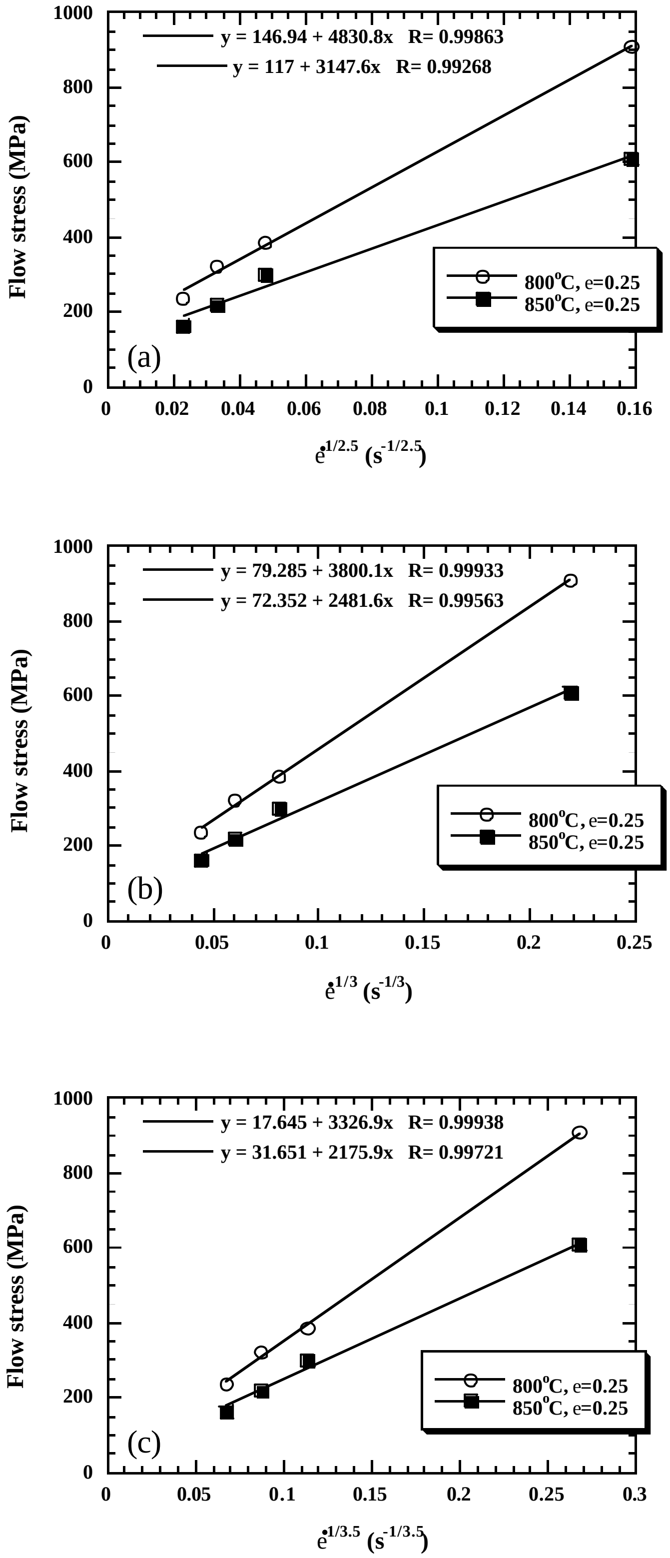

Fig. 64 The plot for extracting the threshold stress σ_{th} at 800-850°C by substituting n_t=2.5, 3, and 3.5.

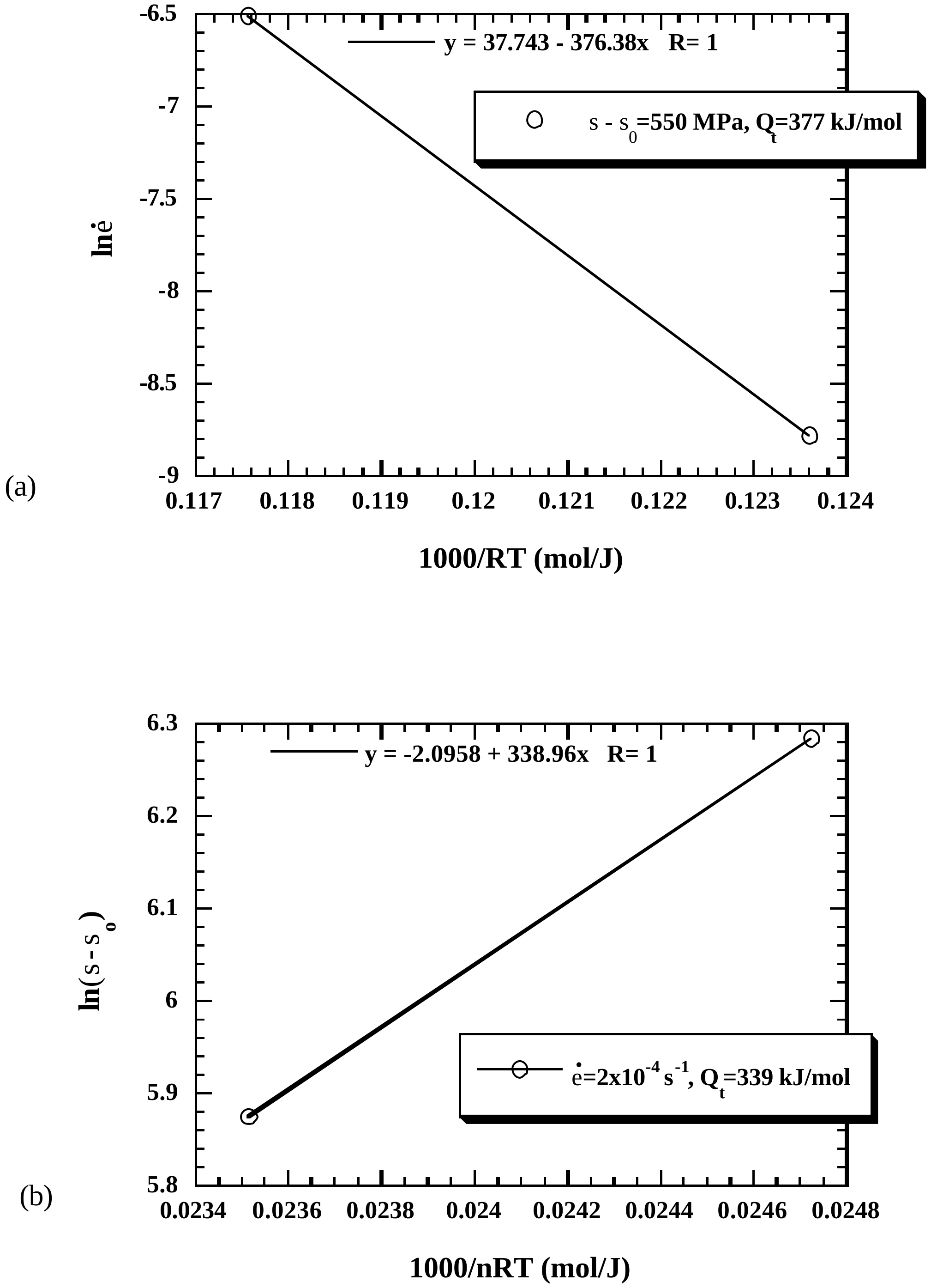

Fig. 65 Dependence on (1/T) for (a) ln ($\dot{e}$) under a fixed stress condition, and (b) ln ($\sigma-\sigma_0$) under a fixed strain condition for 700-750^{o}C. From the slope, the apparent activation energy can be extracted.

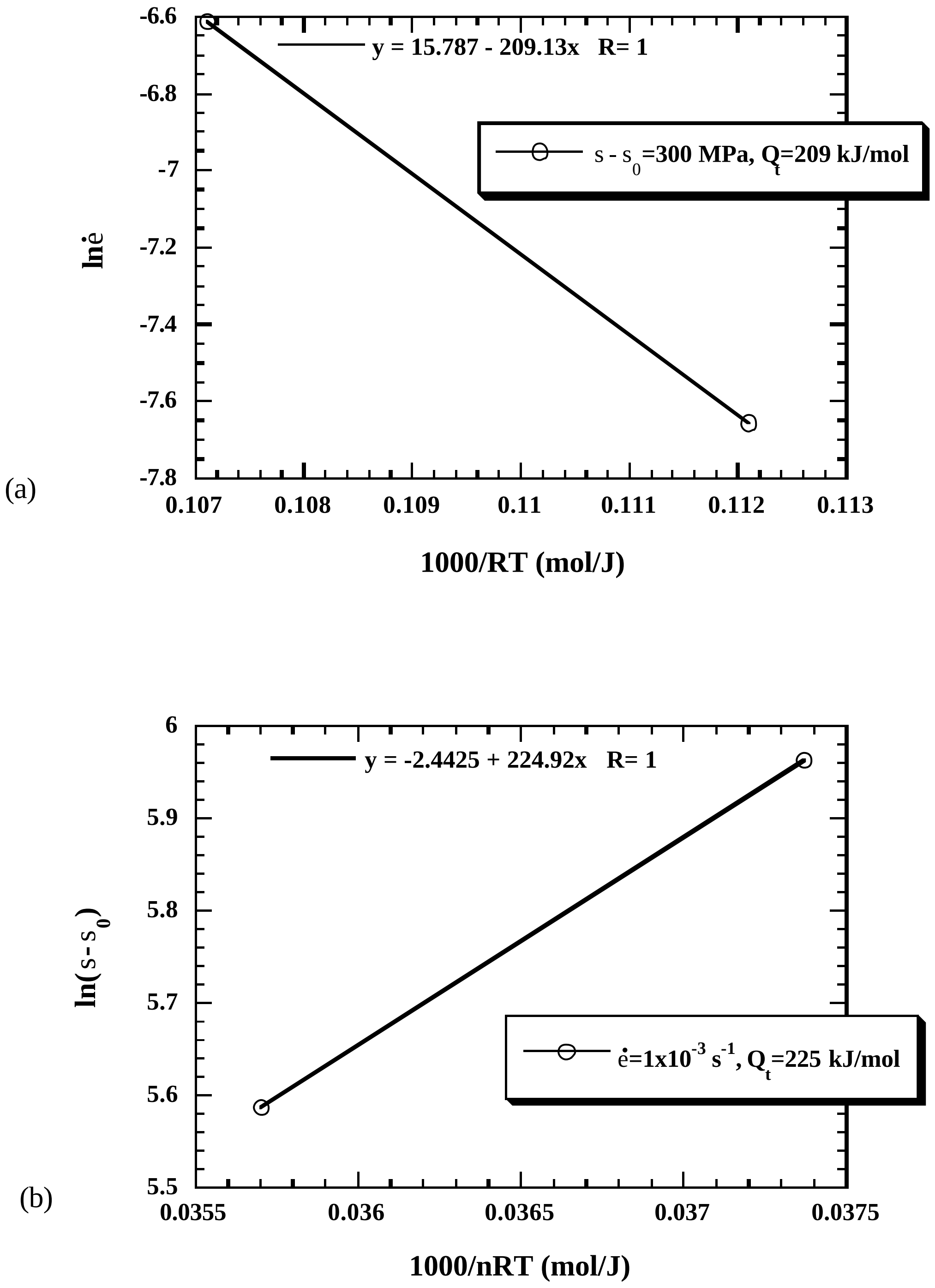

Fig. 66 Dependence on (1/T) for (a) ln ($\dot{e}$) under a fixed stress condition, and (b) ln ($\sigma - \sigma_0$) under a fixed strain condition for 800-850°C. From the slope, the apparent activation energy can be extracted.

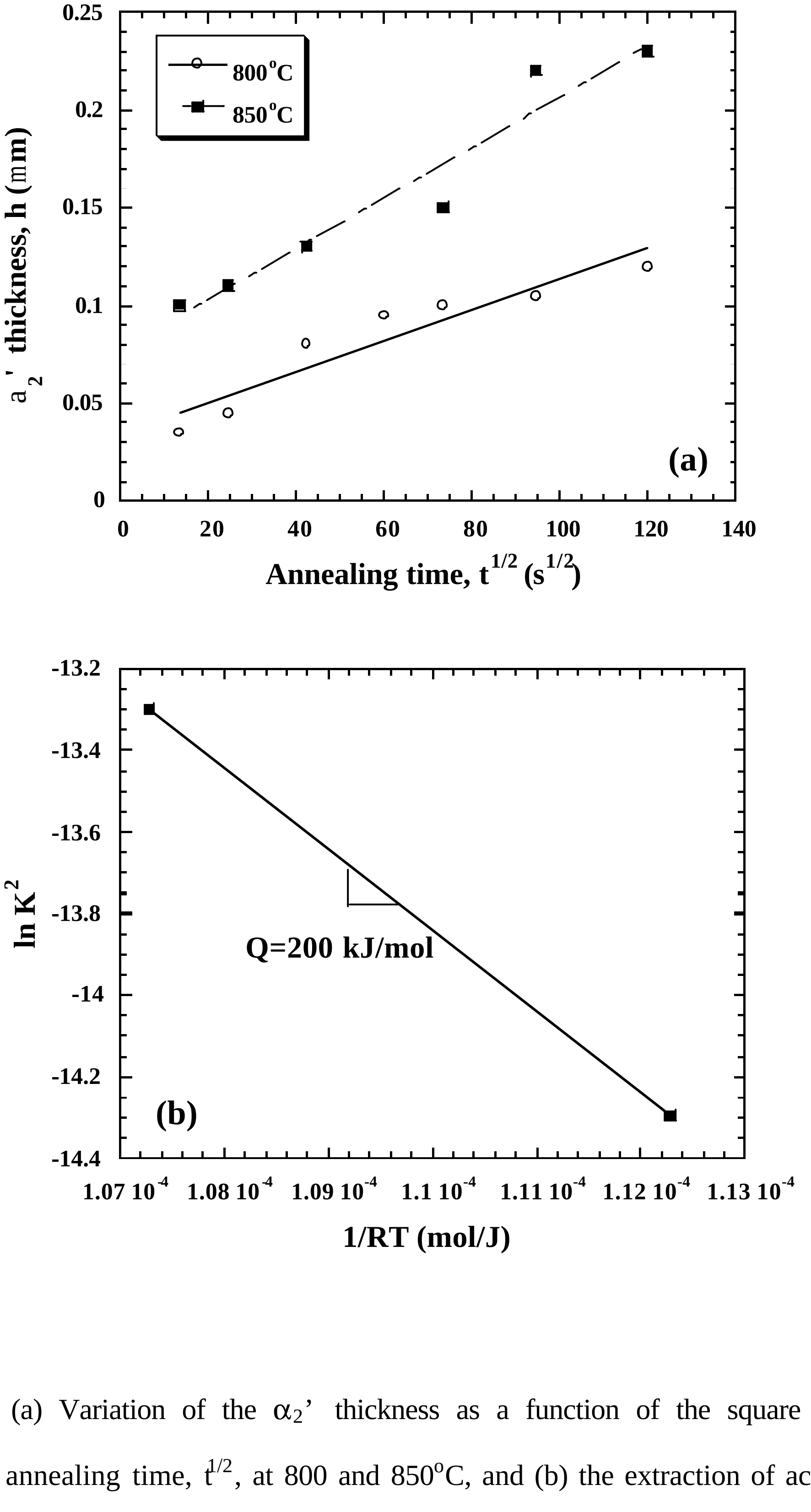

Fig. 67 (a) Variation of the α_2' thickness as a function of the square root of annealing time, $t^{1/2}$, at 800 and 850°C, and (b) the extraction of activation energy Q.

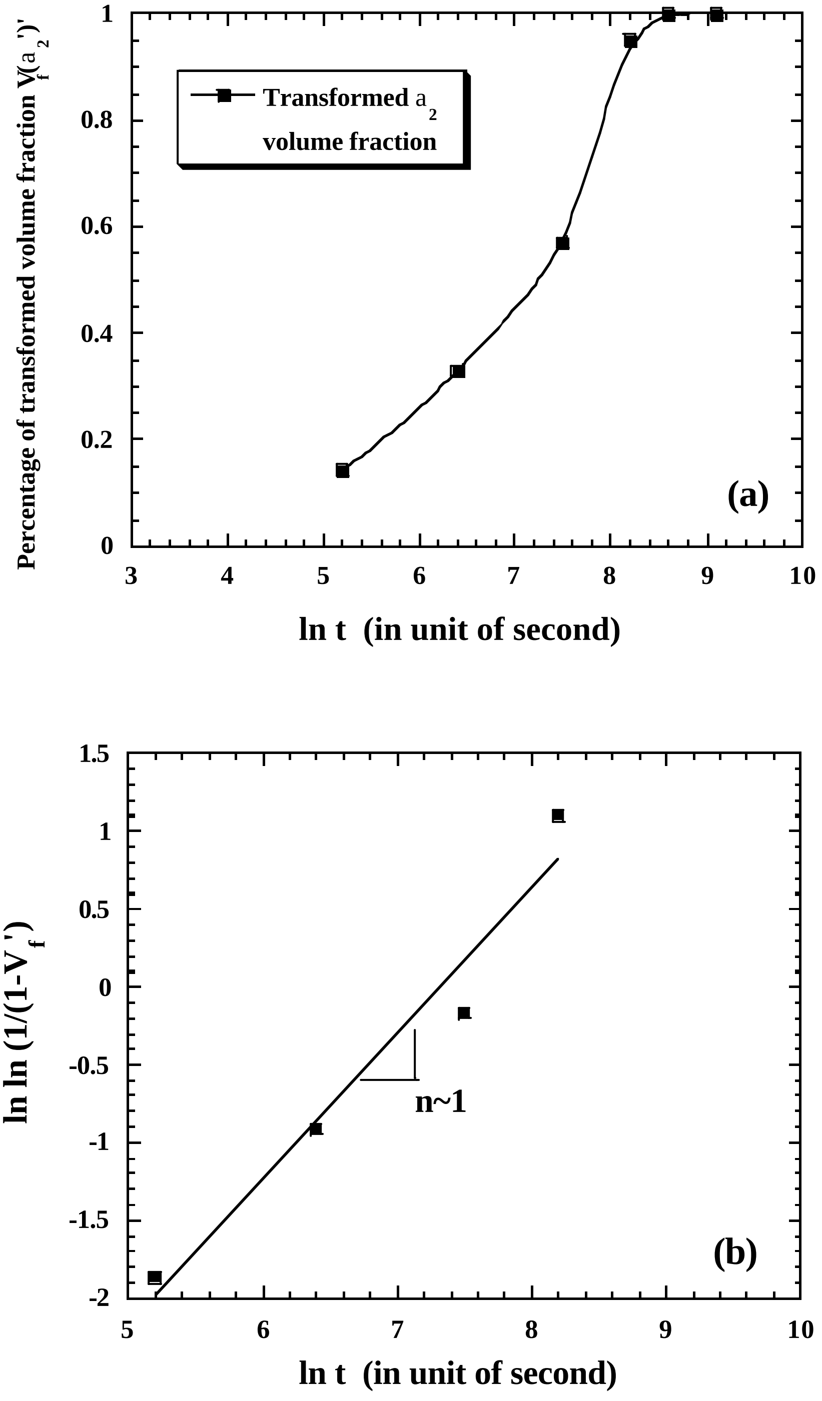

Fig. 68 (a) Variation of the double logarithm of the transformation percentage of the α_2' phase as a function of lnt, and (b) the extraction of transformation exponent n.

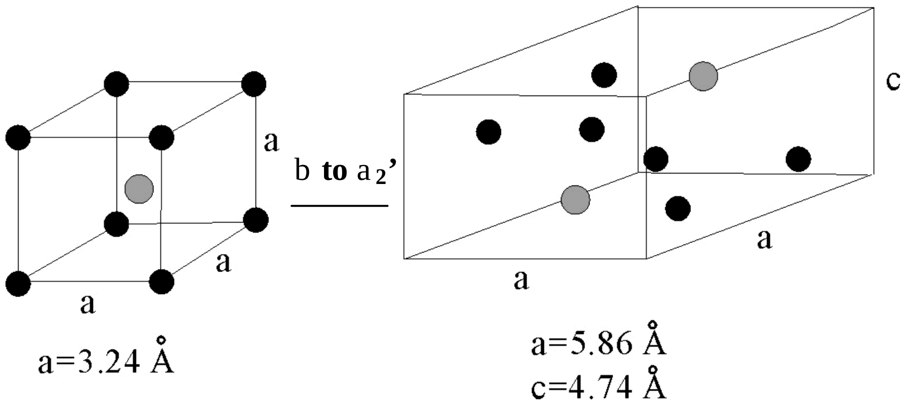

$$\Delta V = \frac{V_{a_2'} - V_b}{V_b} x100\% = \frac{a_1^{\,2} \sin 60^o c - 4 \cdot a^3}{4 \cdot a^3} x100\% = +3.6\%$$

Fig. 69 Illustrations of the volume change from the β to α_2’ phase.

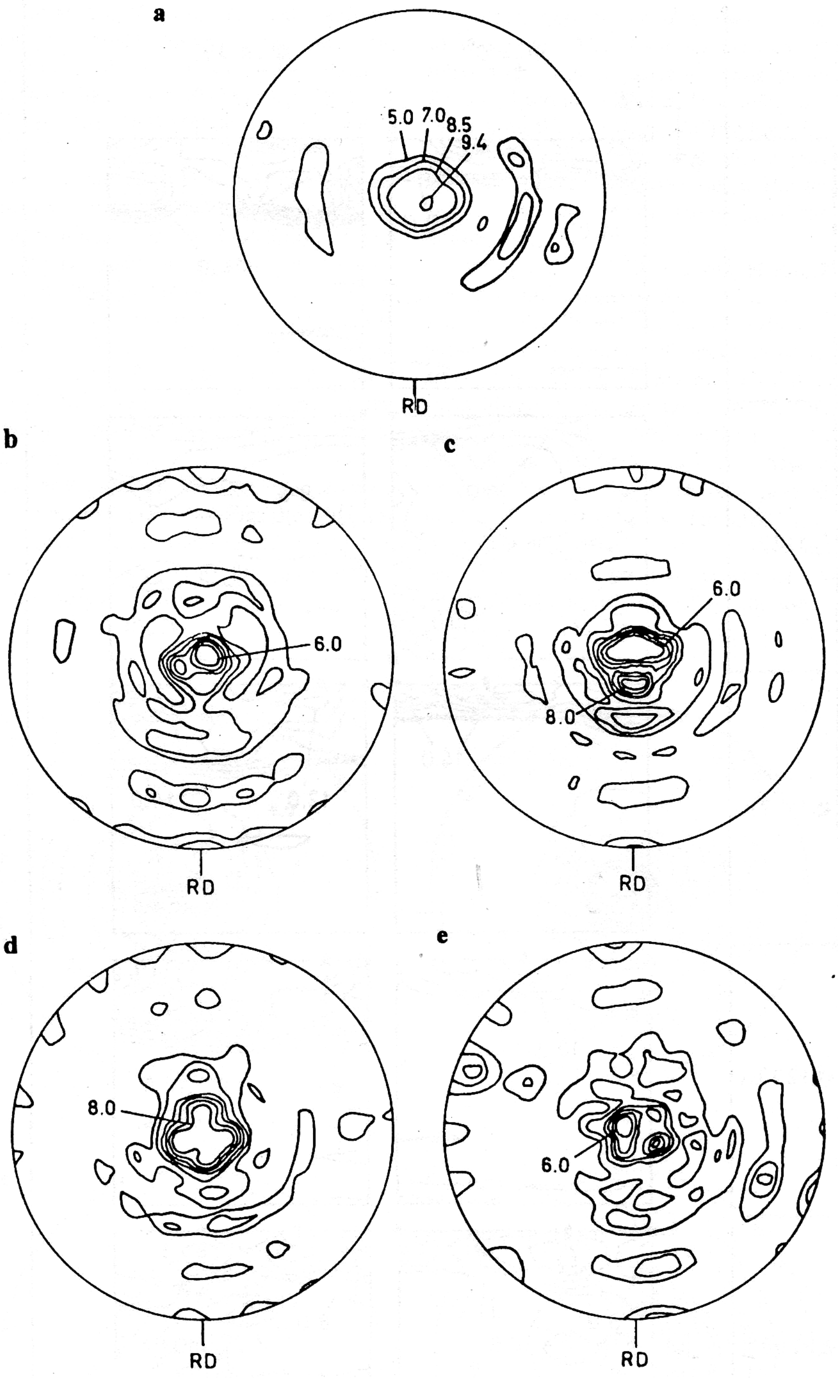

Fig. 70 (0002) pole figures for the specimens under the following conditions: (a) hot rolling and then isochronally annealed for 1 h at (b) 850, (c) 900, (d) 960, (e) 1020°C [91].